SEDIMENTOLOGICAL CHARACTERIZATION OF MATRIX-RICH AND ASSOCIATED MATRIX-POOR SANDSTONES IN DEEP-MARINE SLOPE AND BASIN-FLOOR DEPOSITS

JAGABIR NINGTHOUJAM

Thesis submitted to the University of Ottawa in partial fulfillment
of the requirements for the Ph.D. degree in Earth Sciences

Ottawa-Carleton Geoscience Centre and Department of
Earth and Environmental Sciences, Faculty of Science,
University of Ottawa

ABSTRACT

Deep-marine sandstones containing significant (> 10%) detrital mud (silt and clay) matrix have become increasingly recognized, but mostly in drill core or poorly exposed outcrops where details of their vertical and lateral variability are poorly captured. Exceptional vertical and along-strike exposures of matrix-rich and associated matrix-poor deposits in deep-marine strata of the passive margin Neoproterozoic Windermere Supergroup and foreland basin Ordovician Cloridorme Formation, provide an unparalleled opportunity to document such characteristics.

In both study areas, strata form a 100s m long depositional continuum that at its upflow end consists of thick-bedded matrix-poor sandstone (<20% matrix) that transforms progressively downflow to medium- to thick-bedded muddy sandstone (20 – 50% matrix) to medium-bedded bipartite facies with a basal sandy (30 – 60% matrix) part overlain sharply by a muddier part (40 – 80% matrix), and then to thin-bedded sandy mudstone (50 – 90% matrix). This depositional continuum is then overlain everywhere by a thin- to very thin-bedded traction-structured sandstone and/or silty mudstone cap. This consistent lithofacies change is interpreted to reflect particle settling in a rapidly but systematically evolving, negligibly-sheared sand-mud suspension developed along the margins (Windermere) and downflow terminus (Cloridorme) of a high-energy, mud-enriched avulsion jet.

Stratigraphically upward, beds of similar lithofacies type succeed one another vertically and transform to the next facies in the depositional continuum at about the same along-strike position, forming stratal units 2–9 beds thick whose grain-size distribution gradually decreases upward. This spatial and temporal regularity is interpreted to be caused by multiple surges of a single, progressively waning turbidity current, with sufficient lag between successive surges for the deposition of a traction-structured sandstone overlain by mudstone cap. Furthermore, the systematic backstepping or side-stepping recognized at the stratal unit scale in both the Windermere and Cloridorme is interpreted to be driven by a combination of knickpoint migration and local topographic steering of the flows, which continued until the supply of mud from local seafloor erosion became exhausted, the main channel avulsed elsewhere, or a new stratal element developed.

RÉSUMÉ

Les grès marins profonds contenant une matrice importante (> 10 %) de boue détritique (limon et argile) sont de plus en plus reconnus, mais principalement dans des carottes de forage ou des affleurements mal exposés où les détails de leur variabilité verticale et latérale sont mal saisis. Des expositions exceptionnelles, verticales et le long de la strie, de dépôts riches en matrice et de dépôts pauvres en matrice associés dans les strates marines profondes de la marge passive du supergroupe néoprotérozoïque de Windermere et de la formation ordovicienne de Cloridorme du bassin d'avant-pays, offrent une occasion sans précédent de documenter ces caractéristiques.

Dans les deux zones d'étude, les strates forment un continuum de dépôt des centaines mètres de long qui, à son extrémité amont, consiste en un grès pauvre en matrice à lit épais (<20% de matrice) qui se transforme progressivement dans la direction de courant en un grès boueux à lit moyen à épais (20-50% de matrice), en un faciès bipartite à lit moyen avec une partie basale sableuse (30-60% de matrice) fortement recouverte par une partie plus boueuse (40-80% de matrice), puis en un mudstone sableux à lit mince (50-90% de matrice). Ce continuum de dépôt est ensuite recouvert partout par une couverture de grès à structure de traction et/ou de mudstone silteux en couche mince à très mince. Ce changement cohérent de lithofaciès est interprété comme le reflet de la sédimentation de particules dans une suspension de sable et de boue à cisaillement négligeable, à évolution rapide mais systématique, qui s'est développée le long des marges (Windermere) et du terminus aval (Cloridorme) d'un jet d'avulsion à haute énergie, enrichi en boue.

Vers le haut de la stratigraphie, les lits de type lithofaciès similaire se succèdent verticalement et se transforment en faciès suivant dans le continuum de dépôt à peu près à la même position dans la direction de courant, formant des unités stratales de 2 à 9 lits d'épaisseur dont la distribution granulométrique diminue graduellement vers le haut. Cette régularité spatiale et temporelle est interprétée comme étant causée par de multiples poussées episodiques d'un seul courant de turbidité qui s'atténue progressivement, avec un décalage suffisant entre les poussées successives pour permettre le dépôt d'un grès structuré par traction et recouvert d'une couverture de mudstone. De plus, le recul systématique ou le déplacement latéral reconnu à l'échelle de l'unité stratale dans le Windermere et le Cloridorme est interprété comme étant le résultat d'une combinaison de la migration des points d'inflexion et de l'influence de la topographique locale sur le flux, qui s'est poursuivie jusqu'à ce que l'approvisionnement en boue provenant de l'érosion locale du fond marin soit épuisé, que le chenal principal soit avulsé ailleurs ou qu'un nouvel élément stratale se développe.

ACKNOWLEDGMENTS

First and foremost, I would like to profoundly thank my supervisor Dr. Bill Arnott for giving me the opportunity to pursue this project and for generously supporting me through the course of my PhD. Thank you for being an incredible mentor over the past few years. Your dedication and passion for sedimentary geology, and your enthusiasm for teaching are contagious and inspiring, and I feel very lucky to have had the opportunity to work under you. This thesis would not have been possible without the many thought-provoking discussions we had and the countless hours you spent editing and improving my mediocre-at-best writing. I would also like to thank Drs. Elisabeth Steel, Rob Rainbird, Don Cummings and Quentin Gall who agreed to read and referee this thesis and serve on my defense committee.

This project was provided by the Windermere Consortium, which is an industry and government supported research program directed by Dr. Arnott. Past and present sponsors of this consortium include Natural Sciences and Engineering Council of Canada, Husky Energy (Cenovus), Anadarko (Occidental Petroleum), Canadian Natural Resources Ltd., Apache, Nexen, and Equinor.

Thanks for financial awards, grants and aids I received during my PhD, particularly Brian Rust Memorial Graduate Scholarship, R. Dana Russell Memorial Grant 2019 (American Association of Petroleum Geologists Grants-In-Aid Foundation), and University of Ottawa Financial Aid Bursary and CUPE Financial Aids.

Many thanks to the past and present Windy crew including Alex Pipe, Anika Bergen, Celeste Cunningham, Curran Wearmouth, Dylan Cochrane, Gabriela Milczarek, Jessie Kehew,

Dr. Lilian Navarro, Mary Macquistin, Miguel St-Denis, Dr. Mike Tilston, Dr. Omar Al-Mufti, Patricia Fraino, Sean Ludzki, Simona Ruso, and Tyler Billington for all the intellectual discussions both in the field and on Friday afternoons at office. All of you are incredibly talented individuals and I am certain you will succeed wherever you go. I would also like to give a very special thanks to Tyler Billington, Miguel St-Denis, and Jessie Kehew for their field assistantship, and Alain Mauviel for preparing the numerous thin-sections for this project. The fascinating dataset of this thesis could not have been put together without your help.

A heartfelt thanks to my family for their everlasting love and support, especially to my parents Bapuchand Ningthoujam and Khoibi Waribam, my brother Jagabanta Ningthoujam, my sisters Bina and Babina Ningthoujam, my father-in-law Shyamananda Rajkumar, and my two fur-babies Bugzy and Phoebe.

Last, but certainly not the least, I would like to thank my wife Sheetal for loving me and always being there to support me through my ups and downs. Thanks for being the shoulder I can always depend on. You are the best partner anyone could have. I am incredibly lucky.

TABLE OF CONTENTS

LIST OF FIGURES

LIST OF TABLES

CHAPTER 1: THESIS INTRODUCTION

1.1 THESIS RATIONALE

The description, classification, and origin of deep-marine matrix-rich sandstones (i.e., sandstone with significant (> 10%) clay and silt matrix) have been debated since the 18th century when the term greywacke was introduced into the geological literature as 'grauwache' by Lasius (1789 in Huckenholz 1963). Sedimentologists have generally attempted to either define them based on their texture and/or composition (see review in Klein, 1963), or origin of the matrix (detrital vs. diagenetic) (see review in Cummins, 1962). However, it has been increasingly recognized in the distal reaches of both ancient (e.g., Haughton et al., 2003) and modern turbidite systems (e.g., Twichell et al., 1991) that there exists a variety of matrix-rich strata that are unlike classical turbidites or debrites and should be examined and interpreted based on their physical origin and associated depositional environments. Importantly, due to their high mud content, these matrix-rich strata have been reported to exhibit poor reservoir quality, and therefore are of concern in deep-water reservoirs (e.g., Lowe et al., 2003; Haughton et al., 2003; Kane and Pontén, 2012). Distinctively, these strata are made up of two-parts—a lower sandy part and an upper muddy part, but uncommonly, an intervening cm- to m-thick banded unit comprising light (mud-poor) and dark (mud-rich) bands is present (e.g., Barker et al., 2008; Haughton et al., 2009; Southern et al., 2017). Collectively, these strata have been variously termed slurry beds (Lowe and Guy, 2000), linked debrites (Haughton et al., 2003), co-genetic debrite turbidite beds (Talling et al., 2004), hybrid event beds (Haughton et al., 2009), transitional flow deposits (Kane and Pontén, 2012) and bipartite facies of matrix-rich sandstones (Terlaky and Arnott, 2014; Angus et al., 2019). Furthermore, these strata are reported to develop downflow of clean (i.e., less muddy) sands over

distances of hundreds meters (e.g., Terlaky and Arnott, 2014; Angus et al., 2019; Ningthoujam et al., 2022) to few kilometers (e.g., Lowe et al., 2003; Haughton et al., 2003; Fonnesu et al., 2018), to tens of kilometers (e.g., Davies et al., 2009; Talling et al., 2012a, 2012b, 2013). In all cases, deposition of the two superimposed layers are interpreted to be genetically related but explained by very different physical mechanisms including slurry flows that are an intermediate flow type between non-cohesive turbidity currents and cohesive debris flows (Lowe and Guy, 2000); hybrid flows consisting of at least two discrete and mechanistically different parts, namely a turbidite overlain by debrite (Haughton et al., 2009); longitudinal flow transformation (Kane and Pontén, 2012); vertical stratification effects and turbulence suppression in a high-concentration suspension (Talling, 2013; Kane et al., 2017); and particle settling in a negligibly sheared mixed mud-sand suspension (Angus et al., 2019). Much uncertainty arises because many of the examples are described from core or from discontinuous and generally poorly exposed outcrops and, as such, details of any vertical, and especially, lateral variability, remain poorly understood.

Accordingly, the objective of this thesis is to improve our understanding of the spatial and temporal distribution of matrix-rich and associated matrix-poor strata by investigating their lateral and vertical changes in two exceptionally well-exposed outcrops: slope to proximal basin-floor strata of the Neoproterozoic Windermere Supergroup exposed at Castle Creek, British Columbia, and distal basin-floor strata of the Cloridorme Formation exposed at Petite Vallee, Quebec. The superb exposure of these two outcrops permitted centimeter- to millimeter-scale observations to be carried out continuously over distances of tens of meters vertically, but more importantly, several hundreds of meters parallel to bedding.

1.2 GEOLOGICAL AND STRATIGRAPHIC SETTINGS OF THE WINDERMERE SUPERGROUP

The Neoproterozoic (740–570 Ma) Windermere Supergroup (WSG) is an unconformity bounded, 2 to 9 km-thick succession representing rift to drift sedimentation associated with the break-up of the Rodinia supercontinent and subsequent formation of the Proto-Pacific Ocean (Ross and Arnott, 2007; McMechan, 2015). The WSG crops out for over 4000 km from the Yukon-Alaska boarder to the Sonoran Desert in northwestern Mexico (Fig. 1.1A). In Mexico and the United States, the outcrops are discontinuous and comprise continental and shallow-marine strata (Link et al., 1993). Further north, the WSG crops out continuously from southeastern British Columbia to northwestern Yukon and consists of deep-marine siliciclastic rocks in the southern Canadian Cordillera (Campbell et al., 1973; Ross et al., 1995), and shelf and upper-slope strata farther north in the Mackenzie Mountains (Ross et al., 1995).

Initiation of WSG sedimentation is interpreted to have coincided with Neoproterozoic rifting of the supercontinent Rodinia and subsequent development of small rift basins (Stewart, 1972). In southeastern B.C. these isolated basins are filled with coarse-grained glaciomarine deposits of the Toby Formation intercalated with mafic volcanic rocks of the Irene Formation (Aalto, 1971; Ross et al., 1995) (Fig. 1.1B). Continued rifting ultimately led to the development of a deep-ocean basin (proto-Pacific Ocean) and formation of an extensive passive continental margin along the northern (now western) margin of Laurentia (Ross et al., 1995). The overlying post-rift succession (Fig. 1.1B), which is particularly well exposed in the Cariboo Mountains of east central British Columbia, consists of an up to 5 km-thick, upward-shoaling succession composed of sheet-like basin-floor sandstone and mudstone (Kaza Group) overlain successively by slope leveed-channel complexes (Isaac Formation), upper slope to outer shelf limestones

(Cunningham Formation), and high-energy mixed carbonate-siliciclastic continental shelf deposits (Yankee Belle Formation) interpreted to represent the progradation of the Laurentian (ancestral North America) continent margin into the thermally subsiding proto-Pacific Ocean (Ross, 1991; Ross et al., 1995; Ross and Murphy, 1988; Hadlari et al., 2021).

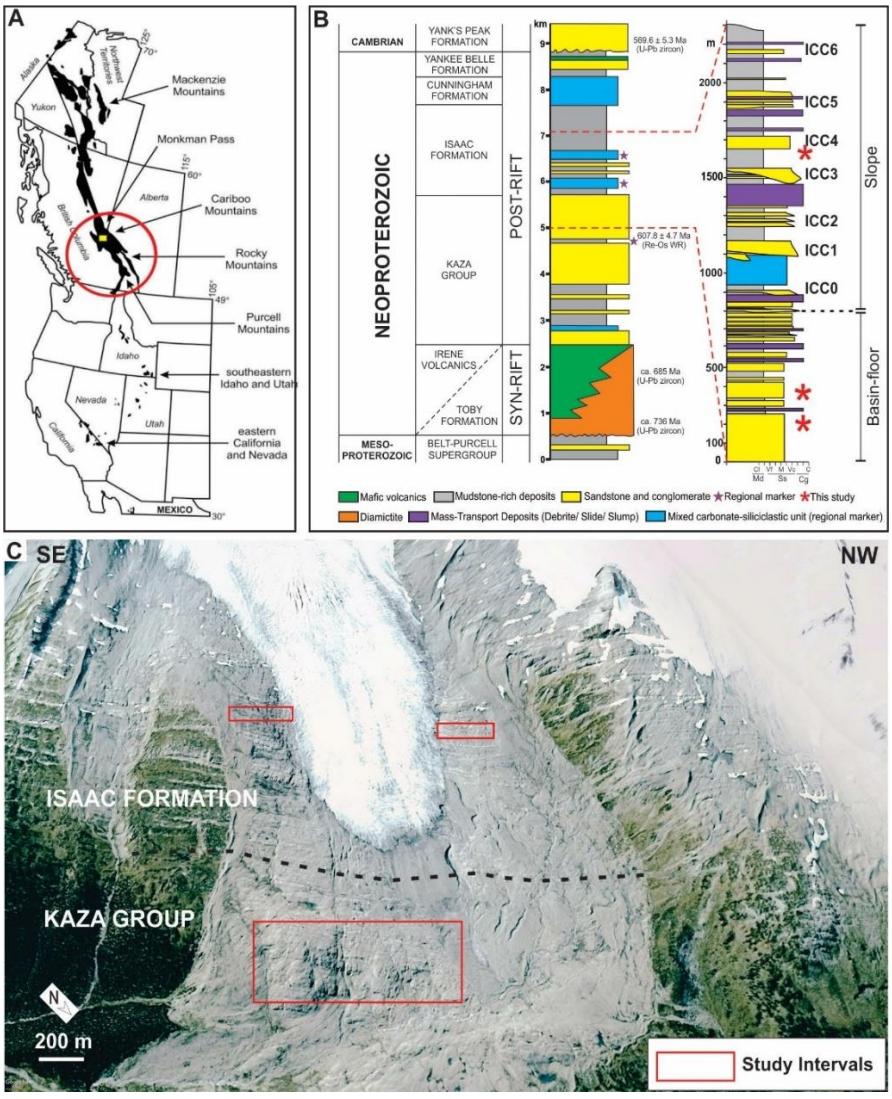

Figure 1.1: A) Distribution of exposed Windermere Supergroup strata in western North America. Red circle indicates the location of the Windermere turbidite system in the southern Canadian Cordillera and the yellow rectangle indicates the location of the Castle Creek study area (modified after Smith et al., 2014, from Ross, 1991). B) (Left side) Correlated schematic stratigraphy of the Windermere Supergroup. Age control is provided on the right of the log. (Right side) Generalized stratigraphic log of the Castle Creek outcrop. Here, strata consist of basin floor deposits of the Upper Kaza Group conformably overlain by slope channel deposits of the Isaac Formation. Labels on the right (ICC0 to ICC6) are informal names for Isaac slope channel complexes. Location of intervals described here are indicated by the red stars. C) Overview of the Castle Creek study area in the Cariboo Mountains, east central British Columbia, Canada (satellite image from Google Earth, 2019). The study intervals are highlighted by the red rectangles.

The geochronological control of the WSG in the southern Canadian Cordillera is poor due to a paucity of datable volcanic rocks, absence of biostratigraphic control, and the predominantly siliciclastic nature of the strata. Nevertheless, maximum and minimum ages of WSG are constrained by ages obtained from rocks occurring below and above the WSG sedimentary succession. U-Pb dating of crystalline basement rocks that unconformably underlie the WSG provide a maximum depositional age of WSG of 740–728 Ma (Evenchick et al., 1984; Parrish and Scammell, 1988). On the other hand, U-Pb dating of rhyolites in the Gog Group that unconformably overlie the WSG provide a minimum depositional age of 569.6 ± 5.3 Ma (Colpron et al., 2002). Furthermore, indirect ages derived from detrital zircons in syn-rift volcanic and magmatic rocks at the base of the Windermere sedimentary pile in other areas of western North America indicate rift associated volcanism between ~ 700–680 Ma, including the Gataga volcanics in the northern Canadian Cordillera (696–690 Ma) (Macdonald et al., 2018) and 700–680 Ma rift volcanic rocks in Idaho (e.g., Lund et al., 2003; Keeley et al., 2013). Most recently, a minimum age for rift-related volcanism was indicated by a zircon peak at ~ 666 Ma, which was interpreted to be coincident with continental break up, and therefore the maximum depositional age of the Windermere turbidite system (Hadlari et al., 2021). The only direct date reported from within the WSG is a Re-Os date from organic-rich mudstones in the Old Fort Point Formation at 607.8 ± 4.7 Ma (Fig. 1.1) (Kendall et al., 2004).

Despite the absence of biostratigraphic markers, regional correlations of the WSG strata throughout the southern Canadian Cordillera have been made possible by three regionally extensive marker units that include the Old Fort Point Formation and two deep-water limestone units. The ~ 50–450 m thick Old Fort Point Formation is characterized by a distinctive lithofacies

succession consisting of purple-coloured siltstone grading upward into rhythmic limestone–siltstone, organic-rich mudstone, and a heterolithic interval of conglomerate, sandstone, siltstone–mudstone and limestone. The OFP extends across the entire deep-marine WSG outcrop belt in the southern Canadian Cordillera and in the Cariboo Mountains separates the Middle and Upper Kaza groups (Smith et al., 2014). Strata are suggested to have been deposited during an abrupt basin-wide eustatic rise associated with the end of the Marinoan glaciation (Ross et al., 1995; Kendall et al., 2004) followed by a dramatic eustatic fall (Smith et al., 2014). In the Isaac Formation, two carbonate marker units are present and informally are termed the first and second Isaac carbonates (Fig. 1.1B). The Isaac carbonates are 10–250 cm thick units consisting of thin-to medium-bedded calciturbidites, calcidebrites, and large carbonate slump blocks that are interpreted to have been deposited during highstand conditions with attendant carbonate production on shelf and reduced siliciclastic input into the deep-water basin (Ross et al., 1995; Ross and Arnott, 2007; Cochrane, 2018; Cochrane et al., 2019).

Provenance studies of the WSG in the southern Canadian Cordillera reveal a bimodal distribution of 1950–1750 Ma (Paleoproterozoic) and > 2600 Ma (Archean) zircon ages suggesting that sediment was sourced mainly from the southern Canadian Shield and the eastern Belt Basin (Ross and Parrish, 1991; Hadlari et al., 2021). However, a single sample from the slope channel deposits of the Isaac Formation shows a subpopulation of 2300 –1900 Ma zircons suggesting a temporary change in provenance from east/southeasterly to northerly and then back to east/southeasterly (Hadlari et al., 2021). Aside from this temporary shift, regional paleocurrent data within the WSG indicate a general west–northwest direction of sediment transport, which is consistent with an eastern to southeastern sediment source (Ross and Arnott, 2007).

This study focuses on deep-marine strata of the WSG basin that are well exposed at Castle Creek (Fig. 1.1C) where vertically dipping, recently deglaciated, vegetation free strata of the Upper Kaza Group and Isaac Formation form an outcrop belt that is up to 2.5 km thick and 8 km wide, and where individual beds and bedsets can be traced for several tens to hundreds of meters along-strike. However, due to the paucity of three-dimensional outcrop in the study area, accurate assessment of paleoflow was difficult. Instead, in this study the consistent along-strike thinning and fining of individual beds and bedsets was assumed to broadly approximate local paleocurrent direction, and also represent a maximum length for any observed facies changes. Moreover, at Castle Creek, due to Mesozoic tectonism associated with the Cordilleran orogeny, the rocks have undergone low-grade (greenschist facies) metamorphism, which has resulted in alteration of primary clay mineral matrix to muscovite and chlorite and strain-induced structures like bulging recrystallization and sub-grain rotation along some grain boundaries (Popović, 2016). Despite these conditions, primary sedimentary features and most sedimentary textures, namely grain size, grain shape and sorting are well preserved, and therefore are described and classified as sedimentary rocks (Ross and Arnott, 2007).

1.3 PREVIOUS WORK (WINDERMERE SUPERGROUP)

This study is one of several that have described matrix-rich sandstones in the Windermere Supergroup (Arnott, 2007a, 2007b; Altosaar, 2007; O' Byrne et al., 2007; Davis, 2011; Terlaky, 2014; Terlaky and Arnott, 2014; Dumouchel, 2015; Popović, 2016; Angus, 2016; Terlaky and Arnott, 2016; Wearmouth, 2018; Angus et al., 2019; Arnott et al., 2021). The first comprehensive study of these strata was, undertaken by Terlaky and Arnott (2014), in which matrix-rich sandstones from the Upper and Middle Kaza groups were observed to undergo an along strike

facies transition from relatively matrix-poor (20 to 30% matrix) to matrix-rich sandstone (30 to 50% matrix) and then to thin-bedded turbidites over distances of 10s to 100s of meters. Moreover, matrix-rich strata were observed laterally adjacent to coarse-grained, matrix-poor, scour-based sandstones that contained large (up to 15 cm thick and 1 m long), often angular sandstone or mudstone clasts near their bases. Furthermore, Terlaky and Arnott (2014) reported matrix-rich strata to occur exclusively as several-meters-thick stratigraphic units in various depositional environments including the Isaac Formation (base of slope setting), Upper Kaza Group (proximal basin floor setting), and Middle Kaza Group (medial basin-floor setting), where they abruptly underlie matrix-poor architectural elements of coarse sandstone (slope channels, distributary channels and splays). These observations collectively led to the interpretation that matrix-rich strata represent deposition during activation of the local sedimentary system, most likely due to avulsion of an upflow channel. During avulsion, highly energetic flows likely scoured the mud-rich seafloor and charged the flows with fine-grained sediment. On the margins of the avulsed high-energy jet flow, particle settling resulted in deposition of matrix-poor followed by matrix-rich sandstones, and finally thin bedded turbidites. Notably, the occurrence of matrix-rich strata in a variety of paleogeographic settings, including base-of-slope and proximal to medial basin floor suggested that deposition of these strata was not paleogeographically, but rather mechanistically controlled.

Popović (2016) provided further insight into the along-strike facies changes of matrix-rich strata by conducting a detailed facies analysis in proximal basin-floor deposits of the Upper Kaza Group. In this study, an along-strike succession of facies from amalgamated matrix-poor sandstones (< 25% matrix) to amalgamated to better stratified clayey sandstones (25–40% matrix), to sandy claystones (> 50–70% matrix) and then to either fine-grained, banded couplets or thin-

bedded, upper division turbidites was reported over distances of 10s to 100s of meters. Like Terlaky and Arnott (2014), this systematic arrangement of facies was interpreted to represent deposition along the margins of an avulsed flow.

Angus (2016) further described the lateral depositional continuum of matrix-rich strata in the Upper Kaza Group, but also slope deposits of the Isaac Formation. In this study, strata were reported to exhibit a rapid lateral lithofacies transition from clayey sandstone (10–30% matrix) to a two-part bed consisting of a basal sandy part (10–45% matrix) overlain abruptly by a planar-based, clayey upper part (20–65% matrix), collectively termed bipartite bed. Laterally, the basal sandy part of the bed progressively thinned whereas the upper clayey part initially thickened and then remained constant in thickness thereafter. Further laterally, the basal sandy part pinched-out and the bed comprised entirely of sandy claystone, which then thinned and ultimately pinched-out. The entire transect was then overlain by a matrix-poor, thin-bedded turbidite that extended beyond the pinch-out of the clayey sandstone. This 10s to 100s m long lateral continuum was interpreted to reflect particle settling in a rapidly but systematically evolving, negligibly-sheared sand-mud suspension developed along the margins of a high-energy, mud-enriched avulsion-related wall jet (Angus et al., 2019).

Most recently, Wearmouth (2018) studied the vertical stacking pattern of matrix-rich strata in the Isaac Formation. In this study, based on field observation and statistical analysis (first order Markov chain analysis), lithologically similar facies were reported to typically succeed one another and form packages comprising 2 to 7 beds. Additionally, within a single package, beds were observed to undergo transformation from one part of the depositional continuum to the next at about the same lateral position. Based on these observations, the individual beds within a single package were interpreted to be deposited from successive avulsion related flows of similar

hydraulic and compositional character. Furthermore, at a larger scale (several meters), packages were observed to stack in three distinctive stratal assemblages: SA-1, composed of multiple packages of intercalated matrix-rich (clayey sandstone, bipartite bed and sandy claystone) and matrix-poor strata; SA-2, composed exclusively of matrix-rich packages; SA-3, made up of classical (matrix-poor) turbidites. Vertically, SA-1 and SA-2 were reported to stack together and were sharply bounded by successions consisting exclusively of SA-3. Additionally, SA-1 was observed to transition laterally into SA-2. This lateral and vertical juxtaposition of SA-1 and SA-2 was interpreted to reflect the abrupt lateral displacement of the axis of the main avulsion jet followed by a period of temporary stabilization.

1.4 GEOLOGICAL AND STRATIGRAPHIC SETTINGS OF THE CLORIDORME FORMATION

The Ordovician Cloridorme Formation (CF (460–445 Ma)) is one of several turbidite systems deposited along an elongate foreland basin located between cratonic North America to the northwest and the developing Taconic orogen and its associated volcanic arcs to the southeast (St-Julien and Hubert, 1986; Hiscott et al., 1986). This foreland basin extends from Newfoundland to Alabama and is separated into ~100 km long segments by structural highs (Hiscott et al., 1986). The CF crops out semi-continuously over about 150 km in intertidal exposures along the north shore of the Gaspé Peninsula, Quebec, Canada, and stretches from L'Anse-à-Valleau in the east to Marsoui in the west (Awadallah and Hiscott, 2004) (Fig. 1.2A). The Cloridorme sedimentary pile is interpreted to be sourced from an accretionary collage to the southeast that consisted of older cratonic clastic and carbonate rocks, a large ophiolite, and volcanic arcs associated with the ongoing Taconic orogeny (Enos, 1969; Beeden, 1983, Hiscott, 1984; Ma, 1996).

The depositional age of the CF (460–445 Ma) is constrained based on the presence of late Caradoc–Ashgill age graptolite assemblage zones ranging from *Nemagraptus gracilis* to *Climacograptus spiniferous* zone (Fig. 1.2B) (Riva, 1968). During this time period, at least 4000 m of basin-plain and submarine-fan deposits accumulated in the Quebec segment of the foreland basin forming the CF (Enos, 1969; Hiscott et al., 1986, Pickering, 1987). Here, based on lithofacies and extensive marker beds (megaturbidites), Hiscott et al. (1986) divided the CF into six members (Fig. 1.2B). The oldest St-Hélier member is up to 1140 m thick and represents distal basin-floor mudstones. Overlying the St-Hélier member is ~ 580 m thick outer-fan lobes and fan-fringe deposits of Pointe-à-la-Frégate member that transitions westward to basin-floor mudstone deposits of Manche d' Epée member (Fig. 1.2B). Stratigraphically upward, an ~ 835 m thick succession of outer fan lobes strata forms the Petite-Vallée member, which then is blanketed by a ~ 475 m thick mudstone deposit of Mont-St-Pierre member interpreted to have accumulated during the late Caradoc eustatic highstand. The youngest Marsoui member is ~ 1000 m thick and is interpreted to comprise mixed sand-and-mud deposits of the mid-fan setting. More recently, Awadallah and Hiscott (2004) reassessed the lower subdivisions (St-Hélier to Petite-Vallée member) of the CF by tracing and correlating 71 megaturbidite beds and 9 K-bentonite horizons and identified three allostratigraphic members (St-Hélier allomember, St-Yvon allomember, and Petite-Vallée allomember). The ~ 1150 m thick St-Hélier allomember is identical to the St-Hélier member of Hiscott et al. (1986), whereas the St-Yvon allomember makes up the lower ~ 320–350 m of the Pointe-à-la-Frégate member of Hiscott et al. (1986). The overlying Petite-Vallée allomember is ~ 1100 m thick and constitutes the remaining upper part of the Pointe-à-la-Frégate member and the Petite-Vallée member of Hiscott et al. (1986). Overall, paleocurrent analysis of the CF members indicates an initially westward-prograding deep-marine system (St-Hélier to Petite-Vallée

member), followed by deposition of a mud blanket during the late Caradoc global sea level rise (Mont-St-Pierre member), and succeeded by an eastward-prograding deep-marine system (Marsoui member) (Hiscott et al., 1986; Pickering, 1987).

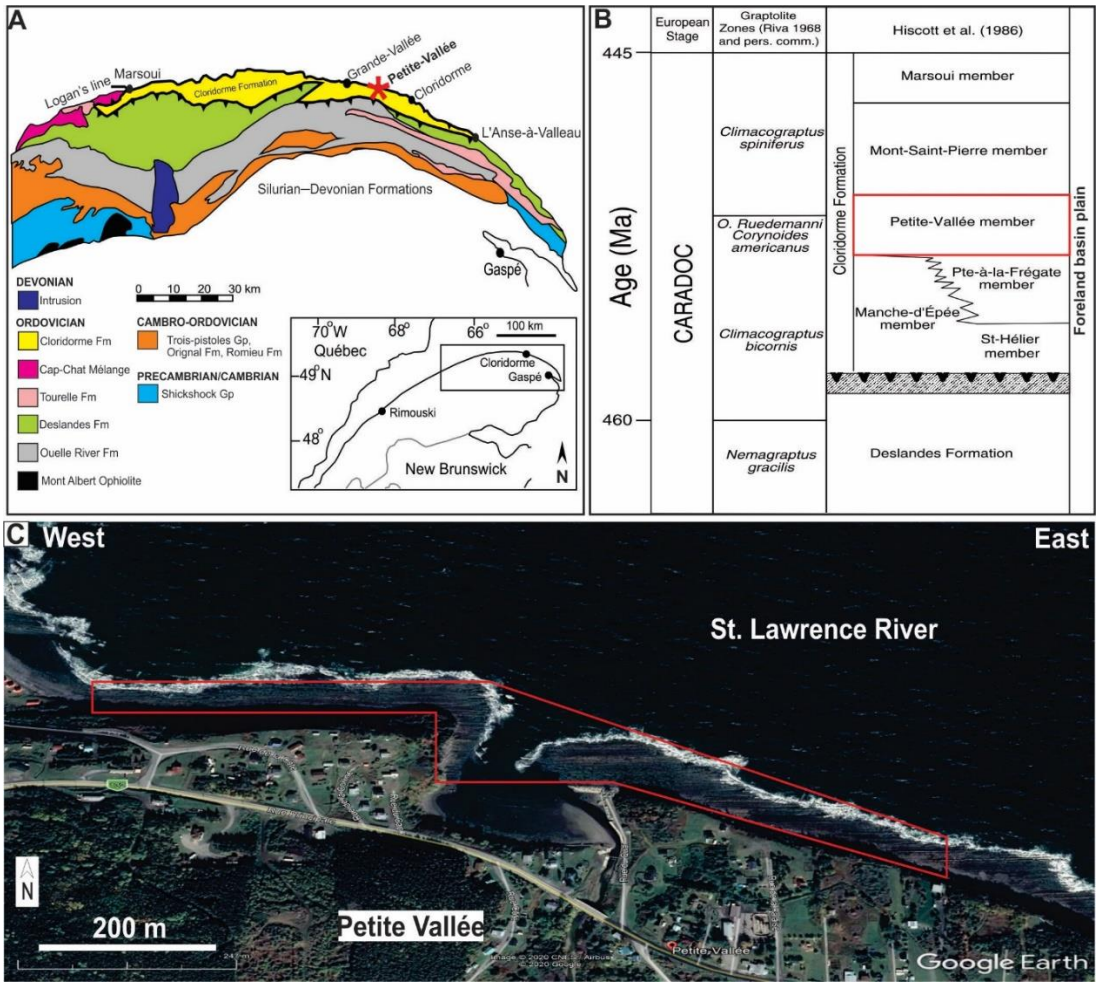

Figure 1.2: A) Distribution of the exposed Taconic foreland basin in the Appalachian orogen, and the location of the Cloridorme Formation in the Quebec Reentrant. Location of the study area is indicated by the red star (modified after Ma, 1996). B) Stratigraphic framework for the Middle Ordovician Cloridorme and Deslandes formations in southeastern Quebec (modified after Awadallah and Hiscott, 2004). C) Study area is located near the village of Petite Vallée, Quebec, Canada (satellite image from Google Earth, 2020). Rocks are exposed on a broad wave-cut platform and are overturned, dipping south at 65°– 88°. Red polygon indicates the study interval.

The CF study area is located near the village of Petite Vallée, Quebec (Fig. 1.2) where steeply dipping (average 78°), east-to-west (271°) striking exposures of the Petite Vallée member (*sensu* Hiscott et al., 1986) (ca. 300 m thick and ca. 1 km wide) crop out along an intertidal wave-

cut platform (Fig. 1.2C). Excellent outcrop conditions allowed individual bed and bedsets to be continuously traced and correlated over several tens to hundreds of meters along the strike of the outcrop. In this study area, average paleocurrent measured from troughs of three-dimensional ripples and tool marks on the base of beds (n=102) is 272° and therefore parallel to the strike of the outcrop. Additionally, paleocurrents elsewhere in the CF are generally reported to be towards the west (e.g., Enos, 1969; Parkash and Middleton, 1970; Pickering and Hiscott, 1985; Awadallah, 2002). Moreover, the rocks in CF have undergone very low-grade (zeolite to prehnite-pumpellyite facies) metamorphism associated with regional tectonic activity during the Taconic Orogeny (Jiang and Peacor, 1994) and as a result the primary clay mineral matrix has been altered to illite/muscovite and chlorite; however, this change has negligible effect on the sedimentary structures and textures, enabling these rocks to be described and classified using conventional sedimentary terminology.

1.5 PREVIOUS WORK (CLORIDORME FORMATION)

All of the earlier studies of matrix-rich sandstones in the Cloridorme Formation have been from the β7 member strata of Enos (1969) which is equivalent to the Petite Vallée member of Hiscott et al. (1986) exposed between Grande Vallée and Petite Vallée. These strata were initially termed greywackes (type 1 and 2) by Enos (1969). Type 1 greywacke was described as thin- to thick-bedded, massive to normally graded sandstone with an average matrix content of 34%. Type 2 greywacke, also referred to as argillaceous greywacke, was described as thin- to thick-bedded, ungraded to coarse-tail graded sandstone with an average matrix content of 56%. Both type 1 and type 2 greywackes were reported to contain common mud clasts and less common clasts of other lithologies. Notably, a consistent downflow transition from type 1 greywacke to type 2 greywacke

and then to laminated silty mudstone (also referred to as argillite facies) was reported over a distance of a few 100s m (see fig. 28 in Enos, 1969). This downflow facies transition was further investigated by Parkash (1970) by tracing eight greywacke beds belonging to the β7 member of Enos (1969) exposed in the Grande Vallée area over an along-strike distance of ~ 3 km. Like Enos (1969), Parkash (1970) and Parkash and Middleton (1970) reported a consistent downflow transition from graded type 1 greywacke to ungraded type 2 greywacke and then to argillite facies over a distance of several 100s m. Moreover, along the transect, type 1 greywacke beds were reported to develop a two-part (bipartite) character consisting of a sandy, coarser grained basal part overlain abruptly by a planar-based, muddier and finer grained, mudclast-rich upper part. This bipartite greywacke bed was interpreted to be deposited from a mixed sand–mud suspension in two phases. In the first phase, settling of sand particles formed a high-concentration, coarser-grained lower layer known as a "quick bed" in which the particles were supported by dispersive pressure. Subsequently, consolidation of this quick bed gave rise to the lower part of the bipartite bed. This was then followed by deposition from the muddier residual suspension which gave rise to the finer-grained upper part of the bipartite bed.

Besides lithofacies changes, Parkash (1970) noted a general downflow change in sole mark type, from groove marks, prod marks and isolated flute marks, to longitudinal ridges, and finally to occasional groove marks. In addition, the orientation of the sole marks was reported to become more dispersed with distance along the transect. Parkash (1970) suggested this downflow change was caused by downflow deceleration of turbidity currents. More specifically, in the proximal part of the depositional transect, the flow was interpreted to be highly turbulent that allowed some of the tools (i.e., argillite and calcisiltite clasts) to be transported close to the base of the flow by dragging or by saltation resulting in the formation of groove and prod marks. Additionally,

scouring of the bed in favourable places, like small bed-surface irregularities, formed the isolated flutes. As the flow decelerated further downstream, secondary helical cells developed close to the base of the flow which led to the formation of longitudinal ridges. At the same time, settling of sediment formed a high-concentration basal layer that caused the tools to be suspended higher in the flow where they eventually became deposited. Further downflow some of the remaining tools in the now mud-rich residual flow settled into the lower part of the flow and formed the occasional groove marks. Notably, the downflow increase in the variance of sole mark orientation was attributed to the decelerating turbidity current becoming increasingly influenced by seafloor topography.

1.6 THESIS OBJECTIVES AND STRUCTURE

The first aim of this thesis is to investigate the spatial evolution of matrix-rich and associated matrix-poor strata present in slope to basin-floor deposits. To accomplish this goal, 61 and 15 bed-by-bed stratigraphic logs were measured in the slope to proximal basin-floor strata exposed at Castle Creek and distal basin-floor strata exposed at Petite Vallée, respectively. In both outcrops, superb exposure allowed for detailed documentation of stratal thickness, bedding contacts, grain size, sedimentary structures, presence of clasts, and for beds to be traced continuously for at least several 100s of meters along the strike of the outcrops. In addition, over 200 thin-sections were analyzed to better characterized the sedimentary texture, and matrix and cement contents of these strata. The second objective of this study is to provide a comprehensive review of deep-marine matrix-rich sandstones that are documented in the geological literature with emphasis on their stratal make-up, stratigraphic occurrence, spatial scales and proposed physical origin. To do this a total of 95 publications between 1808 and 2022 were reviewed and critically

compared and contrasted. The third thesis objective is to better elucidate the vertical stacking character of matrix-rich and associated matrix-poor strata in the slope and proximal basin-floor deposits of the Neoproterozoic Windermere turbidite system and distal basin-floor deposits of the Ordovician Cloridorme Formation. This was carried out by combining field-based observations and statistical analyses. Field observations included lithofacies identification and qualitative determination of vertical stacking patterns at individual bed and stratal units (beds of similar lithofacies) scales. The observed stacking patterns at both stratigraphic scales were then quantitatively assessed using a first-order Markov chain analysis.

This dissertation is organized into five main chapters, and is a combination of thesis monograph and a series of paper-style manuscripts. In chapter 2, a review of sediment gravity flows, particle settling behavior in non-cohesive and cohesive suspensions as well as interaction between suspended sediment and fluid turbulence are presented as they collectively form the basis of the interpretations and discussions in later chapters. Chapters 3 to 5 are prepared as paper-style manuscripts, out of which chapter 3 is published in the Journal of Sedimentary Research, whereas Chapters 4 and 5 are intended for further modification and publication in peer-reviewed journals in the future. Chapters 3 and 5 are based on data collected from Castle Creek (WSG) and Petite Vallée (CF) study areas. Chapter 4 is a review article on matrix-rich sandstones.

Chapter 3 is an expanded version of the manuscript published in the *Journal of Sedimentary Research*, titled "Stratal characteristic and depositional origin of two-part (mud-poor overlain by mud-rich) and associated deep-water strata—components in a lateral depositional continuum related to particle settling in negligibly sheared mud-rich suspensions." (https://doi.org/10.2110/jsr.2021.053). The co-authors of this publication are Curran Wearmouth and Dr. R.W.C Arnott.

Chapter 4 is a manuscript in preparation for submission to *Earth-Science Reviews* and titled "From greywache to variously named sand- and associated mud-rich strata—clearing the muddy waters on a longstanding debate." The co-author of this publication is Dr. R.W.C Arnott.

Chapter 5 is a manuscript in preparation for submission to the *Journal of Sedimentary Research*, titled "Systematic vertical organization of matrix-rich and associated matrix-poor sandstones in ancient deep-marine slope and basin-floor deposits." The co-authors of this publication are Curran Wearmouth and Dr. R.W.C Arnott.

1.7 STATEMENT OF AUTHORSHIP AND CONTRIBUTION

Chapter 3 is based on fieldwork in the Castle Creek and Petite Vallée study areas that was carried out by the author, with assistance from Tyler Billington, Miguel St-Denis, Jessie Kehew, Curran Wearmouth and Dr. Arnott. Lithofacies analysis and thin-section petrography was carried out by the author to minimize operator bias and standardize potential error. Some of the data and interpretations for this chapter have been taken from previous matrix-rich sandstone studies including Terlaky and Arnott (2014), Angus (2016), Popović (2016), and Wearmouth (2018). All figures were drawn by the author, except where indicated. The initial manuscript for the chapter was written by the author and later revised through discussion with Dr. Arnott.

Chapter 4 is a literature review of a total of 95 articles on matrix-rich sandstones published between 1808 to 2022. All figures are author's own, except where indicated. The initial manuscript for the chapter was written by the author and later modified following discussions with Dr. Arnott.

Chapter 5 is based on the same fieldwork as chapter 3 and has benefitted from assistance by Tyler Billington, Miguel St-Denis, Jessie Kehew, Curran Wearmouth and Dr. Arnott. Some of the data for this chapter have been taken from previous matrix-rich sandstone studies including

Terlaky and Arnott (2014), Angus (2016), Popović (2016), and Wearmouth (2016). All figures were prepared by the author, unless original sources are cited. The initial manuscript was written by the author and later revised after discussions with Dr. Arnott.

CHAPTER 2: THEORETICAL OVERVIEW

2.1 SEDIMENT GRAVITY FLOWS

It is established from observations in lakes, fjords, flume experiments, as well as historical occurrences like the 1929 Grand Banks event (Heezen and Ewing, 1952), that the dominant agents for transporting and depositing sediment in the deep sea are sediment gravity flows (Normark and Piper, 1991). As their name implies, these are mixtures of sediment and water propelled by gravity. Unlike rivers, where fluid moves the sediment (fluid gravity flow), sediment gravity flows are generated by gravity acting on the density difference between a local sediment suspension and the surrounding ambient fluid (Middleton and Hampton, 1973; Navarro, 2016). Flows are initiated near the continental shelf break and along the continental slope by triggering mechanisms like earthquakes (e.g., Heezen and Ewing, 1952), local oversteepening of slope (Shanmugam, 2019), salt movement (e.g., Tripsanas et al., 2004), hyperpycnal river outflows (e.g., Piper and Normark, 2009), local storm re-suspension near the shelf edge (e.g., Piper and Normark, 2009), and tsunamis (e.g., Gutenberg, 1939). Once formed, these flows can transport over 100 km^3 of sediment 100s to 1000s of kms across the seafloor at speeds up to 100 km/h (Talling et al., 2012a, 2014). These submarine sediment movements can be broadly subdivided into two end-member types: mass movements (i.e., slides and slumps) and sediment flows (i.e., debris flows and turbidity currents). Mass movements are initiated when gravity exceeds the tensile strength of the sedimentary pile. Movement continues downslope until the resisting forces, mainly basal friction, overcomes the gravitational force and the entire sedimentary pile comes to rest. During movement mixing of ambient fluid into the sedimentary mass can cause it to inflate and particles to eventually become suspended in the fluid, generating a sediment gravity flow (Shanmugam, 2006). In this study mass

movement deposits are absent and therefore are not reviewed here. Instead, the remainder of the section focuses on the description and physical basis of sediment gravity flows.

Sediment gravity flows are traditionally classified into two end-member kinds—frictional flows (or turbidity currents) and cohesive flows (or debris flows) (e.g., Middleton and Hampton, 1973; Lowe, 1982; Mulder and Alexander, 2001); however, findings from ancient and modern deep-sea deposits, experiments, and theoretical models suggest a variety of intermediate flow types. To capture the key parameters and variations between flows, Mulder and Alexander (2001) proposed a comprehensive classification scheme based on physical flow properties, grain support mechanisms, and characteristics of flow deposits. In their classification, sediment-gravity flows are separated into two groups: (1) cohesive flows (mud flows and debris flows), and (2) non-cohesive friction flows (hyperconcentrated density flows, concentrated density flows and turbidity currents) (Fig. 2.1).

Cohesive flows, also termed debris flows, are sediment gravity flows with a pseudoplastic rheology and laminar flow character. Cohesion is generated in these flows by electrostatic bonding of clay particles forming a network structure of aggregated clay particles that increases fluid viscosity and develops mechanical strength, termed matrix-strength. This matrix-strength is the primary sediment support mechanism in cohesive flows; however, other mechanics like buoyancy effect, dispersive pressure, and elevated pore fluid pressure may also be important (Mulder and Alexander, 2001). Along the transport path, these cohesive flows may transform partially or completely into non-cohesive flows either through dilution at the head, and/or fluid entrainment along the upper boundary, or by passage through a hydraulic jump (Fisher, 1983; Weirich, 1988). Deposition of debris flows occurs *en masse* when the base of the downward thickening non-deforming plug reaches the bed. Debris flow deposits, or debrites are typically structureless and

massive, with particles up to boulders commonly dispersed in a matrix of mostly clay and silt grains (Mulder and Alexander, 2001).

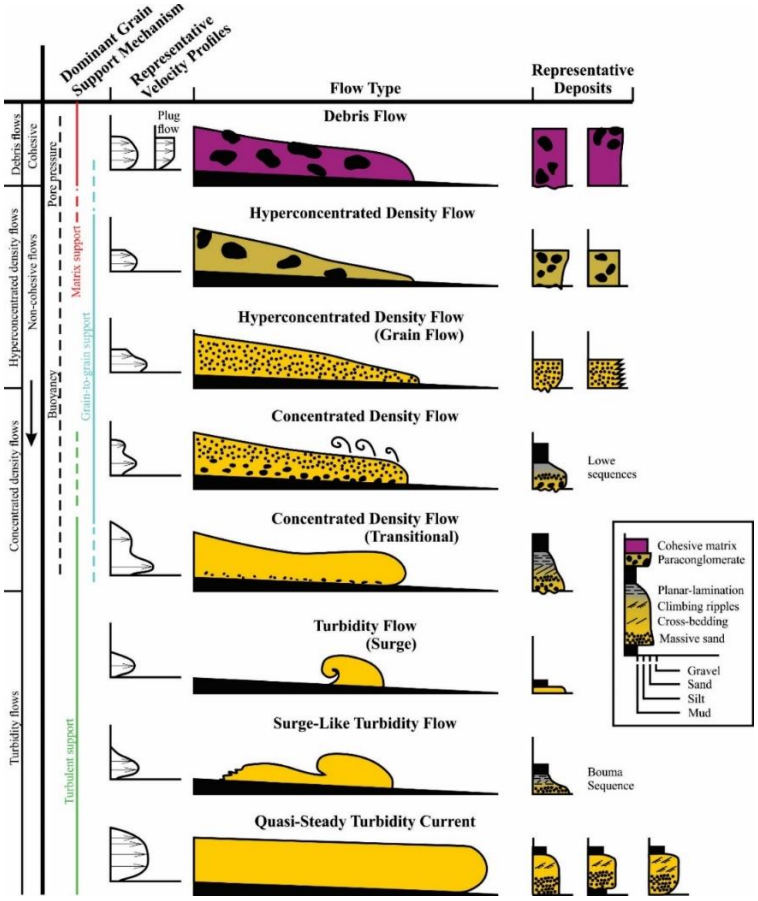

Figure 2.1: Schematic diagram showing the classification scheme for subaqueous sediment gravity flows. Flows are classified into two types: cohesive flows and frictional flows. Frictional flows are subdivided into hyperconcentrated flows, concentrated flows and turbidity currents. Also shown in this schematic are the dominant grain-support mechanisms, idealized velocity profiles, flow shapes, and representative stratigraphic logs (redrawn by Billington (2019) from Mulder and Alexander, 2001).

Unlike cohesive flows, frictional flows are sediment gravity flows composed dominantly of discrete particles that generally do not interact electrostatically, although limited cohesive strength may develop in some flows with concentrations of clay particles. Three kinds of frictional flows—hyperconcentrated density flows, concentrated density flows, and turbidity currents are recognized based on dominant sediment-support mechanisms including grain-to-grain interaction,

buoyancy, pore pressure, fluid turbulence, and bed support, all of which are dependent on flow conditions, sediment concentration, sediment type and grain-size distribution (Mulder and Alexander, 2001).

Hyperconcentrated density flows are made up of > 25 vol.% sediment, with < 2% mud content, and have a similar sediment-to-water ratio as cohesive flows. These conditions allow hyperconcentrated density flows to behave as a non-Newtonian fluid; however, due to the lack of cohesive sediment, flows do not exhibit matrix strength. Instead, sediment is supported principally by dispersive pressure (i.e., grain-to-grain interaction) (Mulder and Alexander, 2001). Deposition from these flows occurs by frictional freezing and results in deposits that consists of massive coarse silt, sand or gravel that locally is inversely graded. Notably, hyperconcentrated density flows may transform downflow into concentrated density flows, provided the flows becomes sufficiently diluted by fluid entrainment and the intensity and diffusion of fluid turbulence increases so that the particle suspension inflates (Mulder and Alexander, 2001).

Compared to hyperconcentrated density flows, concentrated density flows have a lower sediment concentration (9–25 vol.% sediment). The main particle support mechanism is dispersive pressure, although fluid turbulence is the dominant support mechanism near the top of the flow. Deposits typically have erosional bases and are coarse-tail graded, although massive and less commonly inverse graded beds are observed (Mulder and Alexander, 2001). Traction-transport structures are observed at the base of some beds.

A lower sediment concentration, specifically < 9 vol.% sediment (i.e., the Bagnold limit), particles are sufficiently spaced that grain-to-grain interaction is much reduced and the dominant particle support mechanism is the upward component of fluid turbulence. A turbidity current deposit, or turbidite, was first described in detail by Bouma (1962), and idealistically consisted of

five parts, termed the Ta through Te divisions (Fig. 2.2). The Ta division consists of structureless normally graded or massive sandstone interpreted to be the result of overcapacity conditions and deposition from direct suspension fallout with negligible bedload transport (Arnott and Hand, 1989). The overlying Tb division consists of planar-laminated sandstone deposited under conditions of reduced rates of sediment fallout with more prolonged bed-load transport (Navarro, 2016). The Tc division overlies the Tb division and comprises ripple cross-laminated sandstone deposited by migrating current ripples (Khan, 2012). The Tc division, in turn, is overlain by interlaminated siltstone and mudstone of the Td division, which reflects deposition by mixed traction and suspension sedimentation process (Lowe, 1982). Lastly, the top of the sequence is marked by mudstone Te division interpreted to be deposited by fine-grained suspension fallout (Lowe, 1982).

Finally, despite ongoing efforts in the scientific community to develop an all-encompassing classification scheme for sediment gravity flows and their associated deposits, interpretations based on characteristics observed in the sedimentary record remains problematic and controversial, especially in flows interpreted to be enriched in fine-grained sediment (e.g., Lowe and Guy, 2000; Haughton et al., 2003; Baas et al., 2011; Talling et al., 2012a). These flows are suggested to exhibit characteristics that are attributed to both laminar and fully turbulent flows (e.g., Lowe and Guy, 2000; Baas et al., 2011), but to date, only a small number of laboratory experiments have been conducted (Baas and Best, 2002; 2008; Baas et al., 2009, 2011, 2016a, 2016b; Sumner et al., 2009; Perillo et al., 2015; Hermidas et al., 2018; Koo et al., 2019), and accordingly our understanding of these enigmatic flows and their deposits remains poor. In the ancient sedimentary record strata interpreted to be deposited by such flows are termed “slurry beds” (Lowe and Guy, 2000), “linked debrites” (Haughton et al., 2003), “cogenetic debrite–turbidite bed” (Talling et al., 2004), “hybrid

event bed" (Haughton et al., 2009), "transitional flow deposits" (Kane and Pontén, 2012), and "matrix-rich sandstones" (Terlaky and Arnott, 2014). A comprehensive review of this plethora of terminologies and the various proposed physical origins is presented in Chapter 4.

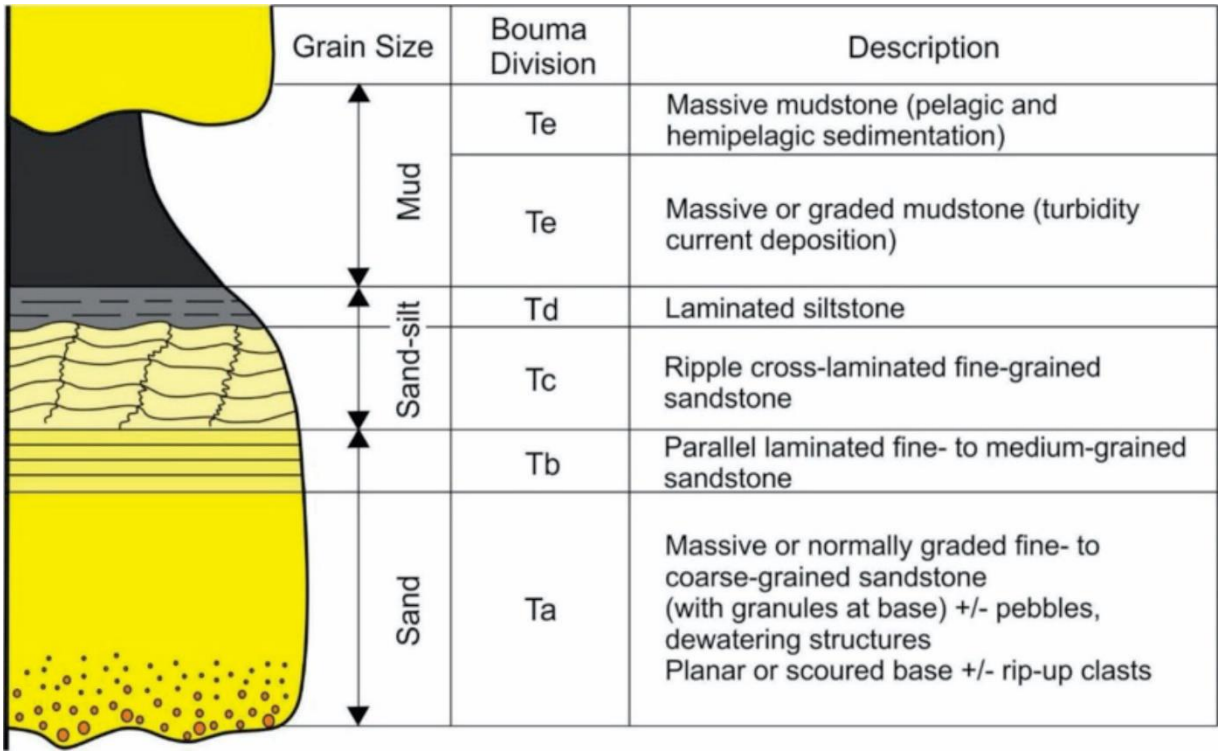

Figure 2.2: An idealized sequence of sedimentary textures and structures formed by a decelerating, low-density turbidity current. Note that the full succession is rarely preserved in turbidites (redrawn by Angus (2016) from Bouma, 1962).

2.2 PARTICLE SETTLING FROM NON-COHESIVE AND COHESIVE PARTICLE SUSPENSIONS

Deposition of lithofacies described in later chapters is interpreted to result from particle settling in a mixed sand–mud suspension undergoing negligible shear. Therefore, this section presents a brief discussion on particle settling from non-cohesive and cohesive particle suspensions to provide some theoretical background.

2.2.1 Settling behavior of a single non-cohesive particle

A non-cohesive particle's settling behaviour in a low Reynolds number (Re < 0.4) viscous fluid is described by Stokes law, where the terminal velocity of a single rigid sphere can be determined by equating the viscous drag force to the submerged weight of the particle:

$$u = \frac{d^2(\rho_s - \rho)g}{18\mu}$$

where u is the terminal settling velocity of the sphere, d is the diameter of the sphere, ρ_s is density of the sphere, ρ is the fluid density, μ the fluid viscosity, and g is the acceleration due to gravity. At low Re (< 0.4), viscous forces dominate, and the flow remains attached to the surface of the settling particle (Fig. 2.3). However, with increasing Re, inertial forces become increasingly prominent, and the flow becomes detached from the solid surface, causing flow separation and development of a wake on the downflow side of the particle (Fig. 2.3). Flow separation thereby reduces the skin friction drag and increases the importance of pressure drag, which changes with increasing Re (Chein and Wan, 1999). Stokes law, however, neglects the importance of fluid inertia, and in natural systems it can only be applied to particles with diameter up to ~ 0.14 mm (lower fine sand); larger particles will settle faster than predicted by Stokes law as inertial forces become increasingly more significant (Rubey, 1933).

At Re ~ 0.4–10^3, fluid inertia and viscous forces remain important. This, then, results in the development of large oscillating von Kármán vortices on the downflow side of the particle, which reduces skin friction, but generates considerable pressure drag (Fig. 2.3) (Smits, 2000). At still higher Re (10^3–2×10^5), viscous forces are negligible, and the particle's fall velocity depends

mostly on pressure drag. Under these conditions, turbulent eddies separate continuously on the downflow side of the particle, which decreases the particle's coefficient of drag (Chien and Wan, 1999). As Re exceeds 2×10^5 the boundary layer changes from laminar to turbulent. This, then, increases momentum exchange near the particle's surface, which decreases the adverse pressure gradient and shifts the separation point further downstream, and subsequently reduces the size of the wake and the overall drag force on the particle (Fig. 2.3) (Smits, 2000). Furthermore, if the surface of the particle is sufficiently rough turbulence will develop in the boundary layer at lower Re and decrease the drag force on the particle (Chien and Wan, 1999).

Sedimentation behaviour of a particle is also dependent on the shape and orientation of the settling particle. Specifically, for a nonspherical particle, changing the orientation of the particle can change the projected area that is normal to the direction of fall (Chien and Wan, 1999). Moreover, if flow separates from a particle, the location of the point of separation and the size of the wake could also depend on the particle shape (i.e., blunt bodies have higher coefficient of drag than streamlined bodies) (Chien and Wan, 1999).

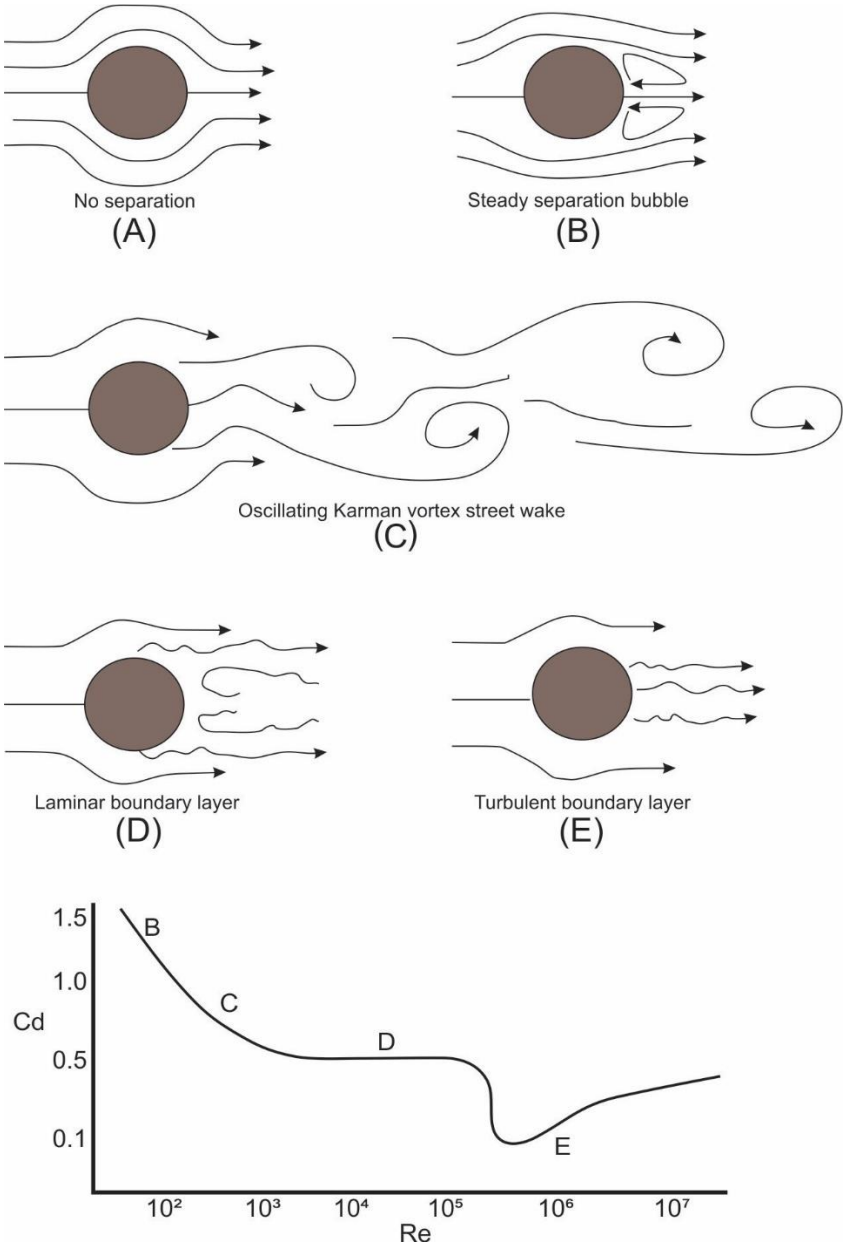

Figure 2.3: Characteristics of flow past a smooth blunt body (modified after Smits, 2000). Schematic of flow patterns around a spherical particle (A–E), and plotted as a function of fluid drag (Cd) and Reynolds number (Re) (F). A) At low Reynolds number of < 0.4 (A) no flow separation takes place and as such no viscous wake occurs downstream of the particle. Note that Reynolds number < 0.4 corresponds to a fluid drag of > 10 and therefore is not present in the accompanying graph (F). As Reynolds number increases (B), a steady separation bubble is developed which is marked by a pair of stable vortices. These vortices then impart a high drag on the particle. At Reynold s number of ~10^3 (C) Oscillating von Karman Vortex Street Wakes form. Downstream, these vortices progress and begin to separate on alternating sides of the body. Here, the wake is wide and as such the drag high. D) Laminar boundary layer with a chaotic wake downstream of the particle. E) Boundary layer becomes turbulent with vortices of many different scales being shed from the body. Additionally, the separation point moves further downstream, thereby reducing the size of the separation bubble and eventually the drag on the particle.

Importantly, the presence of sediment suspended in the fluid can also influence particle settling by increasing the effective viscosity of the fluid. For a dilute (< 2% volume sediment concentration) sediment suspension, the effective viscosity is defined by: $\mu_{eff} = \mu_0(1 + 2.5\,\phi)$, where μ_0 is the viscosity of the pure fluid in absence of particles, ϕ the volumetric concentration of the suspended particles (Einstein, 1905, 1911). Following Einstein's work, numerous expressions have been developed to determine the effective fluid viscosity for higher concentration (> 2% volumetric concentration) sediment suspensions. They are either theoretical expansions of Einstein's equation (e.g., Batchelor and Green, 1972; Thomas and Muthukumar, 1991b), or empirical expressions that were obtained based on experimental data (e.g., Barnes et al., 1989; Metzner, 1985; Mooney, 1951; Thomas and Muthukumar, 1991a). In all cases, increasing particle concentration results in increasing effective viscosity, or more fundamentally, greater perturbation of the flow field around the particles and increased total drag on the return-flow fluid, which then increases energy dissipation, and hence viscosity. Importantly also, increasing viscosity results in increasing buoyancy effects that serve to decrease particle settling velocity. Additionally, sediment finer than about lower fine sand would add mass to the fluid continuum, and therein augment buoyancy effects.

2.2.2 Settling behavior in a non-cohesive particle suspension

At low sediment concentrations (i.e., a few percent or less by volume), grains are spaced apart so widely that particle interactions are negligible, and the grains settle independently according to their size, shape and density (Amy et al., 2006). Under such conditions, a polydispersed suspension comprising 'n' discrete sizes of similar density and shape will develop 'n' layers during sedimentation. Here, segregation of particles takes place according to their

relative fall velocities, with the fastest settling particles deposited first, followed by the second fastest and so on until the slowest settling particles settle last (Davies and Birdsell, 1988). Due to their relative settling velocities, deposits of low concentration polydispersed suspensions are graded and well-sorted (Amy et al., 2006).

As particle concentration reaches a critical value of about 30–60% by volume, settling behaviour becomes influenced by hindered settling effects (Davies, 1968; Druitt, 1995). In these suspensions, settling particles generate a return flow of ambient fluid that imparts an upward drag force on the settling particle, and accordingly hinders its settling (Davies, 1968). In addition, finer particles may be carried upward with the return flow, which would increase the density and buoyancy effects of the fluid, and in turn further decrease the settling velocity (Davies, 1968; Amy et al., 2006).

Notably, an empirical settling equation that accommodated for the effects of hindered settling was formulated by Richardson and Zaki (1954):

$$\omega = \omega_{s,0}(1 - \phi)^n$$

where $\omega_{s,0}$ is the terminal velocity of a single particle in a still water, ϕ is the volume concentration of the suspension, and n is the model exponent, which under turbulent conditions (Re > 500) was reported to be 2.39; subsequent work (e.g., Cuthbertson et al. 2008) has shown that n can vary from 2.4 to 8 depending on the particle Reynolds number. Richardson and Zaki (1954) also showed an inverse relationship between particle concentration and sedimentation rate; specifically, sand particles in highly concentrated suspensions settled more slowly compared to similar sand particles in a suspension of lower concentration.

As particle concentration increases beyond 30–60% by volume, particle segregation is increasingly hindered and ultimately suppressed through either interlocking of grains or by

hydrodynamic effects, which results in an unsorted massive deposit (Davies, 1968; Lockett and Al-Habbooby, 1974; Amy et al., 2006). Grain interlocking is suggested to commence at the critical concentration when the space between the particles is reduced to less than the diameter of the particles thereby causing the grains to become geometrically trapped in a network of grains (Davies, 1968). Alternatively, based on the hindered settling equation, Richardson and Zaki (1954) demonstrated that beyond a critical concentration, hydrodynamic effects like the return flow of ambient fluid may completely suppress particle segregation. Later, Lockett and Al-Habbooby (1974) showed experimentally that beyond a concentration of 40% by volume, a bimodal suspension comprising particles of same size and shape, but different densities can settle together, or what was termed batch settling. In this case, hindered settling effects associated with grain size difference like grain interlocking was excluded as the bimodal suspension consisted of particles of same size and shape, and instead attributed to hydrodynamic effects (Lockett and Al-Habbooby, 1974). Additionally, Lockett and Al-Habbooby (1974) indicated that the critical concentration for batch settling was dependent on the relative proportion of grain sizes in a bimodal suspension—particularly, increasing the proportion of fines increased the critical concentration for batch settling. Nevertheless, both processes (i.e., grain interlocking and hydrodynamic effects) were suggested to potentially influence batch settling (Lockett and Al-Habbooby, 1974).

More recently, a theoretical model for the sedimentation behaviour of bidispersed and polydispersed suspensions was proposed by Dorrell and Hogg (2010) and Dorrell et al. (2011). This work was then extended to explain the development of a basal massive deposit overlain by a well sorted, graded deposit reported in the particle settling experiments of Amy et al. (2006). Dorrel et al. (2011) demonstrated quantitatively that the ungraded basal part of the deposit was the result of a constant mass flux of particles from a polydispersed suspension. Here, regardless of

different size particles settling at different velocities, the mass flux of sediment into the deposit remained constant and constituted the same grain size distribution as in the initial suspension (i.e., "n" particles) (Fig. 2.4). However, with time, the largest grains became depleted, and the deposit becomes populated by n-1 particles and so on until only the finer particles remain in suspension, which eventually settle to form the top of the deposit.

2.2.3 Settling behavior of cohesive particles

The atomic lattice of clay minerals consists of one or two silicon tetrahedral sheets and one octahedral alumina or magnesium sheet. Clay minerals generally develop a net negative charge on the face of the mineral due mainly to isomorphous substitution of Al^{3+} for Si^{4+} in the tetrahedra, or Mg^{2+} for Al^{3+} in the octahedra (van Olphen, 1963). If these minerals are suspended within a fluid that contains cations such as sea water, the net negative charge of the clay minerals is counterbalanced by bonding of cations and water molecules to the exterior surfaces of the clay minerals. This arrangement on the surface of the clay minerals is referred to as the electric double layer (van Olphen, 1963). The first layer of the double layer comprises a thin film of adsorbed cations on the surface of the clay mineral, whereas the second layer is loosely associated with the clay mineral and contains counter ions that move in the fluid under the influence of electrostatic attraction rather than being firmly anchored (Tan, 1982). This layer of counter ions is often referred to as the 'diffuse' or 'Gouy layer' and has a cation concentration gradient that decreases with distance from the clay mineral (van Olphen, 1963). Overall, the presence of this electric double layer causes the clay minerals to become neutrally charged at a certain distance from the surface of the mineral. At this distance, the attractive Van der Waals forces exceed the interparticle double layer repulsive forces and the net force becomes attractive. This, then, allows the clay particles to

aggregate together in a process known as coagulation or flocculation (Winterwerp and van Kesteren, 2004). Clay particle flocculation results in three different particle arrangements: face-to-face, edge-to-face, and edge-to-edge (van Olphen 1963). An edge-to-edge and edge-to-face arrangements can create a house of card framework, whereas a face-to-face can produce a band-like network (Lagaly, 1989).

In terms of their settling behaviour, at low concentrations, clay particles settle according to their settling velocities. However, in high concentration clay suspension, the collision rates of the clay particles increase, and by extension the potential for clay particles to interact and bond with adjacent clay particles (McAnally et al., 2007). Accordingly, progressive flocculation and aggregation increase the aggregated clay particle size and thus the fall velocity. McAnally et al. (2007) also added that fluid turbulence may enhance aggregation by increasing collision rates; however, if too intense can lead to the break-up of the delicate clay aggregates.

As clay-particle aggregates continue to grow in size, a point may be reached where they form a pervasive, volume-filling network termed a gel (e.g., Baas et al., 2009). At this point, the suspension develops sufficient viscosity to impart a yield strength to the suspension, which then impedes the settling of all particles (Berlamont et al., 1993; Amy et al., 2006). Additionally, increase in buoyancy effects is suggested to further reduce or arrest the settling of suspended sediments (Berlamont et al. 1993).

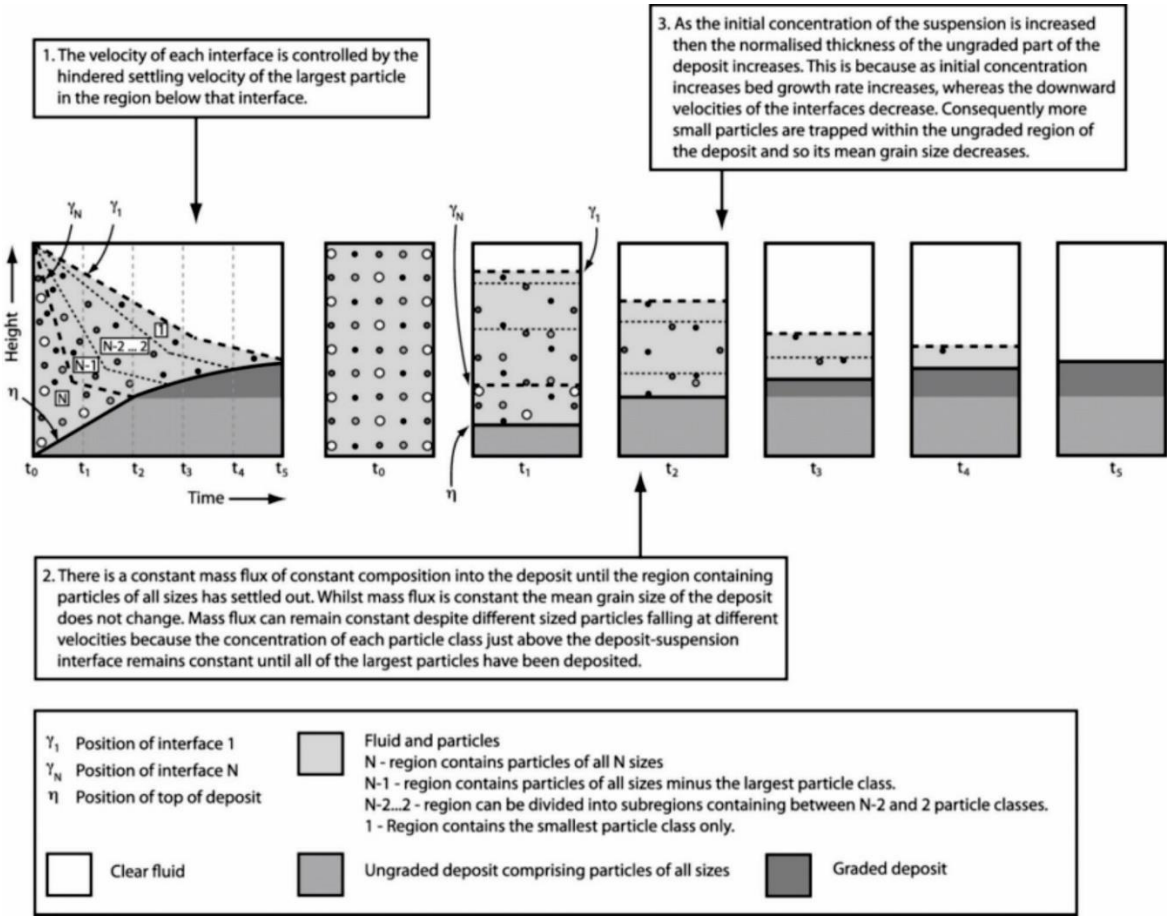

Figure 2.4: Schematic showing the temporal sedimentation behaviour of a polydisperse (particle) suspension. The initially well-mixed suspension comprises N+2 layers—the deposit at the bottom of the suspension, N layers containing particles, and layer of clear fluid above the suspension. Notably, the settling velocity of each layer in the N layer is controlled by the hindered settling velocity of the largest particle in the region below the interface (after Dorell et al., 2011).

2.3 SUSPENDED SEDIMENT AND FLUID TURBULENCE

As some of the discussions in the later chapters deal with the influence of suspended sediment on characteristics of fluid turbulence. This section, therefore, presents a brief overview of some of these interactions.

Experimental investigations and numerical simulations have shown that suspended sediment particles can either enhance or suppress turbulence depending on their size and concentration (e.g., Gore and Crowe, 1989; Hetsroni, 1989). Several mechanisms have been proposed for the observed modulation of fluid turbulence by the presence of suspended sediment.

For dilute suspensions, turbulence reduction or suppression has been associated with the enhanced inertia and effective viscosity of the particle-laden flow, as well as increased dissipation resulting from particle drag (Balachandar and Eaton, 2010). On the other hand, turbulence enhancement has been linked to increased velocity fluctuations related to wake dynamics and vortex shedding, and buoyancy induced instabilities linked to variation in density caused by local differences in particle concentration (Balachandar and Eaton, 2010).

In sediment-laden turbulent flows, three parameters have been used to define and characterize the effects of suspended sediment on fluid turbulence. The first criterion suggests that when particle diameter *D* is much smaller than the most energetic eddy, assumed to be equivalent to the integral length scale of turbulence λ, the particle will follow the eddy for part of its transit time (Gore and Crowe, 1989). As a result, a portion of the turbulent energy of the eddy is expended to accelerate the particle (via fluid drag), thereby reducing turbulent energy in the carrier fluid (Gore and Crowe, 1989). On the other hand, if the *D* is relatively larger, particles tend to develop turbulence in their wakes that is close to the scale of the most energetic eddy λ, which then increases the total turbulent energy in the fluid. Additionally, Gore and Crowe (1989) indicated that the critical threshold for the transition from turbulence suppression to turbulence enhancement occurs at $D/\lambda = 0.1$. The second parameter controlling turbulence modulation is the presence of slip velocity between the particle in transport and the carrier fluid. This slip velocity can be expressed in terms of particle Reynolds number $\mathrm{Re_p}$ ($Re_p = (u_f - u_p)D/v$, where u_f is the local mean stream velocity of fluid, u_p is the local mean stream velocity of the particle, and v is the kinematic viscosity of the sediment-laden flow). According to Hetsroni (1989), if $\mathrm{Re_p}$ is low ($\mathrm{Re_p} < 400$), turbulence tends to be reduced in the presence of suspended sediment, whereas if $\mathrm{Re_p}$ is relatively high ($\mathrm{Re_p} > 400$), vortices shed from particles in transport increases fluid

turbulence. The third parameter relates to the difference in response time of the particle in transport t_p to that of the carrier fluid t_f. The ratio of the particle response time t_p to the characteristic time scale of the fluid flow t_f is defined by the Stokes number (St):

$$St = \frac{t_p}{t_f} = \frac{\frac{1}{18\upsilon} D^2 \frac{\sigma}{\rho}}{\lambda / u_{rms}}$$

where υ is the kinematic viscosity, σ is particle density, ρ is fluid density, λ is the turbulence length scale and u_{rms} is the root-mean-square of the streamwise velocity fluctuations. According to Elghobashi (1994), if St < 1, the surface area of suspended particles increases for a given volumetric suspended sediment concentration (i.e., as grain diameter (D) decreases, surface area increases), which causes the rate of turbulence dissipation ε to increase. On the other hand, if St > 1, the particle Reynolds number increases resulting in vortex shedding and increase in turbulence intensity.

Recently, experiments and numerical simulations studying the interaction between suspended sediment and fluid turbulence has been focused mostly on understanding the influence of particle concentration. Bennett et al. (2014) measured turbulence in a mixing box with an oscillating grid and using a range of suspended particle concentration. Here, as suspended sediment concentration increased for a given oscillation frequency (i.e., turbulence generation), the intensity and kinetic energy of fluid turbulence exhibited a systematic and marked decrease. Although local turbulence enhancement and suppression were observed simultaneously in the same flow field, the net effect of suspended sediment was to reduce fluid turbulence and total kinetic energy. This suppression of fluid turbulence was suggested to be caused by the transfer of turbulent fluid kinetic energy to the suspended particles, and therein the maintenance of the particle suspension.

More recently, Eggenhuisen et al. (2017) used a force balance approach to analyze particle suspension in the near-boundary region of a no-slip, particle-suspending turbulent flow. The force balance parameter (Γ), termed the suspension capacity parameter, is the ratio of gravity and buoyancy forces acting on the sediment, and vertical turbulent fluid forces:

$$\Gamma = \frac{F_{turb}}{F_g} = \frac{u_*^3}{140\upsilon g R C_b}$$

where u_* is the shear velocity, υ is the kinematic viscosity of water, g is the acceleration due to gravity, C_b is the volumetric sediment concentration near the bed, $R = (\rho_s - \rho_f)/\rho_f$ is the relative density of the sediment where ρ_s and ρ_f are particle and fluid densities, respectively, and 140 is a numerical constant derived from universal scales of vertical turbulence in boundary layer flow.

When $\Gamma > 1$, the average turbulent force in the flow exceeds the net gravitational pull on the suspended particles and the suspension is considered under-saturated. Here, turbulent conditions are able to maintain more sediment in suspension and as such if additional sediment is available it will be entrained. At $\Gamma = 1$, average turbulent forces in the near-wall region of the flow are of similar magnitude to the gravitational pull on the suspended sediment particle load. This condition prevents net vertical acceleration of the particles and the fluid between them. The flow is precisely saturated with suspended sediment near the boundary, and C_b can be considered the saturation concentration, and the flow at capacity. When gravitational pull on the sediment exceeds the upward turbulent forces (i.e., $\Gamma < 1$), the flow cannot suspend all the particles in the near-boundary region, and the flow becomes over-saturated. According to Eggenhuisen et al. this condition can be interpreted from two perspectives—a particle perspective and a continuum perspective, but both result in sediment being deposited from the base of the flow. From a particle perspective, particles are postulated to, on average, experience a wall-bound gravitational body force that exceeds turbulent pressure and viscous forces acting on the particle surfaces. This, then,

causes the particles to accelerate towards and settle onto the boundary. On the other hand, if this condition is observed from a continuum perspective, the upward turbulent forces are less than downward gravitational forces applied to the fluid by the particles, which prevents turbulent accelerations and results in turbulence extinction. Moreover, sediment stratification increases towards the base of the flow as there is no mechanism countering the gravitational settling of sediment.

This second perspective is consistent with some of the more recent numerical simulations of sediment-laden turbulent flows (Cantero et al., 2009, 2011, 2012) that show how turbulence at the base of the sediment suspension is rapidly suppressed in over-saturated conditions. In these studies, the complete suppression of turbulence at oversaturation is demonstrated by the disappearance of the streak vortices that form the legs of hairpin vortices. Being the dominant feature of near-boundary turbulence (Smith and Walker, 1995; Zhou et al., 1999), the loss of hairpin vortices indicates a complete shutdown of the production of near-boundary turbulence. Ultimately, turbulence suppression results in a stably stratified flow condition that becomes manifest as a concentration profile that increases monotonically toward the wall (i.e., bed).

Aside from non-cohesive sediments, the presence of cohesive sediment (i.e., clay) in suspension can significantly influence fluid turbulence due to their unique ability to aggregate and form aggregated particle networks termed flocs, and ultimately develop strength to form a gel. The contribution of clay in turbulence modulation is discussed in detail in chapter 4, and as such only a brief overview is provided in this section.

In the open-channel flow experiments by Wang and Plate (1996), it was demonstrated that at > 2% volume clay concentration, flows exhibited both turbulent and laminar characteristics. More specifically, the flow consisted of three parts, which from base to top are laminar sublayer

where turbulence was absent, a turbulent layer, and an upper plug layer with weak or no turbulence. Later work by Wang et al. (1998), showed that at > 3% volume clay concentration, open-channel flows showed a reduction in bed-generated turbulence and turbulence intensity, which were attributed to increase in the local effective fluid viscosity and reduction in the local velocity gradient. Baas and Best (2002) expanded on the work of Wang and co-workers by investigating clay-laden open-channel flows with volume kaolin concentration ranging from 0.002 to 12.9% and a constant depth-averaged flow velocity of 0.33 m/s. These experiments demonstrated that at low clay concentration (< 2 vol. %) flows were fully turbulent and exhibited a logarithmic velocity profile like a clear water flow. However, at 2–4 vol. %, flows where characterized by a tripartite structure similar to Wang and Plate (1996), with a near-bed region of anomalously high turbulence intensity that developed in a region coincident with an abrupt change in the velocity gradient. Additionally, reduced turbulence intensity in the upper part of flows was attributed to particle aggregation that increased yield strength and reduced fluid turbulence with distance from the bed, and as a consequence the upward diffusion of sediment.

CHAPTER 3: STRATAL CHARACTERISTIC AND DEPOSITIONAL ORIGIN OF TWO-PART (MUD-POOR OVERLAIN BY MUD-RICH) AND ASSOCIATED DEEP-WATER STRATA—COMPONENTS IN A LATERAL DEPOSITIONAL CONTINUUM RELATED TO PARTICLE SETTLING IN NEGLIGIBLY SHEARED MUD-RICH SUSPENSIONS

3.1 INTRODUCTION

In the ancient deep-marine sedimentary record, distinctive two-part (bipartite) deposits comprising a sand-rich basal part overlain sharply by a mud-rich upper part have been reported in the distal reaches of basin-floor lobes (e.g., Haughton et al., 2003; Talling et al., 2004; Davis et al., 2009; Hodgson, 2009; Kane et al., 2017), in proximal basin-floor lobes (e.g., Terlaky and Arnott, 2014; Fonnesu et al., 2018), in the channel–lobe transition zone (e.g., Ito, 2008; Brooks et al., 2018; Navarro and Arnott, 2020; Baas et al., 2021), and on the continental slope (Angus et al., 2019). Termed linked debrites (Haughton et al., 2003), cogenetic debrite–turbidite beds (Talling et al. 2004), hybrid event beds (Haughton et al. 2009), transitional-flow deposits (Kane and Pontén, 2012) and bipartite beds (Bed Type 2) of matrix-rich sandstones (Angus et al., 2019), these beds are reported to occur downflow of clean (i.e. less mud-rich) sand over distances of hundreds of meters to tens of kilometers (e.g., Fonnesu et al., 2015; 2016; 2018; Kane et al., 2017; Spychala et al., 2017; Pierce et al., 2018; Angus et al., 2019). The variable distances over which this lithological change takes place has, at least in part, contributed to differing physical models to explain their origin, including hybrid flows consisting of at least two discrete and mechanistically different parts, namely a turbidite overlain by a debrite (Haughton et al. 2009), longitudinal flow transformation (Kane and Pontén, 2012), vertical stratification effects and turbulence suppression in a high-concentration suspension (see review in Talling, 2013; Kane et al., 2017), and particle

settling in a negligibly sheared mixed mud–sand suspension (Angus et al., 2019). Notably also, majority of the interpretations are based on visual observations in core and outcrop, and thus highlight the need for a detailed and systematic analysis of the microscopic textural characteristics of these strata.

In a recent study, Angus et al. (2019) traced individual beds continuously over distances of several hundreds of meters in the Neoproterozoic Windermere turbidite system (British Columbia, Canada). Here, bipartite strata were shown to be part of a systematic depositional continuum that showed a progressive transformation from sand-rich (Bed Type 1) to bipartite (Bed Type 2) to mud-rich strata (Bed Type 3), which, in the absence of physical paleocurrent indicators like sole marks or cross-stratification, was taken to reflect the local paleoflow direction, and that the entirety of these changes was measured over horizontal distances of several tens to a few hundreds of meters. Moreover, the continuum was observed in continental-slope and proximal basin-floor (see also Terlaky and Arnott, 2014) deposits, and where present formed stratal units that only uncommonly were intercalated with other lithologies, and then were overlain sharply by sandy stratal elements including basin-floor splays, distributary-channel fills, and slope channel fills (Terlaky and Arnott, 2014, 2016). Furthermore, Angus et al. (2019) interpreted this depositional continuum to be associated with systematic particle settling along the margins of high-energy flows that had deeply scoured the local mud-rich seafloor during channel avulsion associated with activation of local sedimentary system (see also discussion in Terlaky and Arnott, 2014).

Although the lithofacies trend associated with bipartite facies in the Windermere is broadly similar to many other published stratal examples consisting, at least in part, of two-part strata (e.g., Haughton et al., 2003, 2009; Talling et al., 2004; Amy and Talling, 2006; Kane et al., 2017; Pierce

et al., 2018), it differs from most by the short (several tens to hundreds of meters) horizontal scale over which the entire facies tract, including the bipartite part, is observed. Different also is the paleogeographic occurrence of these mixed sand–mud strata, which in the Windermere occur in proximal basin-floor and continental-slope deposits, rather than the more typically reported distal basin floor (e.g., Haughton et al., 2003; Hodgson, 2009; Spychala et al., 2017). These contrasting observations warrant further investigation about the origin of bipartite strata in proximal deep-marine settings versus those in more distal deep-marine settings. However, distal basin-floor strata are not exposed in the Windermere turbidite system, and therefore distal basin-floor deposits of the Ordovician Cloridorme Formation, Quebec, Canada were studied for comparison. Here bipartite strata resembling those described previously from the Windermere by Angus et al. (2019), and termed argillaceous sandstones by Enos (1969) and Parkash and Middleton (1970), are continuously exposed along extensive wave-cut terraces, and therein provide an opportunity, as in the Windermere, to study the along-flow makeup and origin of these strata. Accordingly, the objectives of this research are (i) to compare the composition (matrix volume) and texture (grain-size distribution and sorting) of the bipartite facies and associated strata in slope and proximal basin-floor deposits of the Windermere turbidite system with distal basin-floor deposits of the Cloridorme Formation, and (ii) to compare the mechanistic origin of the admixed sand–mud strata in both study areas, and therein a sampling of paleogeographic settings extending from continental slope to distal basin floor by taking into account, grain size characteristics, bed thickness and spatial dimensions of the various lithofacies changes.

3.2 GEOLOGICAL BACKGROUND AND STRATIGRAPHY

3.2.1 Windermere Supergroup

The Neoproterozoic (740–570 Ma) Windermere Supergroup (WSG) is an unconformity–bounded succession representing rift-to-drift sedimentation associated with the breakup of the Rodinia supercontinent (Stewart, 1972; Ross and Arnott, 2007; McMechan, 2015) and crops out for over 4000 km from the Yukon–Alaska boarder to the Sonoran Desert in northwestern Mexico (Ross and Arnott, 2007) (Fig. 3.1A). In the southern Canadian Cordillera, the basal rift sequence includes a few-kilometers-thick succession of intercalated glaciomarine diamictite and volcanic rocks of the Toby and Irene formations, respectively (Aalto, 1971; Ross et al., 1995; Warren, 1997). The overlying post-rift consists of an approximately 5–7-km-thick, upward-shoaling succession composed of sheet-like basin-floor sandstone and mudstone (Kaza Group) overlain successively by leveed slope-channel complexes (Isaac Formation), upper-slope to outer-shelf limestones (Cunningham Formation), and high-energy mixed carbonate–siliciclastic continental shelf deposits (Yankee Belle Formation) (Ross, 1991). This stratigraphic succession is interpreted to represent the progradation of the Laurentian (ancestral North America) continent margin into the thermally subsiding proto–Pacific Ocean (Ross, 1991; Ross et al., 1995; Ross and Murphy, 1988; Hadlari et al., 2021).

Deep-marine strata of the WSG basin (Fig. 3.1B), termed the Windermere turbidite system, are well exposed throughout the southern Canadian Cordillera, which extends from the Cariboo Mountains in the north to the Purcell Mountains in the south (Fig. 3.1A). The palinspastically restored areal extent of the exposed part of the turbidite system is of the order of 80,000 to 100,000 km^2 (Ross and Murphy, 1988; Ross, 1991), making it dimensionally comparable to modern passive-margin turbidite systems like the Amazon and Mississippi fans. The study area is located

at Castle Creek (Fig. 3.1D), where vertically dipping, southeast-to-northwest-striking, recently deglaciated, vegetation-free strata of the Upper Kaza Group and Isaac Formation form an outcrop belt that is up to 2.5 km thick and 8 km wide, and where individual beds and bedsets can be traced continuously for several tens to hundreds of meters along strike. However, due to the glacially polished nature of the exposures, paleoflow data are limited to a small number of well-exposed 3D current ripples and dune cross-stratified sets, and flutes which indicate a general transport direction that ranges between west-northwest and northeast (see Ross and Arnott, 2007; Schwarz and Arnott, 2007; Khan and Arnott, 2011; Navarro and Arnott, 2020), and therefore subparallel to the regional paleoflow direction (e.g., Mountjoy and Aitken, 1963).

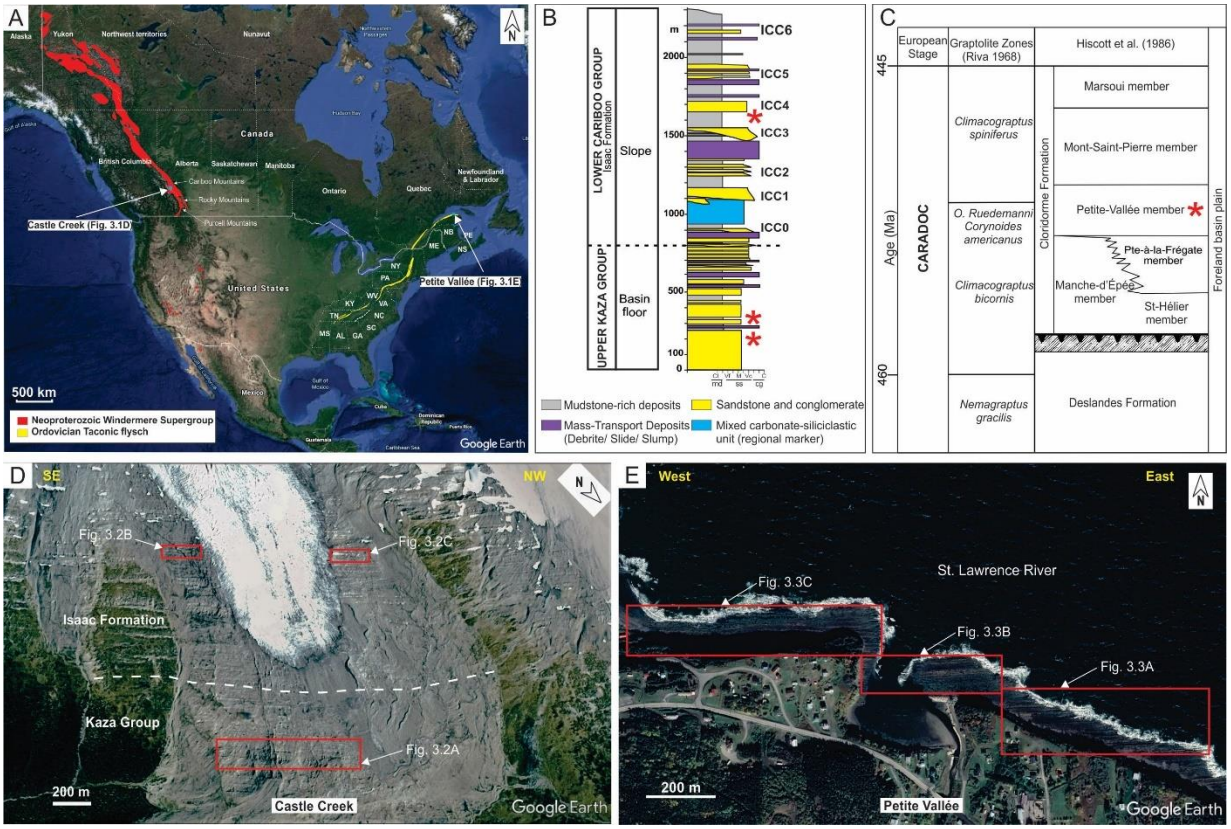

Figure 3.1: A) Map of North America showing the location of exposed Windermere Supergroup (red) and Ordovician Taconic flysch (yellow) strata. The two study areas (Castle Creek and Petite Vallée) are indicated by blue squares (satellite image from Google Earth, 2020). B) Generalized stratigraphic log of the Castle Creek outcrop. Here strata consist of basin-floor deposits of the Upper Kaza Group overlain conformably by slope-channel deposits of the Isaac

Formation. Labels on the right (ICC0 to ICC6) are informal names for Isaac slope channel complexes. Location of intervals described here are indicated by the red stars. D) Stratigraphic framework for the Middle Ordovician Cloridorme and Deslandes formations in southeastern Quebec (modified after Awadallah and Hiscott, 2004). Location of the interval described here is indicated by the red star. D) Overview of the Castle Creek study area in the Cariboo Mountains, east central British Columbia, Canada (satellite image from Google Earth, 2020). The study intervals are highlighted by the red rectangles. E) Study area located near the village of Petite Vallée, Quebec, Canada (satellite image from Google Earth, 2020). Rocks are exposed along a broad wave-cut platform and are overturned, dipping south at 65°–88°. Red rectangles indicate the studied intervals.

Rocks have undergone low-grade (greenschist facies) metamorphism due to Mesozoic tectonism, which has resulted in alteration of detrital clay minerals to muscovite and chlorite and strain-induced deformational structures like bulging recrystallization and sub-grain rotation along some grain boundaries. Despite these conditions, primary sedimentary features and most sedimentary textures, namely grain size, grain shape, and sorting are well preserved, and therefore these rocks are described and classified as sedimentary rocks (Ross and Arnott, 2007). At Castle Creek, bipartite facies and associated strata are particularly common in proximal basin-floor strata of the Upper Kaza Group, where they are often sharply overlain by several-meter-thick, sand-rich distributary channel fills and up to decameter-thick terminal splays (Terlaky and Arnott, 2014, 2016; Popovic, 2016; Terlaky et al., 2016; Angus et al., 2019) (e.g., Fig. 3.2A). Although less common in channel–lobe transition zone and continental-slope strata, these strata are overlain, respectively, by sand-rich distributary-channel and terminal-splay deposits (Navarro and Arnott 2020), and leveed slope channel fills (Arnott, 2007a, 2007b: Schwarz and Arnott, 2007; Angus et al., 2019; Wearmouth, 2018) (e.g., Fig. 3.2B, C).

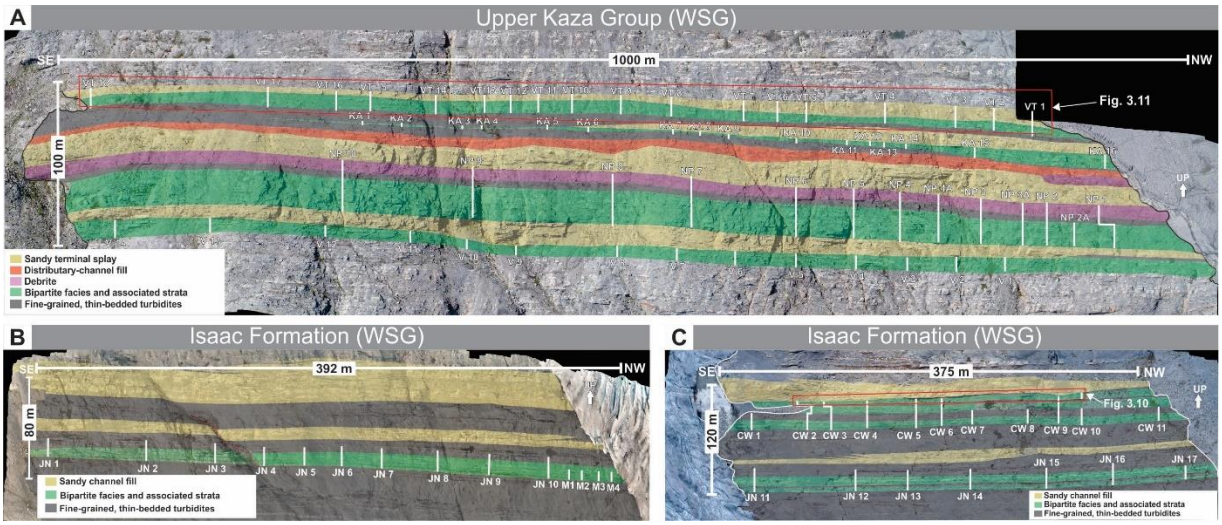

Figure 3.2: Interpreted drone photomosaics of A) Upper Kaza Group, and B, C) Isaac Formation at the Castle Creek outcrop. Locations of the stratigraphic logs are indicated by vertical white lines and are labelled above or below the logs. Note the sharply defined boundaries of the various stratal elements that are shown in different colors.

3.2.2 Cloridorme Formation

The Middle Ordovician (460–445 Ma) Cloridorme Formation (CF) is one of several turbidite systems deposited along an elongate foreland basin located between cratonic North America to the northwest and the developing Taconic orogen and its associated volcanic arcs to the southeast (St-Julien and Hubert, 1975; Hiscott et al., 1986). This foreland basin extended from Newfoundland to Alabama and was separated into ~ 100-km-long segments by structural highs (Hiscott et al., 1986) (Fig. 3.1A). The CF is at least 4 km thick, with neither its base or top exposed. Based on lithofacies and extensive marker beds (megaturbidites), the CF is divided into five members, which from oldest to youngest are: distal basin-floor mudstones (St-Hélier Member), sand lobes and inter-lobe deposits (Pointe-à-la-Frégate and Petite-Vallée members), mudstone deposits related to eustatic highstand (Mont-Saint Pierre Member), and mixed sand-and-mud basin-floor fan (Marsoui Member) (Hiscott et al., 1986) (Fig. 3.1C). The CF crops out semi continuously over about 150 km in intertidal exposures along the north shore of the Gaspé Peninsula, Quebec, Canada. The estimated areal extent of this turbidite system is 10,000 to 22,500

km^2 (Hiscott et al., 1986), and is therefore similar in size to the present-day Astoria Fan and the Miocene Marnoso Arenacea Formation.

The CF study area is located near the village of Petite Vallée, Quebec (Fig. 3.1E) where overturned, steeply dipping (average 78°), east-to-west (271°)-striking exposures of the Petite Vallée member (ca. 300 m thick and ca. 1 km wide) crop out along an intertidal wave-cut platform. Excellent outcrop conditions allowed individual bed and bedsets to be continuously traced and correlated over several tens to hundreds of meters along strike. In this study area, average paleocurrent measured from troughs of three-dimensional ripples and tool marks on the base of beds (n = 102) is 272°, and therefore parallel to the strike of the outcrop. Additionally, paleocurrents elsewhere in the Cloridorme are generally reported to be towards the west (Awadallah, 2002; Parkash and Middleton, 1970; Pickering and Hiscott, 1985). Rocks have undergone very low-grade (zeolite to prehnite–pumpellyite facies) metamorphism associated with regional tectonic activity during the Taconic Orogeny (Jiang and Peacor, 1994), and as a result detrital clay minerals have been altered to illite–muscovite and chlorite; however, this change has negligible effect on primary sedimentary structures and textures, enabling these rocks to be described and classified using conventional sedimentary terminology. Distal basin-floor strata in the Petite Vallee Member consist of a succession of sandy lobes and fine-grained, thin-bedded turbidites (Hiscott et al., 1986). Commonly intercalated in the succession are bipartite and associated strata that form several-meter-thick stratal units, which, like similar strata in the WSG at Castle Creek, typically underlie several-meter-thick, amalgamated, sand-rich lobes (Beeden, 1983; Hiscott et al., 1986; Ma, 1996) (Fig. 3.3).

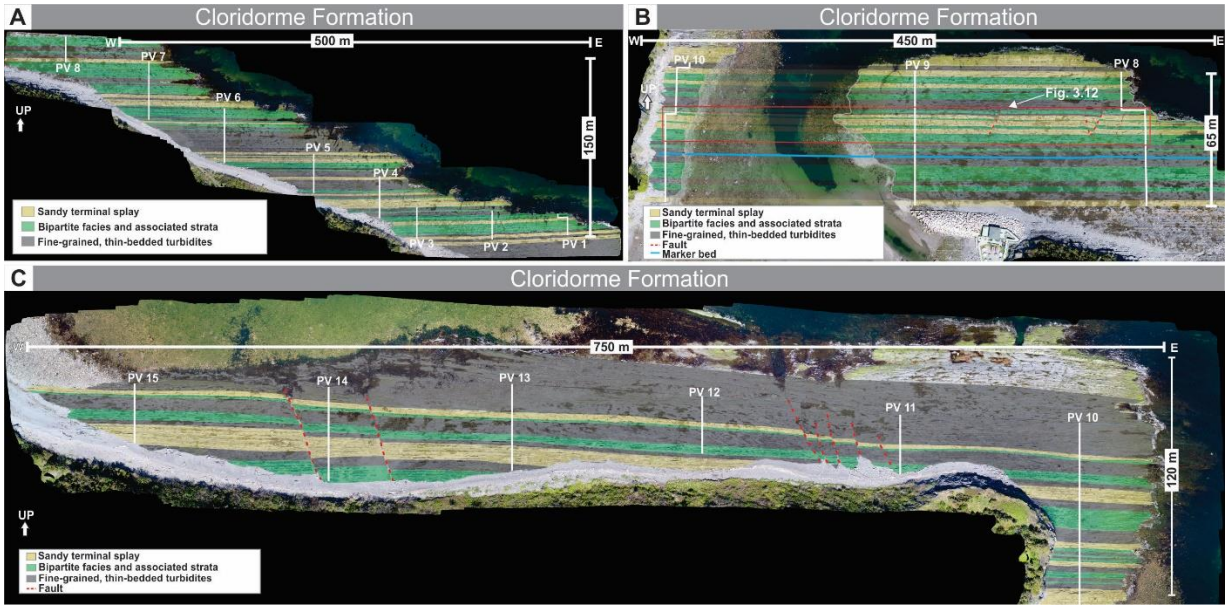

Figure 3.3: Interpreted drone photomosaics of the Petite Vallée outcrop. Stratigraphic logs are indicated by white vertical lines and are labelled above the logs. Note the sharply defined boundaries of the various stratal elements highlighted in different colors.

3.3 METHODOLOGY AND TERMINOLOGY

At Castle Creek (WSG), based on earlier stratigraphic and depositional-framework studies, select intervals containing bipartite and associated strata were chosen for this study, and re-investigated in the field (Fig. 3.1B, D). In proximal basin-floor deposits of the Upper Kaza Group, a stratigraphic interval ~ 100 m thick and 1000 m wide comprising a succession of sandy terminal splays, distributary channel fill, debrite, thin-bedded turbidite, and bipartite facies and its associated strata, which previously was mapped by Terlaky and Arnott (2014, 2016), Terlaky et al. (2016), Popović (2016), and Angus (2016), was selected for re-analysis (Fig. 3.2A). Here, 61 logs (5 to 50 m long) were measured over a lateral distance of ~ 900 m targeting the bipartite facies and associated strata. In slope deposits of the stratigraphically higher Isaac Formation, two stratigraphic intervals, ~ 80 m thick and 400 m wide (Fig. 3.2B) and ~ 120 m thick and 400 m wide (Fig. 3.2C), and comprising sandy channel fills, thin-bedded turbidites, bipartite facies, and

associated strata that were studied previously by Arnott (2007a, 2007b), Altosaar (2007), O' Byrne et al. (2007), Davis (2011), Dumouchel (2015), Angus (2016), Wearmouth (2018), and Arnott et al. (2021), were selected for re-analysis. Here, a total of 32 logs (3.5 to 30 m long) were measured in two transects that targeted bipartite facies and associated strata. In distal basin-floor deposits of the Petite Vallée Member (CF) (Fig. 3.1C, E) particularly well exposed bipartite facies and associated strata were studied. Stratal elements were mapped previously by Enos (1969), Beeden (1983), Hiscott et al. (1986), and Ma (1996) and termed sandy lobes, thin-bedded siltstone–shale units and argillaceous sandstone units, but here termed, respectively, sandy terminal splays, thin-bedded turbidites, and bipartite facies to ensure consistency in terminology. Here, 15 bed-by-bed stratigraphic logs (18 to 146.7 m long) were measured over a total lateral distance of ~ 1.7 km (Fig. 3.3). Superb exposure at both study areas allows detailed documentation of stratal thickness, bedding contacts, grain size, sedimentary structures, presence of clasts, and for beds to be traced continuously for at least several hundreds of meters parallel to bedding along the strike of the outcrops. Also, in both WSG and CF, a few logs were extended upward to capture details in the overlying stratigraphic unit. Additionally, hand samples of bipartite facies and associated lithologies were collected at both study sites, and a total of 257 standard (30 μm thick) thin sections were prepared for conventional petrographic analysis. From these, 253 thin sections were point counted (≥ 300 points per sample) to evaluate the abundance of framework grains (quartz, feldspar and sedimentary, metamorphic, and volcanic rock fragments), matrix, and cement. In addition, the longest dimension of each framework grain (grain size between 0.0625 mm and 6 mm) was measured to determine grain-size distribution in each sample. Notably also, all petrographic work was conducted by a single operator to minimize operator bias and standardize potential error.

Due to low grade (greenschist) metamorphism in rocks of the WSG and zeolite to prehnite–pumpellite metamorphism in CF strata, all detrital clay minerals have been recrystallized to illite–muscovite and chlorite, and as a result details of the original clay mineralogy are unknown. Accordingly, these changes make it difficult to discern the comparative contribution of detrital versus authigenic matrix. However, only minimal to partial dissolution and replacement textures in labile components, like feldspars, rock fragments and mud intraclasts, are observed in thin section, and illite–muscovite and chlorite minerals are uniformly distributed between framework grains (Fig. 3.4), suggesting that degradation of labile components contributed negligibly to overall matrix content. Collectively, this suggests that in addition to siliciclastic silt (grain size < 0.0625 mm), most of illite–muscovite and chlorite, regardless of crystal size, are the result of metamorphic alteration of detrital clay minerals that made up much of the primary detrital matrix. Nevertheless, the contribution of authigenic clay, although negligible, remains poorly constrained and may introduce some amount of error in the estimate of matrix content, but since the range of matrix content between the three principal lithofacies (see next) is measured in tens of percent, minor differences would have little effect on the classification and interpretation of these strata.

Lastly, this study follows a modified classification scheme of Folk (1974) used in Tucker (2001) to classify rock types according to their relative sand (0.0625–2.0 mm), silt (0.0039–0.0625 mm), and clay (< 0.0039 mm) content. Based on matrix (clay + silt) percentage, four main lithofacies are identified: matrix-poor sandstone (0–20% matrix), muddy sandstone (20–50% matrix), bipartite facies with a basal sandy (25–60% matrix) part overlain sharply by a planar- to irregular-based muddier part (40–80% matrix), and sandy mudstone (50–90% matrix).

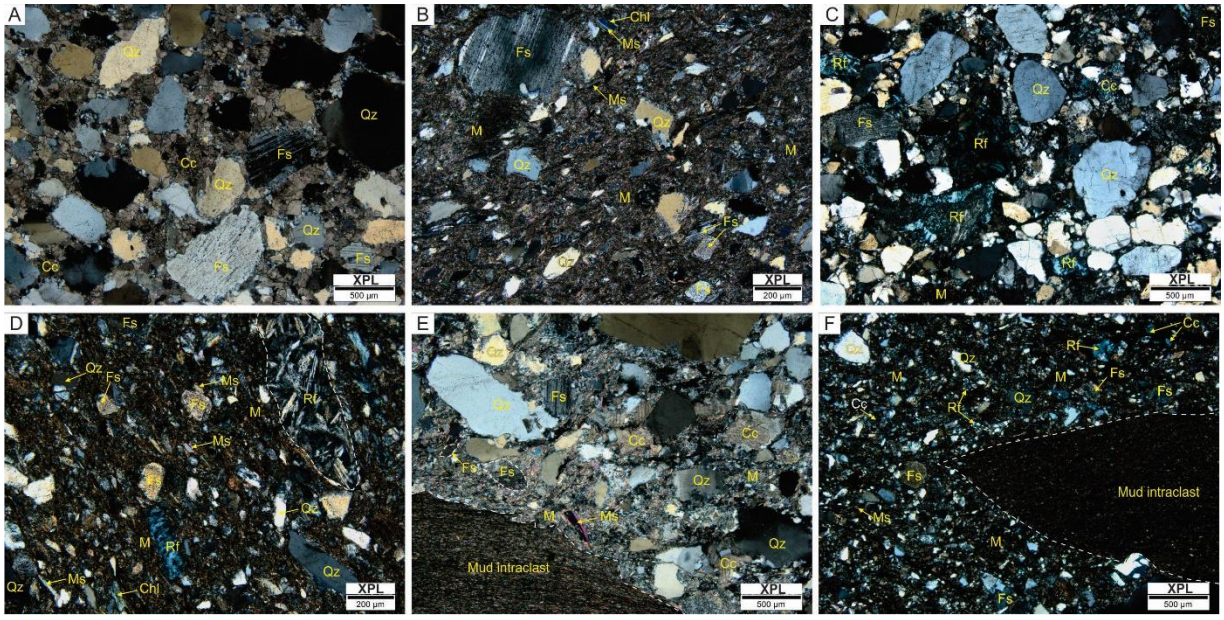

Figure 3.4: Photomicrographs of matrix-poor sandstone and sandy mudstone in A, B) the Windermere Supergroup and C, D) the Cloridorme Formation. Note that feldspars (Fs) and rock fragments (Rf) exhibit only minimal to partial alteration. Photomicrographs of a muddy sandstone in E) the Windermere, and F) sandy mudstone in the Cloridorme showing the prominent difference in color and fabric between the mud intraclasts, and illite–muscovite and chlorite matrix (M). Mineral components are: Qz—quartz grains, Fs—feldspar grains, Rf—rock fragments, Ms—muscovite and Chl—chlorite crystals, Cc—carbonate cement, and M—matrix (silt and clay).

3.4 LITHOFACIES DESCRIPTIONS

The compositional and textural characteristics of matrix-poor sandstone, muddy sandstone, bipartite facies, and sandy mudstone are summarized in Tables 3.1A and 3.1B. All four facies are structureless (i.e., lack tractional sedimentary structures), coarse-tail graded or massive, and composed of framework grains that range from very fine to very coarse sand. Furthermore, they are poorly to very poorly sorted with rounded to angular, equant to elongate framework grains composed mostly of quartz (80–98%) and less commonly feldspar (3–20%) in the WSG, and quartz (59–87%), feldspar (2–25%) and rock fragments (9–29%) in the CF. Matrix is composed of illite–muscovite with dispersed chlorite crystals and silt grains, and cement consists of calcite (ferroan and non-ferroan) or rhombohedral dolomite. Minor (< 1%) euhedral pyrite is also observed. Strata also commonly contain elongate, subangular to subrounded mud clasts and lesser

very fine to medium-grained sandstone clasts that are oriented with their apparent long axes subparallel to bedding (Figs. 3.5, 3.6). Where present, these four facies are overlain by laminae to thin beds of traction-structured sandstone and/or silty mudstone facies, which are described next (Figs. 3.5, 3.6). Interpretations of these facies are based principally on their systematic lateral arrangement, and therefore will be presented following the description of the lateral facies association.

A	Windermere Supergroup									
Facies	Bed thickness	Basal contact	Grading	Sedimentary structures	Framework (>0.0625 mm) grain size	Matrix (silt and clay) content	Carbonate cement	Framework grains composition		
								Quartz	Feldspar	Rock Fragments
Matrix-poor sandstone (MPS)	5–216 cm (avg. 50 cm)	Undulatory (82% of beds), planar (18% of beds)	Coarse-tail graded (67%), massive (33%)	Structureless	Very fine sand–pebble (avg. upper coarse sand)	10–18% (avg. 14%)	Up to 9% (avg. 3%)	81–97% (avg. 88%)	3–19% (avg. 12%)	0%
Muddy sandstone (MS)	2–91 cm (avg. 24 cm)	Undulatory (66% of beds), planar (34% of beds)	Coarse-tail graded (25%), massive (75%)	Structureless	Very fine sand–pebble (avg. lower coarse sand)	29–48% (avg. 37%)	Up to 3% (avg. 1%)	81–98% (avg. 89%)	3–19% (avg. 11%)	0%
Bipartite facies (BF)	3–55 cm (avg. 15 cm)	Undulatory (58% of beds), planar (42% of beds)	Lower part: coarse-tail graded (31%), massive (69%)	Structureless	Very fine sand–granule (avg. upper medium sand)	31–60% (avg. 42%)	< 1%	89–95% (avg. 92%)	5–11% (avg. 8%)	0%
			Upper part: coarse-tail graded (15%), massive (85%)	Structureless	Very fine sand–granule (avg. lower medium sand)	47–76% (avg. 68%)	< 1%	86–96% (avg. 91%)	4–14% (avg. 9%)	0%
Sandy mudstone (SM)	1–40 cm (avg. 8 cm)	Undulatory (37% of beds), planar (63% of beds)	Coarse-tail graded (13%), massive (87%)	Structureless	Very fine sand–granule (avg. lower medium sand)	53–76% (66%)	< 1%	80–94% (avg. 89%)	6–20% (avg. 11%)	0%

B	Cloridorme Formation									
Facies	Bed thickness	Basal contact	Grading	Sedimentary structures	Framework (>0.0625 mm) grain size	Matrix (silt and clay) content	Carbonate cement	Framework grains composition		
								Quartz	Feldspar	Rock Fragments
Matrix-poor sandstone (MPS)	11–135 cm (avg. 41 cm)	Undulatory (67% of beds), planar (33% of beds)	Coarse-tail graded (82%), massive (18%)	Structureless	Very fine sand–granule (avg. upper medium sand)	6–18% (avg. 14%)	Up to 14% (avg. 6%)	66–83% (avg. 73%)	2–15% (avg. 10%)	13–21% (avg. 17%)
Muddy sandstone (MS)	10–67 cm (avg. 26 cm)	Undulatory (51% of beds), planar (49% of beds)	Coarse-tail graded (70%), massive (30%)	Structureless	Very fine sand–granule (avg. lower medium sand)	21–48% (avg. 32%)	Up to 12% (avg. 5%)	59–87% (avg. 69%)	4–20% (avg. 11%)	10–27% (avg. 20%)
Bipartite facies (BF)	5–95 cm (avg. 23 cm)	Undulatory (40% of beds), planar (60% of beds)	Lower part: coarse-tail graded (34%), massive (66%)	Structureless	Very fine–very coarse sand (avg. lower medium sand)	25–53% (avg. 41%)	2 - 12% (avg. 4%)	60–76% (avg. 67%)	6–23% (avg. 14%)	11–29% (avg. 19%)
			Upper part: coarse-tail graded (15%), massive (85%)	Structureless	Very fine–very coarse sand (avg. upper fine sand)	40–73% (avg. 56%)	Up to 4% (avg. 2%)	61–83% (avg. 70%)	5–25% (avg. 13%)	9–29% (avg. 17%)
Sandy mudstone (SM)	3–38 cm (avg. 15 cm)	Undulatory (4% of the beds), planar (96% of beds)	Coarse-tail graded (7%), massive (93%)	Structureless	Very fine sand–very coarse sand (avg. upper fine sand)	55–79% (avg. 67%)	< 2%	59–72% (avg. 65%)	11–19% (avg. 14%)	17–24% (avg. 21%)

Table 3.1: Lithological characteristics of the four main facies in A) the Windermere Supergroup and B) the Cloridorme Formation. See text for details.

3.4.1 Matrix-poor sandstone (MPS)

Beds of MPS are pink colored in WSG, yellow to brown in CF, and average 50 cm thick in WSG and 41 cm thick in CF (Figs. 3.5A–C, 3.6A–C). The basal contacts are sharp and planar (18% of the beds in WSG and 33% of the beds in CF) or undulatory (82% of the beds in WSG and 67% of beds in CF). Average grain size is coarse sand in WSG and medium sand in CF (Figs. 3.7A, 3.8A). Strata are mostly coarse-tail graded (67% in WSG and 82% in CF) but also massive (33% in WSG and 18% in CF). Matrix content ranges from 10 to 18% in the WSG and from 6 to 18% in the CF (Figs. 3.7A, 3.8A). Framework grains in WSG consist of 81 to 97% (average 88%) quartz and 3 to 19% (average 12%) feldspar, whereas in CF they are composed of 66 to 83% (average 73%) quartz, 2 to 15% (average 10%) feldspar, and 13 to 21% (average 17%) rock fragments. Carbonate cement in these strata constitutes 3% in WSG and 6% in CF on average. Mud clasts make up 1 to 5% of the bed, and on average are 1.4 cm thick and 16.5 cm long in WSG, whereas in CF, they are 2.2 cm thick and 17.2 cm long. MPS is similar to the sand-rich Bed Type 1 described by Angus et al. (2019).

3.4.2 Muddy sandstone (MS)

MS is light gray in WSG and brown in CF (Figs. 3.5D – F, 3.6D – F). Beds consist of coarse sand (Fig. 3.7B) and average 24 cm in thickness in WSG, and medium sand (Fig. 3.8B) and 26 cm thick in CF. The basal contacts are sharp and planar (34% of the beds in WSG and 49% of the beds in CF) or undulatory (66% of the beds in WSG and 51% of beds in CF). Strata are coarse-tail graded (55% in WSG and 70% in CF) or massive (45% in WSG and 30% in CF). Matrix content ranges from 29 to 48% in WSG and from 21 to 48% in CF (Figs. 3.7B, 3.8B). Framework

grains are made up of 81 to 98% (average 89%) quartz and 3 to 19% (average 11%) feldspar in WSG, whereas in CF they comprise 59 to 87% (average 69%) quartz, 4 to 20% (average 11%) feldspar, and 10 to 27% (average 20%) rock fragments. Carbonate cement makes up an average of 1% in WSG and 5% in CF. Mud clasts make up ~ 5 to 10% of the bed, and on average are 2.0 cm thick and 13.3 cm long in WSG, whereas in CF they are 1.8 cm thick and 16.8 cm long. MS is similar to matrix intermediate Bed Type 1 in Angus et al. (2019).

3.4.3 Bipartite facies (BF)

Distinctively, BF, which averages 15 cm thick in WSG and 23 cm thick in CF, is composed of two sharply bounded parts—a lower sand-rich part overlain sharply by a planar- or irregular-based muddier upper part. Across the interface grain-size decreases slightly but the matrix content increases by a few tens of percent, which in outcrop is marked by a very noticeable darkening of the strata (Figs. 3.5G–I, 3.6G–L). In the WSG the interface is exclusively planar, but in CF it is either planar (57% of beds) or shows an intermittent lateral alternation between planar and irregular (43% of beds). The irregular interface in CF strata is characterized by local synforms and antiforms that have 1–9.5 cm (average 4.3 cm) relief and are 8.5–122 cm (average 38.3 cm) wide (Figs. 3.6J–L). In addition, local overhangs and injections of sand from the sand-rich basal part into the overlying mud-rich part are observed (Figs. 3.6K, L). Where sand intrusions are observed, mud clasts tend to be more abundant in the overlying mud-rich part, which also exhibits a distinctive patchy texture marked by a mosaic of sand-rich and sand-poor areas (Fig. 3.6L). The bases of this facies are typically sharp and planar (58% of the beds in WSG and 60% of the beds in CF) or undulatory (42% of the beds in WSG and 40% in CF).

In both study areas, the lower part of BF is typically massive (69% in WSG and 85% in CF) and less commonly coarse-tail graded (31% in WSG and 15% in CF) with an average grain size of medium sand (Figs. 3.7C, 3.8C). Matrix content ranges from 31 to 60% in WSG and from 25 to 53% in CF (Figs. 3.7C, 3.8C). Framework grains in WSG consist of 89 to 95% (average 92%) quartz and 5 to 11% (average 8%) feldspar, whereas in CF they are composed of 60 to 76% (average 67%) quartz, 6 to 23% (average 14%) feldspar, and 11 to 29% (average 19%) rock fragments. Carbonate cement is ≤ 1% in WSG but ~ 4% in CF. The overlying muddier part is similarly massive (85% in WSG and CF) and less commonly coarse-tail graded (15% in WSG and CF) with medium sand in WSG and fine sand in CF (Figs. 3.7D, 3.8D). Matrix content ranges from 47 to 76% in WSG and from 40 to 73% in CF (Figs. 3.7D, 3.8D). Framework grains are made up of 86 to 96% (average 91%) quartz and 4 to 14% (average 9%) feldspar in WSG, whereas in CF they comprise 61 to 83% (average 70%) quartz, 5 to 25% (average 13%) feldspar, and 9 to 29% (average 17%) rock fragments. Carbonate cement is ≤ 1% in WSG, but ~ 2% in CF. Mud clasts are on average 0.7 cm thick and 5.8 cm long in WSG, whereas in CF, they are 2.0 cm thick and 14.9 cm long, and where present make up ca. 5–10% of the basal part and 5–30% of the upper part of the bipartite facies. BF is similar to Bed Type 2 described in Angus et al. (2019).

3.4.4 Sandy mudstone (SM)

Like the upper, mud-rich layer of the bipartite facies, matrix content in SM beds is high, and ranges from 53 to 76% in WSG and from 55 to 79% in CF (Figs. 3.7E, 3.8E). Accordingly, strata are distinctively dark colored and are blue-gray to dark gray in WSG and green-gray to dark gray in CF (Figs. 3.5J–L, 3.6M–O). Beds average 8 cm in thickness, and sand is usually medium grained in WSG, and 15 cm thick, and sand is fine grained in CF. Bed bases are generally sharp

and planar (63% of the beds in WSG and 96% of the beds in CF), but can also be undulatory (37% of the beds in WSG and 4% of beds in CF). Strata are typically massive 87% in WSG and 93% in CF) but can also be coarse-tail graded (13% in WSG and 7% in CF). Framework grains in WSG consist of 80 to 94% (average 89%) quartz and 6 to 20% (average 11%) feldspar, whereas in CF they are composed of 59 to 72% (average 65%) quartz, 11 to 19% (average 14%) feldspar, and 17 to 24% (average 21%) rock fragments. Carbonate cement constitutes ≤ 1% in WSG and ≤ 2% in CF. Mud clasts are on average 0.6 cm thick and 6.4 cm long in WSG, whereas in CF, they are 1.2 cm thick and 7.9 cm long, and where present make up ca. 5–30% of the bed. SM resembles Bed Type 3 described by Angus et al. (2019).

3.4.5 Traction-structured sandstone (TSS)

TSS is matrix-poor (< 10% matrix), pink to yellow-tan in WSG and yellow to brown in CF. Strata have sharp, undulatory basal contacts, average ~ 2.4 cm in thickness, and consist of well-sorted, massive or normally graded, very fine- to medium-grained sandstone (Fig. 3.9). Distinctively, strata are planar and/or ripple cross-stratified overlain by a layer of diffuse, plane-parallel or wavy-parallel laminated siltstone, or less commonly, very fine sandstone.

3.4.6 Massive or graded silty mudstone (Md)

Md consists of massive to graded silty mudstone that averages 3.5 cm in thickness. Basal contacts are usually sharp and planar or drape topography along the top of the underlying TSS layer (Fig. 3.9). Md strata consist of alternating silt-rich and silt-poor laminae (< 2mm) (Fig. 3.9A); the latter becoming thicker and more abundant upward in some beds.

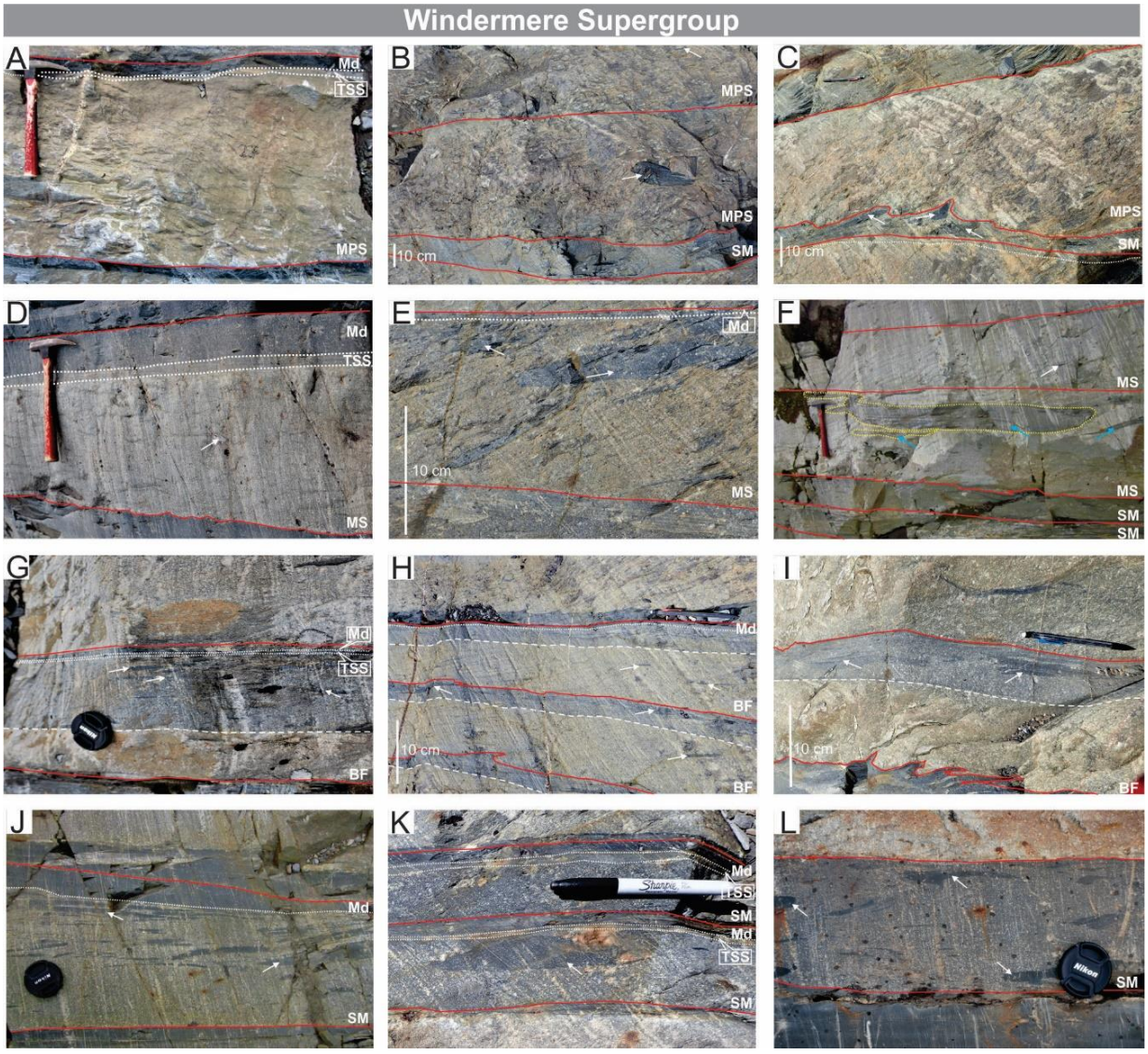

Figure 3.5: Representative photographs of the four main lithofacies in the Windermere Supergroup. A–C) Matrix-poor sandstone (MPS), D–F) Muddy sandstone (MS), G–I) Bipartite facies (BF), J–L) Sandy mudstone (SM). Solid red lines mark the base and top of a single bed; white arrows point to mud intraclasts; blue arrows indicate sandstone clasts; and dashed white lines separate the two parts of a bipartite facies (BF). Note that where present, these facies are overlain by a thin, traction-structured sandstone (TSS) and/or massive or graded silty mudstone (Md). Hammer for scale (28 cm long), camera lens cap (5.2 cm diameter), pen (13.5 cm long).

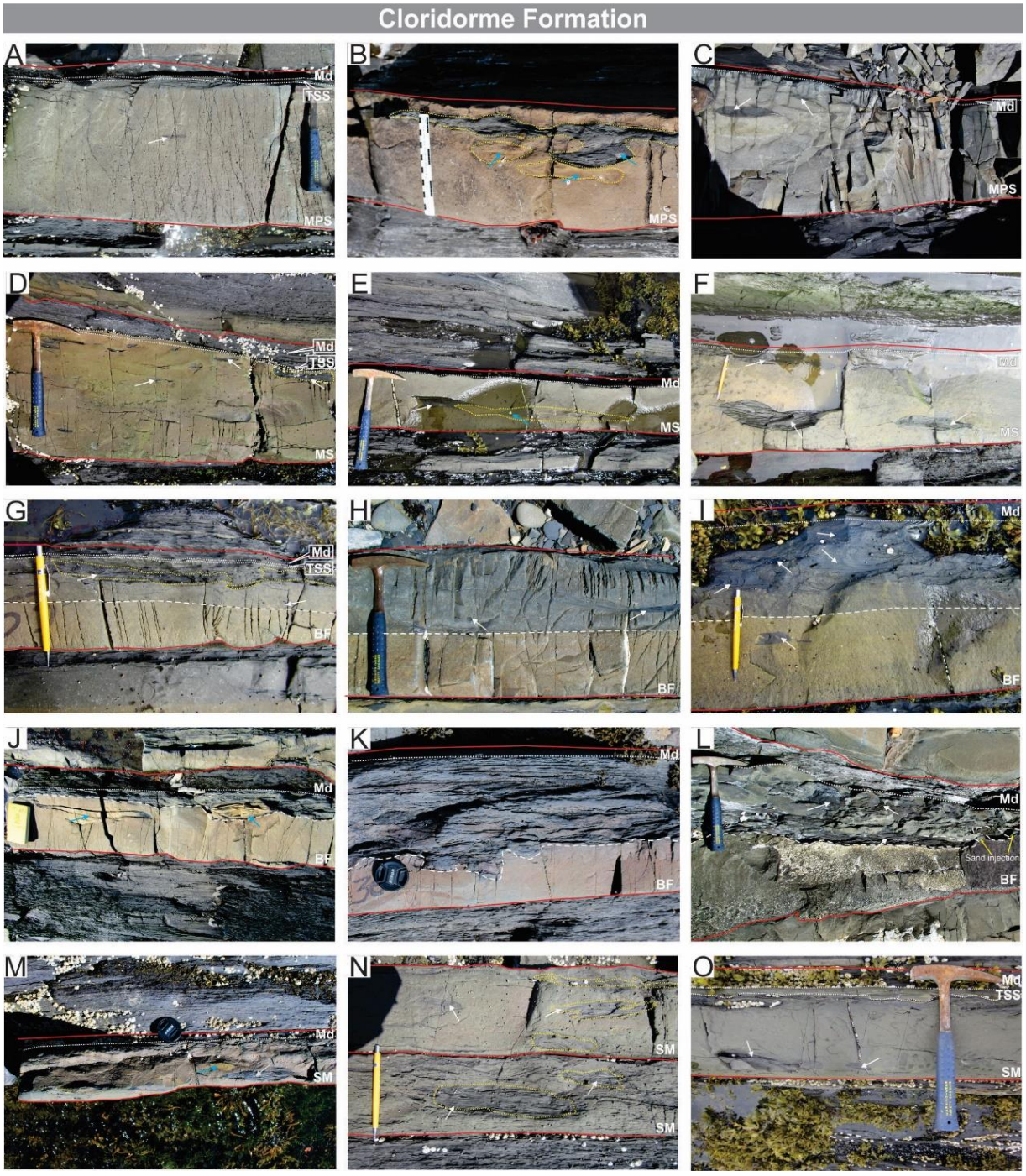

Figure 3.6: Representative photographs of the four main lithofacies in the Cloridorme Formation. A–C) Matrix-poor sandstone (MPS), D–F) Muddy sandstone (MS), G–L) Bipartite facies (BF), M–O) Sandy mudstone (SM). Solid red lines mark the base and top of a single bed; white arrows point to mud intraclasts; blue arrows indicate sandstone clasts; and dashed white lines separate the two parts of a bipartite facies (BF). Note that where present, these facies are overlain by a thin, traction-structured sandstone (TSS) and/or massive or graded silty mudstone (Md). Scales are: hammer (33 cm long), pencil (14 cm long), camera lens cap (5.2 cm diameter), field notebook (19 cm long).

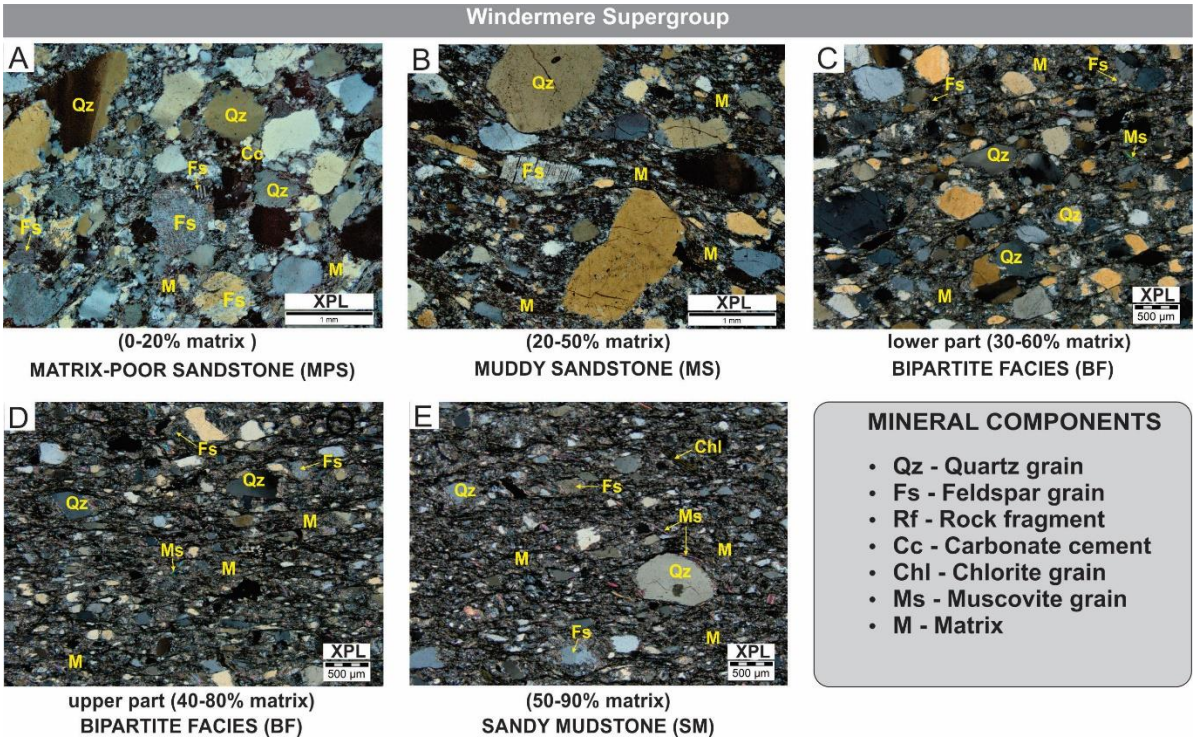

Figure 3.7: Representative cross-polarized photomicrographs of the four main lithofacies in the Windermere Supergroup.

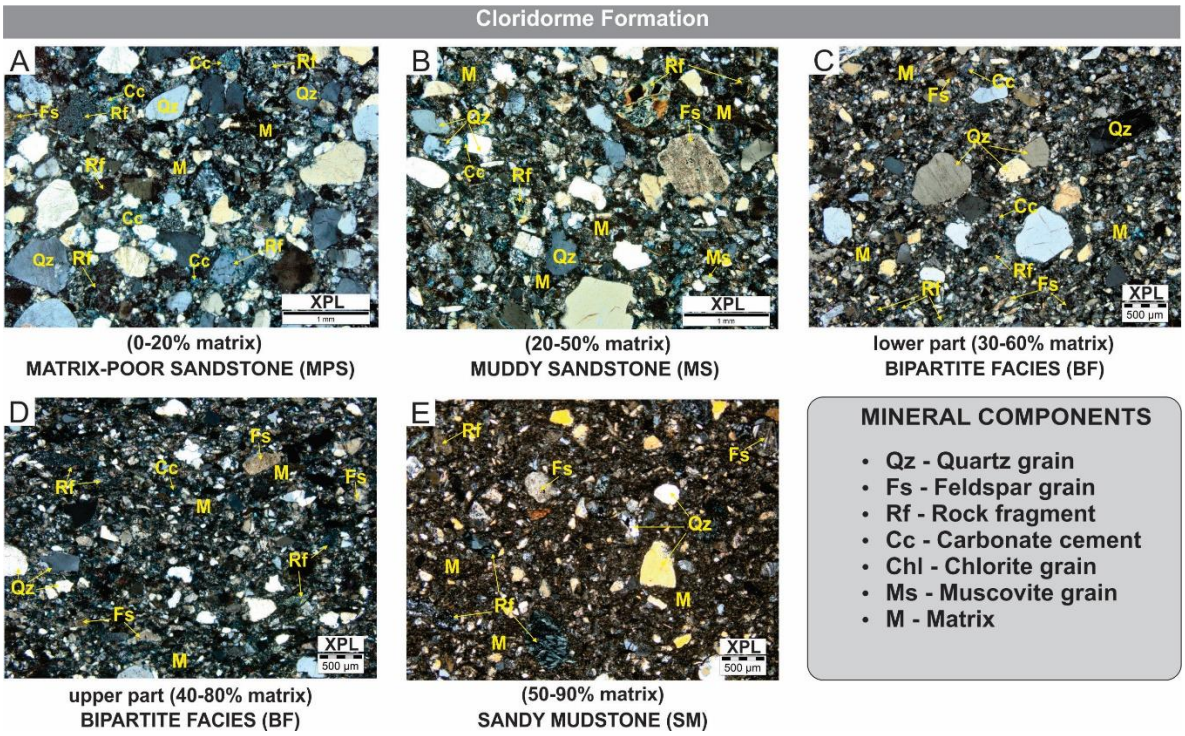

Figure 3.8: Representative cross-polarized photomicrographs of the four main lithofacies in the Cloridorme Formation.

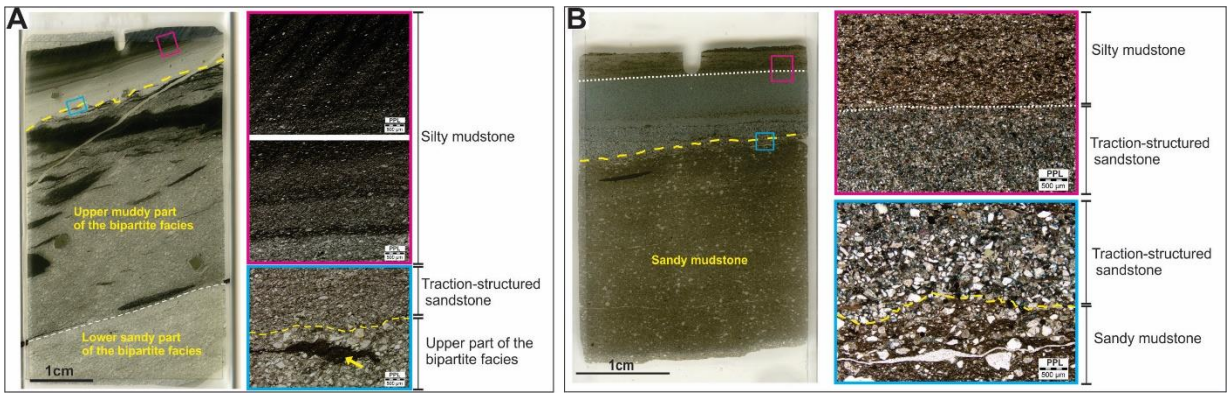

Figure 3.9: A) Thin-section photograph and associated photomicrographs in plane-polarized light of a bipartite facies (BF) overlain abruptly (dashed yellow line) by well-sorted, traction-structured sandstone (TSS) and massive or graded silty mudstone (Md) in the Windermere Supergroup. B) Thin-section photograph and associated photomicrographs in plane-polarized light of a sandy mudstone (SM) overlain abruptly (dashed yellow line) by well-sorted, traction-structured sandstone (TSS) and massive or graded silty mudstone (Md) in the Cloridorme Formation. Note that the inclination of layering in Part A is only an artifact of thin-section preparation. Blue and pink rectangles indicate the locations of the associated photomicrographs. Yellow arrow points to a mud intraclast.

3.5 LATERAL FACIES ASSOCIATION

In both study areas, individual beds in the bipartite and related strata units are observed to form a systematic proximal-to-distal change in lithofacies from MPS to MS to BF and then to SM along the strike of the outcrops. More specifically, MPS transforms to MS, which in turn develops into a two-part, bipartite facies (BF) consisting of a basal muddy sandstone part overlain sharply by an upper sandy mudstone part. Further laterally, the basal part of BF progressively thins and then pinches out, whereas the upper part initially thickens, then changes little in thickness, followed by thinning to a pinch-out. The entire transect is capped everywhere, except where eroded, by a laminated to thin-bedded, traction-structured sandstone (TSS) overlain by a silty mudstone (Md) (Fig. 3.10). Note that a similar lithofacies trend was documented previously by Terlaky and Arnott (2014), Angus (2016), Wearmouth (2018) and Angus et al. (2019) from basin-floor and continental-slope deposits of the WSG.

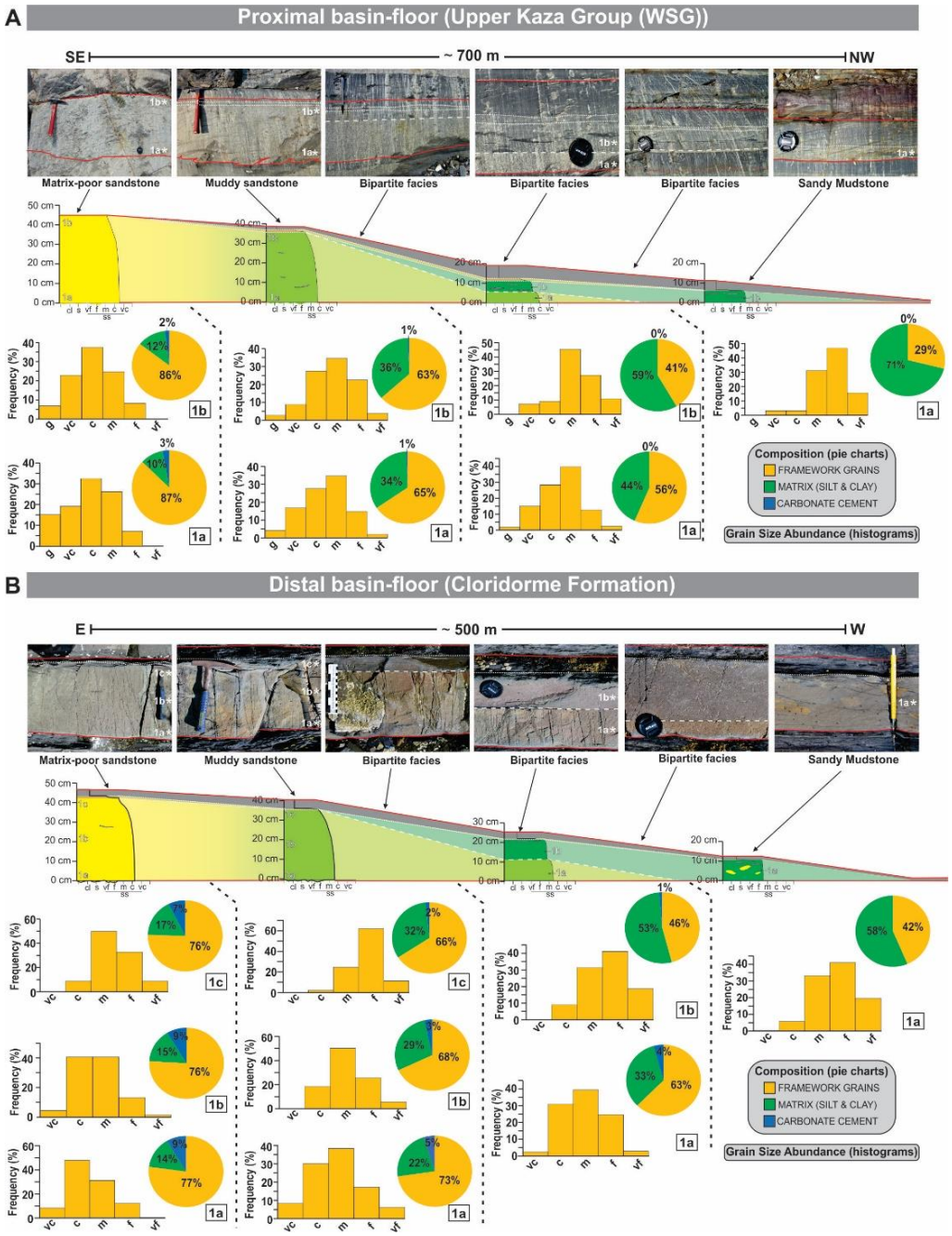

Figure 3.10: A, B) Lithofacies transect from matrix-poor sandstone (MPS) to muddy sandstone (MS) to bipartite facies (BF) to sandy mudstone (SM) in A) proximal basin-floor, Upper Kaza Group, Windermere Supergroup and B) distal basin-floor, Cloridorme Formation (see Appendix A2 and Appendix A10 for transect locations). Note that the transect, and the associated outcrop photographs, are from the same bed. Along the transect bed thickness changes from thick- to medium- to thin- to very thin-bedded, suggesting a proximal to distal trend. Additionally, modal grain size decreases from coarse-grained sand in the proximal to fine-grained sand in the distal part of the transect, but notably the range of grain sizes changes little. Pie charts illustrate point-count data showing composition of the constituent components along the transect. From proximal to distal (left to right) note the increase in matrix content but decrease in the abundance of framework grains and carbonate cement. Vertical position of samples in each bed is indicated by 1a, 1b, and 1c. Red hammer for scale (28 cm long) in Part A. Pencil (14 cm long) for scale in Parts A and B. Camera lens cap (5.2 cm diameter) for scale in both Parts A and B. Blue hammer (33 cm long) for scale in Part B. Scale card (15 cm long) for scale in Part B.

This complete depositional continuum was, however, observed in only nine event beds in the WSG and three beds in CF, which is interpreted to be a consequence of insufficient length of either outcrop. Nevertheless, in the more common case where only part of the transect is exposed, lithofacies are arranged in the same along-strike order as those in the complete succession (e.g., Figs. 3.11–3.13). Data compiled from partial and complete transects, specifically 43 beds in WSG and 40 beds in CF, provide a comprehensive description of horizontal extent, bed thickness, grain-size distribution, and matrix content (see Figs. 3.10, 3.14–3.16)

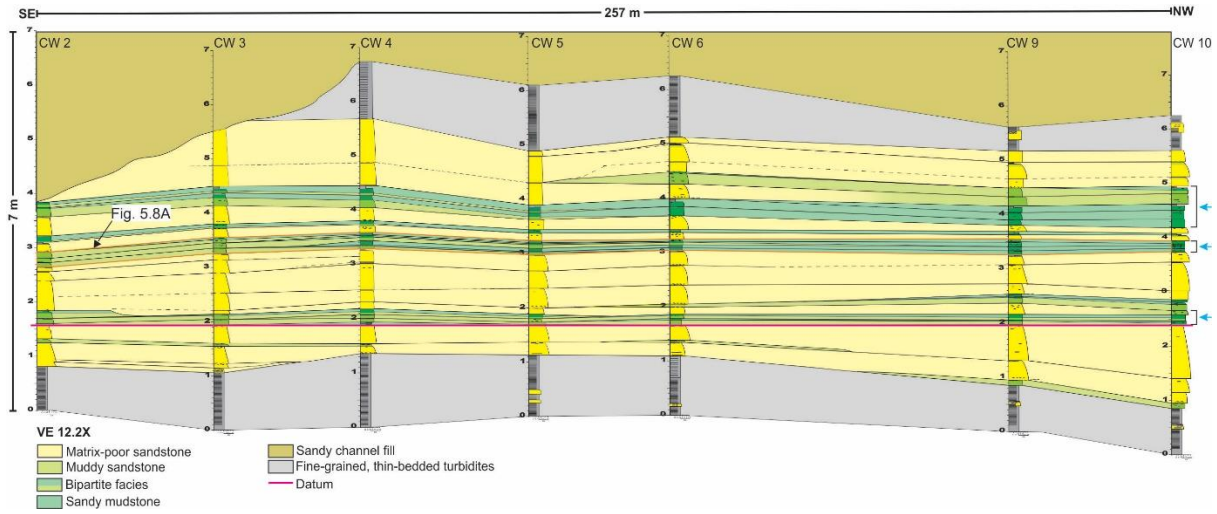

Figure 3.11: Stratigraphic correlation panel (vertical exaggeration 12.2X) of an ~ 7-m-thick unit in the Isaac Formation (for location see Fig. 3.2C). Note the exclusive occurrence of bipartite facies and associated strata that show a general proximal-to-distal trend from left to right. Based on well-developed lateral-accretion surfaces and cross-stratification, paleoflow in the overlying sandy channel fill is oriented into the plane of the figure (see Arnott et al. 2021, their Unit 14 in fig. 4A). Blue arrows point to beds that expose only part of the complete lithofacies transect (see text and Fig. 3.10 for details). Stratigraphic datum is the top of a matrix-poor sandstone bed that extends across the width of the outcrop.

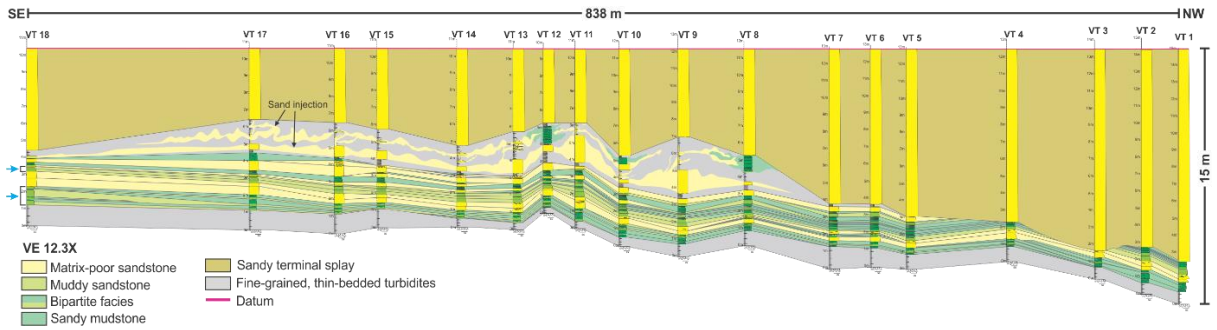

Figure 3.12: Stratigraphic correlation panel (vertical exaggeration 12.3X) of an ~ 15-m-thick unit in the Upper Kaza Group, Windermere Supergroup (for location see Fig. 3.2A). Bipartite facies and associated strata are overlain by a sandy terminal splay that ranges from 4 to 12 m thick and fills a scour incised into the mud-rich strata. Note that between logs VT 8 and VT 17, the upper part of the bipartite facies and associated strata are disrupted extensively by injected sand (sills and dikes). Bipartite facies and associated strata show a proximal-to-distal trend from left to right across the correlation panel, whereas the overlying terminal splay is oriented at a high angle and coming out of the page. Blue arrows point to beds that expose only part of the complete lithofacies transect (see text and Fig. 3.10 for details). Stratigraphic datum is the top of the terminal splay.

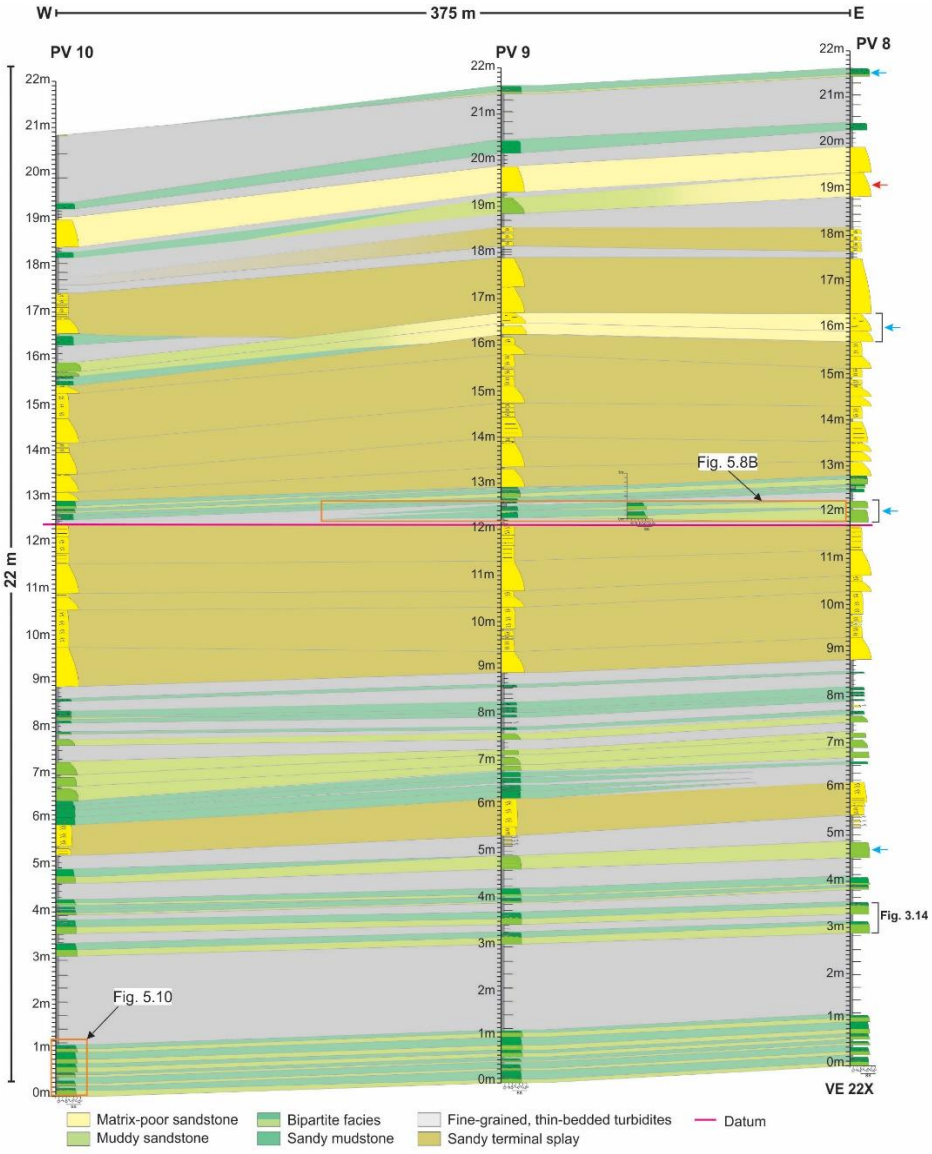

Figure 3.13: Stratigraphic correlation panel (VE 22X) of an ~ 22-m-thick unit in the Petite Vallée Member, Cloridorme Formation (for location see Fig. 3.3B). Note the bipartite facies and associated strata stack exclusively to form several-meters-thick stratigraphic units sandwiched between sand-rich terminal splay deposits and units composed of thin-bedded turbidites. The correlation panel is oriented parallel to the main flow direction (to the west). Arrows point to beds showing part (blue) or all (red) of the downflow depositional continuum. Stratigraphic datum is the top of the terminal splay.

In WSG, this systematic lateral change in lithofacies was observed in opposing directions (see Appendix A4, A6), but only in a single direction in the CF. Like previous studies (Terlaky and Arnott, 2014; Angus et al., 2019), the observed lithofacies trend (MPS → MS → BF → SM) in the WSG is interpreted to represent systematic changes in sedimentation along a proximal to distal depositional transect oriented at a high angle to the main flow, and that the opposing directions indicate deposition on opposite sides of the main flow. In contrast, in the CF outcrop, the observed lithofacies trend parallels associated paleocurrent indicators (average 272°), and similarly the regional westward transport direction in the Cloridorme Formation (Awadallah, 2002; Parkash and Middleton, 1970; Pickering and Hiscott, 1985). Therefore, the lithofacies trend observed in CF represents changes oriented more or less parallel rather than perpendicular to the main flow (see discussion below).

Furthermore, in the BF part of the lithofacies transect, the interface separating the sand-rich lower part from the mud-rich upper part is always planar in the WSG, but in 43% of the measured examples in the CF alternates irregularly between irregular and planar (e.g., Fig. 3.14). As described earlier, irregular surfaces are marked by centimeters-scale synforms and antiforms with local overhangs and injections of sand from the sand-rich part into the overlying mud-rich part. The alternation between irregular and planar intervals occurs on a horizontal scale that ranges from decimeters to several meters, although it is most typically a few meters, and with no consistent lateral spacing or character of the irregular parts. Also, whether the interface is planar or a combination of irregular and planar, the rate of downflow thinning of the basal sand-rich part, and compensatory thickening of the upper mud-rich part, remains unchanged (e.g., Fig. 3.14).

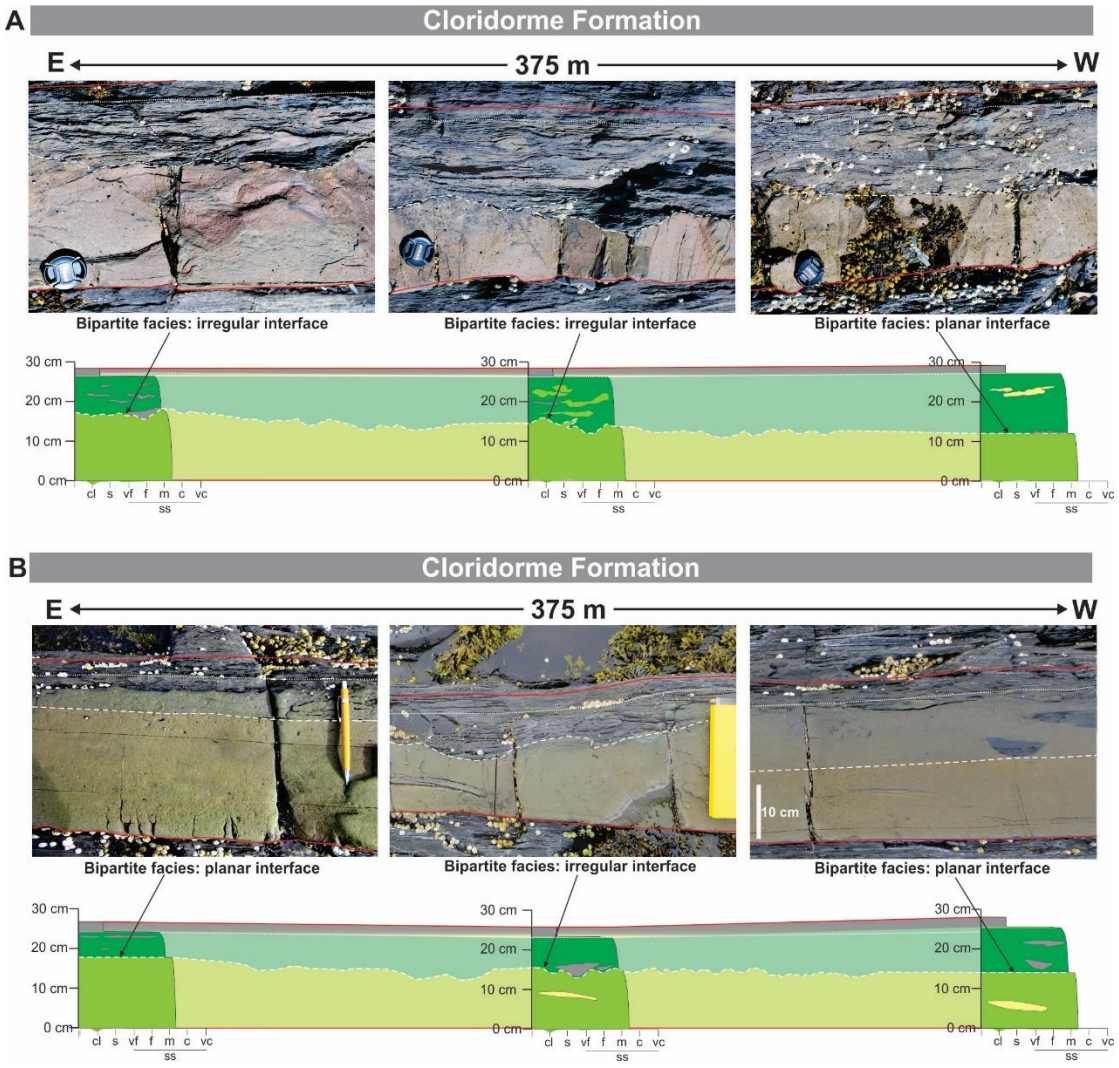

Figure 3.14: A, B) Outcrop photographs and accompanying stratigraphic logs of two bipartite facies beds in the CF (for location see Fig. 3.13) showing the irregular alternation of a planar and irregular interface. Note the downflow (east to west) thinning of the basal sandy part and compensatory thickening of the upper muddy part.

3.5.1 Dimensions

The transition from pink or yellow MPS to gray or brown MS occurs over a median distance of 553 m in WSG and 315 m in CF (Fig. 3.15). Taken from its initial transition from MPS, the distance from MS to the initiation of the upper muddy sandstone part in BF has a median distance of 90 m in WSG and 122 m in CF (Fig. 3.15). Over a median distance of 85 m in WSG and 120 m in CF, the basal sand-rich part progressively thins and then pinches out (Fig. 3.15). The

upper mud-rich part (i.e., SM) continues beyond the pinch-out of the lower sandy layer, but then similarly progressively thins over a median distance of 145 m in WSG and 120 m in CF to its pinch out (Fig. 3.15). The length of the entire transect, therefore, is of the order of 100–1500 m, in which 35 to 65% of the transect is made up of the MPS to MS transition. Interestingly, the remaining parts of the transect, specifically, the MS to BF, BF to SM transitions, and SM to its pinch-out, are of proportionate length (Figs. 3.15, 3.16). Finally, the entire transect is draped by laminated to thin-bedded, traction-structured sandstone (TSS) and/or silty mudstone (Md) that extend beyond the pinch-out of the underlying sandy mudstone.

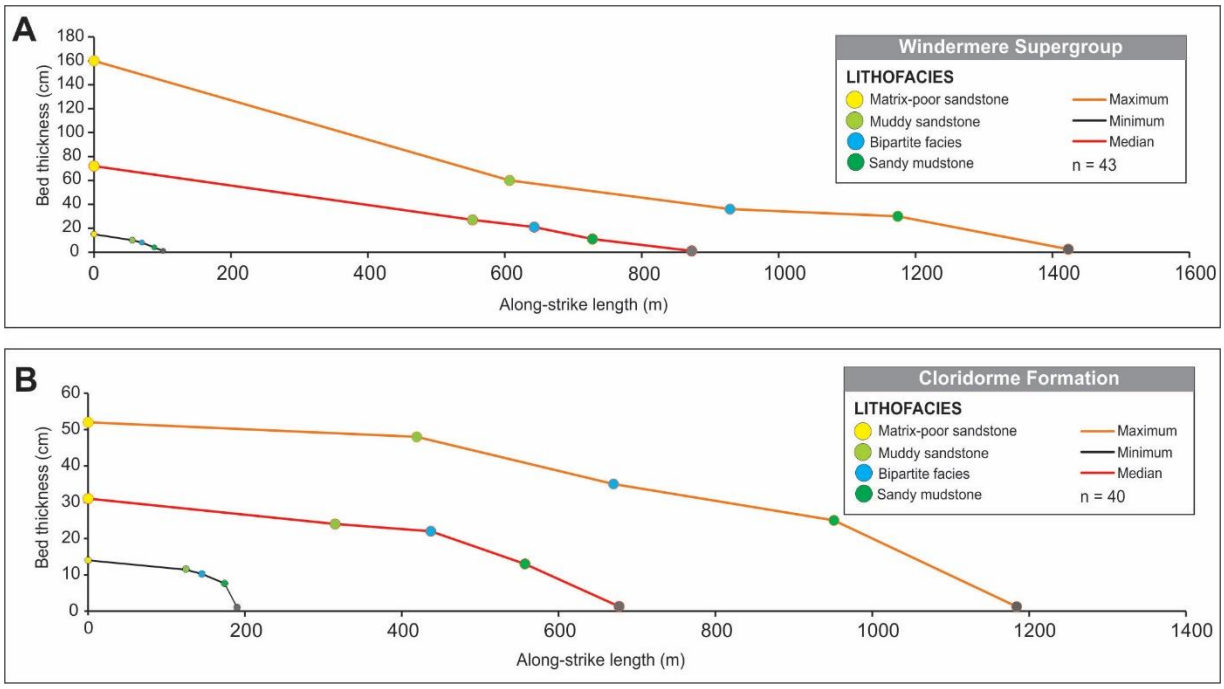

Figure 3.15: A, B) Graphs showing bed thickness versus along-strike length of the lithofacies transitions from matrix-poor sandstone (MPS) (yellow circle) to muddy sandstone (MS) (light green circle) to bipartite facies (BF) (blue circle) to sandy mudstone (SM) (dark green circle) and ultimately to the pinch-out of SM (gray circle) in A) the Windermere Supergroup (WSG) and B) the Cloridorme Formation (CF). Note that in all cases beds exhibit a gradual thinning along the transect. "n" refers to number of transects observed in each study area.

3.5.2 Thickness

In both study areas, there is a general thinning from the sand-rich proximal part of the transect towards the mud-rich distal part (Fig. 3.15). More specifically, thick-bedded MPS

gradually thins to medium-bedded MS and then changes little through the MS and much of the BF interval (Fig. 3.15). However, once the basal sand-rich part of a BF pinches out, the now exclusively sandy mudstone (SM) steadily thins and then pinches out. The traction-structured sandstone (TSS) and silty mudstone (Md) that drapes the depositional transect remains about 1–2 cm thick along the length of the transect.

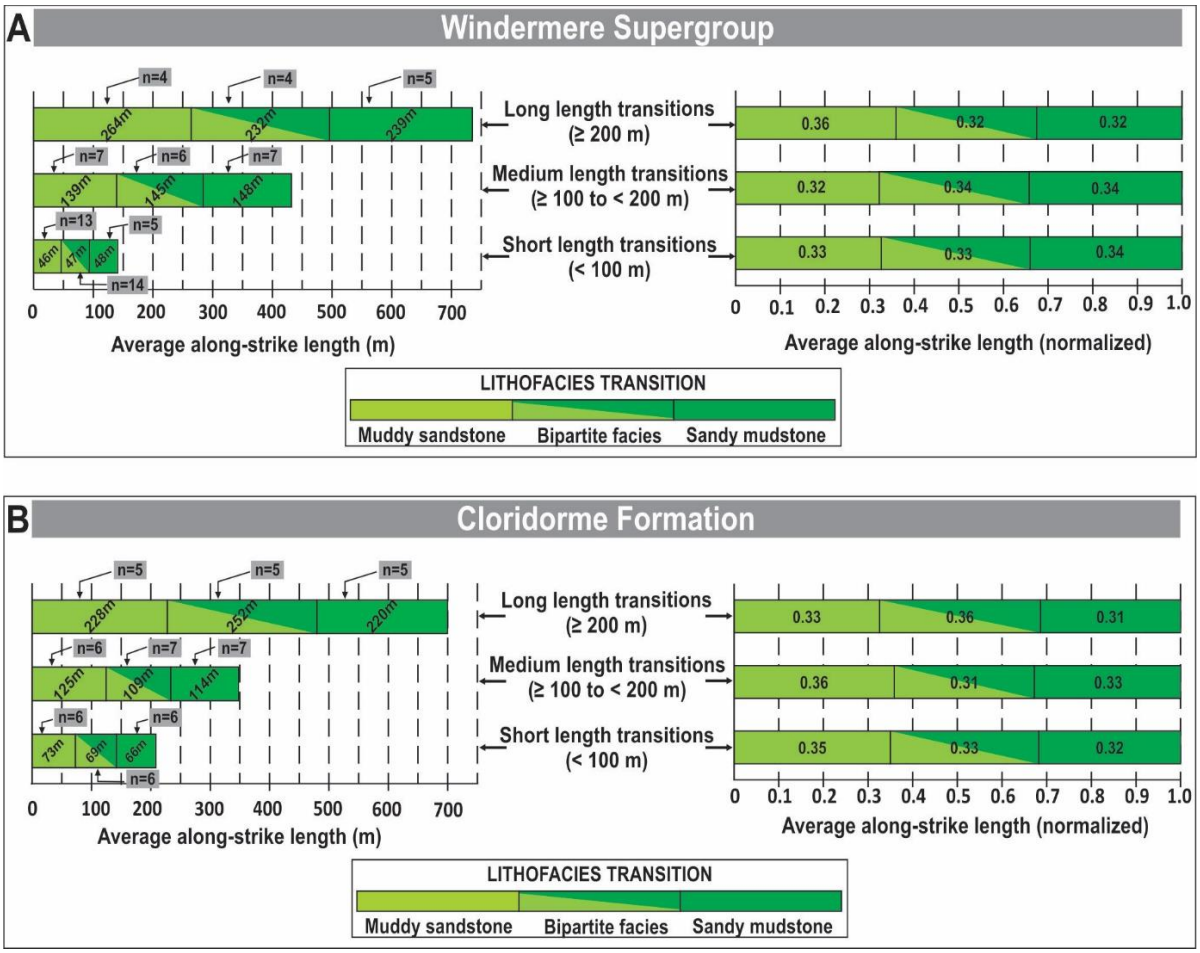

Figure 3.16: Bar graphs on the left show the average along-strike length of each component in the depositional continuum consisting of muddy sandstone (MS) to bipartite facies (BF) to sandy mudstone (SM) and ultimately to the pinch-out of SM in A) the Windermere Supergroup and B) the Cloridorme Formation. Along-strike length of the depositional continuum is categorized as long (≥ 200 m), medium (≥ 100 to < 200 m) and short (< 100 m). In each, the "n" refers to the number of individual beds where that particular transition was observed and used to calculate the average along-strike length for each transition (labelled on the bar graphs). Bar graphs on the right show the same data but normalized by the total length of the depositional transect (i.e., from MS to the pinch-out of SM). Significantly, note that irrespective of overall transect length, and Windermere versus Cloridorme, the normalized length of each lithofacies transition is proportionately similar.

3.5.3 Grain-size distribution

In both study areas, modal grain size of the framework grains progressively decreases along the transect (e.g., Fig. 3.10). Significantly, however, the range of grain sizes, which varies from very fine to very coarse sand, and also dispersed granules in WSG, changes little, or only slightly, with an absence of the coarsest grains in the most mud-rich (distal) part of the transect (e.g., Fig. 3.10). In the most sand-rich (proximal) part of the transect (MPS) modal grain size is generally medium to coarse sand but typically fines to fine to medium sand in MS. In the BF interval the modal grain size in the sand-rich basal layer is similar to that in the MS interval but decreases to very fine to lower medium sand in the upper mud-rich layer. As the basal layer thins and pinches out, modal grain size of the framework grains in the now exclusively SM is commonly very fine to fine sand. Grain size in the overlying traction-structured layer is coarse silt to very fine sand and changes negligibly over the length of the transect. The silty mudstone cap that drapes the entire transect shows no change in grain size over the length of the transect.

3.5.4 Matrix percentage

In both study areas the matrix content increases from the proximal to the distal end of the transect (e.g., Fig. 3.10). More specifically, in the most proximal part of the transect, pink or yellow MPS contains ≤ 17% matrix, which transitions gradually to grey or brown MS containing 23–38% matrix in WSG and 22–37% in CF. Farther along the depositional transect, matrix content in MS strata increases to 38–44% in WSG and 33–40% in CF. At this point, an upper sandy mudstone develops with an initial matrix content of 46–48% that steadily increases to 56–63% over the length of the BF interval. After the pinch-out of the basal muddy sandstone of BF, the upper sandy mudstone progressively thins and increases in matrix content to 57–76% in WSG and 58–72% in

CF and then pinches out. The overlying traction-structured unit consistently contains < 10% matrix.

3.6 DISCUSSION

3.6.1 Development of the lateral facies transect

Based on field observations in this and previous studies (see above), bipartite facies and associated strata typically underlie sandy channel fills and splays in the WSG (e.g., Figs. 3.11, 3.12) and sandy terminal splays in Petite Vallée (CF) (e.g., Fig. 3.13), and were attributed to avulsion associated with the lateral shift of the local sedimentary system (Beeden, 1983; Hiscott et al., 1986; Arnott, 2007b; Terlaky and Arnott, 2014; Angus et al., 2019; Navarro and Arnott, 2020). Downflow of the avulsion node, high-energy, momentum-driven turbulent wall jets eroded previously off-axis sediment and charged the flow with easily suspended very fine sand to clay, in addition to low-density mud clasts—a model similar to other studies, for example the Cretaceous–Paleocene Gottero Sandstone (Fonnesu et al., 2016), the Upper Cretaceous Bordighera Sandstone (Mueller et al., 2017), the Upper Oligocene–Lower Miocene Castagnola Formation (Patacci et al., 2020), the Plio-Pleistocene Mississippi submarine fan deposits (Fildani et al., 2018), and modern delta front strata in the Taiwan Strait (Jin et al., 2021). The rapid addition of easily suspended fine-grained sediment would have increased local effective fluid viscosity and reduced the local velocity gradient, which in turn caused a reduction in bed-generated turbulence and turbulence intensity (e.g., Wang et al., 1998). Moreover, turbulent wall ejections, which are essential for particle suspension, are reduced in number and more widely spaced in time (Rashidi et al., 1990), in addition to energy being dissipated by shear between the newly entrained fine sediment particles

and the slightly more-faster-moving fluid. These effects, in addition to reduced upward turbulent diffusion of suspended sediment, enhanced also by particle settling and stratification effects, caused the suspension to collapse, and under its own momentum, deposit a systematic downflow succession of lithofacies consisting of matrix-poor sandstone (MPS) to muddy sandstone (MS) to bipartite facies (BF), and then sandy mudstone (SM) from the rapidly depleting and negligibly sheared suspension (Fig. 3.17). Initially, the rapidly collapsing, mud-enriched, polydispersed sediment suspension was most likely uniformly mixed, and despite different-size particles settling at different velocities, there was a constant downward mass flux of particles onto the aggrading bed (Dorrell and Hogg, 2010; Dorrell et al., 2011), and as a result the most proximal deposits (Fig. 3.17, Zone 1), namely coarse-tail graded MPS, to have grain-size characteristics resembling that in the initial suspension (Fig. 3.10). Farther along the transport path (Fig. 3.17, Zone 1), faster-settling particles, like granules and very coarse sand, became preferentially depleted from the suspension by deposition on the bed. At the same time the proportion of fine particles and matrix progressively increased, eventually resulting in the transition from MPS to coarse-tail graded MS (Fig. 3.10). As deposition of MS continued, particle settling resulted in a compensatory upward flux of ambient fluid. Shear applied by this upward fluid flux was sufficient to carry with it more buoyant particles like mud particles and low-density mud clasts (Amy et al., 2006; Dorrell and Hogg, 2010; Angus et al., 2019; Hussain et al., 2020), which then accumulated in the upper part of the slowly advecting and negligibly sheared suspension. Ultimately, this caused the upper part of the suspension to develop sufficient cohesive strength and/or density to inhibit the settling of the few remaining sand and coarser grains (Fig. 3.17, Zone 2 or "stratified suspension zone" *sensu* Angus et al., 2019). Accordingly, this two-part suspension deposited the bipartite facies (BF) consisting of a basal sandy layer overlain sharply by a markedly more mud-rich upper layer (Fig.

3.10). Negligible shear in the suspension allowed the preservation of the two-layer makeup, but more significantly, the sharp, and in most cases planar, surface that separates the two parts. Note that a similar mechanism for particle segregation was shown experimentally by Perillo et al. (2015), and more recently by Koo et al. (2019), wherein sand particles settling in a negligibly sheared, sand–mud suspension deposited a sandy basal layer overlain sharply by a suspension of (upward) elutriated mud that quickly developed sufficient matrix-strength to arrest the settling of some sand particles and form an upper sandy mud layer that ultimately deposited en masse. Farther along the depositional continuum being described here, the reservoir of coarse settling particles became progressively depleted due to deposition in the basal sandy layer of BF, while fine-grained sediment continued to accumulate, albeit more slowly, in the upper muddy layer. This is manifested in the progressive downflow thinning, but negligible increase in matrix content, in the basal sandy part of BF, and the concomitant reduced thickening and increase in matrix content in the upper muddy part. Eventually, the basal part of the suspension became completely depleted of sediment and the base of the upper mud-rich part of the suspension intersected the surface of the static bed. The now exclusively mud-rich flow resembled a slow-moving quasi-plug flow with progressively increasing cohesive strength (e.g., Baas et al., 2009) and deposited the nongraded or subtly coarse-tail graded, mud-clast-rich SM (Fig. 3.10), which gradually thinned and then pinched out over several tens of meters (Fig. 3.17, Zone 3, or "plug zone" *sensu* Angus et al. (2019)). It is useful to note that a similar lithofacies transition (BF to SM) characterized by downflow thinning and pinch-out of the basal sandy layer, and a compensatory thickening of the muddy upper layer, followed by its extension beyond the pinch-out of the basal layer, was shown in the experimental work of Perillo et al. (2015). Finally, following the emplacement of the depositional continuum from the collapsed suspension, a remnant low-density turbulent suspension reworked the top of

the deposit and formed the layer of very fine-grained laminated or thin-bedded, upper-division turbidite (TSS), which then is capped by silty mudstone (Md) from a gelled near-bed fluid-mud layer (Fig. 3.17) (equivalent to the H4 and H5 divisions of Haughton et al. (2009)).

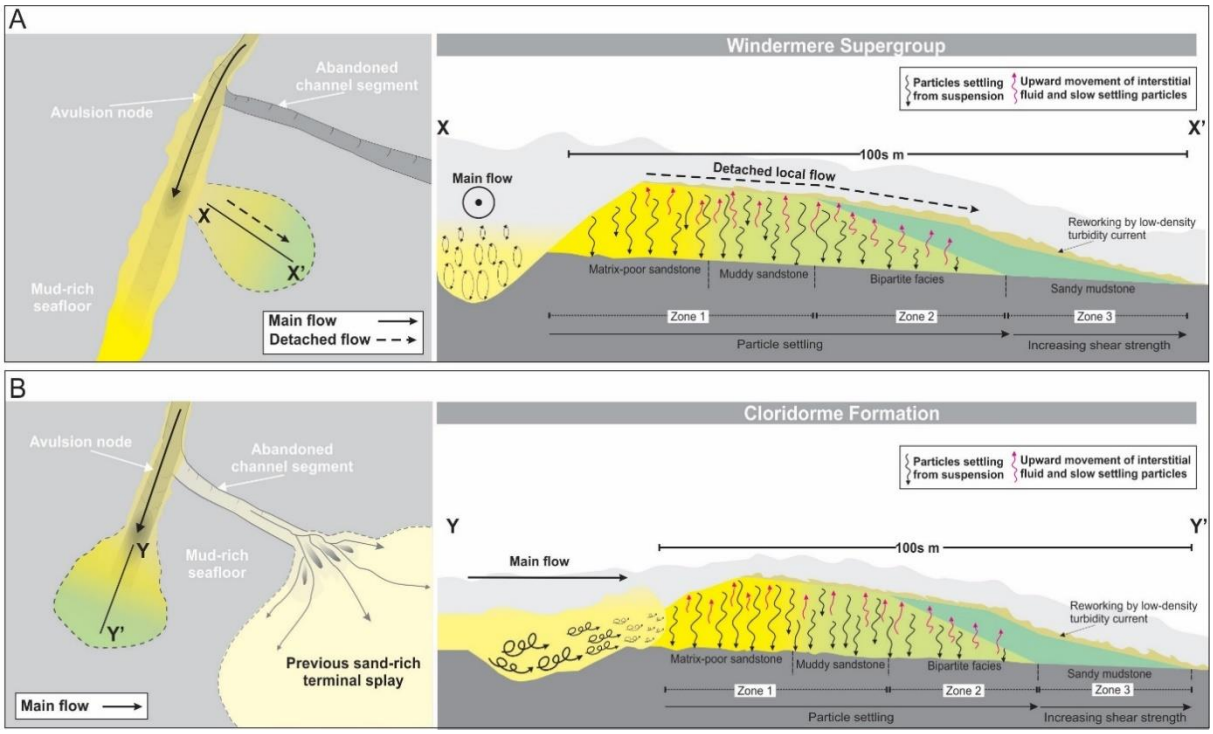

Figure 3.17: A, B) Schematic (left side) of avulsed flows entering the interchannel area and scouring the mud-rich seabed to charge the flow with fine-grained sediment including very fine sand to clay, in addition to mud clasts in both study areas. A) Schematic (right side) showing the depositional continuum of matrix-poor to matrix-rich sandstone developed along the margins of the high-energy wall jet in continental-slope and proximal basin-floor settings of the Windermere turbidite system (not to scale). B) Schematic (right side) showing a similar matrix-poor to matrix-rich sandstone depositional continuum, but here in distal basin-floor deposits of the Cloridorme Formation, makes up a mouth-bar deposit at the downflow terminus of the flow (not to scale). In zone 1, the constant (downward) mass flux of particles settling from a well-mixed, mud-rich, polydispersed, concentrated-dispersion deposits coarse-tail graded, matrix-poor (yellow) and farther downflow muddy sandstone (light green). Continued particle settling (black arrows) results in the upward displacement (pink arrows) of interstitial fluid and easily suspended fine-grained sediment and low-density mud transforms the flow into a two-part suspension that deposits a bipartite facies (zone 2). Eventually the basal part of the suspension becomes depleted of settling particles and pinches out, leaving the mud-rich upper part, now resembling a viscous plug flow (zone 3), which then extends for a few tens of meters farther downflow and pinches out. At all times the suspension is overlain by a low-density turbidity current that formed a well-sorted, traction-structured layer composed of sediment reworked from the underlying deposit.

3.6.2 Paleogeographic occurrence of bipartite facies and associated strata

Bipartite facies and associated strata spanning continental-slope to proximal basin-floor deposits in the Castle Creek study area have been interpreted to have formed along the margins of an avulsion-related wall jet (Fig. 3.17A) (Terlaky and Arnott, 2014; Terlaky et al., 2016; Angus et al., 2019; Navarro and Arnott, 2020). Specifically, downflow of an avulsion node, previously channelized turbidity currents became unconfined, forming a high-energy, momentum-driven wall jet (Terlaky and Arnott, 2014, see also Lang et al., 2021), resembling conditions in the up-flow parts of better-known sedimentary environments like deltas (e.g., Bates, 1953; Wright, 1977; Wellner et al., 2005; Ahmed et al., 2014; Fidolini and Ghinassi, 2016; Daniller-Varghese et al., 2020) and ice-contact outwash fans (e.g., Powell, 1990; Russell and Arnott, 2003; Winsemann et al., 2009). At its upflow end, the momentum-driven wall jet deeply scoured the bed (e.g., Lang et al., 2021), possibly augmented by secondary circulation in a hydraulic jump (e.g., Russell and Arnott, 2003; Hamilton et al., 2015), and charged the flow with silt, clay, and low-density mud clasts eroded from the local mud-rich interchannel seabed (Terlaky and Arnott, 2014). Within the scour, intense and complex turbulent flow patterns fully mixed the suspension, especially during episodic high-energy pulses (e.g., Lang et al., 2021). During these high-energy pulses it is interpreted that a volume of well-mixed sediment became detached and, under its own inertia and residual momentum advected away from the margins of the main jet, where it then collapsed and deposited the depositional continuum (MPS → MS → BF → SM) described above (Fig. 3.17A) (Terlaky and Arnott, 2014; Angus et al., 2019). Farther downflow, the wall jet would be expected to expand laterally, which initially would lower the height of the velocity maximum toward the bed and increase basal shear (Pohl et al., 2019), thereby extending the zone of erosion. Nevertheless, continued lateral and vertical expansion, and attendant energy loss by turbulent

mixing along its margins, eventually resulted in decreased velocity, and like commonly observed in experimental flows, deposit a "mouth bar" (*sensu* Lang et al., 2021) with positive topography (see also Alexander et al., 2008). However, these elements are not observed in the Windermere system, and instead deposition of the MPS to SM continuum is interpreted to have taken place outward from the margins, and therefore at a high angle rather than parallel, to the main flow (Fig. 3.17A). The absence of a mouth bar is possibly related to differences in the scale of laboratory versus natural turbidity currents. In turbulent laboratory density flows the Reynolds number (Re), which is the ratio of inertial to viscous forces, is typically of the order to 10^3 to 10^5 (e.g., Leclair and Arnott, 2005; Lang et al., 2021). In natural turbidity currents, on the other hand, Re is orders of magnitude higher; for example, Re is estimated to be of the order of 10^9 to 10^{10} on the continental slope (Meiburg and Kneller, 2010), and measured at ~ 2.5 x 10^6 in the modern Black Sea saline density current (Dorrell et al., 2019). As a consequence, the high-energy momentum-dominated proximal part of the turbulent wall jet, which experiences little interaction with the ambient fluid, and therefore little deceleration, would have extended a significant distance downflow of the avulsion node. Nevertheless, at some distance downflow, basal friction and interaction with the ambient fluid would eventually cause the flow to decelerate. However, these conditions would cause particles to settle and if maintained in suspension concentrate mass in the lower part of the flow, thereby increasing density and causing the now fully gravity-driven flow to remain energetic and bypass downslope.

In contrast to the Windermere, the depositional continuum of matrix-rich lithologies in strata of the low-gradient distal basin-floor Cloridorme is oriented parallel to the main direction of transport (Fig. 3.17B). Here the incoming flow is interpreted to have been much less energetic compared to the more proximal settings in the Windermere. Upon losing confinement at the

downflow end of channels the flow scoured the mud-rich seafloor (e.g., Hodgson, 2009; Kane et al., 2017; Mueller et al., 2017; Spychala et al., 2017; Brooks et al., 2018), and as described above, resulted in increased local effective fluid viscosity and significant changes in the character, intensity and transfer of fluid turbulence needed to maintain the particle suspension. These changes, along with the rapid expansion and deceleration of the flow, caused the transport capacity to be exceeded, and in turn, a constant mass flux of settling sediment to the seabed. This, then, built up a mouth bar whose deposits exhibit the same systematic downflow succession of matrix-poor to matrix-rich lithologies, but instead is oriented in the same direction as the main flow (Fig. 3.17B).

3.6.3 Variable length of the lithofacies transect

In the WSG (Angus 2016; Wearmouth 2018; Angus et al. 2019), and shown here in the CF, the depositional continuum consisting of MPS → MS → BF → SM takes place over a horizontal distance of tens to several hundreds of meters (Fig. 3.15). The varying length of the continuum could be argued to reflect the degree of obliquity between the strike of the outcrop and trend of the continuum, i.e., longer transects are oriented at a higher angle to the strike of the outcrop. However, as noted earlier, the length of the continuum is related directly to maximum bed thickness in the proximal end of the continuum (Fig. 3.15). Orientation of the continuum would have no effect on bed thickness, and therefore it is argued that denser, more energetic flows resulted in more extensive erosion of the seabed, forming larger-volume, more dense extractions from the main flow in the more proximal parts of a turbidite system, and denser suspensions with greater particle momentum in distal settings, resulting in deposition of a thicker, longer deposit. Additionally, irrespective of the length of the depositional continuum, after MPS transitions to

MS, the subsequent lithofacies transitions, namely, MS to BF to SM and ultimately to the pinch out of SM, occur in equally proportioned downflow lengths (Figs. 3.15, 3.16). This shows that regardless of the variable size of the initial mud-enriched flows, once developed, the now completely momentum-driven flow evolved in a spatially systematic and dimensionally proportionate manner.

3.6.3 Nature of the interface in bipartite facies

As described above, bipartite facies consist of two layers: lower sand-rich layer overlain sharply by a significantly more mud-rich upper layer. In rocks of the WSG, the interface in BF is exclusively planar. In the CF, on the other hand, the interface is mostly planar, but in many beds alternates between irregular and planar (e.g., Fig. 3.14). The irregular interface is characterized by centimeters-scale synforms and antiforms with local overhangs and injections of sand from the sand-rich basal part (Fig. 3.6J–L). Furthermore, the alternation between planar and irregular surfaces occurs on horizontal scale of decimeters to several meters without any systematic lateral variation in spacing or character of the irregular parts. Also, regardless of the nature of the bipartite facies interface (i.e., planar or a combination of planar and irregular), the rate of downflow thinning of the basal sandy part, and the compensatory thickening of the upper muddy part, does not change (e.g., Fig. 3.14).

In many subsurface and outcrop studies that describe two-part (bipartite) facies, the surface separating the two parts often exhibits meters-scale relief and evidence of liquefaction and upward injection (fluidization) of sand from the lower sandy part into the upper muddy part. The origin of these features has been attributed to erosion of the basal sandstone by an overriding clast-rich muddy debris flow (i.e., linked debrite) (e.g., Talling, 2013; Fonnesu et al., 2015); postdepositional

loading of a debrite into an underlying sand-rich turbidite (e.g., Haughton et al., 2003; Fonnesu et al., 2015); or a combination of the two (e.g., Hodgson, 2009; Fonnesu et al., 2015). Additionally, Fonnesu et al. (2015) suggest a systematic downflow thinning of bipartite facies with an initially highly rugose interface to a planar interface over hundreds of meters, and attributed the downflow transformation to a weakening of the interaction between the (linked) debris flow and the previously deposited bed of clean sand.

In this study, however, the interface in all BF in WSG and most in the CF are planar, and where exhibiting both in the CF, they appear to alternate irregularly with no apparent systematic downflow trend (e.g., Fig. 3.14). Here, similar to Angus et al. (2019), planar interfaces are interpreted to have formed in a vertically segregated suspension, where, following deposition of the basal part of the suspension, the inertia-driven, mud-rich upper part continued moving (albeit most probably slowly) and formed a planar, non-erosional contact (Fig. 3.18)—the sharp, planar shape and the abrupt change in stratal composition and sorting across the contact necessitates negligible shearing in the flow, which otherwise would cause it to be at least diffuse, and more probably, eliminated by extensive mixing. The local development of irregular segments along the otherwise planar interface in some CF beds is interpreted to be a consequence of postdepositional deformation caused by variations in water saturation and pore-fluid pressure in the lower, sand-rich part of bipartite facies. More specifically, following deposition of the event bed, upward movement of pore fluids due to bed consolidation became restricted along the BF interface, where mud content in the upper layer increases abruptly by 15–25%. Overpressure of pore fluids and reduction in bulk density at the top of the lower sand-rich layer, which resulted in foundering of the upper mud-rich layer (e.g., Rassat et al. 2014) (Fig. 3.18), or in more extreme cases, the upward injection of sandy sediment into the base of the mud-rich layer (see also Fonnesu et al. 2015) (Fig.

3.18), were quite possibly linked to sudden tectonically induced liquefaction events—a phenomenon that was most likely commonplace in the tectonically active Taconic foreland basin (e.g., Pickering and Hiscott, 1985; Hiscott et al., 1986; Awadallah and Hiscott, 2004), but rare in the passive margin WSG. Alternatively, the difference in the BF interface between the WSG and CF basins may be related to differences in clay mineralogy and its effect on permeability and pore-fluid pressure. However, due to low and very low-grade metamorphism in the WSG and CF, unequivocally determining the original mineralogy is not possible. Nevertheless, sediment in the WSG was sourced from weathered felsic rocks of the North American craton (Ross and Arnott, 2007; Hadlari et al., 2021), and therefore kaolinite most probably made up most of the clay fraction (e.g., Hamilton, 2002; Liu et al., 2010; Nielsen et al., 2015). In the CF, on the other hand, sediment was sourced from older cratonic clastic and carbonate rocks, but also a large ophiolite and volcanic arcs associated with the ongoing Taconic orogeny (Enos, 1969; Beeden, 1983; Hiscott, 1984). This, then, suggests a dominantly mafic source with abundant smectitic clay minerals in the clay-size fraction (e.g., Ogg and Smith, 1993; Hamilton, 2002; Liu et al., 2009; Nielsen et al., 2015). The specific surface area (SSA) of smectite is 700–900 m^2/g but only 10–40 m^2/g in kaolinite (Revil and Cathels, 1999; Cerato and Lutenegger, 2002), and for the same porosity, kaolinite is five orders of magnitude more permeable than smectite (Mesri and Olsen, 1971; Revil and Cathles, 1999). Therefore, for a similar clay content in the basal sand-rich part of BF, kaolinite in the WSG would have allowed pore fluids to be easily expulsed during postdepositional compaction, which then preserved the planar BF interface. In the CF, on the other hand, less permeable smectitic clay would have retained pore fluids and in some beds caused local overpressure that may have inverted the local density gradient and caused the now more dense upper mud-rich layer to founder and deform the BF interface.

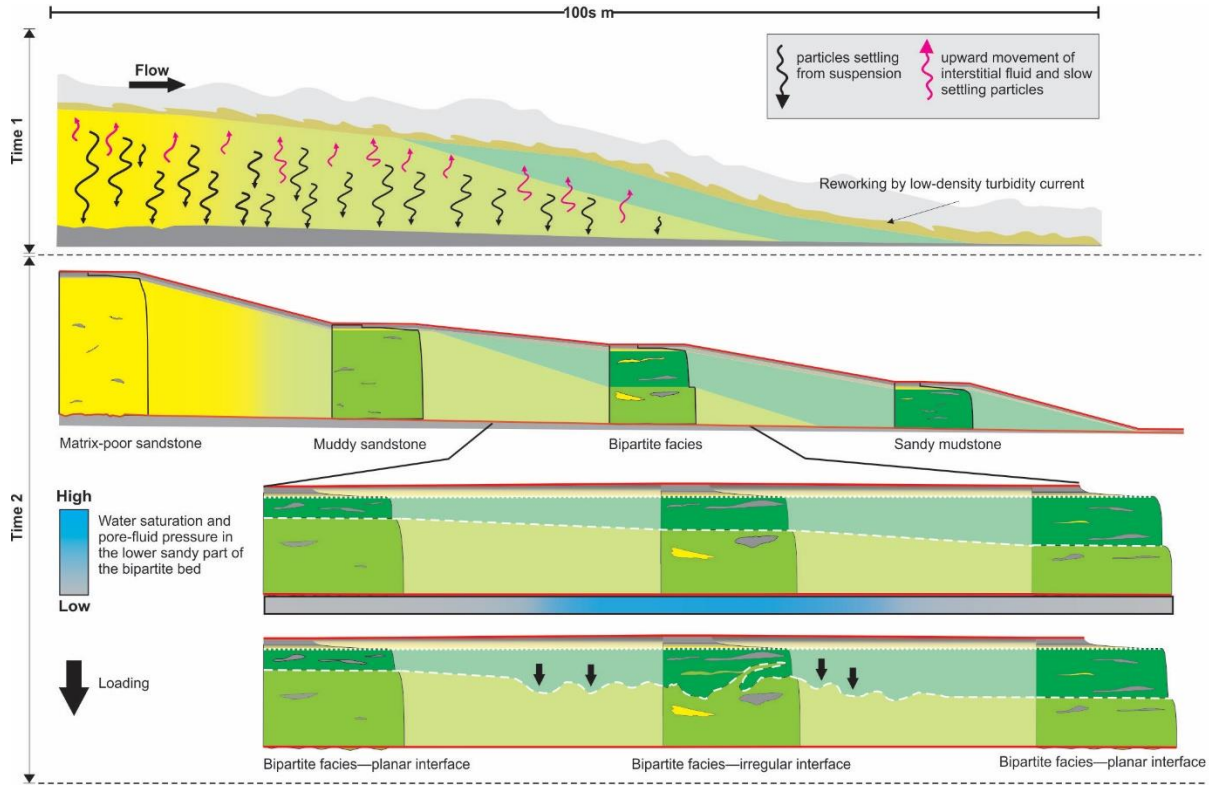

Figure 3.18: Schematic showing the postdepositional development of an irregular bipartite facies interface. Time 1 shows deposition of the lithofacies continuum from matrix-poor sandstone (MPS) to muddy sandstone (MS) to bipartite facies (BF) and then to sandy mudstone (SM). Note that the interface in the bipartite part of the continuum is planar. Sometime later (time 2) locally elevated pore-fluid pressure in the top region of the comparatively more sand-rich basal part of the bipartite facies caused the planar interface to deform as local areas of the overlying mud-rich layer foundered (black arrows), augmented locally by the upward injection of sand into the mud-rich upper layer.

3.6.4 Comparison with other composite sand–mud strata

Like bipartite facies described in this study, hybrid event beds (e.g., Haughton et al., 2009; Hodgson, 2009; Fonnesu et al., 2015; Spychala et al., 2017) and transitional flow deposits (e.g., Kane and Pontén, 2012; Kane et al., 2017; Southern et al., 2017) are principally composed of two parts—a sand-rich part overlain sharply by a mud-rich part, which in an ideal succession is then capped by a well-sorted, finer-grained and commonly traction-structured layer overlain by massive to graded silty mudstone. As noted earlier, these texturally different parts are interpreted to be genetically related but explained by very different physical models. In the longitudinal segregation

model (e.g., Haughton et al., 2009; Fonnesu et al., 2015, 2016, 2018; Hussain et al., 2020), superposition of the argillaceous upper layer (H3) over the basal sandy layer (H1) is attributed to longitudinal partitioning of the mud-enriched flow into a noncohesive forerunning-turbidity current followed by a more cohesive flow, which at some point farther downflow stack to form a single hybrid event bed. In contrast, transitional-flow deposits are attributed to vertical particle segregation (e.g., Sumner et al., 2009; Baas et al., 2011; Kane et al., 2017; Spychala et al., 2017), wherein deceleration of a mud-enriched flow results in the selective settling of sand and coarser grains to form a dense (i.e., high-concentration) basal layer that then inhibits the upward diffusion of near-bed-generated turbulence and allows mud particles in the upper part of the suspension to flocculate and form a high-yield-strength network. Most recently, Baas et al. (2021) proposed a two-stage depositional model marked by an initial longitudinal segregation of clasts as bedload in an erosive debris flow, followed by vertical segregation of suspended sediment in the trailing body of the flow as it decelerates. Nevertheless, all of the mechanistic models result in a common succession of facies characterized by a downflow change from clean sandstone to hybrid-event-bed or transitional-flow deposit and eventually to an abrupt thinning and termination of the strata, and that all these changes occur over a horizontal distance of several kilometers (e.g., Davies et al., 2009; Fonnesu et al., 2015; Hussain et al., 2020) to tens of kilometers (e.g., Talling et al., 2012a, 2012b, 2013; Kane et al., 2017; Hussain et al., 2020). However, composite strata describe here, and termed the bipartite facies, form part of a depositional continuum typically < 1 km long, and occur downflow of muddy sandstone that over 10s to 100s of meters show a consistent and systematic downflow thinning and then pinch-out of the basal sand-rich part followed by thinning and then pinch-out of the upper mud-rich part (i.e., the sandy mudstone)—the horizontal distance between the two pinch-outs approximating the length of the preceding bipartite facies. Such

systematic changes in lithology, proportionate lengths of those changes, and notably the short spatial scales over which they occur are difficult to reconcile with processes like longitudinally fractionated or vertically stratified flow (see also discussion in Terlaky and Arnott, 2014; Angus et al., 2019). Furthermore, bipartite facies and associated strata form sharply bounded stratal units that only rarely are interstratified with other lithologies (see also Terlaky and Arnott, 2014; Angus et al., 2019), indicating that these sedimentologically unique conditions began abruptly, were sustained for a period of time, and then replaced abruptly by more typical styles of slope and basin-floor sedimentation, for example, leveed slope-channel complexes, distributary-channel fills, and terminal splays. Accordingly, the localized, episodic, and short-lived nature of these composite strata are inconsistent with them being associated with regional-scale processes like the onset of fan initiation and growth (e.g., Haughton et al., 2009; Hodgson, 2009; Spychala et al., 2017) or the general enrichment of fine-grained sediment along the margins of turbulent suspensions (e.g., Barker et al., 2008; Pyles and Jennette, 2009). Here it is argued that bipartite facies and its associated strata are instead formed locally and downflow of an avulsion node where the now momentum-driven, turbulent wall jet scoured the seabed and rapidly enriched the suspension with mud (see also Terlaky and Arnott, 2014; Angus et al., 2019), and then outward from its margins in continental slope and proximal basin-floor settings (WSG), or at the downflow terminus of the main flow in more distal basin-floor settings (CF), rapidly, but systematically, deposited a consistent and dimensionally proportionate along-flow suite of distinctive lithologies.

3.7 CONCLUSIONS

In slope to proximal basin-floor deposits at the Castle Creek study area (WSG), and distal basin-floor strata in the Petite Vallée study area (CF), bipartite facies and associated strata are commonly overlain abruptly by sand-rich stratal elements, including slope channels, distributary channels and terminal splays. This suggests that deposition of these strata is not paleogeographically but rather mechanistically controlled. Here it is argued that the initiation of the local transport system caused by an upflow avulsion formed a wall jet that locally scoured the mud-rich interchannel area and charged the flow with fine-grained sediment, namely very fine sand to clay, in addition to low-density mud clasts. The local incorporation of easily suspended fine-grained sediment resulted in the rapid increase in local effective fluid viscosity, but also a dramatic change in the characteristics and reduction in the intensity and transfer of fluid turbulence needed to maintain the particle suspension. This caused the sediment suspension to rapidly exceed transport capacity and collapse, forming a negligibly sheared suspension that deposited a systematic along-flow depositional continuum consisting of matrix-poor sandstone (MPS) to muddy sandstone (MS) to bipartite facies (BF) and then sandy mudstone (SM) over a distance of hundreds of meters, which is overlain everywhere by a thin-bedded, traction-structured sandstone and/or silty mudstone cap. In continental-slope and proximal basin-floor deposits of the WSG, deposition took place along the margins of the high-energy wall jet. In the low-gradient distal basin-floor setting of the CF, on the other hand, flow deceleration caused by flow expansion, in addition to abrupt changes in effective fluid viscosity and turbulence in these lower-energy flows, marks the downflow terminus of the flow, and accordingly, deposition of a mouth bar from the collapsing sediment suspension. Importantly, irrespective of paleogeographic location, the length of the various lithological elements that build up the depositional continuum, after MPS transitions

to MS (i.e., MS to BF to SM and ultimately to the pinch-out of SM), occur in equally proportioned lengths. This suggests that, once formed, the mud-enriched, momentum-driven flow evolved in a spatially systematic and dimensionally proportionate manner, suggestive, therefore, of mechanistic consistency. Such uniformity is difficult to reconcile with deposition by mechanistically different flows forming a single deposit, or flows that undergo spatial and/or temporal changes in rheology or flow state. These interpretive differences point to the need for more examples of ancient matrix-rich and associated matrix-poor strata that can be traced continuously along strike and their macroscopic and microscopic characteristics studied in detail.

CHAPTER 4: FROM GREYWACKE TO VARIOUSLY NAMED SAND- AND ASSOCIATED MUD-RICH STRATA—CLEARING THE MUDDY WATERS ON A LONGSTANDING DEBATE

4.1 INTRODUCTION

Poorly sorted, matrix-rich (> 10% mud, i.e., silt and clay) sandstones with varying amounts of quartz, feldspar and rock fragments have been widely reported in the geologic literature. Termed 'greywacke' by Robert Jameson in 1808 (see Bailey, 1930), and typically associated with deep-water deposits, this type of sandstone has been the subject of a long-standing debate in the geological literature. One of the first obstacles was identifying the appropriate criteria for classifying these sandstones, including a classification based exclusively on mineral composition (i.e., ratio of quartz, feldspar and rock fragments) (e.g., Krynine, 1948; Shrock, 1948; Dunbar and Rogers, 1957; Hubert, 1960), a combination of mineral composition and texture (i.e., ratio of quartz, feldspar+rock fragments, and matrix (silt+clay)) (e.g., Pettijohn, 1949; Tallman, 1949; Dapples et al., 1953; Packman, 1954; Bokman, 1955; Crook, 1960), or by separately assessing mineral composition, texture and grain size (e.g., Folk, 1954; Van Andel, 1958). These differences resulted in various matrix-rich but non-deep-water rocks to be termed greywacke (e.g., Krynine, 1937; Hay, 1957; Dapples and Mitchum, 1955; Potter and Glass, 1958), and caused Dott (1964) to propose that the term 'greywacke' be discontinued and instead an adapted version of the Gilbert (1954) sandstone classification scheme, based on percent detrital matrix content (arenite <10% < wacke matrix), be used. Dott further categorized the arenite and wacke sandstones based on their mineralogical composition (i.e., proportion of quartz, feldspar, and rock fragments). The second, and maybe more significant debate concerned the

origin of the matrix, and whether it was detrital (e.g., Bailey, 1930; Bosewell, 1930; Woodland, 1938, Sherman, 1953; Hollister and Heezen, 1964; Rust, 1965; Audley-Charles, 1967; Parkash and Middleton, 1970; Hiscott and Middleton, 1979), or authigenic (e.g., Cummins, 1962; Kuenen, 1966; Rahmani, 1968; Reimer, 1971; Lovell, 1972; Buller and McManus, 1973; Galloway, 1974; Wilson and Pittman, 1977; Shannon, 1978). However, in the absence of consensus, the study of matrix-rich sandstones largely fizzled out from the early 1980s to late 1990s. In the 2000s, spurred on by extensive hydrocarbon exploration in deep-sea offshore turbidite systems, in particular the North Sea, interest in deep-marine matrix-rich sandstones regained momentum with a focus on understanding their physical origin and associated depositional environments. In their seminal paper, Lowe and Guy (2000) describe matrix-rich sandstones that they termed slurry beds, and in which, the fine-grained matrix was interpreted to be detrital. Since then, a wide variety of terms, some descriptive, other interpretative, have been proposed, including linked debrites (Haughton et al., 2003), co-genetic debrite-turbidite beds (Talling et al., 2004), hybrid event beds (Haughton et al., 2009), transitional flow deposits (Kane and Pontén, 2012) and matrix-rich sandstones (Terlaky and Arnott 2014). Irrespective of differences in terminology, there is general consensus that like Lowe and Guy (2000), the matrix is detrital, but its origin, and the relationship between matrix-rich and matrix-poor parts of individual event deposits, is still a matter of vigorous debate. In this review, these distinctive deposits are discussed with emphasis on stratal make-up, stratigraphic occurrence, spatial scales, and proposed physical origin.

4.2 SLURRY BEDS

The term ‘slurry beds’ (*sensu* Lowe and Guy, 2000) is an adaptation of the term ‘slurried

beds' introduced by Wood and Smith (1958) to describe mud-rich, poorly sorted, ungraded sandstones that occur in association with sandy turbidites in the Silurian, Aberystwyth Grits Group. The slurry beds of Lowe and Guy (2000) were reported in drill core from the Lower Cretaceous Britannia Formation (North Sea), and interpreted to be deposited on the broad, low-relief basin plain of a deep-water turbidite system. Strata comprise 1 – 30 m-thick sandstone beds containing 10 – 35% detrital mud matrix and a unique assemblage of sedimentary structure divisions that differ from those in classical turbidites and debris-flow deposits, including current structured and/or massive division (M1), banded units with distinctive alternating cm- to m-thick, light (mud-poor) and dark (mud-rich) bands (M2), mm- to cm-scale wispy laminated sandstones (M3), mud poor dish-structured sandstone (M4), fine-grained, micro-banded to flat-laminated units (M5), foundered and mixed sandstone/mudstone (M6), and vertical water escape structured division (M7) (Fig. 4.1).

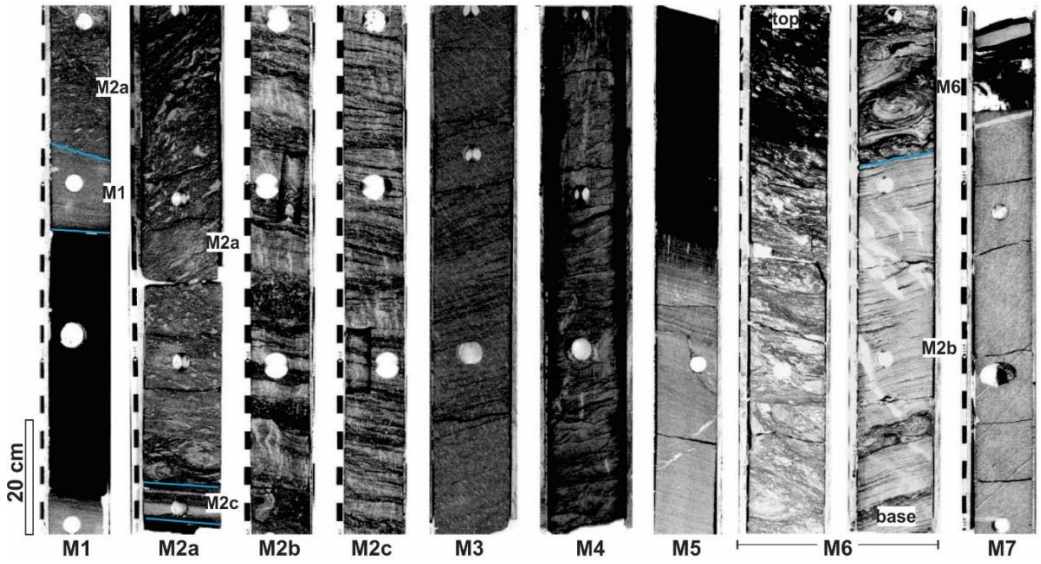

Figure 4.1: Core photographs showing the sedimentary structure divisions (M1, M2, M3, M4, M5, M6 and M7) of slurry beds (Lowe et al. 2003, figs. 4, 5). M1 = current structured division. M2a = mixed slurried to megabanded division. M2b = macrobanded sandstone. M2c = mesobanded sandstone. M3 = wispy laminated unit. M4 = dish-structured sandstone. M5 = fine-grained, micro-banded to flat-laminated division. M6 = foundered and mixed sandstone/mudstone. M7 = vertical water-escape structured division. Blue lines mark the boundaries of the different divisions.

Similar strata were then reported in outcrop from the Oligocene flysch of the East Carpathians, Romania by Sylvester and Lowe (2004), which like slurry beds in the Britannia Field, contained > 15% detrital mud matrix, generally lacked tractional structures and exhibited cm-scale alternating mud-poor and mud-rich bands. These distinctive strata were interpreted to be deposited by mud-enriched sediment gravity flows, termed "slurry flows", that were an intermediate flow type between non-cohesive turbidity currents and cohesive debris flows (Lowe and Guy, 2000; Sylvester and Lowe, 2004). More specifically, Lowe and Guy (2000) proposed the following interpretations for the various sedimentary structured divisions that make up slurry beds. M1 division, which occurs almost exclusively at the base of individual beds, is interpreted to reflect deposition from flows that were initially fully turbulent (Fig. 4.2A). As flows waned, mud, sand and coarser particles settled and increased sediment concentration and density in the lower part of the flow (Fig. 4.2B). In this near-bed region, dense, sand-sized quartz and feldspar grains settled to the bed forming a light-colored cm- to dm-thick band in the M2 division (Fig. 4.2C). Lower density mud particles, on the other hand, remained suspended, and with time steadily increased in concentration until the near-bed mud layer developed sufficient viscosity to freeze and deposit a cm- to m-thick mud-rich dark band in the M2 division (Fig. 4.2C). These conditions then repeated and built-up a succession of alternating light and dark bands that make up the M2 division (Fig. 4.2D, E). The wispy-laminated M3 division is interpreted to be deposited in a manner similar to M2, but from a less muddy suspension in which the near-bed mud layer was thinner and instead deposited mm- to cm-thick muddy bands. The sand-rich dish-structured M4 division is interpreted to have formed by mud-poor flows with high rates of direct suspension sedimentation and syndepositional dewatering. The M5 division, which is analogous to the Tbde sequence in a classical turbidite, typically overlies thick slurry beds and marks the waning stages

of the flow with fine sand to silt deposited on the bed. Where the M5 division is modified by post-depositional loading, it is termed the M6 division, and by pervasive upward pore fluid escape, M7. Based on a Markov chain analysis of the various stratal divisions, Lowe and Guy (2000) postulated a number of different bed types, including (I) dish-structured beds; (II) dish-structured and wispy-laminated beds; (III) banded and wispy laminated and/or dish-structured beds; (IV) predominantly banded beds; and (V) thickly banded and mixed slurried beds. All bed types had a thin M1 division at their base and M5, M6 or M7 divisions at the top. These different motifs were interpreted to reflect differences in the mud content and rate of suspended sediment fallout from the depositing flows.

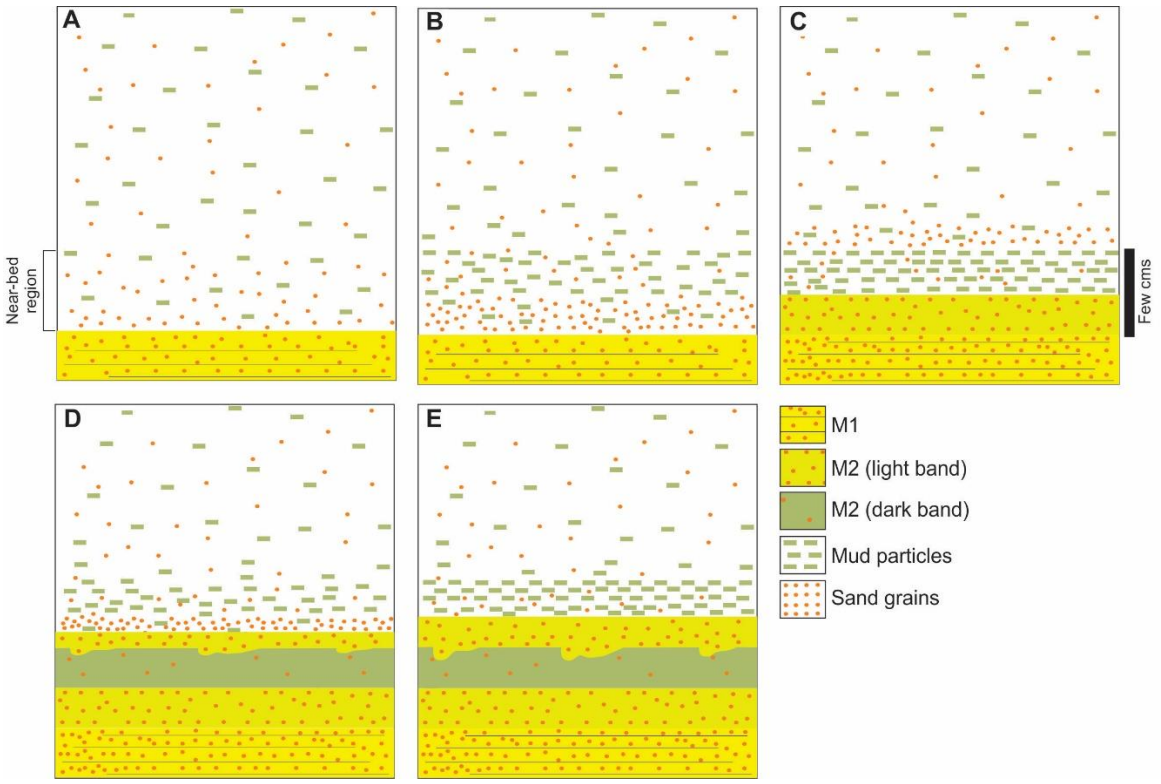

Figure 4.2: Interpreted origin of banding in slurry beds. A) Deposition of planar- or cross-stratified M1 division from an initially fully turbulent sediment suspension. B) As the flow wanes, sand and mud particles settle increasing sediment concentration and density in the near-bed region. C) Dense sand grains settle to the bed and form a light-coloured band; lower density mud particles remain suspended and increase in concentration. D) Near-bed mud suspension develops sufficient viscosity to form a plug layer that freezes forming a dark band. E) Repetition of parts B to D build-up the alternating light and dark bands of the M2 division. Modified after Lowe and Guy (2000).

Later, Lowe et al. (2003) conducted a more detailed petrographic analysis of the facies and textural trends in several laterally extensive (5 – 6 km long), sheet-like, slurry beds in the Britannia Field. This work showed that individual slurry beds exhibited two styles of downflow facies changes over horizontal distances of several hundreds meters to a few kilometers: mud-poor, dish-structured (M4) and wispy-laminated sandstone (M3) transitioning to mud-rich banded and mixed slurried sandstone (M2); and mud-rich banded and mixed slurried sandstone (M2) to less mud-banded sandstone (M2) to wispy-laminated sandstone (M3). Each trend was interpreted to be associated with a unique suite of hydraulic and sediment conditions. More specifically, the former trend was attributed to flows consisting of sand grains that were slightly coarser than the associated mud flocs, and resulted in the preferential deposition of sand in the proximal region followed by a progressive downflow enrichment in mud. Conversely, the latter trend was deposited by flows containing mud flocs that were slightly coarser than the associated sand grains, causing proximal sedimentation of mostly mud with progressive distal enrichment in the finer-grained sand fraction. The Lowe et al. study was then re-evaluated by Barker et al. (2008) using a different correlation and palaeoflow scheme (see also, Hailwood and Ding, 2000) that took into consideration the effects of slope remobilization that locally overprinted the original depositional fabrics. Barker et al. suggested that the reported downflow transition from mud-rich to mud-poor slurry beds was in fact a consequence of the transition being oriented at a high angle rather than parallel to the main paleoflow direction, and that mud-poor facies constitute axial deposits, whereas mud-rich facies were deposited on the lateral margins of the main flow. In addition to this spatial organization, Barker et al. (2008) reported that individual slurry beds typically transition vertically from sand-rich to banded to clay-rich facies, and that based on these consistent lateral and vertical relationships, were deposited by a single mud-

enriched sediment gravity flow that variously exhibited turbulent, transitional and laminar flow conditions in both time and space.

At about the same time that the slurry beds model was being developed, another type of deep-marine matrix-rich strata was recognized in Upper Jurassic deep-water strata of the North Sea by Haughton et al. (2003). Distinctively, these strata lacked the multiple light-dark banding typical of slurry beds, and instead, were characterized by a single light-coloured, sand-rich layer overlain sharply by a mud-clast-rich, darker, argillaceous layer, and then capped by a thin-bedded traction-structured sandstone and a structureless mudstone – these strata are discussed next.

4.3 LINKED DEBRITE AND COGENETIC DEBRITE-TURBIDITE BEDS

In the distal fringe of several small (5 – 25 km radius) Late Jurassic deep-water fans (i.e., Miller-Kingfisher and Magnus-Penguin fans) in the northern North Sea, Haughton et al. (2003) described sandstone beds overlain sharply by clast-rich argillaceous sandstone with no intervening mudstone. Based on this relationship, Haughton et al. proposed that these strata were deposited from cogenetic sand-rich and mud-rich sediment gravity flows, specifically a sand-rich turbidite overlain by a mud-rich debrite. The term ‘linked debrite’ was introduced for the upper argillaceous interval to highlight its genetic relationship with the underlying clean sandstone, and therefore differentiate it from standalone debrites. More specifically, these strata were reported to be a few cm to > 1.5 m thick and consist of a sharp-based, structureless, graded or ungraded, dewatered, clean (i.e., less muddy) lower part overlain directly by an ungraded argillaceous part comprising abundant mud clasts, fragments of exotic lithologies and a heterogenous mud matrix made up of sandy patches containing sand grains that often were coarser than those in the basal sand-rich part (e.g., Fig. 4.3). Additionally, Haughton et al. (2003) described the interface

separating the two parts to be typically highly irregular (i.e., up to several decimeter relief) with evidence of liquefaction and upward sand injection from the lower part (Fig. 4.3). Stratigraphically upward, these two-part strata are often, but not always, overlain by thin (mm- to cm-thick), parallel- to ripple- cross-stratified sandstone and a structureless mudstone cap (e.g., Fig. 4.3C) interpreted to be deposited by the dilute, turbulent wake of the flow. Similar two-part beds, but with some differences, were later described in outcrop (e.g., Fig. 4.4) and termed 'cogenetic debrite-turbidite beds' by Talling et al. (2004) from unchannelized distal basin-plain strata of the Miocene Marnoso Arenacea Formation, Italian Appennines; the Silurian Aberystwyth Grits in western Wales; and in core from the Late Quaternary Agadir Basin, offshore north-west Africa. The distinguishing features of these beds included gradational interface (< 2 – 10 cm thick) separating the basal clean (< 10 – 15% mud) sandstone and the overlying mud-rich (> 15 – 20% mud) sandstone (e.g., Fig. 4.4); cm-scale linear corrugations along the contact between the clean and mud-rich sandstone parts (see Talling et al. 2004, fig. 4E); and absence of large mud clasts in the upper mud-rich sandstone interval (Fig. 4.4B). Subsequently, similar debrite-turbidite couplets were reported from outcrops of the channel-lobe transition zone strata in the lower Pleistocene Otadai Formation, Boso Peninsula, Japan (Ito, 2008), basin-margin strata of the Carboniferous Ross Sandstone in Ireland (Pyles and Jennette, 2009), and from mid-lobe strata in the Oligo-Miocene West Crocker Fan, NW Borneo (Jackson et al., 2009).

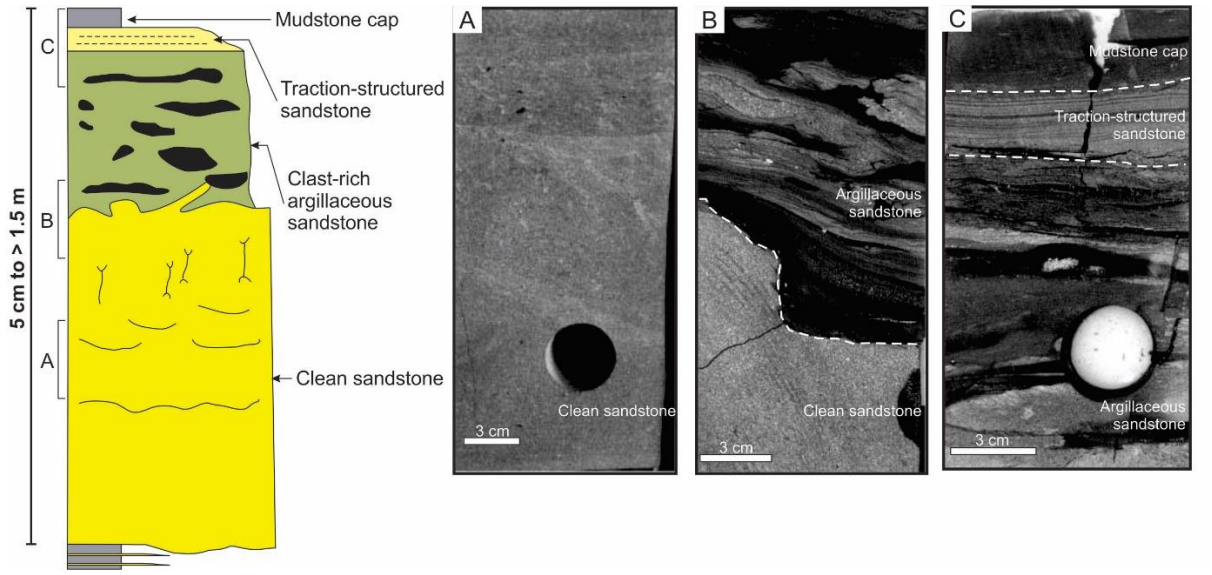

Figure 4.3: Idealized stratigraphic log of a co-genetic debrite-turbidite bed from (Late Jurassic) deep-water fans in the northern North Sea (modified after Haughton et al., 2003). A) Core photograph of basal clean sandstone (Haughton et al., 2003, fig. 5A). B) Core photograph of irregular contact separating basal clean sandstone and overlying argillaceous sandstone (Haughton et al. fig. 5D). C) Core photograph of clast-rich argillaceous sandstone overlain by planar-laminated sandstone capped by structureless mudstone (Haughton et al., fig. 7A).

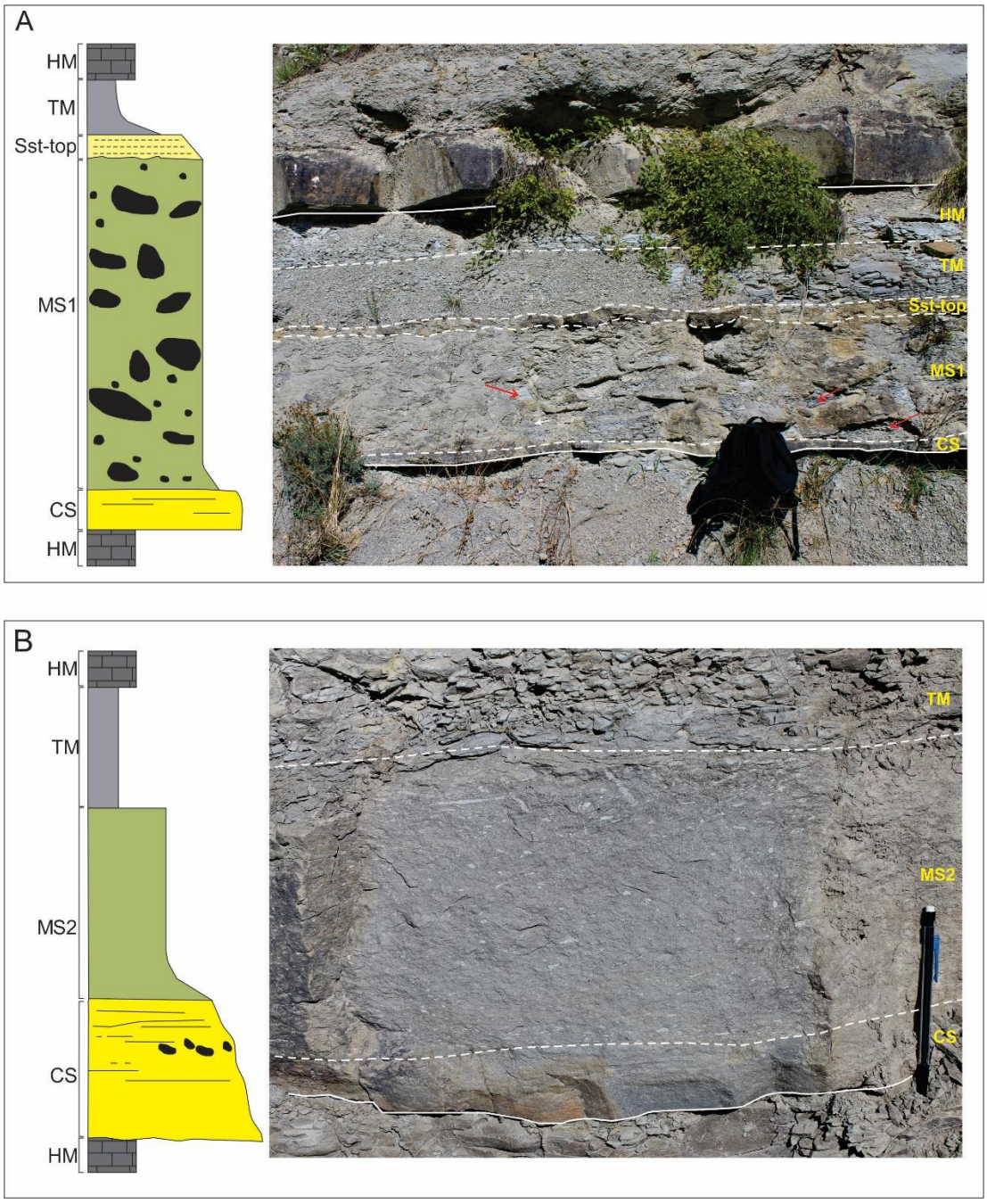

Figure 4.4: A, B) Stratigraphic logs (left) (modified after Talling et al. 2004) and outcrop photos (right) of cogenetic debrite-turbidite beds (Miocene) Marnoso Arenacea Formation, Italy consisting of basal clean sandstone (CS) overlain abruptly by A) clast-rich muddy sandstone (MS1), or B) clast-poor muddy sandstone (MS2). Note the sharp and planar contact separating the clean sandstone and the overlying muddy sandstone, which then is overlain by a traction-structured sandstone (Sst-top) capped by a turbiditic mudstone (TM) in Part A, or overlain directly by TM in Part B. HM = Hemipelagic mudstone. Red arrows point to mud clasts. Scales are: knapsack (50 cm long) and pencil (14 cm long).

In all these studies, a consistent facies trend from proximal clean sandstone to a cogenetic debrite-turbidite bed was noted in both downstream and crossflow directions. However, the horizontal scale of the trend was quite variable, ranging from a few kilometers (e.g., Haughton et al. 2003), to few tens of kilometers (e.g., Talling et al., 2004; Amy and Talling, 2006), to hundreds of kilometers (e.g., Talling et al., 2004, 2007) (Fig. 4.5). Nonetheless, in all cases, the cogenetic debrite-turbidite-bed part of the facies transect showed a proximal to distal thinning of the basal clean sandstone and a concomitant thickening of the upper mud-rich sandstone (Fig. 4.5). Additionally, Talling et al. (2004) and Amy and Talling (2006) showed that mud clasts present in the upper mud-rich sandstone interval of the cogenetic debrite-turbidite beds systematically decreased in size and abundance downflow until none remained (Fig. 4.5B).

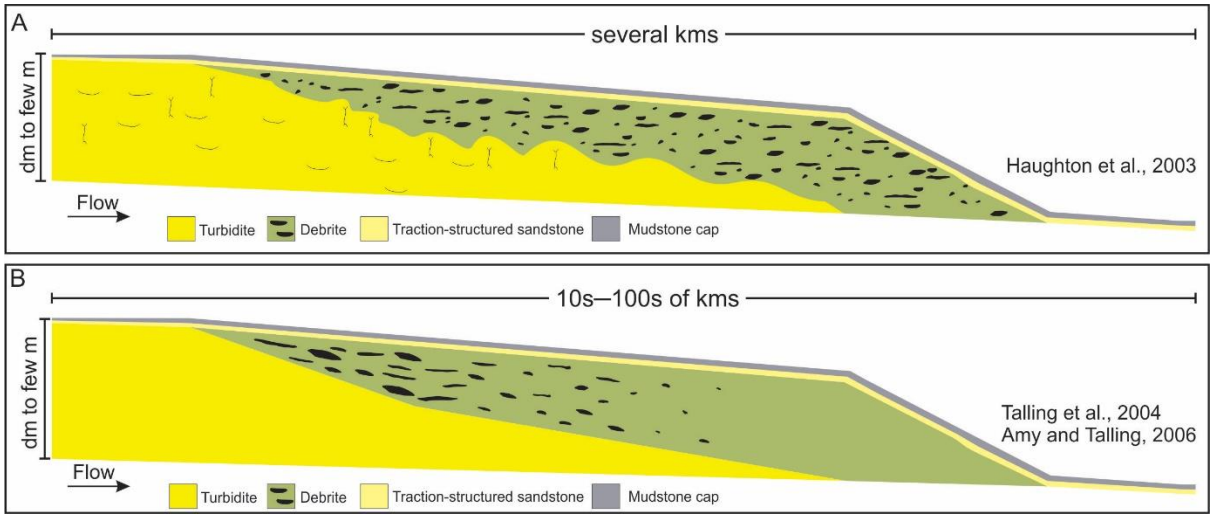

Figure 4.5: Inferred downflow facies transition from clean sandstone to co-genetic debrite-turbidite measured over A) several kms (e.g., Haughton et al., 2003) to B) several tens to hundreds of kms (e.g., Talling et al., 2004). Note the proximal to distal thinning and pinch-out of the basal clean sandstone (turbidite) but thickening and then thinning to a pinch-out of the upper argillaceous sandstone (debrite). In part (A) the basal clean sandstone contains abundant dewatering structures and the interface separating the lower sand-rich and upper mud-rich parts is irregular (Haughton et al., 2003). B) The basal clean sandstone lacks dewatering structures and the contact separating the lower sand-rich and upper mud-rich parts is sharp and planar. Additionally, in the upper mud-rich part mud clast size and concentration decreases downflow until none remains (Talling et al., 2004; Amy and Talling, 2006).

Furthermore, in some of the outcrop studies (e.g., Amy and Talling, 2006; Jackson et al., 2009), the cogenetic debrite-turbidite bed portion was observed to terminate with abrupt thinning and pinch-out of both the lower sand-rich and upper mud-rich parts at about the same along-flow position. Beyond the pinch-out, the remainder of the facies transect consisted of a thin bed of mud-poor, traction-structured sandstone and mudstone cap that extended for tens to hundreds of kilometers (Fig. 4.5B). Based on this spatial relationship, several depositional models were proposed to explain the origin of these debrite-turbidite couplets, and are briefly outlined next.

To explain these observations, both Haughton et al. (2003) and Talling et al. (2004) proposed two rather similar physical models. In the first, a debris flow was initially generated from a slope failure and with downslope movement, mixed with the surrounding ambient fluid causing part of it to dilute and transform into a cogenetic turbidity current. The turbidity current then outran the slower moving debris flow and deposited the basal clean sandstone interval (Fig. 4.6A). Later, the trailing debris flow caught up and deposited the overlying debrite. A similar depositional origin was also suggested for cogenetic debrite-turbidite beds in the West Crocker Formation, NW Borneo by Jackson et al. (2009). In the second model, a turbidity current initiated at the shelf-break accelerated as it moved downslope. As this energetic flow passed over the basin plain it eroded the mud-rich substrate and enriched the lower and lateral parts of the flow with mud clasts and fine-grained sediment. Increased sediment concentration, especially in the mud fraction, suppressed turbulence and transformed those parts of the flow into a laminar debris flow (Fig. 4.6B). The debris flow then trailed behind the remainder of the turbulent flow, which farther downflow deposited a tapering sand-rich layer. Eventually, the slower-moving debris flow arrived and deposited a debrite over the clean sandstone. A similar mechanism was invoked for the deposition of cogenetic debrite-turbidite beds in the lower Pleistocene Otadai Formation,

Japan (Ito, 2008). Although mechanistically similar, the Haughton et al. (2003) and Talling et al. (2004) models differ in regards to the mechanism that permitted long-distance (>> tens km) travel of the debris flow. Based on the presence of pervasive dewatering structures in the basal clean sandstone, including upward injection of the basal sand into the overlying debrite, and a highly irregular interface separating the turbidite and debrite intervals (Fig. 4.5A), Haughton et al. (2003) interpreted the mobility of the linked debris flow to be related to a low-friction, overpressured horizon at the top of the previously deposited sand layer due to dewatering of the sand as the debris flow passed over top. Talling et al. (2004), on the other hand, reported no evidence of extensive dewatering, and the contact between the turbidite and debrite intervals was flat and gradational (Fig. 4.5B). Here, the long runout distance of the linked debris flow was attributed to its low yield strength, specifically, << ~ 50 Pa.

Additionally, Talling et al. (2004) proposed several other models to explain the origin of co-genetic debrite turbidite beds. In their third model, an initially fully turbulent mixed sand-mud suspension enters the basin plain and begins to decelerate. As flow speed declines and turbulence intensity decreases, larger sand grains settle and deposit a normally to coarse-tail graded sand-rich turbidite. With time, a critical sediment grain size is reached that can be maintained in suspension by the yield strength of the now more mud-rich residual flow. This flow then deposits *en masse* forming the ungraded mud-rich sandstone interval (Fig. 4.6C). Alternatively, the fourth model begins with a relatively low viscosity, low yield strength debris flow, which upon deceleration, causes coarser grains that were initially suspended to settle and deposit a layer of normally to coarse-tail graded sand. The residual debris flow, which is now muddier and finer grained, then continues to move downslope until it deposits by *en masse* freezing (Fig. 4.6D). Although both models may ultimately form cogenetic debrite-turbidite beds, Talling et al. (2004)

point out that the third model only forms clast-less cogenetic debrite-turbidite beds, whereas both clast-less and clast-rich cogenetic debrite-turbidite beds can be explained by the fourth model.

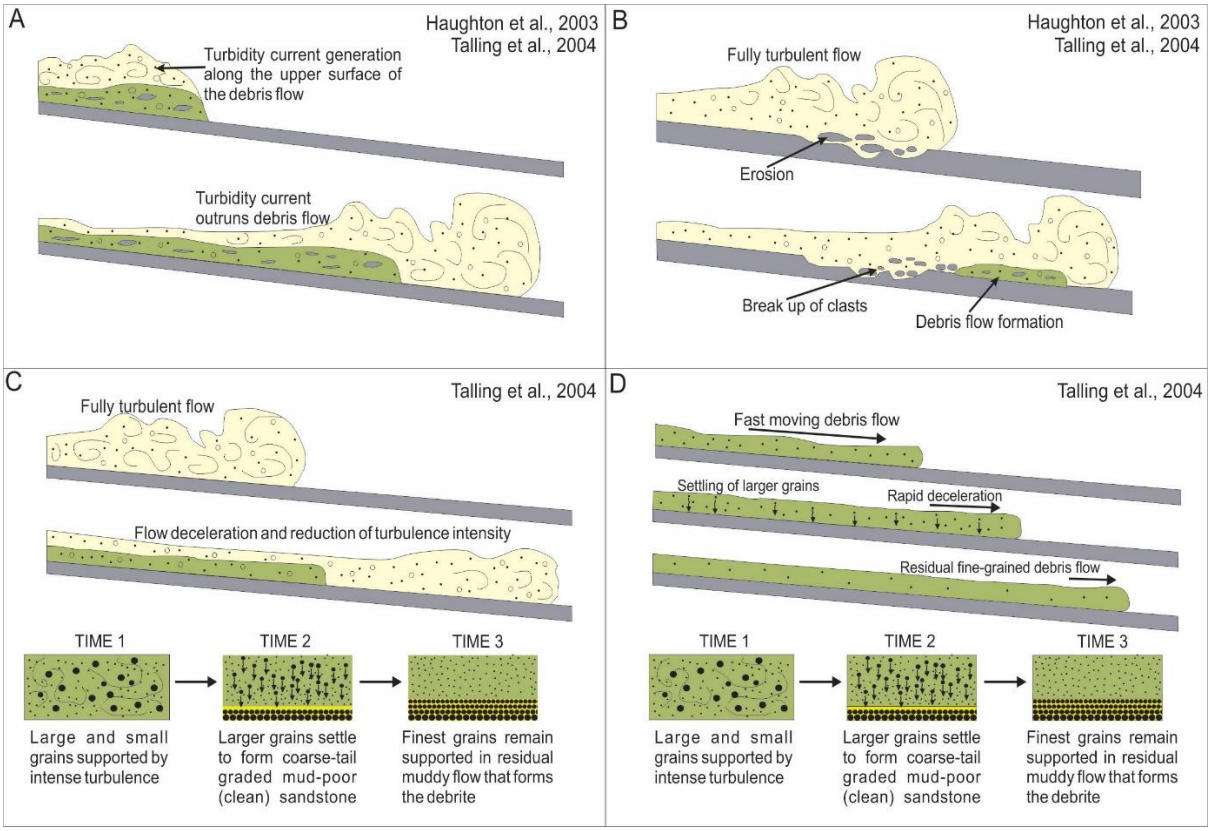

Figure 4.6: Schematic models showing the origin of co-genetic debrite–turbidite beds (modified after Talling et al., 2004, fig. 14). Note that all flows are from left to right. A) Mixing along the upper surface of a debris flow generates a turbidity current that outruns the debris flow and deposits the basal clean sandstone; the trailing debris flow arrives later and emplaces the overlying debrite. B) Turbidity current erodes the mud-rich seafloor and locally charges the flow with mud clasts and fine-grained sediment. Turbulence is suppressed in the mud-enriched lower part that transforms locally into a debris flow that then trails the turbulent flow, and deposit, respectively, the debrite and turbidite parts of the bed. C) Deceleration and reduced turbulence intensity of a fully turbulent mixed sand-mud suspension causes sand grains to settle and deposit a mud-poor sandstone. The increasingly mud-rich residual flow eventually develops sufficient yield strength to support smaller sand grains in suspension but then freeze *en masse* forming the upper mud-rich sandstone. D) Deceleration of a low yield strength, low viscosity debris flow causes sand grains to initially settle and deposit a clean sandstone. Later, the now more mud-rich residual debris flow freezes and deposits the overlying debrite.

Talling et al. (2004) also proposed a model that predicts the possible association of linked debrites with basin margin and levee crest settings. In this model, Talling et al. suggest that loading of an unstable substrate, such as along a basin margin or levee crest by an overriding

turbidity current, can trigger slope failure and an associated local debris flow. This debris flow then overruns the deposited turbidite of the forerunner turbidity current and forms the linked debrite of the cogenetic debrite-turbidite bed. Alternatively, Pyles and Jennette (2009) explain abundant cogenetic debrite-turbidite beds in basin-margin strata of the Carboniferous Ross Sandstone, Ireland to be result of an initially turbulent flow that erodes the muddy substrate in the axial region of the basin floor, and now mud-enriched, expands outward and evolves into a flow with mixed turbulent and laminar characteristics. In the center of the basin, the flow remains in a state of bypass, whereas the adverse gradient along the basin margin forces the expanding flow into deposition. Here, Pyles and Jennette (2009) postulate that "suspension and tractive deposition from turbulent flow and *en masse* deposition from laminar debris flow were operating simultaneously or at least alternating from one to the other," resulting in the emplacement of a co-genetic debrite–turbidite bed.

Next, building on a critical observation made by Barker et al. (2008) that slurry beds in the Britannia Field typically transition vertically from sand-rich to banded to clay-rich facies, Haughton et al. (2009) analyzed vertical facies transitions in co-genetic debrite-turbidite beds and slurry beds using a comprehensive dataset consisting of subsurface cores from Jurassic, Cretaceous and Cenozoic deep-water strata of the North Sea, Cenozoic deep-marine deposits of the UK Atlantic margin, and Cretaceous deep-marine strata of offshore Norway. Additionally, outcrop data from the Carboniferous Ross Sandstone Formation, Ireland, and Macingo Formation and Cilento flysch of the Italian Apennines were included in the analysis. The outcome of this study, in combination with the earlier concepts of linked debrites (Haughton et al. 2003) and slurry beds (Lowe and Guy, 2000), led to the introduction of the term "hybrid event bed" (see next).

4.4 HYBRID EVENT BEDS

Haughton et al. (2009) introduced the term hybrid event bed (HEB) to describe a common bed motif observed in deep-water deposits that was unlike classical turbidites or debrites, but more similar to co-genetic debrite-turbidite beds. A complete HEB comprises five divisions that from bottom to top are graded or ungraded sandstone (H1), banded sandstone with alternating bands of paler, cleaner sand and darker, muddier sand (H2), argillaceous sandstone with clasts of various sizes and lithologies (H3), well-sorted, fine to very fine-grained, parallel- to ripple-laminated sandstone (H4), and a massive silty mudstone cap (H5) (Fig. 4.7A). The thickness of HEBs is highly variable and ranges from a few centimeters to several meters. Moreover, not all divisions are present in every event-bed, H2, followed by H4, commonly being absent, but the ordering of the various divisions (e.g., H1 overlain by H3) is always maintained (see Haughton et al., 2009; Talling, 2013) (Fig. 4.7A). The greatest variability in textural make up was noted in the H1 and H3 divisions, and also the nature of the contact between the basal clean sandstone (H1) and typically overlying argillaceous sandstone (H3). The basal H1 division contains ≤ 25% mud matrix and is usually structureless, although local dewatering structures, like dish structures and vertical pipes, are observed (e.g., Davies et al. 2009; Haughton et al., 2009; Hodgson, 2009). Less commonly, traction structures including parallel lamination, ripple and dune cross-stratification have been reported in the upper part of the H1 division (see Talling, 2013, fig. 1). Also, Fonnesu et al. (2015) recognized a mud-clast-rich zone termed H1b in the upper part of the otherwise clast-poor H1 in rocks from the Miocene San Mauro Formation and Cretaceous-Paleocene Gottero Sandstone (Italy), Carboniferous Mam Tor Sandstone (northern England), and Carboniferous Ross Sandstone Formation (western Ireland) (e.g., Fig. 4.7B).

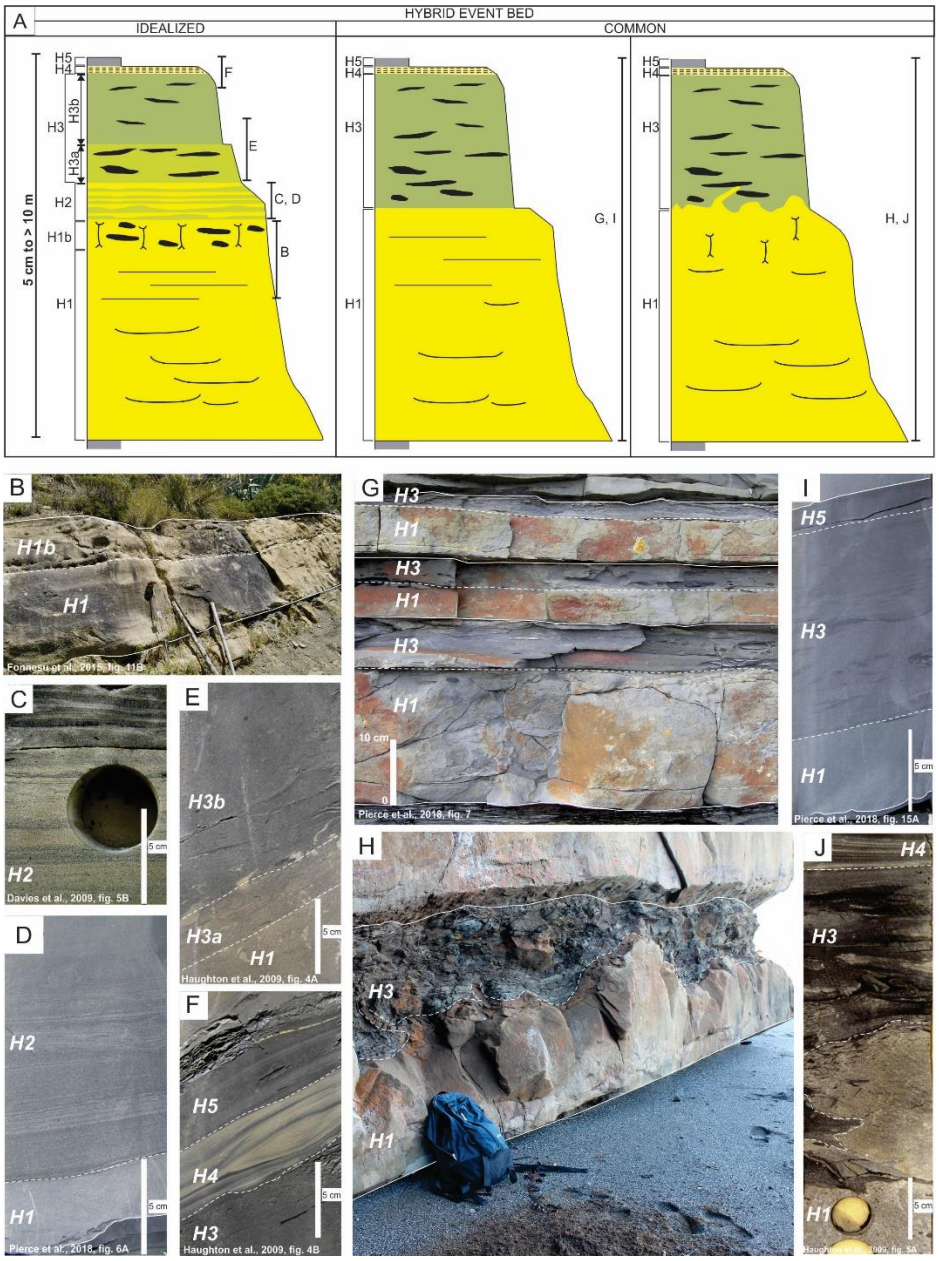

Figure 4.7: A) Idealized stratigraphic log (left) of a hybrid event bed (HEB) comprising, from bottom to top—graded or ungraded sandstone (H1), mud-clast-rich clean sandstone (H1b), banded sandstone with alternating bands of lighter, cleaner sand and darker, muddier sand (H2), clast-rich muddy sandstone (H3a), clast-rich sandy mudstone (H3b), parallel- to ripple-laminated sandstone (H4), and massive silty mudstone cap (H5). Note that not all divisions are present in every hybrid event bed— typically H1 is overlain directly by a planar- (center) or irregular-based (right) H3 division. B) Outcrop photograph of H1 and H1b divisions. Jacob staff (1.5 m long) for scale. C) Core photograph of H2 division. D) Core photograph showing sharp and planar transition from H1 to H2 division. E) Core photograph of the transition from H1 to H3a and then to the darker, more mud-rich H3b. F) Core photograph of sandy mudstone (H3) overlain by clean, well-sorted, ripple cross-stratified sandstone (H4) and mudstone cap (H5). G) Outcrop photograph showing a stack of three HEBs, each consisting of H1 overlain abruptly by a planar-based, darker, more mud-rich H3. H) Outcrop photograph showing the highly irregular contact separating the H1 and H3 divisions. Knapsack (50 cm long) for scale. I) Core photograph of a HEB composed of H1, H3, and H5 divisions. Note the planar H1–H3 contact. J) Core photograph of a HEB consisting of H1, H3, and

H4 divisions. Note the irregular H1–H3 contact but planar H3–H4 contact. Citations for parts B–G and I–J are shown in the lower left corner of each photograph.

The upper argillaceous H3 division is poorly sorted, contains ~ 10 – 70% mud matrix, and typically consists of sand grains that are finer than in the underlying H1 division, but note that coarser sand grains have also been reported in several studies (e.g., Haughton et al., 2009; Davies et al., 2009; Hussain et al., 2020). Distinctively, clasts of mud, and less commonly other lithologies, are dispersed randomly throughout the H3 division (e.g., Hodgson, 2009; Talling et al., 2012a, 2012b; Fonnesu et al., 2018; Hussain et al., 2021; Jin et al., 2021), although some studies have reported a local weakly developed upward decrease in clast size (e.g., D2 facies in Hodgson, 2009; A1 facies in Davies et al., 2009; HEB-3 and HEB-4 in Fonnesu et al., 2018). Furthermore, within the H3 division, Hussain et al. (2020) report a sharp upward increase in K_2O wt.%, reflecting an abrupt increase in the clay content from a lower muddy sandstone (H3a) overlain by a sandy mudstone (H3b) (e.g., Fig. 4.7E).

In most HEBs the basal sand-rich H1 division is overlain sharply by the mud-rich H3 division (see Talling, 2013). However, rarely the two are separated by a banded H2 division (e.g., Fig. 4.7C, D) that ranges from a few cm- (e.g., Davies et al., 2009; Hodgson, 2009) to few tens of cm- (e.g., Southern et al., 2017; Pierce et al., 2018) to few m-thick (e.g., Lowe and Guy, 2000; Barker et al., 2008). Where the H3 division immediately overlies the H1 division the contact is planar (e.g., Haughton et al., 2009; Talling et al., 2012a; Talling, 2013; Pierce et al., 2018) (e.g., Fig. 4.7G, I), or irregular with cm- to m-scale relief and evidence of injection of sand from the H1 part into the upper muddy H3 part (e.g., Haughton et al., 2009; Fonnesu et al., 2015, 2016, 2018; Southern et al., 2015) (e.g., Fig. 4.7H, J). Additionally, the contact has also been reported to be undulatory where it drapes regularly-spaced dune formsets developed along the top of the

underlying H1 division (Talling, 2013, fig. 5A), gradational and marked by an upward increase in mud content (e.g., Davies et al., 2009; Hodgson, 2009; Mueller et al., 2017), or stepped with mud content intermediate between the basal clean sandstone and the overlying argillaceous interval (e.g., Haughton et al., 2009; Kane et al., 2017; Pierce et al., 2018; Hussain et al., 2020).

In addition to documenting the internal bed characteristics of hybrid event beds, the longitudinal and lateral lithofacies trends of HEB and associated strata have been investigated by several authors through correlation of individual beds or bed packages between subsurface wells (e.g., Davies et al., 2009; Southern et al., 2017), isolated outcrops (e.g., Talling et al., 2012a, 2012b, 2013; Southern et al., 2015; Kane et al., 2017; Spychala et al., 2017a; Pierce et al., 2018), modern seabed cores (Talling et al., 2012b), and by continuously tracing individual beds in outcrop (e.g., Hodgson, 2009; Patacci et al., 2014; Fonnesu et al., 2015, 2018; Spychala et al., 2017a). Collectively, these studies show a consistent along-flow proximal to distal progression of lithofacies beginning with a clean sandstone transitioning to a HEB with the development of a mud-rich (H3) layer overlying a clean basal sandstone (H1). Further along the transport path H1 thins to a pinch-out whereas H3 initially thickens but then it too thins to a pinch-out. The full facies transect is then sharply overlain by a well-sorted, traction-structured sandstone (H4) capped by a silty mudstone (H5) that extends beyond the pinch-out of the transect (Fig. 4.8). Although the progression of lithofacies is consistent between studies, the length over which the changes take place is highly variable, and ranges from less than 2 kilometers (e.g., Hodgson, 2009; Patacci et al., 2014; Fonnesu et al., 2015; Spychala et al., 2017a), to a few kilometers (Spychala et al., 2017a; Fonnesu et al., 2018; Pierce et al., 2018) (Fig. 4.8A), to tens of kilometers (e.g., Davies et al., 2009; Talling et al., 2012a, 2012b, 2013, Kane et al., 2017; Pierce et al., 2018) (Fig. 4.8B).

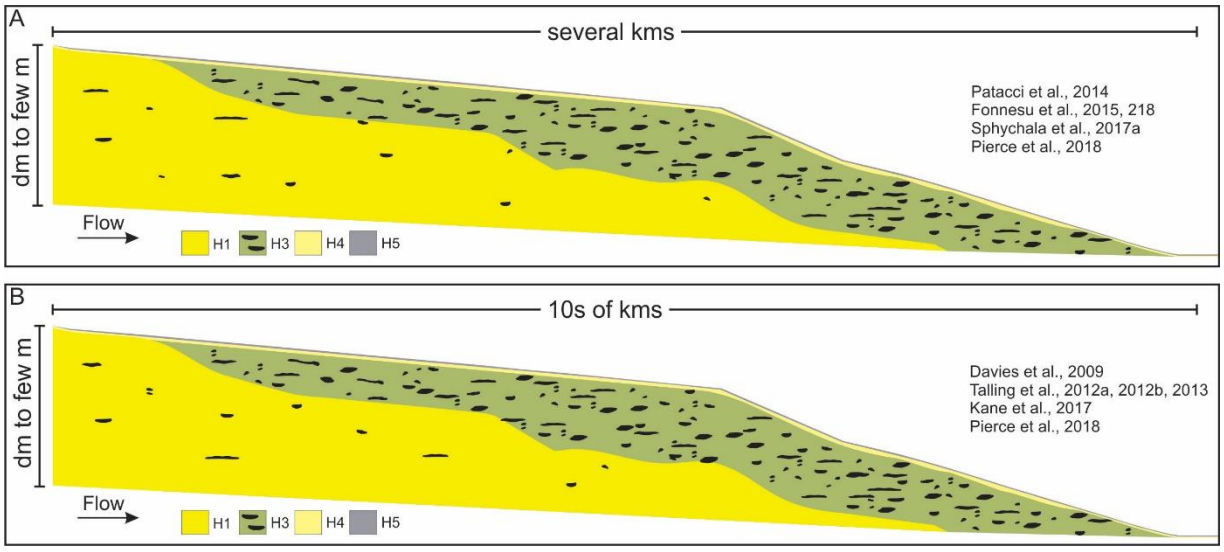

Figure 4.8: Inferred downflow facies transition from clean sandstone to hybrid event bed measured over A) several kms (Patacci et al. 2014; Fonnesu et al. 2015, 2018; Spychala et al. 2017a; Pierce et al. 2018) to B) several tens of kms (Davies et al. 2009; Talling et al. 2012a, 2012b, 2013; Kane et al. 2017; Pierce et al. 2018). Note the proximal to distal thinning of H1 but thickening and then thinning to a pinch-out of H3.

In addition to consistent along-flow changes in lithofacies, across-flow changes have been documented in a small number of studies. In the proximal part of the facies transect, Patacci et al. (2014) and Fonnesu et al. (2015) show discrete areas (tens of m wide) with abundant mud clasts (H1b) interspersed within the generally more clast-poor sandstone (H1) (Fig. 4.9A). Further along the transport path, Fonnesu et al. (2015) and Southern et al. (2015) report the local development of tens of m wide two-part HEB comprising a basal H1 layer overlain by a mud-clast-rich H3 layer within clean sandstone with dispersed mud clasts (H1b) (Fig. 4.9B). Even further downflow, the H1 and H3 layers extend continuously across-flow, with the surface separating them being planar (e.g., Talling et al., 2012a, 2012b, 2013), or irregular with cm- to m-scale relief and evidence of upward injection of sand from the lower sandy part into the upper muddy part (e.g., Patacci et al., 2014; Fonnesu et al., 2015, 2016, 2018; Southern et al., 2015) (Fig. 4.9C). Interestingly, despite the irregularity of the interface and local differences in the thickness of the H1 and H3 divisions, the overall bed thickness varies little as thickness changes

in one layer is compensated by thickening or thinning in the other (see Southern et al., 2015; Fonnesu et al., 2015). Finally, in the distal part of the depositional transect H1 and then the H3 divisions progressively thin and then pinch-out (Fonnesu et al., 2015) (Fig. 4.9D, E).

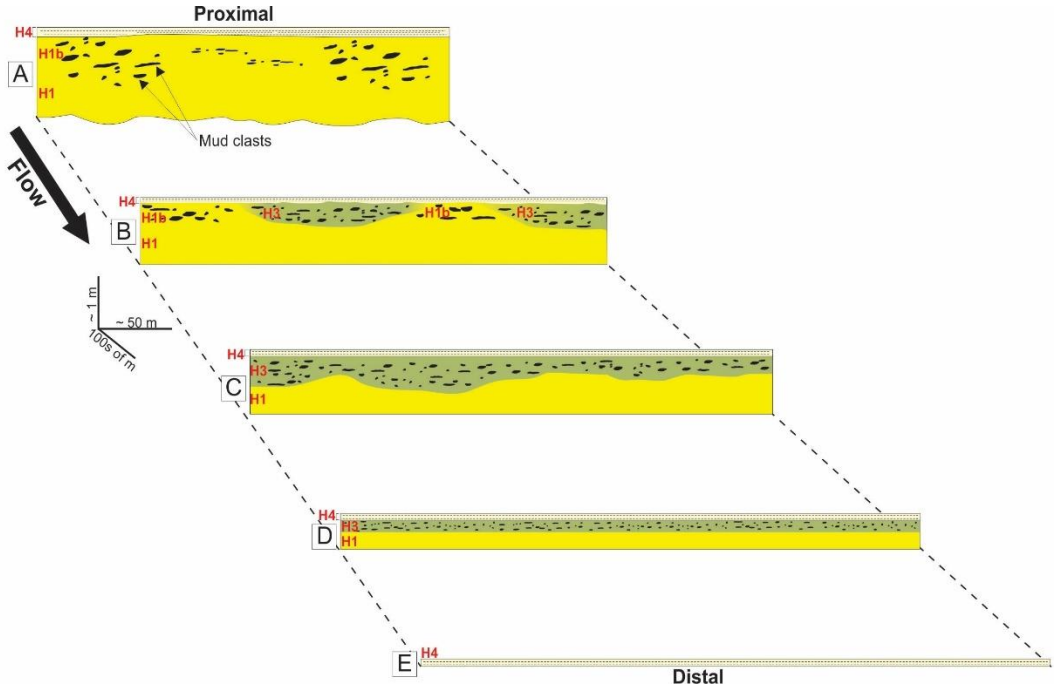

Figure 4.9: A–E) Schematic showing across-flow changes in lithofacies along a downflow (proximal to distal) transect (modified after Fonnesu et al. 2015). Where preserved a well-sorted H4 layer is observed everywhere. A) Clean, clast-poor sandstone (H1) overlain locally by discrete regions (tens of m wide) of clean, mud-clast-rich sandstone (H1b). B) Development of tens of m-wide, mud-clast-rich H3 overlying H1interspersed between regions of H1b overlying H1. C) Continuous development of H3 above H1 – contact between the two layers is irregular with cm- to m-scale relief. D) Continuous lateral development of H1 overlain sharply by a planar-based, mud-clast-rich H3. E) Following the downflow pinch-out of H3 all that remains is H4.

HEBs and their associated strata are most commonly reported from the distal parts of unconfined deep-marine depositional systems, and more specifically basin-floor sheet systems (e.g., Haughton et al., 2009; Talling et al., 2012a, 2012b, 2013; Fonnesu et al., 2015, 2016, 2018; Pierce et al., 2018; Hussain et al., 2020, 2021), and along the fringes of mid- to outer-submarine fan lobes (e.g., Haughton et al., 2009; Davies et al., 2009; Hodgson, 2009; Talling et al., 2010; Fonnesu et al., 2015, 2018; Kane et al., 2017; Mueller et al., 2017; Spychala et al., 2017a, 2017b;

Southern et al., 2017; Fildani et al., 2018; Pierce et al., 2018; Hussain et al., 2020, 2021). Less commonly, HEBs have been recognized in more proximal locations including the fringes of proximal fan lobes (Mueller et al., 2017; Brooks et al., 2018), and in the channel-lobe transition zone (CLTZ) (e.g., Brooks et al., 2018; Baas et al., 2021). Although much less commonly, HEBs have also been reported from some confined deep-marine settings, either as localized deposits along the margins of the basin (e.g., Barker et al., 2008; Patacci et al., 2014), or as extensive sheet-like deposits across the basin (see Southern et al., 2015), in addition to marginal-marine delta front environments, like Upper Ordovician proglacial deposits in the Murzuq Basin, Libya (Girard et al., 2012), and modern (Holocene) deposits of the Choshui River, Taiwan Strait (Jin et al., 2021).

Although several mechanisms have been proposed to explain the origin of HEBs, one common element is the presence of mud and its influence on flow behaviour. Suggested first by Haughton et al. (2009), two part HEBs were the result of a longitudinal and lateral transformation of an originally fully turbulent non-cohesive flow, which because of the incorporation of muddy sediment from erosion of the seafloor up-flow (e.g., Haughton et al. 2009; Davies et al. 2009; Fonnesu et al. 2015) or locally (e.g., Hodgson, 2009; Mueller et al., 2017; Fonnesu et al., 2016, 2018), fluid turbulence was damped and the flow was transformed into a cohesive debris flow. Entrained mud particles and small mud clasts were interpreted to be preferentially displaced in suspension toward the rear of the flow, whereas larger mud clasts that moved as bedload, disintegrated and added mud chips and mud particles to the rear of the flow (Fig. 4.10A). Eventually the abundance of cohesive sediment in the rear of the flow came to suppress near-bed turbulence and transformed it into a slower moving plug flow with mechanical strength (Fig. 4.10A). Accordingly, the flow now consisted of a forerunning turbulent suspension that deposited

the clean basal sandstone (H1), followed by a transitional zone with alternating laminar and turbulent flow conditions (*sensu* Lowe and Guy, 2000) that emplaced the banded division (H2), and then a cohesive rear that deposited the upper argillaceous sandstone division (H3). Finally, the well-sorted, traction-structured sandstone (H4) and the cap of silty mudstone (H5) that overlie H3 were attributed to a generally accepted process of deposition by a trailing dilute, low-energy turbulent suspension.

As mentioned above, the H2 division is rarely observed, and more typically the H3 division directly overlies the H1. Haughton et al. (2009) attributed the rarity of the H2 division to insufficient time or space for the development of sufficient segregation and/or attrition of entrained materials in less evolved flows that longitudinally passed directly from a turbulent front to a cohesive rear without an intervening transitional flow part. Alternatively, Hussain et al. (2020) report a layer with intermediate mud content between the H1 to H3 divisions and postulate that it is the result of mixing between the trailing debris flow and the top of the previously deposited clean sand.

Further refinement to the longitudinal flow transformation model of Haughton et al. (2009) was proposed by Fonnesu et al. (2015) by integrating the commonly recognized along-flow lithofacies change of clean sandstone to HEB with various across-flow lithofacies changes. In the proximal part of the depositional transect, development of local mud-clast clusters in clean sandstone preserves the early stage of the flow transformation process in which the fully turbulent, and yet to partition flow erodes the seafloor and introduces large numbers of mud clasts into the flow (Fig. 4.9A). Many mud clasts are quickly buried by sediment settling from the rapidly collapsing sandy suspension forming the H1b division, whereas other clasts disintegrated and added fine-grained sediment to the flow (see also Patacci et al., 2014). Moreover, due to the

spatially random nature of seabed scouring, local regions of the flow become sufficiently mud enriched and form a cohesive debris flow, whereas the rest of the flow remains turbulent – a stage termed "incomplete flow transformation" by Fonnesu et al. (2015) and marked by the local across-flow development of HEB (Fig. 4.9B). Further along the transport path, the continued disintegration of mud clast adds additional mud chips and particles that are displaced to the rear of the flow. This mud enrichment then transforms the rear of the flow into a cohesive debris flow — the flow now consisting of a forerunning high-density turbidity current and a trailing debris flow (see above). Subsequent deposition from these two discrete and mechanically different parts of the flow results in the continuous across-flow emplacement of sand-rich overlain by mud-rich parts of a HEB; however, the effects of shearing and loading of the trailing debris flow on the earlier deposited sandy turbidite leads to the development of an irregular (i.e., exhibiting cm- to m-scale relief) surface between the basal clean sandstone (H1) and upper muddy debrite (H3), and also local injection of sand from H1 upward into H3 (see above). Additionally, despite the irregularity of the interface causing variations in the thickness of the H1 and H3 divisions, total bed thickness changes little (Fig. 4.9C), which is attributed to the mechanically weak nature of the trailing debris flow that deposits a self-levelling debrite over the clean basal sand. Finally, as shear at the base of the overriding debris flow weakens downflow, the rugosity of the H1-H3 interface decreases and becomes planar (Fig. 4.9D).

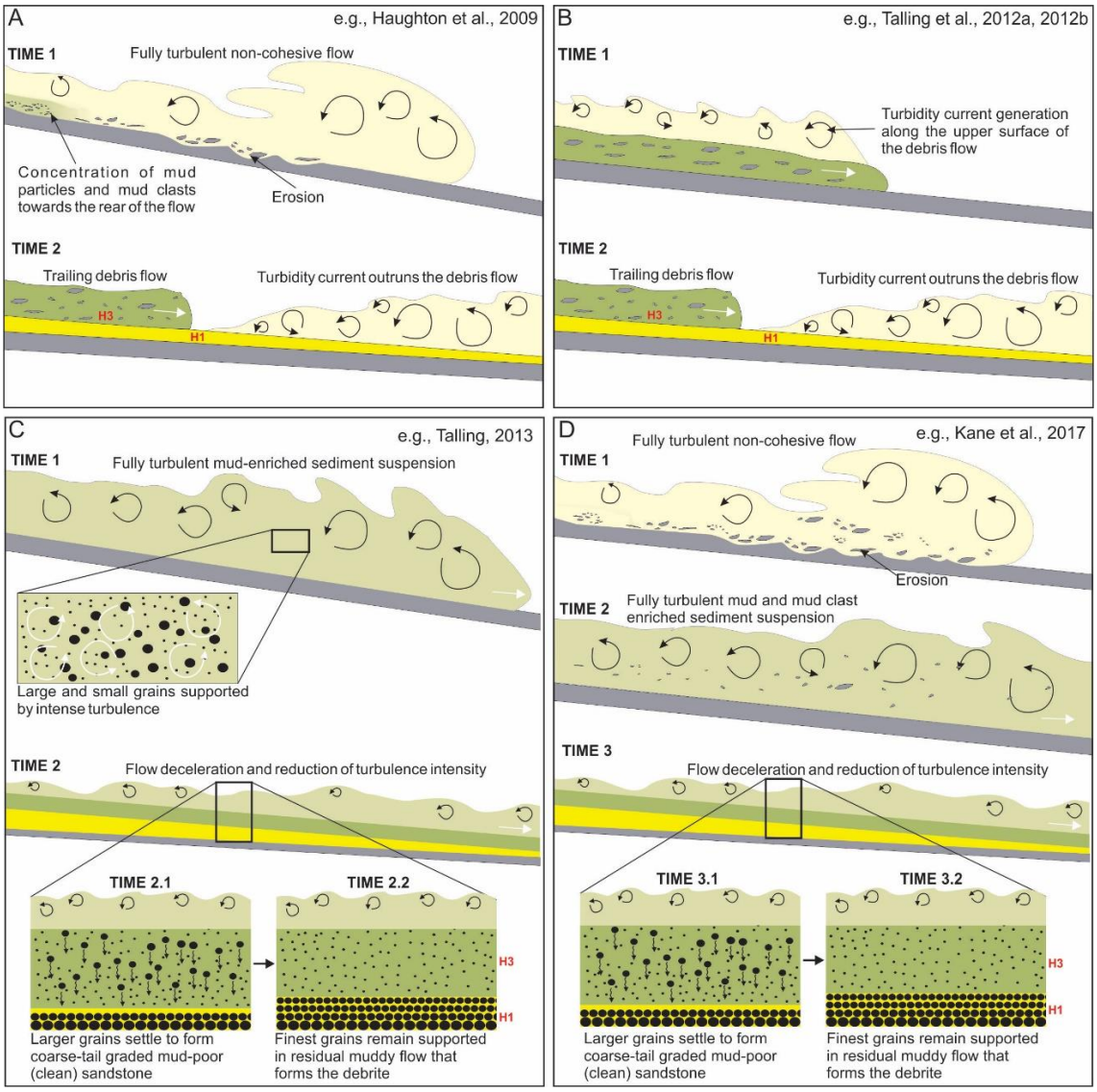

Figure 4.10: Schematic models for hybrid event bed development. Flows are all from left to right. A) Turbidity current erodes the mud-rich seafloor and transfers mud clasts and fine-grained sediment to the rear of the flow. The now partitioned flow consists of a forerunning turbidity current that deposits the clean basal sandstone (H1) followed by a trailing debris flow that deposits the mud-rich H3. B) Mixing along the upper surface of a debris flow spawns a turbidity current that runs ahead and deposits a basal clean sandstone layer (H1) followed by the more slowly moving debris flow and deposition of the overlying H3. C) Deceleration of a fully turbulent mud-enriched sediment suspension results in preferential settling of larger particles that build up a clean basal sandstone layer (H1). Depleted of larger particles the more mud-rich residual flow develops sufficient strength to transform into a debris flow that deposits the overlying H3. D) Fully turbulent, non-cohesive suspension erodes mud-rich seafloor and charges the flow with mud clasts and fine-grained sediment. Farther downflow, deceleration causes sand to settle and deposit a basal sandy layer (H1). High near-bed sediment concentration inhibits the upward transfer of bed-generated turbulence allowing the mud particles to flocculate and form a high-strength plug that ultimately deposits a H3 layer by *en masse* freezing.

An alternative model to explain the origin of HEBs attributes mixing of ambient fluid along the upper surface of a debris flow and the generation of an overriding turbulent suspension that then outruns the debris flow and deposits the basal clean sandstone interval (H1), followed by the arrival of the debris flow and emplacement of the overlying debrite (H3) (Hodgson, 2009; Talling et al., 2012a, 2012b; Talling, 2013) (Fig. 4.10B). Talling et al. (2012a, 2012b) and Talling (2013) also point out that the initial debris flow requires low to intermediate yield strength (0.1 – 100 Pa), as very strong debris flows (> 100 Pa) mix negligibly with the ambient fluid thereby prohibiting the development of the associated high-density turbidity current (see also Hampton 1975), and very low yield strength debris flows (< 0.1 Pa) transition to fluid mud incapable of supporting sand grains. Typically, the H1-H3 contact is reported to be sharp and planar (see Talling et al., 2012a, 2012b, 2013; Talling, 2013). However, in the Permian Skoorsteenberg Formation, Karoo Basin, South Africa, Hodgson (2009) described a few-cm-thick H2 division, which like Haughton et al. (2009) (see above), was interpreted to record the development of transitional flow conditions (*sensu* Lowe and Guy, 2000) between the forerunning (turbulent) turbidity current and trailing cohesive debris flow**.**

In addition to the debris-flow-initiated model, Talling (2013) proposed an alternative explanation for HEBs with a clast-poor H3 division (their model 3). In this case an initially fully turbulent mixed sand-mud suspension decelerates as it expands across the basin floor, resulting in reduced turbulence intensity and the preferential settling of larger particles forming a normally graded basal clean sand layer (H1). With time, the increasingly more mud-rich residual suspension builds cohesive strength and eventually transforms into a debris flow that deposits *en masse* the ungraded muddy sandstone layer (H3) (see also Talling et al., 2004) (Fig. 4.10C). Similarly, Kane et al. (2017) and Spychala et al. (2017a) propose a streamwise flow

transformation for HEBs in the frontal submarine lobe fringes of the Permian Skoorsteenberg Formation, Karoo Basin. However here, unlike model 3 of Talling (2013) where the initial sediment suspension is already mud-enriched, mud and mud clasts are newly introduced into the flow by local seafloor erosion in the channel-lobe transition zone due to the loss of flow confinement (Fig. 4.10D). As the now mud-enriched sediment suspension spreads and decelerates over the basin floor, sand and coarser grains settle and form a dense (i.e. high concentration) basal layer (H1 division) that stably stratifies the flow and inhibits the upward transfer of bed-generated turbulence. Reduced turbulence in the upper part of the flow then allows mud particles to flocculate and form a high-strength plug that ultimately freezes and emplaces *en masse* the H3 division (Fig. 4.10D). Furthermore, the settling of sand particles in the plug during transport results in a more sand-rich region (H3a) beneath a more muddy region (H3b) (see Hussain et al., 2020).

The foregoing models are based principally on interpretations of strata in the sedimentary record. Experimental investigations of mixed sand-mud open channel flows by Baas et al. (2011) and Sumner et al. (2009) also report two-part deposits consisting of a sand-rich basal layer overlain sharply by a mud-rich layer capped by a fine-grained drape (see deposit type III in Sumner et al., 2009, and LTPF-UTPF deposits in Baas et al., 2011) that closely resembled HEBs. These deposits are interpreted to develop under 'transitional plug flow' conditions (*sensu* Baas et al., 2009), consisting of a basal turbulent region and an upper laminar plug where turbulence is absent. Settling of sand grains in the basal region then forms the normally graded clean sand layer (equivalent to H1) and *en masse* freezing of the upper plug region results in the emplacement of ungraded muddy sand (equivalent to H3).

The most recent model for the origin of HEBs was proposed by Baas et al. (2021) with

particular emphasis given to groove marks on the base of the H1 division in channel-lobe transition-zone deposits of the Silurian Aberystwyth Grits Group, west Wales, United Kingdom. In this model, a turbidity current traversing a submarine slope channel erodes the channel floor and introduces unconsolidated mud and mud clasts into the flow. Erosion is inferred to occur mostly beneath the energetic head of the turbidity current and leads to increased flow density, but fluid turbulence exceeds cohesive forces and prevents the transformation to a debris flow. However, as the flow expands and decelerates over the channel-lobe transition zone, turbulence intensity decreases and the dense head transforms into a forerunning debris flow (Fig. 4.11). Clasts at the base of the debris flow are dragged along the seafloor forming groove marks. With the arrival of the rearward body of the flow, sand settling from suspension builds up the H1 division. At the same time mud clasts moving along the aggrading bed surface become buried as randomly dispersed clasts or concentrated along horizons (Fig. 4.11). With continued flow deceleration low-amplitude bed waves develop and migrate along the surface of the basal sand in the 'lower to upper transitional plug flow regimes' (*sensu* Baas et al., 2011) forming the H2 division (see also Baas et al., 2016a). Additionally, sub-mm- to mm-size mud clasts being transported by saltation become incorporated into the H2 layer (Fig. 4.11). With further flow deceleration and reduction of sand settling from suspension, cohesion in the now mud-enriched suspension increases and transforms it into a debris flow that incorporates any remaining mud clasts moving as bed load before depositing *en masse* and forming the H3 division (Fig. 4.11).

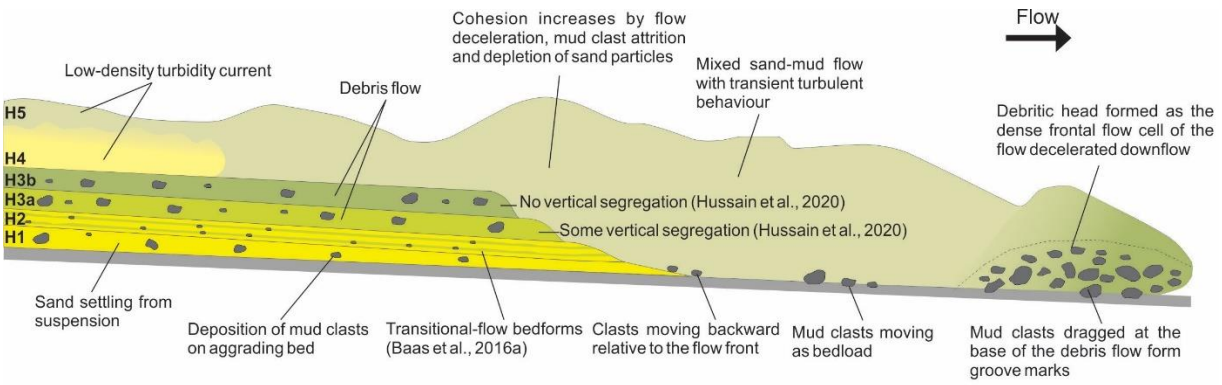

Figure 4.11: Schematic model for the deposition of hybrid event bed with groove marks below the basal turbiditic division in the Silurian Aberystwyth Grits Group, United Kingdom (modified after Baas et al., 2021). Mud clasts formed by erosion at the head of the flow form a dense frontal flow cell that upon deceleration downstream transforms into a debris flow. As the debritic head moves downstream, clasts at the base of the flow are dragged along the seafloor producing groove marks. Later, as the rearward body of the flow arrives, vertical segregation of suspended sediment results in the development of the successive divisions of a hybrid event bed above the grooved seafloor. At the same time, mud clasts moving along the aggrading surface become buried as randomly dispersed clasts or concentrated along horizons. See text for further details.

Contemporaneous with the recognition of various deep-marine matrix-rich strata in the sedimentary record, a series of open-channel flow experiments was carried out to understand turbulence modulation in clay-laden open-channel transitional flows (see Baas and Best, 2002; Baas et al., 2009, 2011, 2016a, 2016b). Although based on concepts derived from open-channel flow experiments, transitional-flow conditions and related turbulence modulation has been used to explain the origin of some deep-marine matrix-rich strata deposited by sediment gravity flows (Kane and Pontén, 2012; Baker and Baas, 2020), in addition to some HEBs (see Baas et al., 2011, 2021; Sumner et al. 2009). The following, therefore, discusses transitional flow and its related deposits.

4.5 TRANSITIONAL FLOW AND ASSOCIATED DEPOSITS

The term “transitional flow” was introduced by Wang and Plate (1996) to describe non-Newtonian clay-laden (up to 10% volume clay concentration) open-channel flows with low to

moderate Reynolds number that simultaneously exhibited both turbulent and laminar characteristics. More specifically, transitional flows comprise three parts, which from base to top are 1) laminar sublayer where turbulence was absent, 2) a turbulent layer and 3) an upper plug layer with weak to no turbulence (Fig. 4.12).

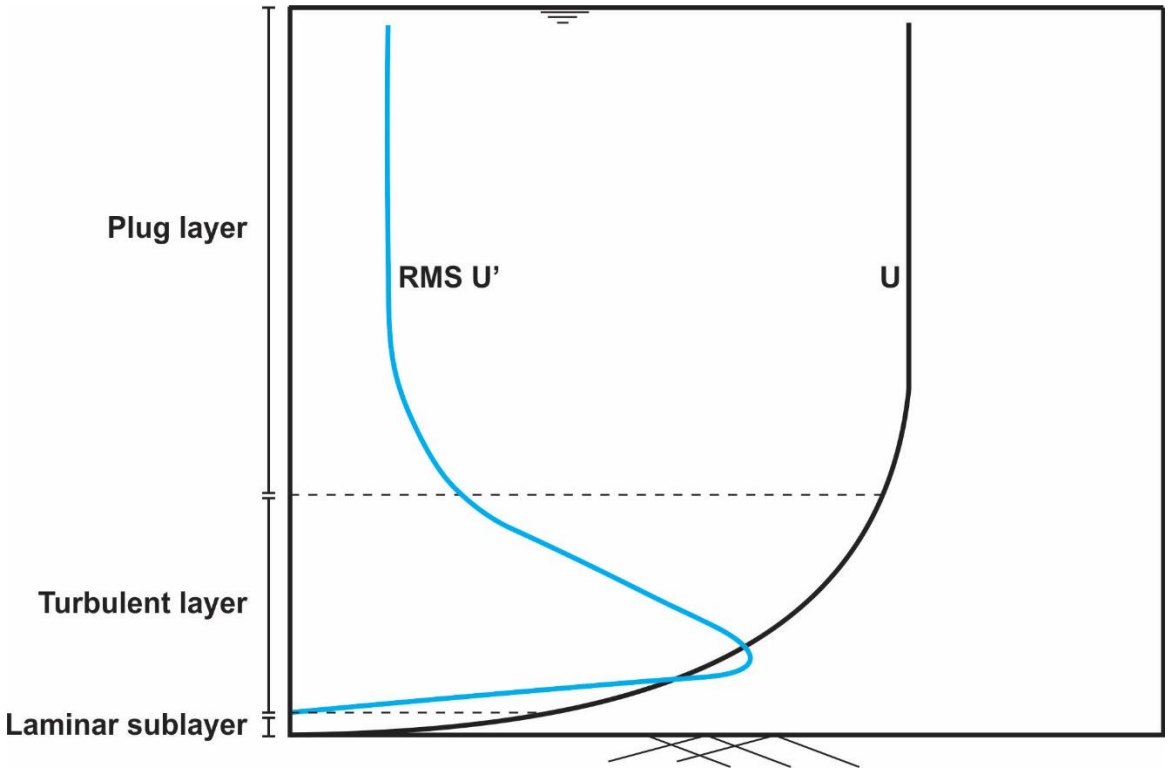

Figure 4.12: Typical vertical profiles of downstream velocity (U – black line) and velocity fluctuations (RMS U' – blue line) in an open-channel transitional flow. Note the flow comprises three parts—a basal laminar sublayer, turbulent layer, and upper plug layer. Modified after Wang and Plate (1996).

Baas and Best (2002) then expanded on this work by investigating clay-laden open-channel flows with volume kaolin concentration ranging from 0.002 to 12.9% and a constant depth-averaged flow velocity of 0.33 m/s. These experiments showed that at low clay concentration (< 2 vol. %) flows were fully turbulent and exhibited a logarithmic velocity profile like in a clear water flow. At 2 – 4 vol. %, however, flows resembled the transitional flows of Wang and Plate (1996), with a near-bed region of anomalously high turbulence intensity that developed in a region

coincident with an abrupt change in the velocity gradient. Additionally, reduced turbulence intensity in the upper part of flows was attributed to particle aggregation that increased yield strength and reduced the upward diffusion of turbulence. With further increase in clay concentration (> 4 vol. %), flows developed a distinct two-part structure made up of a basal layer with high velocity gradient and small-scale to no turbulence, and an upper non-turbulent layer with near constant velocity, termed the laminar plug. Baas et al. (2009) furthered that work by using a wider range of depth-averaged flow velocities (0.13 m/s - 1.47 m/s) and clay concentrations (0.03 - 16.7 vol. %). One of the principal outcomes of that work was a phase diagram that identified five different flow types as a function of clay concentration (Baas et al., 2009, fig. 15A). At the lowest clay concentration flows exhibit a logarithmic velocity profile with turbulence intensity decreasing away from the bed and turbulence present throughout the full flow thickness, much like in a clear-water turbulent flow (TF) (Fig. 4.13A). With a modest increase in clay concentration near-bed velocity decreases but turbulence intensity increases (turbulence-enhanced transitional flow: TETF) – a pattern similar to the transitional flows of Wang and Plate (1996) (see above). Turbulence extends throughout the flow and the typical logarithmic velocity profile is maintained (Fig. 4.13B). With a further increase in clay concentration, near-bed turbulence remains high but in the uppermost part of the flow, cohesive forces begin to dominate and form a non-shearing plug (lower transitional plug flow: LTPF) (Fig. 4.13C) that thickens bedward as clay concentration continues to increase (upper transitional plug flow: UTPF) (Fig. 4.13D). At the highest clay concentration, cohesive forces dominate not only in the much-thickened non-shearing plug, but also in the near-bed region (quasi-laminar plug flow: QLPF) Fig. 4.13E).

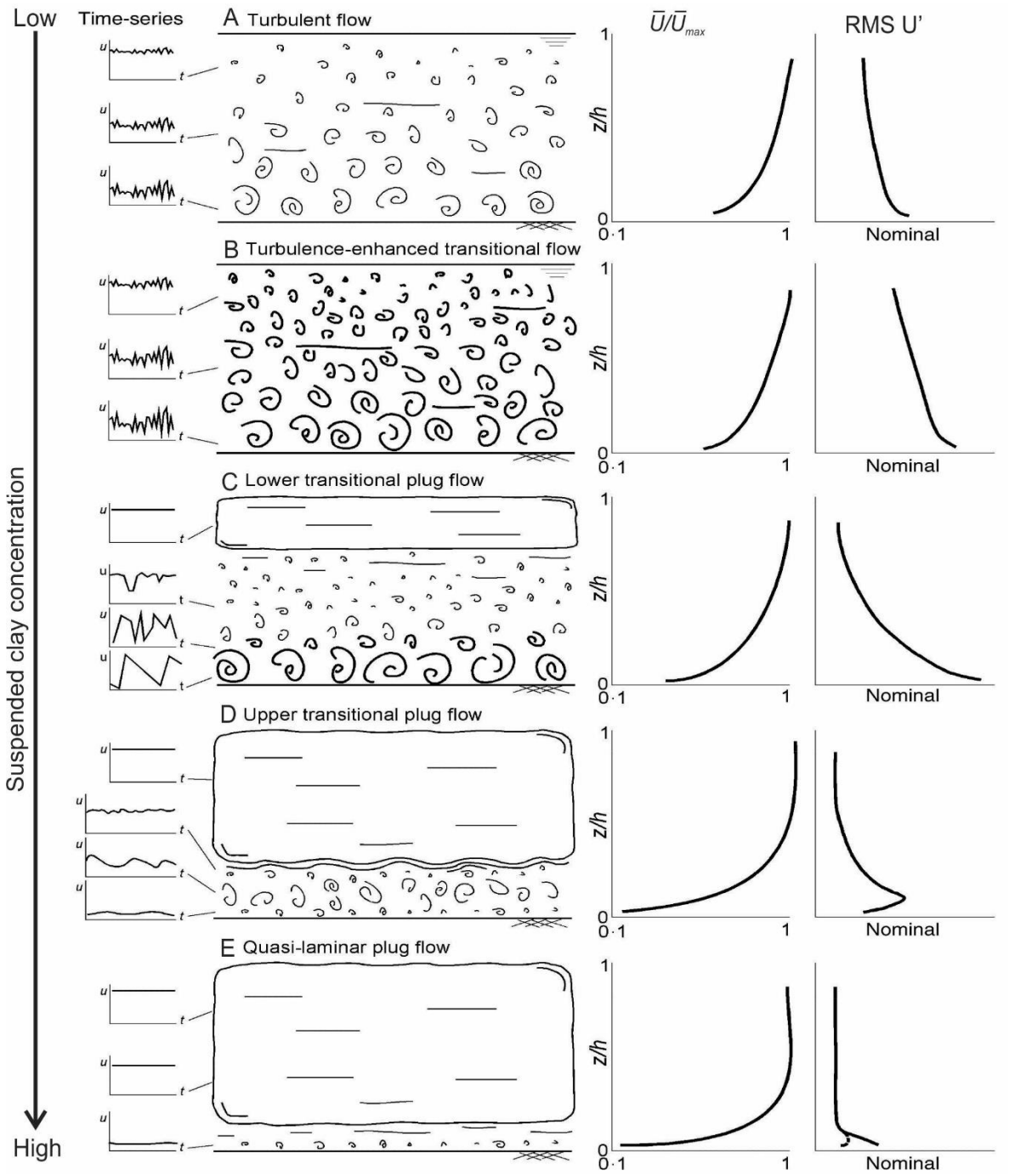

Figure 4.13: Schematic models (left to right) showing representative velocity time series, idealized fluid motions, normalized velocity, and strength of turbulence fluctuations (RMS U' in open-channel flows with increasing clay concentration (Baas et al., 2009, fig. 9): A) turbulent flow, B) turbulence-enhanced transitional flow, C) lower transitional plug flow, D) upper transitional plug flow, E) quasi-laminar plug flow.

Sumner et al. (2009) expanded on the work of Baas and Best (2002) and Baas et al. (2009) by investigating deposition from decelerating open-channel transitional clay-enriched flows. Using an annular flume, Sumner et al. (2009) recognized four deposit types in rapidly decelerating (10 s to 900 s) flows of fixed initial velocity (~ 3 m/s) and sand concentration (10 vol.%), but with varying mud content (0 – 17 vol.%). At the lowest mud content (< 6 vol.%), flows that decelerated over > 300 s deposited a traction-structured sand overlain by a mud cap (type I), whereas flows with < 11.25 vol.% mud and decelerated in < 300 s formed structureless sand overlain by a mud cap (type II). With increased mud content (11.25 – 14.25 vol. %), and independent of deceleration rate, the deposit consisted of structureless sand overlain by a muddy sand (type III), and at > 14.25 vol.% clay a deposit of ungraded muddy sand (type IV). Note that all deposits were overlain by a mud cap related to post-flow settling of residual suspended mud. Sumner et al. (2009) related each of these four deposit types to different parts of the transitional flow phase diagram of Baas et al. (2009) (Fig. 4.14). Type I and II were correlated with deposition in the TF or TETF regimes with sand gradually settling from the fully turbulent suspension (Fig. 4.14). Type III formed in the LTPF and UTPF regimes wherein sand particles settled from the lower turbulent part of the flow, building up the basal clean sand layer that then was sharply overlain by a muddy sand layer deposited *en masse* by the upper laminar plug (Fig. 4.14). Type IV deposits were interpreted to be emplaced by flows that decelerated in the QLPF regime (Fig. 4.14). Here, laminar flow conditions extended to the base of the flow and had sufficient yield strength to prevent sand from settling, thus forming the ungraded muddy sand deposited by *en masse* freezing.

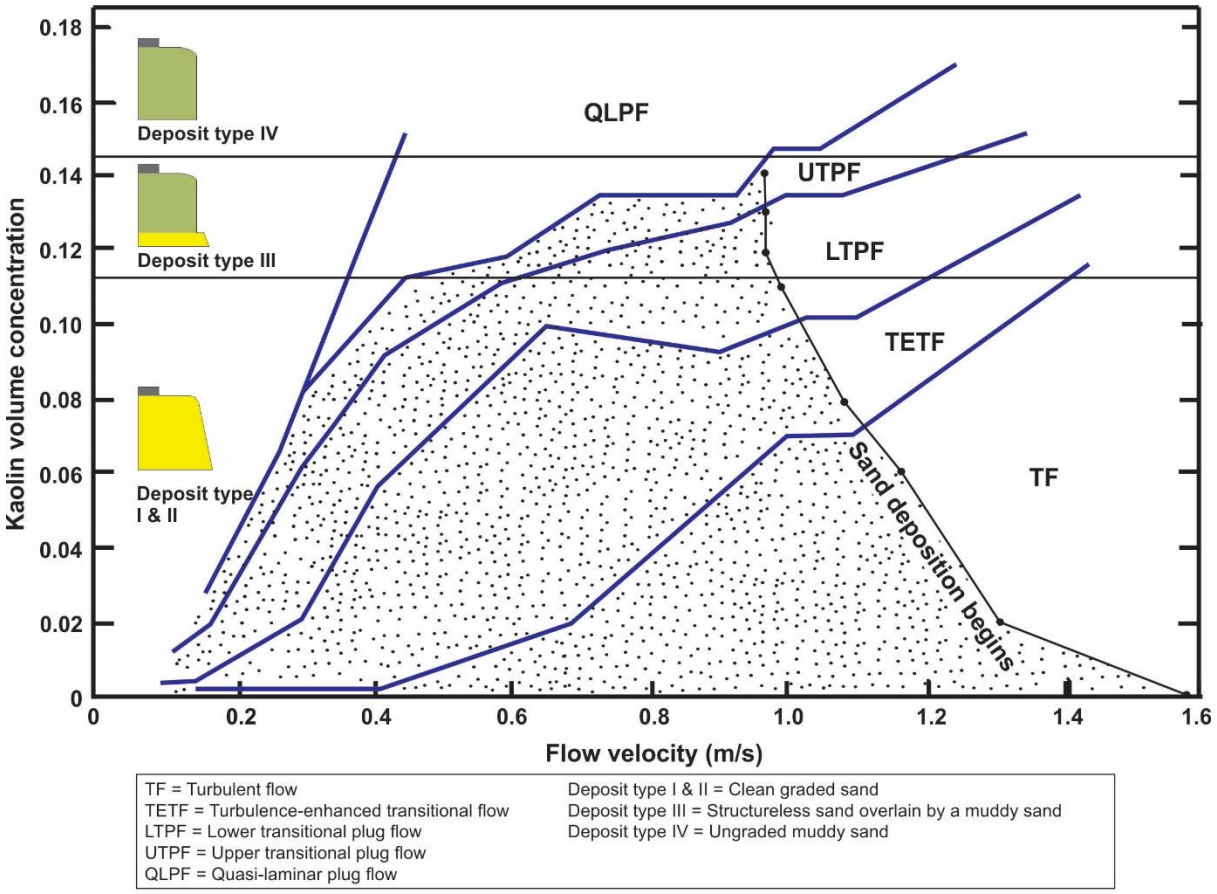

Figure 4.14: Phase diagram showing the relationships between flow velocity, clay volume concentration, vertical flow structure based on the terminology of Baas et al. (2009), and resultant deposit as flows decelerate from an initially fully turbulent suspension (Sumner et al., 2009, fig. 2). At low clay content, the flow is fully turbulent at the onset of sand deposition resulting in the development of type I and II deposits. At high clay content (> 14.25% kaolin clay), flow is fully laminar and forms an ungraded muddy sand deposited by *en masse* freezing. At intermediate clay content, the flow is transitional at the onset of deposition resulting in the development of type III deposit.

In the deep-marine sedimentary record, strata interpreted to be deposited by transitional flow deposits were first reported by Kane and Pontén (2012) from submarine lobes of the Paleogene Wilcox Formation, Gulf of Mexico. In this study, nine bed types were recognized, of which seven were interpreted to be transitional flow deposits (Fig. 4.15) bounded by two end-member types thick sandy turbidites (type 0) (Fig. 4.15A) and thin fine-grained turbidites (type VIII) (Fig. 4.15I). Strata were reported to stack in an upward-coarsening pattern (several m-thick) inferred to reflect submarine lobe progradation. More importantly, based on Walther's law, the

vertical stacking from type VIII to type 0 was interpreted to represent facies changes associated with the downstream evolution of the flow as it spread and decelerated over the basin floor. During flow evolution, the mixed sand-mud suspension initially remained fully turbulent and deposited sandy type 0 – type II strata in the TF – TETF regime (sensu Baas et al. 2009) (Fig. 4.16). With reduced turbulence intensity and preferential settling of larger particles downstream, the sediment suspension became increasingly mud-enriched and developed a laminar plug region in its upper part, resulting in a transition to LTPF – UTPF regimes (sensu Baas et al. 2009) and depositing type III – type VI strata (Fig. 4.16). As the flow became fully laminar further downstream, type VII sandy mudstone was deposited en masse under QLPF regime (sensu Baas et al. 2009) (Fig. 4.16). Finally, all bed types were overlain by thin-bedded turbidite (type VIII) interpreted to represent deposition by the dilute turbulent wake of each flow.

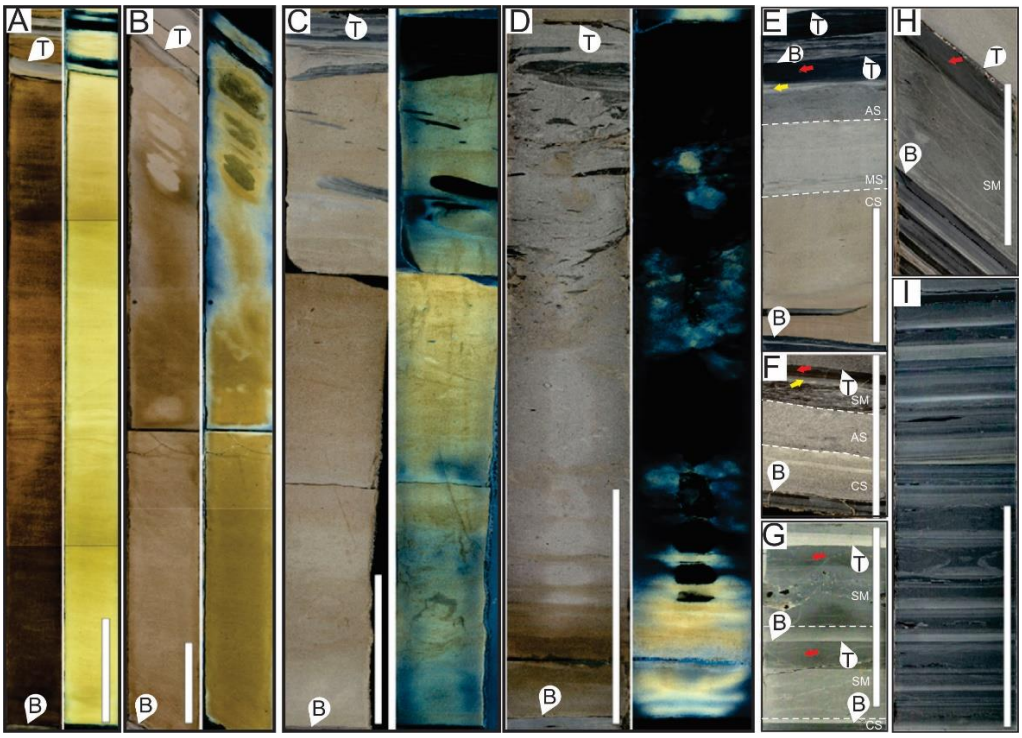

Figure 4.15: A–I) Representative core photographs of bed types 0–VIII in the (Paleogene) Wilcox Formation, Gulf of Mexico (from Kane and Pontén, 2012, fig. 3). Parts A–D are image pairs under white light (left) and ultraviolet light (right) – yellowing being a measure of intensity of hydrocarbon staining (bright yellow), thereby providing a proxy for permeability and clay content of the strata. Note that where preserved, the bed types are overlain by well-

sorted traction-structured sandstone (yellow arrow) and/or a mudstone cap (red arrow). B and T indicate bottom and top of individual beds. Scale bars are 10 cm long. A) Type 0—thick sandy turbidite. B) Type I— normally graded sandstone with subtle parallel lamination. C) Type II—ungraded or normally graded sandstone showing a vertical transition from plane-parallel-laminated to weakly laminated, dish-structured sand with subtle light (mud-poor) and dark (mud-rich) banding. D) Type III—ungraded or normally graded sandstone exhibiting a vertical transition from subtle light and dark banding to massive muddy sand containing mud clasts. E) Type IV—massive relatively clean sandstone (CS) overlain gradationally or sharply by a muddy sandstone (MS), in turn overlain abruptly by a clast-rich argillaceous sandstone (AS). F) Type V—thin, relatively clean sandstone (CS) overlain abruptly by an argillaceous sandstone unit (AS), in turn overlain sharply by a clast-rich sandy mudstone (SM). G) Type VI—very-thin relatively clean sandstone (CS) overlain sharply by a thicker sandy mudstone (SM). H) Type VII—exclusively sandy mudstone (SM). I) Type VIII—thin fine-grained turbidites.

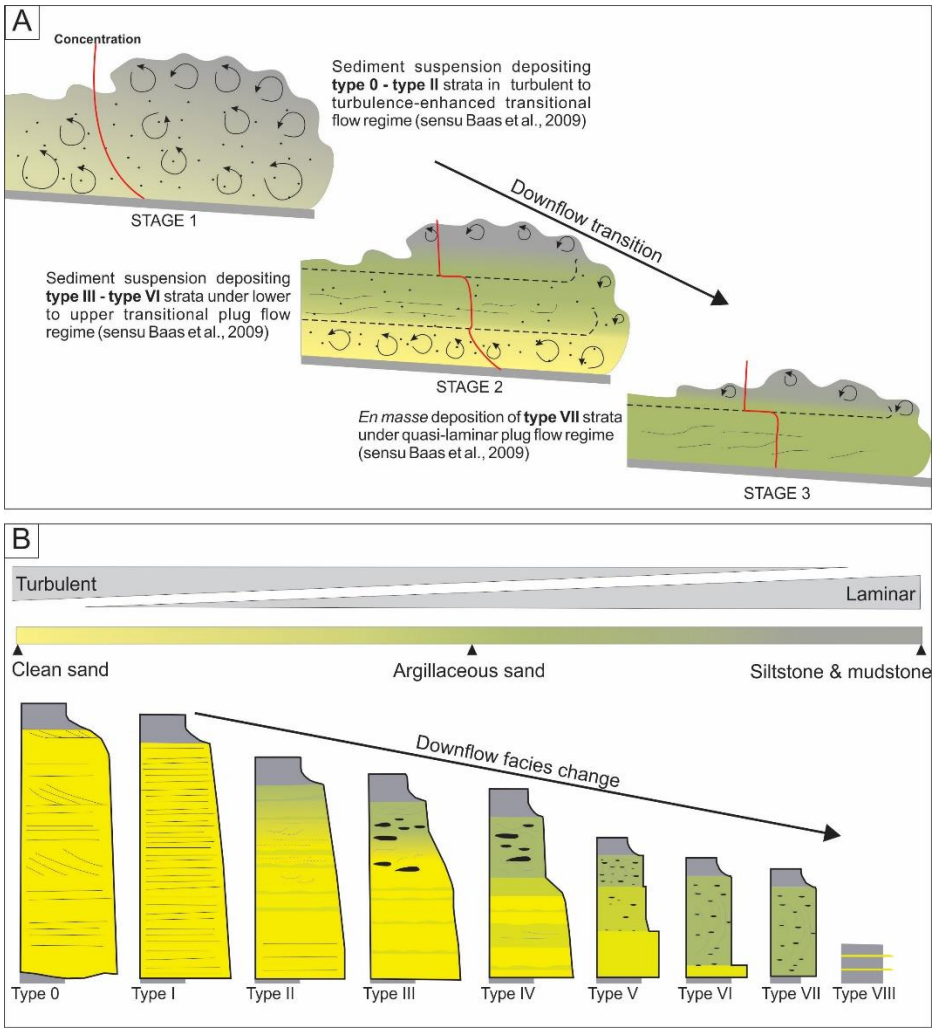

Figure 4.16: A) Schematic model of the downstream evolution of a mud-enriched sediment suspension from turbulent (stage 1) to transitional (stage 2) to laminar (stage 3) flow regime. Vertical sediment concentration profile indicated by red line; abrupt changes in the shape of the profile indicated by black dashed lines. B) Downflow progression of type 0 to type VII as a function of changing flow conditions. Modified after Kane and Pontén (2012). Thin fine-grained turbidite (type VIII) represent deposition from the dilute turbulent wake of the flow. See text for details.

Adding to the experimental work of Sumner et al. (2009), Baas et al. (2011) investigated bedform development, specifically current ripples, in transitional flows by rapidly decelerating mixed sand-mud flows to a steady flow state. In this study, flows with a fixed sediment concentration (3 vol. %) of bimodal medium sand and coarse silt, but varying kaolin clay content (0.2 – 19.2 vol. %), were circulated at ~ 1.2 m/s for several minutes and then decelerated instantaneously to ~ 0.46 m/s, allowing suspended sediment to rapidly settle to the bed. A steady flow velocity of ~ 0.46 m/s (ripple stability field) was then maintained for the duration (~ 2.5 h) of the experiment. Much like Sumner et al. (2009), upon deceleration the bed aggraded in all five flow regimes (i.e., TF, TETF, LTPF, UTPF and QLPF) and traction-transport structures were absent. In the TF and TETF regimes, the deposit consisted of a sandy layer overlain sharply by a silty layer, and therefore resembled type II deposit of Sumner et al. (2009). The sharp upward change from sand to silt was attributed to differences in their settling velocity. In the LTPF and UTPF regimes, the deposit consisted of a sandy layer overlain by a muddy (mixed silt & clay) layer, equivalent to deposit type III of Sumner et al. (2009). Lastly, in the QLPF regime, the initial deposit consisted of a single muddy layer with dispersed sand grains, similar to deposit type IV of Sumner et al. (2009).

Following the deceleration phase and under steady flow conditions, the bed surface was reworked forming current ripples on beds deposited by TF, TETF and LTPF, but absent in UTPF and QLPF due to interpreted turbulence suppression and increased yield strength of the bed. In flows where ripples did form, the equilibrium height and length of the ripples gradually increased from ~ 1.3 cm high and 11 cm long in TF to ~ 1.8 cm high and 20 cm long in LTPF (Baas et al., 2011, fig. 15). This increase was attributed to greater erosion on the lee side of the ripples caused by the steepened velocity gradient and enhanced turbulence generation in the near-bed region of

TETF and LTPF. Associated also with the increase in suspended mud content from TF to LTPF, is a change from sandy to increasingly more heterolithic (i.e., alternating sand- and mud-rich) ripple cross-lamination, interpreted to record the episodic avalanching of coarse-grained sediment down the ripple lee side and draped by the settling of fine-grained sediment from suspension.

Using the same open-channel setup as Baas et al. (2011), Baas et al. (2016a) further investigated bedform development in transitional flows by extending the phase space to washed-out ripples (WOR) (*sensu* Baas and Koning, 1995) and upper-stage plane bed (USPB). Just like Baas et al. (2011), all flows were circulated at ~ 1.2 m/s for several minutes and then decelerated instantaneously to ~ 0.8 – 1.0 m/s (USPB) or ~ 0.7 – 0.9 m/s (WOR). Results of these experiments and those of Baas et al. (2011) were then combined to develop a bedform phase diagram for transitional flows based on cohesive forces, determined by the yield strength (τ_y) of the sediment suspension (see equation 6 in Baas et al., 2016a), versus turbulent forces, estimated by a grain-related mobility parameter (θ') (see equation 3 in Baas et al., 2016a) (Fig. 4.17). At $\theta' < 1.1$, current ripples are stable in TF, TETF and LTPF, but did not develop in UTPF and QLPF due to increased cohesive forces that suppressed flow turbulence and increased strength of the bed to resist erosion. At θ' of 1.1 – 1.2, washed-out ripples were stable in TF and much of TETF (up to τ_y value of 0.06 Pa) (Fig. 4.17), but showed a gradual increase in height and length: ~ 0.5 cm high and 11 cm long (TF) and ~ 0.9 cm high and 24 cm long (TETF). As τ_y exceeded 0.06 Pa in TETF (Fig. 4.17), WOR were replaced by 1.1 – 1.7 cm high and ~ 24 cm long current ripples, which were inferred to develop because of increased near-bed turbulence disrupting the high-concentration bedload layer (i.e., traction carpet) that otherwise would reduce ripple height and impart a more symmetrical shape. Under the same conditions (θ' – 1.1 - 1.2), but in the LTPF (Fig. 4.17), scours and intrascour composite bedforms developed (Baas et al., 2016a, fig. 25) due to strong bed erosion related to

intense near-bed turbulence. However, in the UTPF regime, stronger cohesive forces damped turbulence and strengthened the bed to resist erosion, resulting in low-amplitude (~ 0.3 cm-high), 400 – 500 m-long bed waves (LABW) interbedded with cm-thick muddy layers formed of fine-grained sediment settling from suspension between the passing bed waves. Lastly, in the QLPF regime, even stronger cohesive forces fully suppressed bed-form development and deposited an ungraded structureless muddy sand.

At $\theta' > 1.2$ (Fig. 4.17), upper-stage plane beds were stable in TF, but in TETF, it was replaced by large (2 – 2.5 cm high, 25 – 40 cm long), symmetrical and angular ripples with normal and reverse asymmetry — features termed transitional bedforms previously by Saunderson and Lockett (1983) and Bridge and Best (1988). Baas et al. attributed these transitional bedforms to strong turbulent forces in TETF that disrupted the traction carpet above the USPB and allowed large ripples to form. In the LTPF regime, and at low τ_y values (Fig. 4.17), transitional bedforms were replaced by bed-waves up to 1.6 cm high and 70 – 85 cm long. Although similar in shape, these features differed in dimension to low-amplitude bed-waves formed in UTPF (see above), and as such were considered to be a more regular and longer equivalent of the transitional bedforms developed in TETF. At higher τ_y values in LTPF (Fig. 4.17), LABW were replaced by bed scours and intrascour composite bedforms (Baas et al., 2016a, figs. 21 and 22), which were inferred to be the result of a more mud-rich, water-saturated, more easily eroded substrate. Next, in the UTPF regime, just like the WOR-analogous flows, the USPB-analogous flows developed low-amplitude sandy bed waves interstratified with mud-rich laminae. Finally, in the QLPF regime,-bedforms did not develop and the deposit was an ungraded structureless muddy sand.

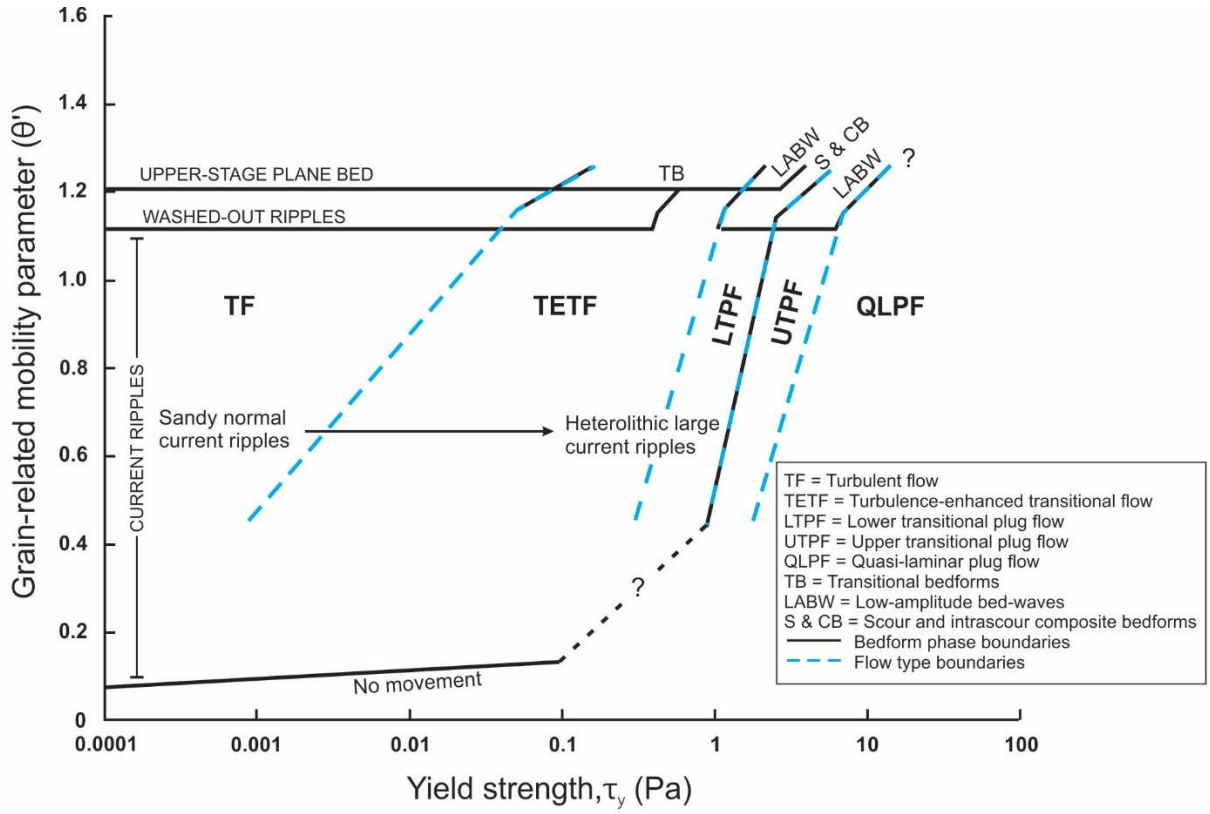

Figure 4.17: Bedform phase diagram for rapidly decelerated mixed sand–mud suspensions in open-channel flows based on grain-related mobility parameter (θ') and yield strength of the sediment suspension (τ_y) (Baas et al., 2016a, fig. 29). Solid black lines indicate bedform phase boundaries; dashed blue lines represent flow phase boundaries. Question marks denote inferred boundaries.

Recently, some of the sand-mud bedforms produced by transitional flows (see above) were reported from the submarine fan fringe strata of the Aberystwyth Grits Group and Borth Mudstone Formation, Wales, UK by Baker and Baas (2020). In this study, strata were classified into three kinds based on average height and length: sandy ripples – 1.1 cm high, 14.1 long cm; heterolithic large current ripples – 1.9 cm high, 27.4 cm long; and low amplitude bed-waves – 1.0 cm high, 35.4 cm long with heterolithic internal layering (e.g., Fig. 4.18). Moreover, these different kinds were reported to be systematically arranged spatially and interpreted to reflect the downflow transformation of flow conditions, specifically, turbulent (sand ripples) to turbulence enhanced to lower transitional plug flow (large current ripples) and then to upper transitional plug flow (low

amplitude bed-waves) (Fig. 4.18). Based on these observations and interpretations, Baker and Baas (2020) refined the bedform phase diagram of Baas et al. (2016a) by extending the mobility parameter of low-amplitude bed-waves development in the UTPF regime from upper-stage plane bed into the current ripple stability fields (Baker and Baas, 2020, fig. 16).

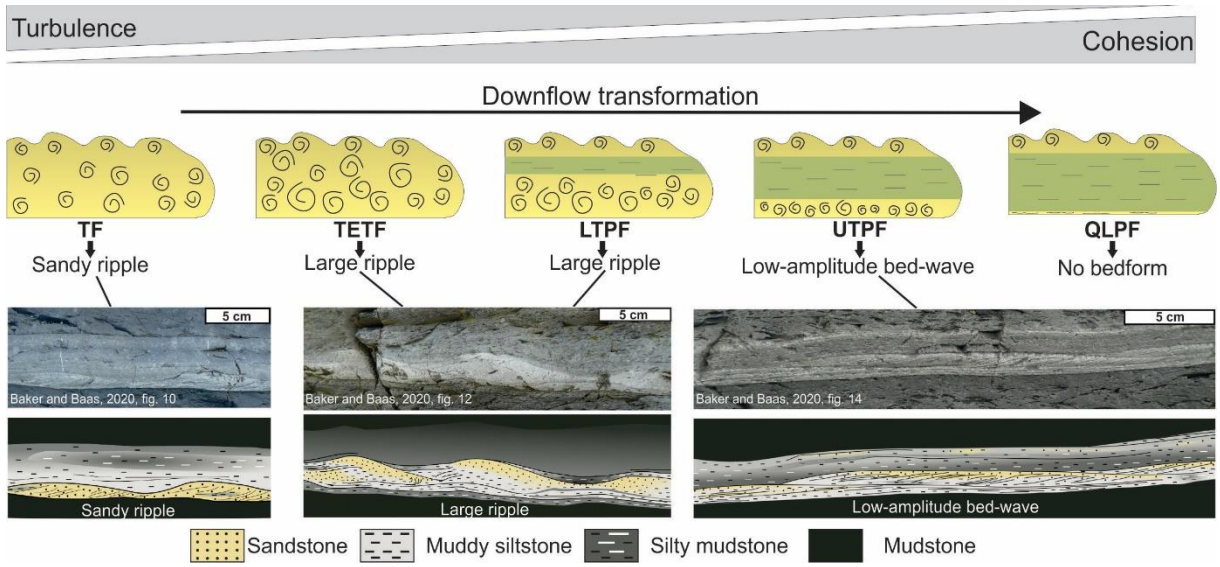

Figure 4.18: Schematic showing the theorized downflow development of bedforms as a sand–mud suspension transforms from a turbulent to transitional to laminar flow. Sandy ripples are inferred to form in the turbulent flow (TF) regime, large ripples in turbulence-enhanced transitional flow (TETF) and lower transitional plug flow (LTPF) regimes, and low-amplitude bed-wave in upper transitional plug flow regime. Bedforms are absent in the quasi-laminar plug flow regime. Modified after Baker and Baas (2020).

Coincident with some of the Baas et al. and earlier Sumner et al. experiments, in addition to the continued development of theoretical models of hybrid event beds based mostly on observations in core and outcrop, was the description of sand- and mud-rich (> 20% silt and clay) strata, termed matrix-rich sandstone, from the Neoproterozoic Windermere turbidite system in British Columbia, Canada (Terlaky and Arnott, 2014). These strata included muddy sandstone, sandy mudstone, but most notably, bipartite facies, comprising a sandy basal part overlain sharply by a mud-rich upper part, and therefore resembling deep-marine deposits described earlier and

termed co-genetic debrite-turbidite bed (Haughton et al., 2003; Talling et al., 2004), hybrid event bed (Haughton et al., 2009), and transitional flow deposit type IV – VI (Kane and Ponten, 2012). Like these other two-part deposits, bipartite facies was reported to be part of a depositional continuum, but one that differed significantly in horizontal scale and interpreted depositional origin. These strata are discussed next.

4.6 MATRIX-RICH SANDSTONES

The term matrix-rich sandstones was first coined by Terlaky and Arnott (2014), and later advanced by Terlaky et al. (2016), Angus et al. (2019) and Ningthoujam et al. (2022) to describe strata composed of a mix of sand and matrix (i.e. silt and clay) in rocks of the Neoproterozoic Windermere Supergroup and Ordovician Cloridorme Formation. Based on matrix content, these authors recognize four main lithofacies: matrix-poor sandstone (0 – 20% matrix), muddy sandstone (20 – 50% matrix), bipartite facies with a basal sandy (25 – 60% matrix) part overlain sharply by a planar- to irregular-based muddier part (40 – 80% matrix), and sandy mudstone (50 – 90% matrix), which collectively are interpreted to form a horizontal depositional continuum (see below) (Fig. 4.19). All four facies are structureless (i.e., lack tractional sedimentary structures), coarse-tail graded or massive, and composed of sand grains that ranged from very fine to very coarse sand with a mud matrix. Mud and lesser very fine to medium-grained sandstone clasts are also common. Clasts are typically elongate, sub-angular to sub-rounded and oriented with their maximum projection plane subparallel to bedding. Where present, these strata are then overlain by lamina to thin beds of traction-structured sandstone capped by silty mudstone (Fig. 4.19).

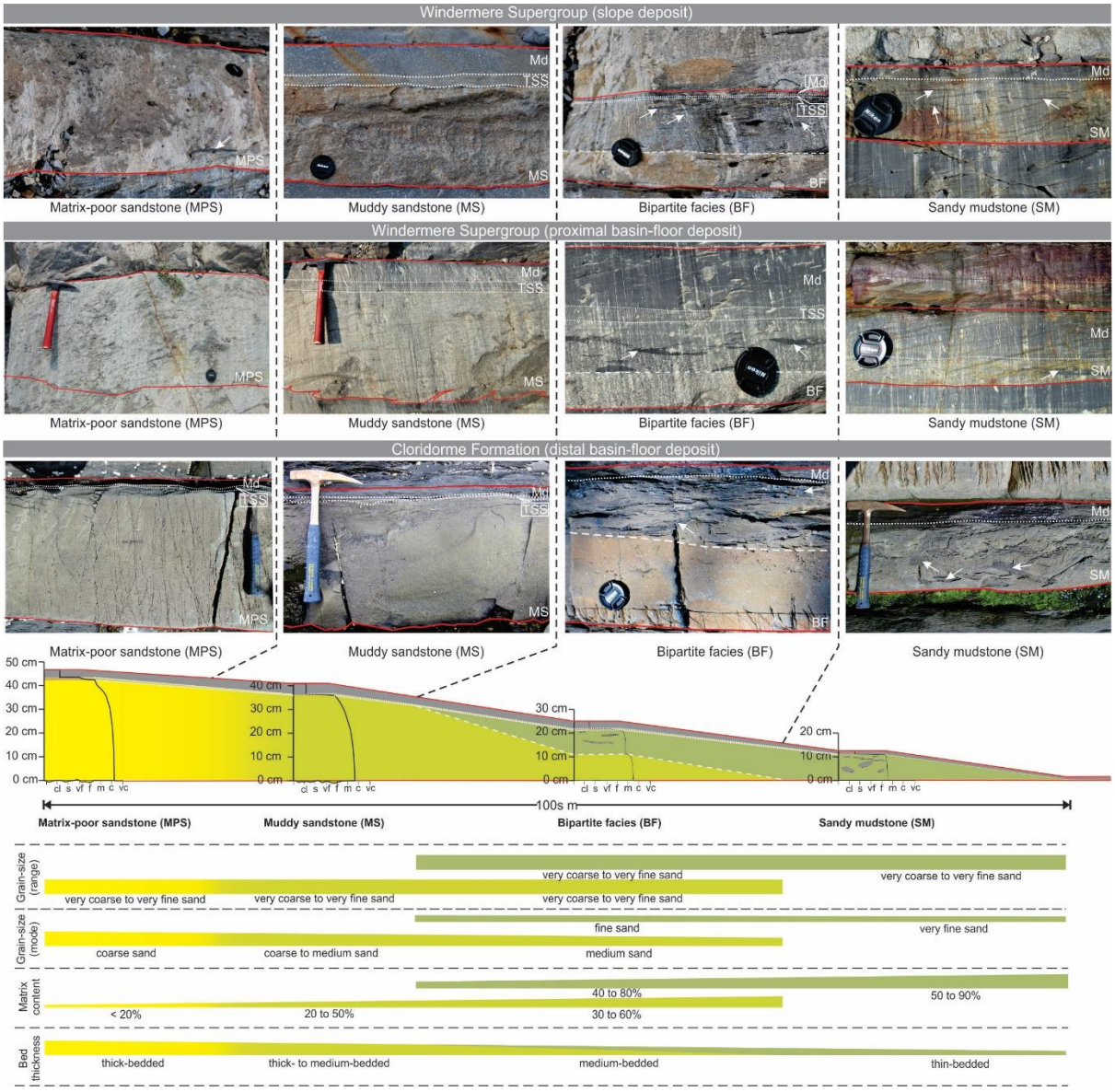

Figure 4.19: Schematic of the idealized proximal to distal (left to right) depositional transect and characteristic lithological trends (bar graphs) from matrix-poor sandstone (MPS) to muddy sandstone (MS) to bipartite facies (BF) to sandy mudstone (SM) over a distance of hundreds meters. Except where eroded, all strata are overlain by a thin-bedded traction-structured sandstone (TSS) capped by silty mudstone (Md). See Ningthoujam et al. (2022) for descriptive details. Representative photographs of each lithofacies in slope and proximal basin-floor deposits of the Windermere Supergroup and distal basin-floor deposits of the Cloridorme Formation are shown above the transect. Solid red lines mark the base and top of a single bed; white arrows point to mudstone clasts; dashed white lines separate the lower and upper parts of a bipartite facies (BF); dotted white lines mark the bases of the traction-structured, very fine-grained sandstone and/or mudstone cap. Scales are: hammer (33 cm long) and camera lens cap (5.2 cm diameter).

Matrix-poor sandstone (MPS) contains 0 - 20% matrix and is generally composed of coarse-grained sandstone forming beds 40 – 50 cm thick with dispersed clasts making up to 5% of

the bed. In comparison, muddy sandstone (MS) which has 20 - 50% matrix, is typically made up of medium- to coarse-grained sandstone and is ~ 25 cm thick on average with dispersed clasts constituting ~ 5 – 10% of the bed. The distinctive bipartite facies (BF), consisting of two sharply bounded parts, is usually 15 – 20 cm thick. The lower part comprises medium-grained muddy sandstone (20 - 50% matrix) overlain sharply by a planar- or irregular-based upper part composed mostly of sandy mudstone (40 - 80% matrix) with dispersed sand grains that range up to coarse sand. Additionally, clasts, consisting mostly of mud, make up ~ 5 – 10% of the basal part and ~ 5 – 30% of the upper part. Across the interface that separates the lower and upper parts, Angus et al. (2019) and Ningthoujam et al. (2022) report that the grain-size distribution fined slightly but the range of grain sizes changed little. More notably, matrix content increased by a few tens of percent, which in outcrop is marked by an abrupt darkening of the strata. Furthermore, in the Windermere Supergroup, the interface was reported to be exclusively planar (Terlaky and Arnott, 2014; Angus et al., 2019), but in the Cloridorme Formation is either planar (Fig. 4.20A) or alternates intermittently between planar and irregular (Ningthoujam et al., 2022) — irregularities marked by local synforms and antiforms with local overhangs and injections of sand from the basal part into the upper part (Fig. 4.20B). Also, where sand intrusions were observed, mud clasts were more abundant, and together created a distinctive patchwork mosaic of sand-rich and sand-poor areas. The final lithofacies, sandy mudstone (SM), is composed of 50 – 90% silt and clay with dispersed fine sand grains – note that although much less common, grains ranging up to coarse sand are also reported. Beds are 8 – 15 cm thick with clasts making up ~ 5 – 30% of the bed.

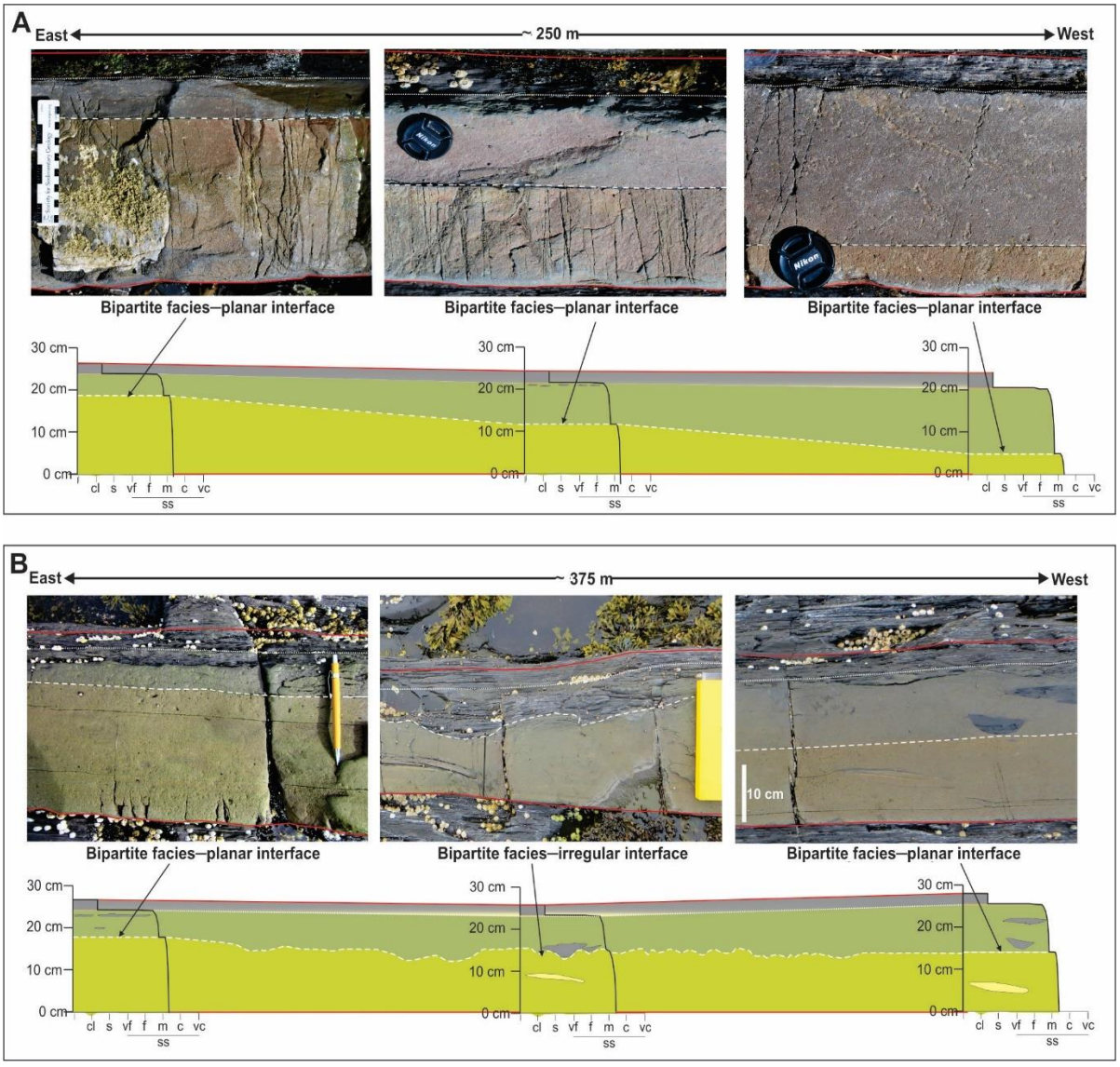

Figure 4.20: Outcrop photographs and stratigraphic logs showing differences in the character of the contact between muddy sandstone (MS) and overlying sandy mudstone (SM) in bipartite facies of the Cloridorme Formation: A) planar and B) along strike alternation of planar and irregular. Note that irrespective of the nature of the contact, all bipartite facies show a consistent downflow (east to west) thinning of the basal MS part and compensatory thickening of the upper SM part (after Ningthoujam et al., 2022).

Tracing of individual beds in continental slope and proximal basin-floor deposits of the Windermere Supergroup (Terlaky and Arnott, 2014; Angus et al., 2019; Ningthoujam et al., 2022) and distal basin-floor deposits in the Cloridorme Formation (Ningthoujam et al., 2022), showed a systematic arrangement of lithofacies, namely, MPS to MS to BF and then to SM, each capped,

except where eroded, by a laminated to thin-bedded, traction-structured sandstone overlain by silty mudstone (Fig. 4.19). More specifically, MPS gradually transforms to MS, which then develops into a two-part, bipartite facies (BF) consisting of a basal muddy sandstone overlain sharply by an upper sandy mudstone commonly containing dispersed mud clasts. Further along strike, the basal part of BF progressively thins and then pinches out, whereas the upper part thickens, but at a diminishing rate laterally (Fig. 4.19). Following the termination of the basal sand-rich part of BF, the now exclusively sandy mudstone thins to a pinch-out (Fig. 4.19). Notably also, where present, clasts progressively decrease in size from large and tabular (ranging up to a few decimeters thick and several meters long — based on fig. 10B in Terlaky and Arnott (2014)) and located near the base of the bed in MPS, to a few cm-thick and -long and positioned much higher in the bed in SM (Angus et al., 2019; Ningthoujam et al., 2022). Significantly, all these changes occurred over a horizontal distance of a few hundreds of meters and were interpreted to reflect a downflow (proximal to distal) depositional continuum, which in the Windermere was interpreted to be oriented at a high angle to the main flow (Terlaky and Arnott, 2014; Angus et al., 2019; Ningthoujam et al., 2022), but more or less parallel to the main flow in the Cloridorme (Ningthoujam et al., 2022). Interestingly, regardless of orientation of the depositional continuum relative to the main flow, or paleoenvironmental setting (continental slope versus proximal/distal basin floor), the transitions from MS to BF, BF to SM and SM to its pinch-out were reported to be of proportionate length (Ningthoujam et al., 2022) (Fig. 4.21), and accordingly, suggest similarity in depositional process.

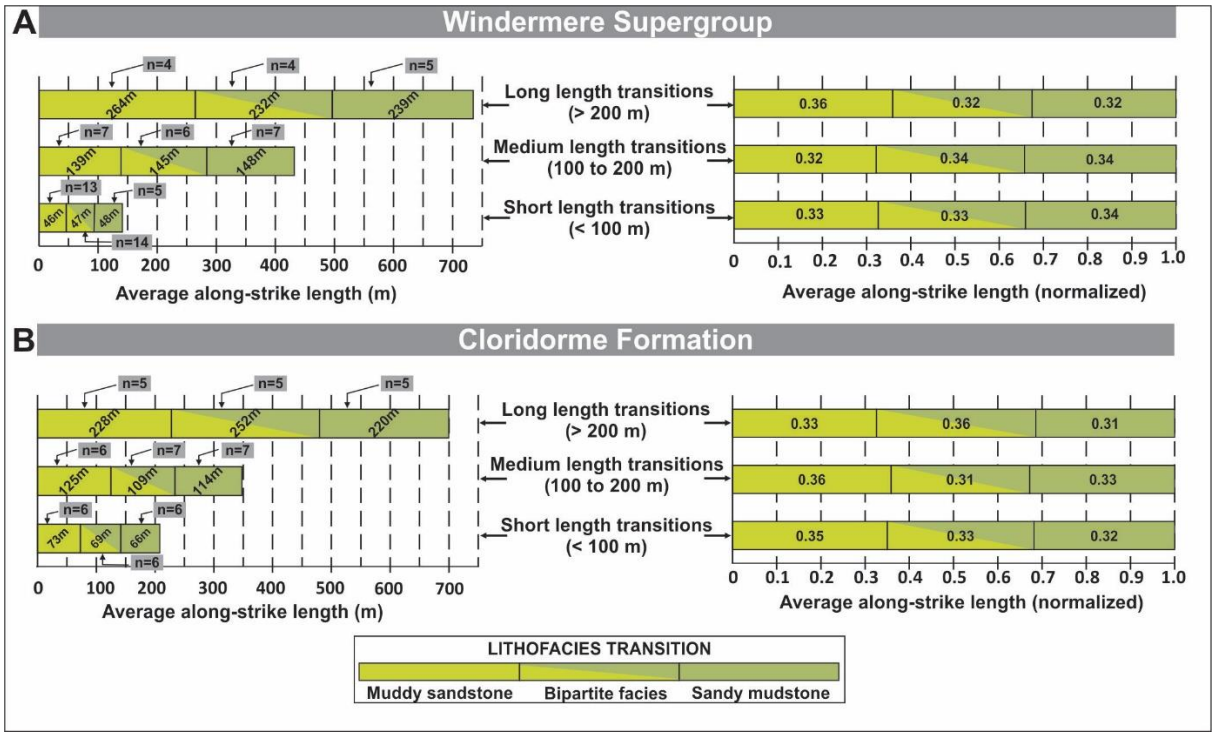

Figure 4.21: Bar graphs on the left show the average along-strike length of the depositional continuum from muddy sandstone (MS) to bipartite facies (BF) to sandy mudstone (SM) and then pinch-out of SM in (A) Windermere Supergroup—proximal basin floor and slope deposits; and (B) Cloridorme Formation—distal basin floor deposits. Depositional continuum is categorized as long (> 200 m), medium (100–200 m) and short (< 100 m). On each bar graph "n" indicates the number of individual beds where that particular transition was observed and used to calculate the average along-strike length for each transition. Bar graphs on the right show the same data but normalized by the total length of the depositional transect (i.e., from MS to the pinch out of SM). Note that irrespective of the length of the depositional transect, or slope–proximal basin floor (Windermere) versus distal basin floor (Cloridorme) the normalized length of each lithofacies transition is proportionately similar. After Ningthoujam et al. (2022).

Based on field observations, matrix-rich and associated matrix-poor sandstones were typically overlain abruptly by sandy channel fills and splays in the continental slope and basin floor settings of the Windermere Supergroup (Terlaky and Arnott, 2014; Terlaky et al., 2016; Angus et al., 2019; Ningthoujam et al., 2022) and sandy terminal splays in the distal basin floor setting of the Cloridorme Formation (Ningthoujam et al., 2022). This stratigraphic relationship was attributed to avulsion which resulted in high-energy, momentum-driven turbulent wall jets that eroded previously deposited fine-grained off-axis sediment and charged the flow with very fine sand to clay and low-density mud clasts (Arnott, 2007b; Terlaky and Arnott, 2014; Angus et

al., 2019; Navarro and Arnott, 2020; Ningthoujam et al., 2022) (Fig. 4.22). The virtually instantaneous addition of easily suspended sediment resulted in the rapid depletion of fluid turbulence to maintain the particle suspension. This, in turn, caused the now completely momentum- and buoyancy-driven sediment suspension to collapse and deposit a systematic and dimensionally consistent succession of lithofacies consisting of MPS to MS to BF and then to SM over a horizontal distance of hundreds of m along the margins of the high energy wall jet in examples from the Windermere (Terlaky and Arnott, 2014; Angus et al., 2019; Ningthoujam et al., 2022) (Fig. 4.22A), and at the downflow terminus of the flow in the Cloridorme (Ningthoujam et al., 2022) (Fig. 4.22B).

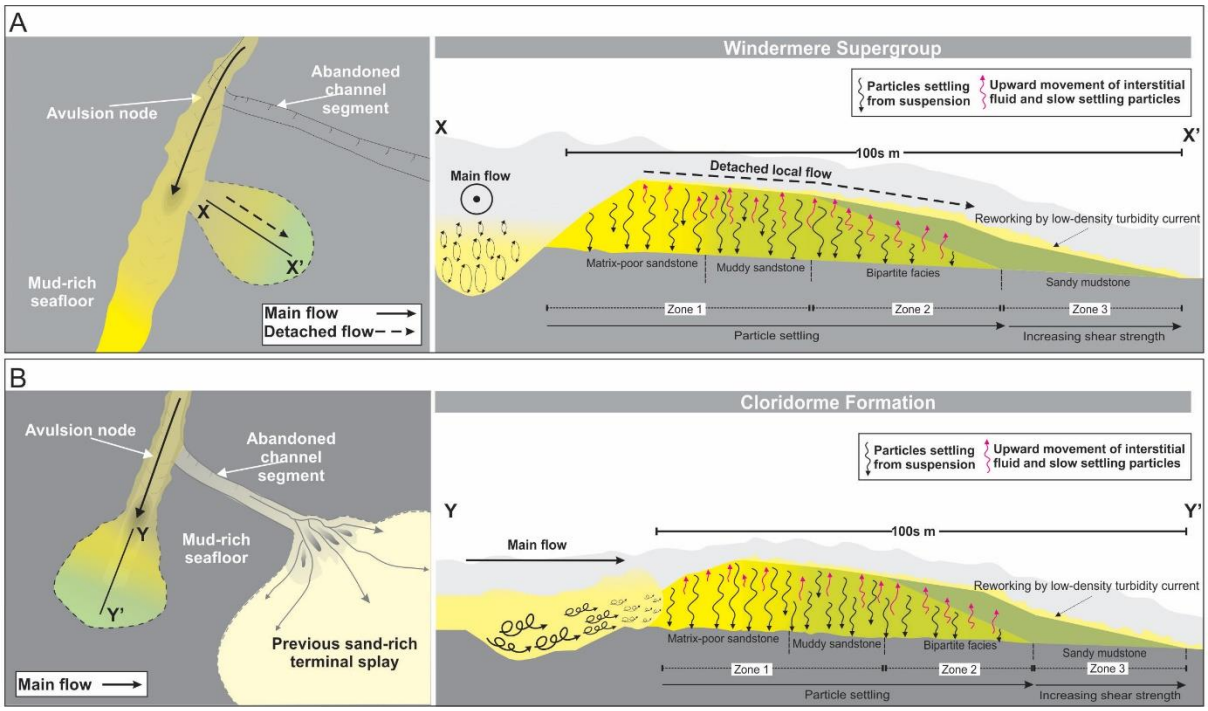

Figure 4.22: A, B) Schematic (left side) downflow of an avulsion node where scouring of the mud-rich seabed charges the flow with fine-grained sediment and mud clasts. Schematic (right side) showing the progression from matrix-poor sandstone to muddy sandstone to bipartite facies and then to sandy mudstone as a result of particle settling in a negligibly sheared sediment suspension A) adjacent to a high-energy wall jet in continental-slope and proximal basin-floor settings (Windermere Supergroup, and B) at the downflow terminus in a distal basin-floor setting (Cloridorme Formation) – see text for details. Diagrams are not to scale. After Ningthoujam et al. (2022).

More specifically, along the depositional transect the rapidly collapsing, mud-enriched, polydispersed sediment suspension was interpreted to be initially uniformly mixed, and despite different size particles settling at different velocities, the constant mass flux of particles to the bed caused the most proximal deposits (i.e., MPS) to have a granulometric make-up similar to that in the initial suspension. Further along the transport path, as faster settling particles like granules and very coarse sand became preferentially depleted, the proportion of fine particles and mud matrix progressively increased as MPS transitioned to MS. Further laterally, the continued settling of the coarsest particles and compensatory upward flux of ambient fluid, slowly settling mud-particles and low-density mud clasts, developed adequate cohesive strength and/or density in the upper part of the suspension to inhibit the remaining sand and coarser grains from settling. At this stage, a two-part suspension consisting of a basal sand-rich part overlain sharply by a significantly more mud-rich upper part formed the bipartite facies (BF) (Fig. 4.22). Here, the preservation of the two-layer make-up, but more importantly, the sharp and typically planar surface that separated the two parts of BF was attributed to negligible shearing within the suspension. Notably, a similar particle segregation mechanism forming a two-part deposit with a sharp internal interface was demonstrated experimentally by Perillo et al. (2015), and more recently by Hermidas et al. (2018) and Koo et al. (2019). In these experiments sand particles settling in negligibly-sheared, mud-enriched (8 – 18 vol. %) sediment gravity flows deposited a sandy basal layer overlain sharply by a suspension of (upward) elutriated mud that quickly developed sufficient matrix strength to arrest the settling of some sand particles, and ultimately the development and deposition of an upper sandy mud layer — features and textures resembling those in BF. Further along the BF part of the depositional transect, the continued depletion of coarse sediment settling from the basal sandy layer resulted in a progressive thinning and then pinch-out of the basal sand-rich layer with

negligible increase in the matrix content. As the basal layer thinned, the upper layer progressively thickened and became more mud-rich but at a diminishing rate with distance along the continuum (see Ningthoujam et al., 2022, fig. 10). Following the termination of the basal sandy layer, the now exclusively mud-rich flow deposited sandy mudstone (SM), that then gradually thinned and pinched out over several tens of meters (Fig. 4.22). At all times, this collapsing suspension was overlain by a low-density turbidity current that reworked the top of the underlying deposit and formed the capping thin-bedded, upper division, very fine-grained sandstone turbidite overlain by silty mudstone formed by gelling of a near-bed fluid-mud layer (Fig. 4.22).

Although the lithofacies and dimensional details of the components that make up the depositional continuum are similar in both the Windermere Supergroup and the Cloridorme Formation, differences in the character of the interface that separates the two parts in a bipartite facies are noted. In the Windermere the BF interface is exclusively planar, whereas in the Cloridorme the interface is mostly planar, but often exhibits an alternation between planar and irregular characterized by cm-scale synforms and antiforms with local overhangs and injections of sand from the sand-rich basal part (Ningthoujam et al., 2022) (Fig. 4.20B). According to these authors irregular segments along the interface were not a primary feature, but instead the result of post-depositional deformation of an otherwise planar interface. More specifically, following deposition the upward movement of pore fluids due to bed consolidation became restricted along the BF interface because of the abrupt few tens of percent increase in mud content in the upper layer. Local overpressure conditions and reduced bulk density at the top of the underlying sand-rich layer caused the upper mud-rich layer to founder, which in some cases resulted in sand from the underlying layer to inject upward into the base of the mud-rich layer. Additionally, Ningthoujam et al. (2022) suggested that post-depositional liquefaction and/or fluidization and

deformation of the interface might also be more common in tectonically active basins (Cloridorme Formation) rather than passive margin settings (Windermere Supergroup), but possibly also in basins where smectite and/or illite rather than kaolinite make up a significant part of the clay-size sediment fraction.

4.7 A CRITICAL PERSPECTIVE

The description, classification, and origin of deep-marine matrix-rich (> 10% detrital mud matrix) strata have been debated since the 18th century when the term greywacke was introduced into the geological literature. Sedimentologists have generally attempted to either define them based on their texture and/or composition, or the origin of their matrix (detrital vs. diagenetic). However, in the last two decades, a variety of matrix-rich strata that are unlike classical turbidites and debrites have been widely recognized in the deep- and less commonly in shallow-marine sediments and sedimentary rocks. Importantly, due to their high mud-content, these matrix-rich strata have been reported to exhibit poor reservoir quality, and therefore are of concern in deep-water reservoirs (e.g., Lowe et al., 2003; Haughton et al., 2003; Kane and Pontén, 2012), necessitating a better understanding of their depositional origin and spatial distribution. Distinctively, these strata are made up of two parts—a lower sandy part and an upper muddy part, but uncommonly, an intervening cm- to m-thick banded unit comprising light (mud-poor) and dark (mud-rich) bands is present (e.g., Barker et al., 2008; Haughton et al., 2009; Southern et al., 2017). Collectively, these strata have been variously termed slurry beds (Lowe and Guy, 2000), linked debrites (Haughton et al., 2003), co-genetic debrite turbidite beds (Talling et al., 2004), hybrid event beds (Haughton et al. 2009), transitional flow deposits (Kane and Pontén, 2012) and bipartite facies of matrix-rich

sandstones (Terlaky and Arnott, 2014). Furthermore, these strata are reported to develop downflow of clean (i.e., less muddy) sands over distances of hundreds meters (e.g., Terlaky and Arnott, 2014; Angus et al., 2019; Ningthoujam et al., 2022) to few kilometers (e.g., Lowe et al., 2003; Haughton et al., 2003; Fonnesu et al., 2018), to tens of kilometers (e.g., Davies et al., 2009; Talling et al., 2012a, 2012b, 2013) (see Table 4.1). In all cases, deposition of the composite strata are interpreted to be genetically related but explained by very different physical mechanisms including slurry flows that are an intermediate flow type between non-cohesive turbidity currents and cohesive debris flows (Lowe and Guy 2000); longitudinal partitioning of a mud-enriched sediment suspension into a forerunning turbidity current and a trailing debris flow (Haughton et al., 2003, 2009); a forerunning turbidity current spawned from mixing along the upper surface of a debris flow (Talling et al., 2004; Talling et al., 2012a); longitudinal flow transformation from turbulent to transitional to laminar flow regime (Kane and Pontén, 2012); vertical stratification effects and turbulence suppression in a high-concentration suspension (Talling, 2013; Kane et al., 2017); and particle settling in a negligibly sheared mixed sand–mud suspension (Angus et al., 2019) (see Table 4.1). This wide diversity in interpretation can be attributed to some the following reasons.

MODEL	NOTABLE STUDIES	DATA SOURCE	MATRIX (SILT & CLAY) CONTENT	GRAIN SIZE	DOWNFLOW LENGTH OF DEPOSIT	DOWNFLOW LENGTH OF COMPONENT LITHOFACIES	ENVIRONMENT OF DEPOSITION
Slurry flows that are an intermediate flow type between non-cohesive turbidity currents and cohesive debris flows	Lowe and Guy, 2000, 2003; Barker et al., 2008	Correlation of subsurface cores	Clean sandstone: < 10% Slurry flow deposits: 10-35%	fine to very coarse sand	Several kilometers	?	Basin plain
Longitudinal partitioning of mud-enirched sediment suspension into a forerunning turbididty current and a trailing debris flow	Haughton et al., 2003, 2009; Jackson et al., 2009; Hodgson, 2009; Davis et al., 2009; Pierce et al., 2018; Hussain et al., 2020	Correlation of subsurface cores or isolated outcrops	Clean sandstone (H1): ≤ 25% Argillaceous sandstone (H3): 10-70%	fine to very coarse sand	Several kilometers to tens of kilometers	?	Typically in basin-floor sheet systems and along the fringe of mid-to outer-submarine fan lobes. Less common along the fringe of proximal fan lobes, channel-lobe transition zone, marginal marine delta front setting.
	Patacci et al., 2014; Fonnesu et al., 2015, 2016, 2018	Continuously tracing individual beds and correlating beds with similar character in outcrop			Several hundreds of meters to < 2 kilometers		
Forerunning turbidity current spawned from mixing along the upper surface of a debris flow	Talling et al., 2004, 2007, 2012a, 2012b; Amy and Talling, 2005; Hodgson, 2009; Talling, 2013	Correlation of subsurface cores, isolated outcrops, or modern seabed cores	Clean sandstone (H1): ≤ 25% Argillaceous sandstone (H3): 10-60%	fine to very coarse sand	Several kilometers to tens of kilometers	?	Basin-floor sheet systems and along the fringe of mid- to outer-submarine fan lobes.
Vertical stratification effects and turbulence suppression in a high concentration mud-eniched sediment suspension	Talling et al., 2004; Talling 2013; Kane et al., 2017; Spychala et al., 2017a; Baas et al., 2021	Correlation of subsurface cores, isolated outcrops, or modern seabed cores	Clean sandstone (H1): ≤ 25% Argillaceous sandstone (H3): 10-60%	fine to very coarse sand	Several kilometers to tens of kilometers	?	Basin-floor sheet systems, along the fringe of mid- to outer-submarine fan lobes, channel-lobe transition zone.
Longitudinal flow transformation from turbulent to transitional to laminar flow regime (Baas et al., 2009)	Kane and Pontén, 2012; Baker and Baas, 2020	Interpretation of downflow facies transformation based on Walther's Law in subsurface cores, or changes in facies distribution in isolated outcrops	?	silt to fine sand	Several kilometers to tens of kilometers	?	Submarine fan fringe
Particle settling in a negligibly sheared mixed sand-mud suspension	Terlaky and Arnott, 2014, 2016; Angus et al., 2019; Ningthoujam et al., 2022	Continuously tracing individual beds in outcrop	Matrix-poor sandstone: < 20% Muddy sandstone: 20-50% Bipartite facies: 25-60% (lower part), 40-80% (upper part) Sandy mudstone: 50-90%	very fine to very coarse sand	Several hundreds of meters to < 2 kilometers	Matrix-poor sandstone: ~ 41-55% of downflow length. Muddy sandstone: ~ 13-20% of downflow length. Bipartite facies: ~ 14-20% of downflow length. Sandy mudstone: ~ 18-19% of downflow length.	Continental slope to distal-basin floor settings

Table 4.1: Summary of main theoretical models and key attributes.

- Generally, much of the current geological literature is based on regional scale correlations between subsurface cores and isolated outcrops spaced kilometers to tens of kilometers apart (see Table 4.1). However, in the few cases where individual beds have been traced continuously in outcrop, lithofacies changes that collectively form a depositional continuum are reported to take place over horizontal distances of tens to hundreds of meters (see Hodgson, 2009; Patacci et al., 2014; Terlaky and Arnott, 2014; Fonnesu et al., 2015, 2018; Spychala et al., 2017a; Angus et al., 2019; Ningthoujam et al., 2022) (Table 4.1). This significant difference in horizontal scale is at the very least a cause for some consideration, especially where changes take place over short (tens to hundreds meters) distances — can some of the reported depositional mechanisms operate to completion over such limited spatial scales? Moreover, when normalized to the total length of the depositional continuum, Ningthoujam et al. (2022) show that in a number of different depositional settings the horizontal length scale of the various lithofacies changes is proportionate. This suggests commonality in depositional process that seemingly operates on a variety of different, but significantly proportionate spatial scales, but notably results in similar thickness, textural and sedimentary structure characteristics in the deposit.
- To-date, most experimental investigations forming two-part deposits (i.e., mud-poor overlain by mud-rich) have been conducted using sediment-laden open channel flows (e.g., Baas and Best, 2002; Baas et al., 2009, 2011, 2016a, 2016b; Sumner et al., 2009), which differ in their velocity and concentration profiles compared to sediment gravity flows, namely turbidity currents (e.g., Tilston et al., 2015; Arnott et al., 2021). Nonetheless, two-part deposits have been generated in the few experimental investigations conducted with mud-enriched sediment gravity flows (see Perillo et al., 2015; Hermidas et al., 2018; Koo

et al., 2019), but significantly the reported depositional origin of a two-part bed differs markedly. In question, therefore, are the results from these two very different flow types in relation to the origin of two-part beds. Also, in the case of sediment gravity flows, experiments have yet to explore the effects of many potentially important sedimentological parameters, including, grain size, grain size distribution, grain sorting, and clay mineralogy on the transport and deposition from mud-enriched flows.

- The majority of deep-marine matrix-rich strata, with only few exceptions (Lowe and Guy, 2000; Barker et al., 2009; Davies et al., 2009; Haughton et al., 2009; Hodgson, 2009; Southern et al., 2017; Pierce et al., 2018), lack banding (i.e., repeated alternation of mud-poor and mud-rich bands), and instead are composed of two parts—a lower sandy part overlain sharply by a muddy part. Accordingly, our understanding of the factor(s) that promote, or more commonly prevent the development of banding is lacking and requires further investigation.

- Although the presence of mud and its influence on flow behaviour is common in all the postulated depositional models, several models have been proposed for the source of mud including present at the inception of the sediment gravity flow (e.g., Talling et al., 2012a, 2012b, 2013; Talling, 2013); incorporation of muddy sediment into an initially non-cohesive flow by up-flow erosion of the seafloor (e.g., Haughton et al., 2003, 2009; Kane and Pontén, 2012; Kane et al., 2017; Baas et al., 2021); and muddy sediment being incorporated into an originally non-cohesive flow by local erosion of the seafloor (e.g., Terlaky and Arnott, 2014; Fonnesu et al., 2016; Mueller et al., 2017; Angus et al., 2019). This lack of consensus on the source of mud has also been a contributing factor for the

variable interpretations of these matrix-rich strata, and as such requires further investigation.

- As stated in the Oxford English Dictionary, "hybrid" is defined as "something that is a product of mixing two or more different things", for example a hybrid automobile having gasoline and electrically sourced propulsion. In the context of matrix-rich deposits, strata identified as hybrid event beds were initially interpreted to be formed by hybrid flows consisting of at least two discrete and mechanistically different parts, namely a turbidity current, depositing a basal turbidite, and a debris flow forming the overlying debrite (e.g., Haughton et al., 2009). However, more recently, this term has been ubiquitously but loosely applied to composite sand–mud strata interpreted to be formed by more than one physical mechanism depositing a single event bed (e.g., Kane and Pontén, 2012; Baas et al., 2011; Talling, 2013; Kane et al., 2017; Spychala et al., 2017a; Southern et al., 2017). Accordingly, the interchangeable use of the term hybrid event bed to define other matrix-rich deposits has added some confusion to the interpretation of these matrix-rich strata. Additionally, similar two-part deposits consisting of a sand-rich overlain by mud-rich part (Terlaky and Arnott, 2014; Angus et al., 2019; Ningthoujam et al., 2022) have been attributed to a single depositional mechanism, specifically particle settling in a negligibly sheared mud-silt-rich suspension depositing a proportionately consistent depositional continuum. Notably also, texturally similar two-part deposits were formed by particle settling in experimental sediment gravity flows (Perillo et al., 2015; Koo et al., 2019) suggesting that beds consisting of two lithologically distinct parts does not necessitate "hybrid" depositional conditions. Such profound mechanistic differences point to the need of a better understanding of these strata, namely are two-part beds necessarily the product

of mixing two or more different depositional mechanisms, or instead two parts formed by a single mechanism?

- The majority of terminologies used to define matrix-rich strata are interpretive and mechanistically derived (e.g., slurry beds – slurry flows; transitional flow deposits – transitional flows; hybrid event beds – hybrid flows; co-genetic debrite-turbidite – forerunning turbidity current followed by trailing debris flow), which then biases objective evaluation and interpretation of these strata. One possible solution is to descriptively define these strata based on their macro- and microscopic characteristics (e.g., matrix-rich sandstone *sensu* Terlaky and Arnott, 2014).

CHAPTER 5: SYSTEMATIC VERTICAL ORGANIZATION OF MATRIX-RICH AND ASSOCIATED MATRIX-POOR SANDSTONES IN ANCIENT DEEP-MARINE SLOPE AND BASIN-FLOOR DEPOSITS

5.1 INTRODUCTION

Deep-marine matrix-rich (>20% clay and silt content) strata that are unlike classical turbidites (sensu Bouma, 1962; Lowe, 1982) or debrites have been increasingly recognized in both modern and ancient turbidite systems (e.g., Lowe and Guy, 2000; Haughton et al., 2003, 2009; Talling, 2013; Hodgson, 2009; Kane and Pontén, 2012; Terlaky and Arnott, 2014). Termed slurry beds (Lowe and Guy, 2000), linked debrites (Haughton et al., 2003), co-genetic debrite-turbidite beds (Talling et al., 2004), hybrid event beds (Haughton et al., 2009), transitional flow deposits (Kane and Pontén, 2012) and bipartite facies (Angus et al., 2019), these strata typically consist of a sandy basal part overlain sharply by a muddier, mud-clast-bearing upper part, with the contact being either planar, less commonly irregular, or rarely gradational and marked by an intervening unit of alternating light (mud-poor) and dark (mud-rich) colored bands. Additionally, these composite strata are reported to occur downflow of clean (i.e., less mud-rich) sand and upflow of argillaceous (i.e. mud-rich) sand over distances of 100s m to 10s kms in what has been interpreted to be an along-flow proximal to distal depositional continuum (e.g., Fonnesu et al., 2015; Kane et al., 2017; Pierce et al., 2018; Angus et al., 2019; Ningthoujam et al., 2022). The central focus of these studies has been aimed largely at understanding either the physical origin of the composite strata at the individual bed scale (e.g., Haughton et al., 2009; Davis et al., 2009; Baas et al., 2011; Talling, 2013; Fonnesu et al., 2015; Angus et al., 2019), or their stratigraphic and geographic distribution at the stratal element scale (several meters-thick stratal package comprising two or

more event beds, and in which > 50% of the beds are composed of a single sedimentary facies) (e.g., Haughton et al., 2009; Kane and Pontén, 2012; Patacci et al., 2016; Terlaky and Arnott, 2016; Kane et al., 2017; Spychala et al., 2017b). Lacking, however, is a discussion of how these beds stack vertically, and therein how the sedimentological conditions that deposited them changed in time. Accordingly, this study describes the vertical stacking character and spatial pattern of matrix-rich and associated matrix-poor lithologies observed at the bed and stratal unit scales in slope and proximal basin-floor deposits of the Neoproterozoic Windermere turbidite system and distal basin-floor deposits of the Ordovician Cloridorme Formation. Stacking patterns derived from field-based observations are then evaluated using a first-order Markov chain (e.g., Krumbein 1968; Carr, 1982; Davis, 1986) to quantitatively determine any systematic stacking arrangement, and if so, identify possible physical drivers responsible for the pattern. This statistical technique has previously been applied to describe and interpret deep-marine matrix-rich strata at either the individual bed scale (e.g., Lowe and Guy, 2000; Haughton et al., 2003; Davis et al., 2009) or at the stratal element scale (e.g., Kane and Pontén, 2012; Terlaky and Arnott, 2016), however, in this study Markov-chain analysis is carried out to assess the stacking patterns of beds and stratal units of matrix-rich and associated matrix-poor lithologies, and therein attempts to address the gap in understanding that remains between the deposition of an individual bed and a stratal element.

5.2 GEOLOGICAL BACKGROUND

5.2.1 Windermere Supergroup

The Neoproterozoic (740-570 Ma) Windermere Supergroup (WSG) is an unconformity-bounded succession of mostly metasedimentary rocks deposited on the passive

continental margin of Laurentia (ancestral North America) during the break-up of the Rodinia supercontinent (Stewart, 1972; Ross and Arnott, 2007; McMechan, 2015). The outcrop belt of the WSG stretches from northwestern Mexico through the western United States and Canada and northward to the Yukon-Alaska border (Ross and Arnott, 2007) (Fig. 5.1A). In the southern Canadian Cordillera, the basal rift sequence includes a few-km-thick assemblage of intercalated glacial diamictites and mafic volcanic rocks of the Toby and Irene formations, respectively (Aalto, 1971; Ross et al., 1995; Warren, 1997). This is then overlain by a 5 – 7 km-thick post-rift, upward-shoaling succession composed of deep-marine basin floor (Kaza Group) followed by continental slope (Isaac Formation) to upper continental slope and shelf (Cunningham and Yankee Belle formations, respectively) deposits (Campbell et al., 1973).

Deep-marine strata of the WSG basin (Fig. 5.1B), termed the Windermere turbidite system, are well exposed throughout the southern Canadian Cordillera (Fig. 5.1A). At the Castle Creek study area (Fig. 5.1D), vertically dipping, recently deglaciated, vegetation-free strata of the Upper Kaza Group and Isaac Formation form an outcrop belt that is approximately 2.6 km thick and 8 km wide (Terlaky et al., 2016; Navarro and Arnott, 2020). Here, field observations of beds and bedsets can be carried out over distances of 10s of meters vertically, but more significantly, 100s of meters along the strike of the outcrop. However, due to the two-dimensionality of the outcrop paleoflow data are limited to a small number of well-exposed 3D current ripples and dune cross-stratified sets, and a small number of flute marks, which collectively indicate a general transport direction ranging from west-northwest to northeast (see Ross and Arnott, 2007; Schwarz and Arnott, 2007; Khan and Arnott, 2011; Navarro and Arnott, 2020), and therefore subparallel to the regional paleoflow direction (e.g., Mountjoy and Aitken, 1963).

Furthermore, rocks in the study area have undergone low-grade (greenschist facies) metamorphism, resulting in the alteration of primary clay matrix to muscovite and chlorite and strain-induced structures like bulging recrystallization and sub-grain rotation along some grain boundaries. Despite these changes, primary sedimentary structures and most sedimentary textures, namely grain size, grain shape and sorting are well preserved, enabling these rocks to be described and classified as sedimentary rocks (Ross and Arnott, 2007; Ningthoujam et al., 2022).

5.2.2 Cloridorme Formation

The Middle Ordovician (460 – 445 Ma) Cloridorme Formation (CF) comprises the Quebec segment of a succession of turbidite systems that were deposited along an elongate foreland basin located between cratonic North America to the northwest and the developing Taconic orogen and its associated volcanic arcs to the southeast (St-Julien and Hubert, 1975; Hiscott et al., 1986). The basin extended from Newfoundland to Tennessee and was up to 150 km wide (Hiscott, 1984). The CF is exposed semi-continuously for ~ 150 km along the north shore of the Gaspé Peninsula, Quebec, Canada (Fig. 5.1A). The CF is at least 4 km thick and based on lithofacies and extensive marker beds (megaturbidites), is divided from oldest to youngest, into five members: St-Hélier Member composed of distal basin-floor mudstones; Pointe-à-la-Frégate and Petite-Vallée members consisting of sandstone-rich lobe and mudstone-rich inter-lobe deposits; Mont-Saint Pierre Member made up of distal basin-floor mudstones; and Marsoui Member made up of sand lobes and inter-lobe deposits (Hiscott et al., 1986) (Fig. 5.1C). This study focuses on strata of the Petite-Vallée Member located near the village of Petite Vallée, Quebec (Fig. 5.1E). Here, strata are nearly vertically dipping (average 78°) and east-to-west (271°) striking and exposed along an intertidal wave cut platform that allowed for field observations of beds and bedsets to be carried

out over 10s meters vertically, but also 10s – 100s meters along the strike of the outcrop. In the study area, average paleocurrent based on base-of-bed tool and flute marks and troughs of three-dimensional current ripples is 272° (n = 102), and therefore sub-parallel to the strike of the outcrop, which is consistent with previous studies in other parts of the CF (Awadallah, 2002; Parkash and Middleton, 1970; Pickering and Hiscott, 1985). Rocks in the study area have experienced very low-grade (zeolite to prehnite-pumpellyite facies) metamorphism associated with the Taconic Orogeny and resulted in the alteration of primary clay minerals to illite and chlorite (Jiang and Peacor, 1994). Despite this change, primary sedimentary structures and textures are well preserved, allowing these strata to be described and classified using conventional sedimentary terminology (Ningthoujam et al. 2022).

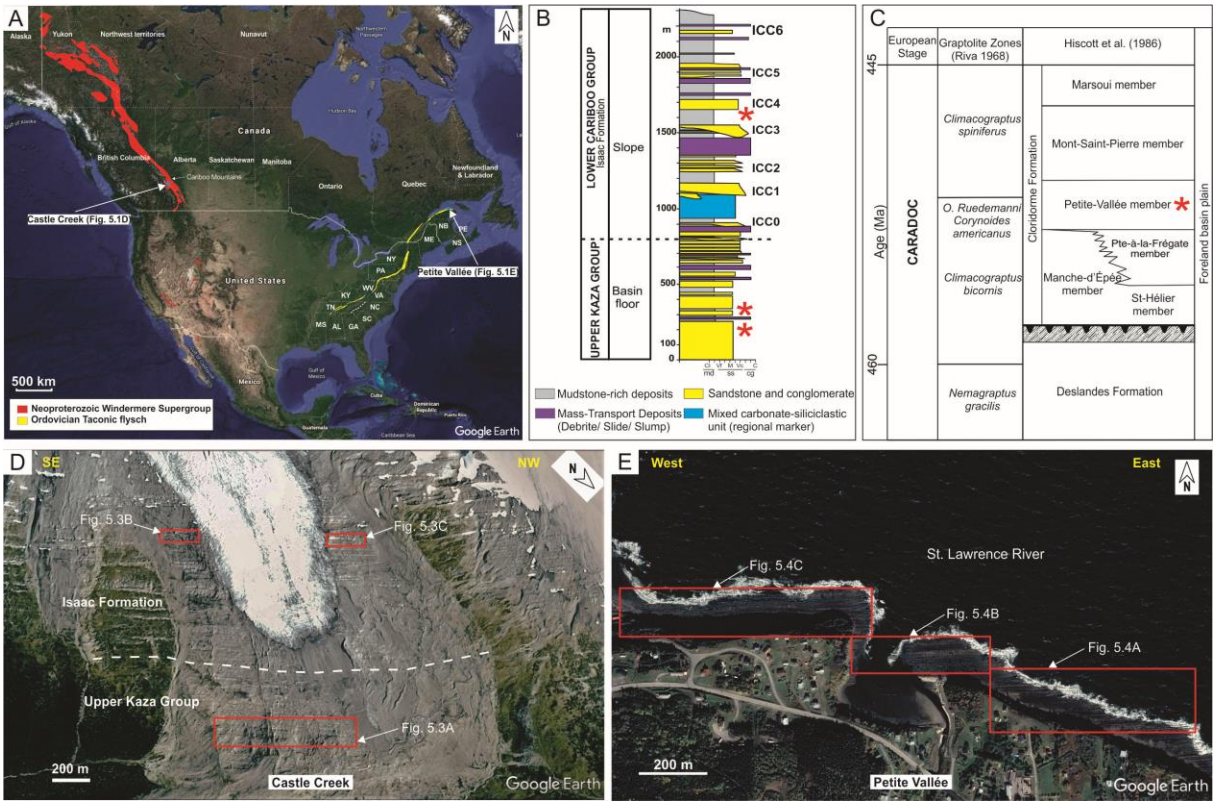

Figure 5.1: A) Map of North America showing the distribution of Windermere Supergroup (red) and Ordovician Taconic flysch (yellow) rocks. Study areas (Castle Creek and Petite Vallée) are indicated by blue squares (satellite image from Google Earth, 2020). B) Windermere stratigraphy at the Castle Creek study area. Here basin floor strata of the Upper Kaza Group are conformably overlain by continental slope deposits of the Isaac Formation. Informal names for Isaac slope channel complexes are numbered from ICC0 to ICC6. Location of the study intervals are indicated by the red stars. C) Stratigraphy of the Middle Ordovician Cloridorme and Deslandes formations in southeastern Quebec. Red star indicates the location of the interval described in this study. D) The Castle Creek study area in the Cariboo Mountains, east central British Columbia, Canada (satellite image from Google Earth, 2020). Note that strata are vertically dipping and recently deglaciated. Red rectangles indicate the study intervals. E) Overview of the study area located in the village of Petite Vallée, Quebec, Canada (satellite image from Google Earth, 2020). Strata are exposed along a broad wave-cut platform and are overturned, dipping south at 65°– 88°. Study intervals are indicated by the red rectangles (after Ningthoujam et al., 2022).

5.3 PREVIOUS WORK – ALONG STRIKE FACIES CHANGES

In slope and proximal basin-floor deposits of the WSG, and distal basin-floor deposits of the CF, four main lithofacies linked with matrix-rich and associated matrix-poor strata were recognized (Terlaky and Arnott, 2014; Angus et al., 2019; Ningthoujam et al., 2022). Based on matrix content, the four lithofacies are: matrix-poor sandstone (MPS) with 0 – 20% matrix content, muddy sandstone (MS) with 20 – 50% matrix content, bipartite facies (BF) with a basal sandy (30 – 60% matrix) part overlain sharply by a planar- to irregular-based muddier upper part (40 – 80% matrix), and sandy mudstone (SM) with 50 – 90% matrix content (Fig. 5.2). All four facies are structureless (i.e., lack tractional sedimentary structures), massive or coarse-tail graded, and composed of rounded to angular, equant to elongate framework grains that range from very fine to very coarse sand. Mud and lesser very fine to medium-grained sandstone clasts are also common. Clasts are typically elongate, sub-angular to sub-rounded and oriented with their maximum projection plane subparallel to bedding. Where present, these strata are then capped by lamina to thin-beds of traction-structured sandstone overlain by silty mudstone.

Tracing of individual beds along the strike of the outcrop in the WSG (Terlaky and Arnott, 2014; Angus et al., 2019; Wearmouth, 2018; Ningthoujam et al., 2022) and CF (Ningthoujam et al., 2022) reveals a systematic arrangement of lithofacies, namely, MPS to MS to BF and then to

SM, each overlain, except where eroded, by a laminated to thin-bedded, traction-structured sandstone and silty mudstone (Fig. 5.2). More specifically, thick-bedded MPS gradually transforms to medium- to thick-bedded MS, which then develops into medium-bedded two-part, bipartite facies (BF) consisting of a basal muddy sandstone overlain sharply by an upper sandy mudstone commonly containing dispersed mud clasts. Further along the transect, the basal part of BF progressively thins and then pinches out, whereas the upper part thickens, but at a diminishing rate. Further laterally, following the termination of the basal sandy part of BF, the now exclusively sandy mudstone (SM) thins to a pinch-out (Fig. 5.2).

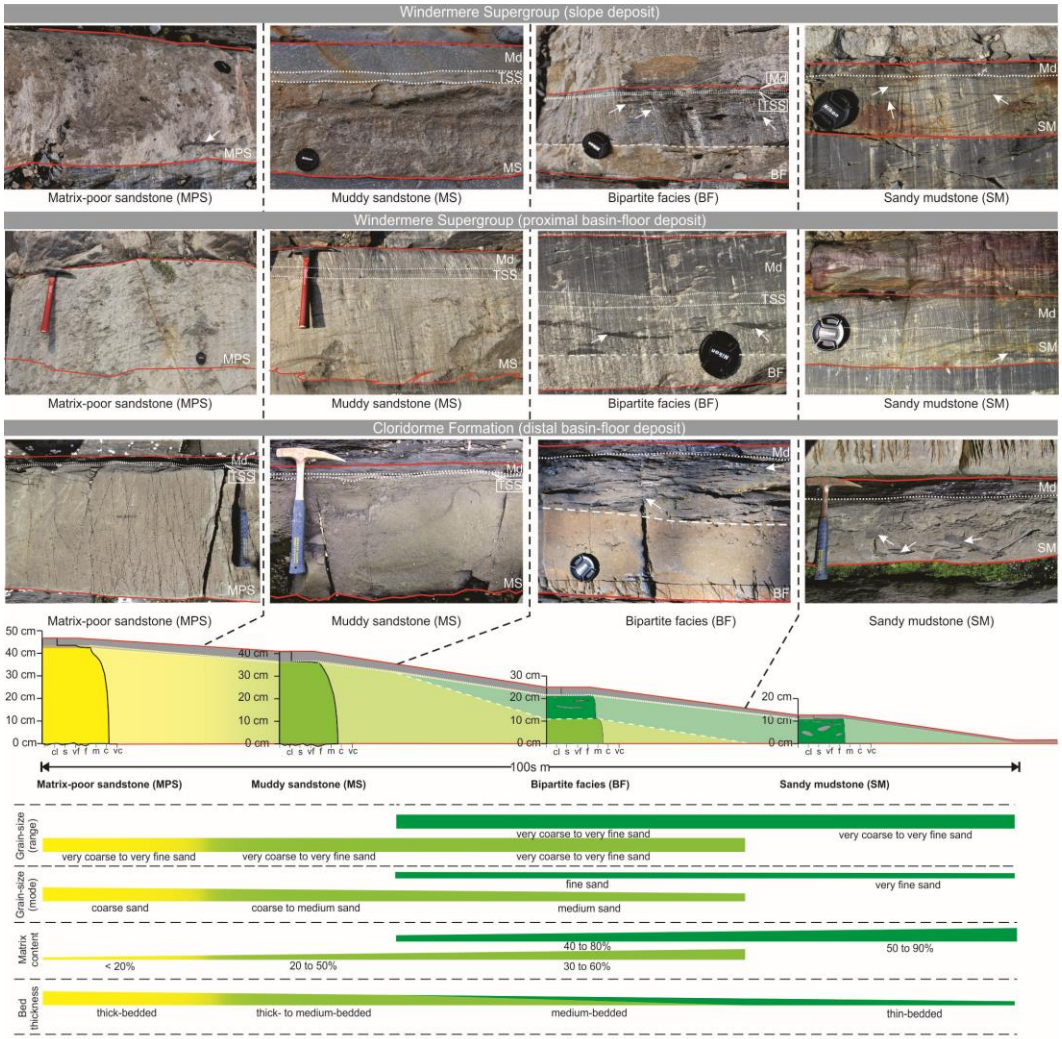

Figure 5.2: Schematic illustrating the idealized proximal to distal (left to right) depositional transect from matrix-poor sandstone (MPS) to muddy sandstone (MS) to bipartite facies (BF) to sandy mudstone (SM) over a distance of 100s meters. Except where eroded, the transect is overlain by a thin-bedded traction structured sandstone (TSS)capped by silty mudstone (Md). See Ningthoujam et al. (2022) for descriptive details. Representative photographs of each lithofacies from the Windermere and Cloridorme are shown above the transect. Solid red lines mark the base and top of a single bed; white arrows point to mudstone clasts; dashed white lines separate the lower and upper parts of a bipartite facies (BF); dotted white lines mark the bases of the traction-structured, very fine-grained sandstone and/or mudstone cap. Scales are hammer (33 cm long) and camera lens cap (5.2 cm diameter). Bar graphs illustrate the general downflow trends in texture (grain size range, modal grain size, and matrix content) and bed thickness (see Ningthoujam et al., 2022 for details).

Importantly, these changes occurred over a horizontal distance of a few hundreds of meters and were interpreted to reflect a downflow (proximal to distal) depositional continuum, which in the WSG was interpreted to be oriented at a high angle to the main flow (Terlaky and Arnott, 2014; Angus et al., 2019; Wearmouth, 2018; Ningthoujam et al., 2022), but more or less parallel to the main flow in the CF (Ningthoujam et al., 2022). Significantly, regardless of the orientation of the depositional transect (parallel or at high angle) to the main flow, or depositional setting (continental slope versus proximal/distal basin-floor), the transitions from MS to BF, BF to SM and SM to its pinch-out were reported to be of proportionate length (Ningthoujam et al., 2022), and accordingly, suggest similarity in depositional process.

Based on field observations, matrix-rich and associated matrix-poor strata stack exclusively to form several meters to 10s of meters thick stratal elements that typically underlie sand-rich stratal elements such as slope channels, distributary channels and terminal splays in the continental slope to proximal basin floor settings of the WSG (Terlaky and Arnott, 2014; Terlaky et al., 2016; Angus et al., 2019; Ningthoujam et al., 2022) (e.g., Fig. 5.3) and sandy terminal splays in the distal basin floor setting of the CF (Ningthoujam et al., 2022) (e.g., Fig. 5.4). This stratigraphic relationship was attributed to avulsion and the stratal elements were identified as ‘avulsion splays’ (sensu Terlaky and Arnott, 2014). Avulsion formed high-energy, momentum-driven turbulent wall jets that eroded the mud-rich interchannel area and charged the flow with

fine-grained sediment, namely very fine sand to clay, in addition to low density mud clasts (Arnott, 2007; Terlaky and Arnott, 2014; Angus et al., 2019; Navarro and Arnott, 2020; Ningthoujam et al., 2022). The local incorporation of easily suspended fine-grained sediment resulted in an abrupt increase in local effective viscosity and a dramatic change in the characteristics and reduction in the diffusion of turbulence required to maintain the particle suspension. This caused the sediment suspension to rapidly exceed transport capacity and collapse, forming a negligibly sheared suspension that deposited a systematic along-flow depositional continuum consisting of matrix-poor sandstone (MPS) to muddy sandstone (MS) to bipartite facies (BF) and then sandy mudstone (SM) over distances of hundreds of meters. Following the emplacement of the depositional continuum from the collapsed suspension, a remnant low-density turbidity current reworked the top of the deposit and formed a thin-bedded, very fine-grained, upper division turbidite capped by a silty mudstone deposited by a gelled near-bed fluid-mud layer. In continental slope and proximal basin floor deposits of the WSG, the depositional transect developed along the margins of the high-energy wall jet, whereas in the distal basin-floor setting of the CF, deposition took place in the same direction as the main flow and formed a mouth bar that marks the downflow terminus of the flow (see discussion in Ningthoujam et al., 2022, and fig 17).

5.4 METHODS AND TERMINOLOGY

5.4.1 Methods

To better elucidate the stacking pattern of matrix-rich and associated matrix-poor strata, a combination of field-based observations and a statistical analysis were used. Field observations include stratal thickness, bedding contacts, grain size and sedimentary structures in each bed. Hand

samples of matrix-rich and matrix-poor lithologies were collected in the field and then analyzed using an optical petrographic microscope. Individual thin-sections were point counted (≥ 300 points per sample) to accurately describe textural characteristics and the longest dimension of each framework grain (grain size between 0.0625 mm and 6 mm) was measured to determine grain size distribution in each sample. Notably, all the petrographic work was conducted by a single operator to minimize operator bias and standardize potential error.

Based on earlier stratigraphic and depositional-framework studies at Castle Creek (WSG), select intervals containing matrix-rich and associated matrix-poor lithologies were chosen for this study. In proximal basin floor deposits of the Upper Kaza Group, a 100 m thick and 1000 m wide stratigraphic interval made up of a succession of terminal splays, distributary channel fill, debrite, thin-bedded turbidite and matrix-rich and associated matrix-poor strata mapped previously by Terlaky and Arnott (2014, 2016), Terlaky et al. (2016), Angus et al. (2019) and Ningthoujam et al. (2022), was selected. In this section, 61 stratigraphic logs (5 to 50 m long) were measured over a lateral distance of ~ 900 m targeting matrix-rich and associated matrix-poor strata (Fig. 5.3A). Similarly, in slope deposits of the stratigraphically higher Isaac Formation, two stratigraphic intervals (~ 80 m thick and 400 m wide, and ~ 120 m thick and 400 m wide) comprising sandy channel fills, thin-bedded turbidites, and matrix-rich and associated matrix-poor strata mapped previously by Arnott (2007a, 2007b), O'Byrne et al. (2007), Angus et al. (2019), Arnott et al. (2021), and Ningthoujam et al. (2022) were selected. Here, a total of 32 logs (3.5 to 30 m long) were measured in two transects targeting matrix-rich and associated matrix-poor strata (Fig. 5.3B, C). In distal basin-floor deposits of the Petite Vallée Member (CF), a ~ 300 m thick and 1700 m wide stratigraphic interval comprising terminal splays, thin-bedded turbidites and matrix-rich and associated matrix-poor strata mapped previously by Enos (1969), Beeden (1983), Hiscott et al.

(1986), and Ningthoujam et al. (2022) was selected. Here, 15 bed-by-bed stratigraphic logs (18 to 147 m long) were measured (Fig. 5.4). Also, in both the WSG and the CF, a few logs were extended upward to capture details of the overlying stratal element (Figs. 5.3 and 5.4). Additionally, hand samples of matrix-rich and associated matrix-poor lithologies were collected at both study sites, and a total of 253 standard (30 µm thick) thin sections were prepared for conventional petrographic analysis and point counting.

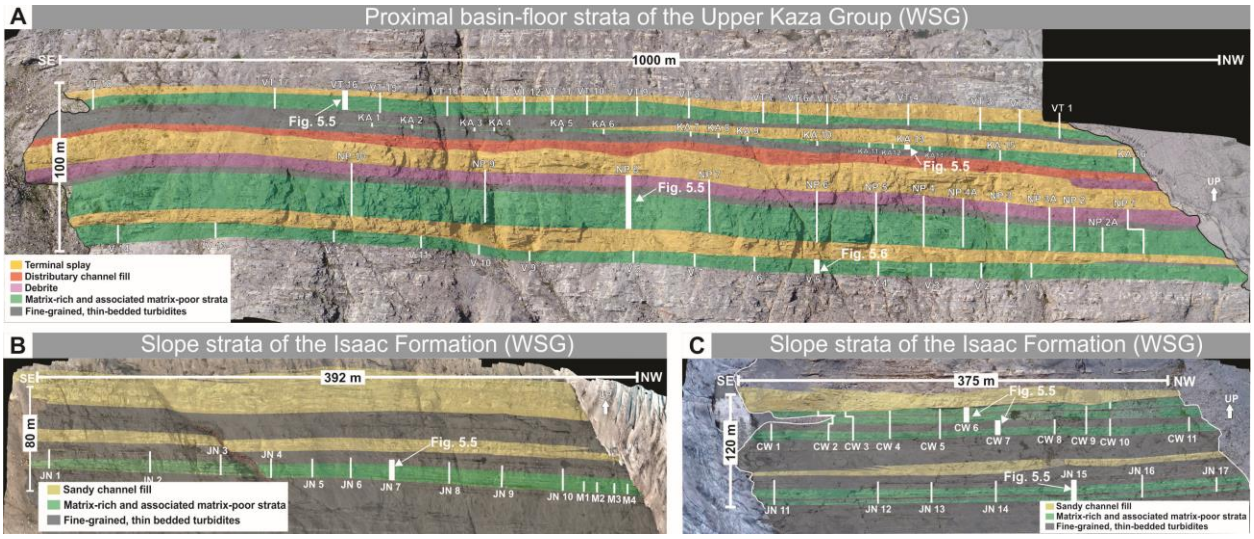

Figure 5.3: Interpreted drone photographs showing the distribution of stratal elements in (A) proximal basin-floor deposits of the Upper Kaza Group, and (B, C) slope deposits of the Isaac Formation at the Castle Creek study area. Labelled vertical white lines indicate the locations of the stratigraphic logs (after Ningthoujam et al., 2022).

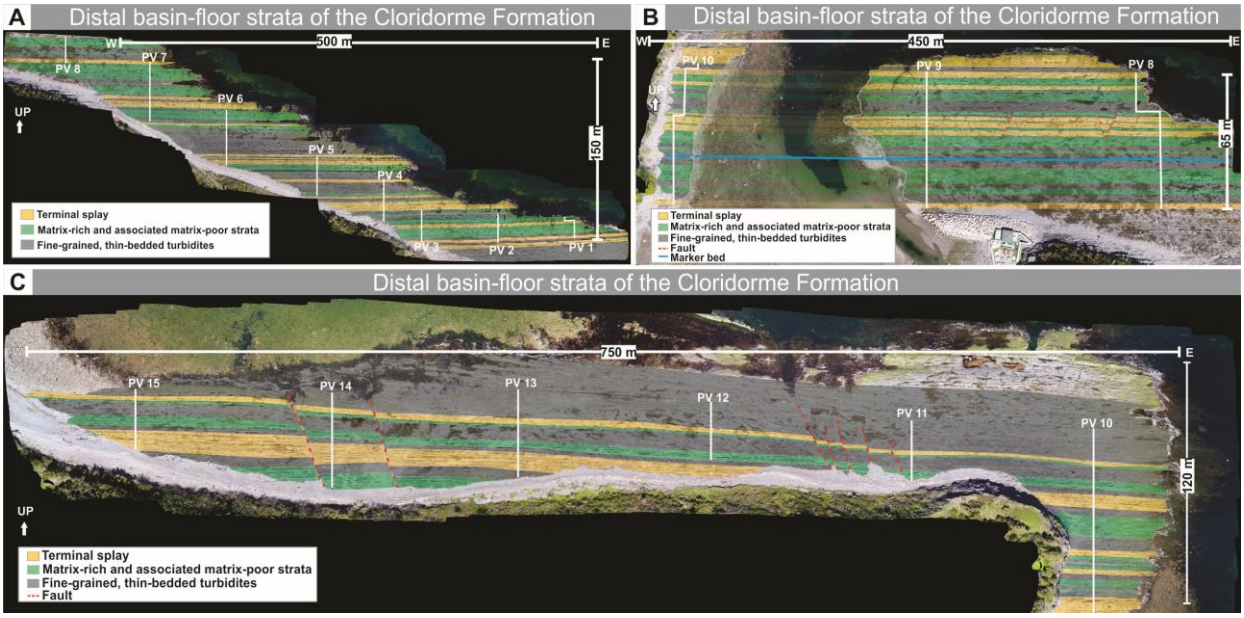

Figure 5.4: Interpreted drone photographs showing the distribution of stratal elements in distal basin-floor deposits of the Petite Vallée study area. Labelled white vertical lines indicate the locations of the stratigraphic logs (after Ningthoujam et al., 2022).

A first-order Markov chain analysis (e.g., Terlaky and Arnott, 2016) was conducted at bed and stratal unit scales to quantitatively assess how matrix-rich and associated matrix-poor strata stack to build-up a stratal element. This statistical technique describes sequential changes in a system composed of discrete, finite states (Krumbein, 1968; Schwarzacher, 1975). The change from one state to the next is considered a transition and is assumed to depend only on the state that precedes it; an assumption termed a first-order Markov property. Also, the system is considered to change randomly from one state to another based on the transition probabilities between states. Furthermore, the stratigraphic sections used in this statistical analysis are assumed to be deposited under static paleoenvironmental conditions with no changes due to external forcing (e.g., climate, tectonism, sediment supply) (e.g., Lehmann and Goldhammer, 1999; Terlaky and Arnott, 2016). Lastly, the vertical transition of states (i.e., from one bed to the next bed, or one stratal unit to the next stratal unit) observed in the stratigraphic sections assumes no erosion and that all states are fully preserved. In the WSG the input data was obtained from a composite stratigraphic log

consisting of all measured matrix-rich and associated matrix-poor strata in the Castle Creek study area. Here, individual logs with the most well-preserved stratigraphy were chosen from each section to build a single continuous 137 m-long stratigraphic section (Fig. 5.5). In the CF, on the other hand, data were derived from a single, vertically continuous stratigraphic log (287 m long) (Fig. 5.6). The observed vertical stacking of these strata was then used to construct the transition matrices, which then were tested against the expected transition matrices (zero-order Markov chain, or the null hypothesis) to evaluate statistical significance.

5.4.2 Terminology

In this study a stratigraphic hierarchy is recognized. At the most basic level, a "bed" consists of one of the four lithofacies recognized by Ningthoujam et al. (2022) namely, matrix-poor sandstone (MPS), muddy sandstone (MS), bipartite facies (BF), and sandy mudstone (SM), which, except where eroded, is then capped by a lamina (< 1cm) to thin-bed (< 10 cm) of traction-structured sandstone overlain by a silty mudstone. Each bed is then named by the principal lithofacies type (e.g., a bed with bipartite facies is called bipartite facies bed) (Fig. 5.7). Beds then stack to form "units", which consist of two or more beds of similar lithofacies type, or less commonly, as a single bed that is overlain and underlain by lithologically dissimilar strata (Fig. 5.7). Like individual beds, stratal units are named according to the principal lithofacies type (e.g., a stratal unit comprising bipartite facies is called a bipartite facies stratal unit). Stratal units then stack together to form a stratal "element", which being composed of matrix-rich and associated matrix-poor lithologies, is termed an "avulsion splay" (sensu Terlaky and Arnott, 2014) (Fig. 5.7).

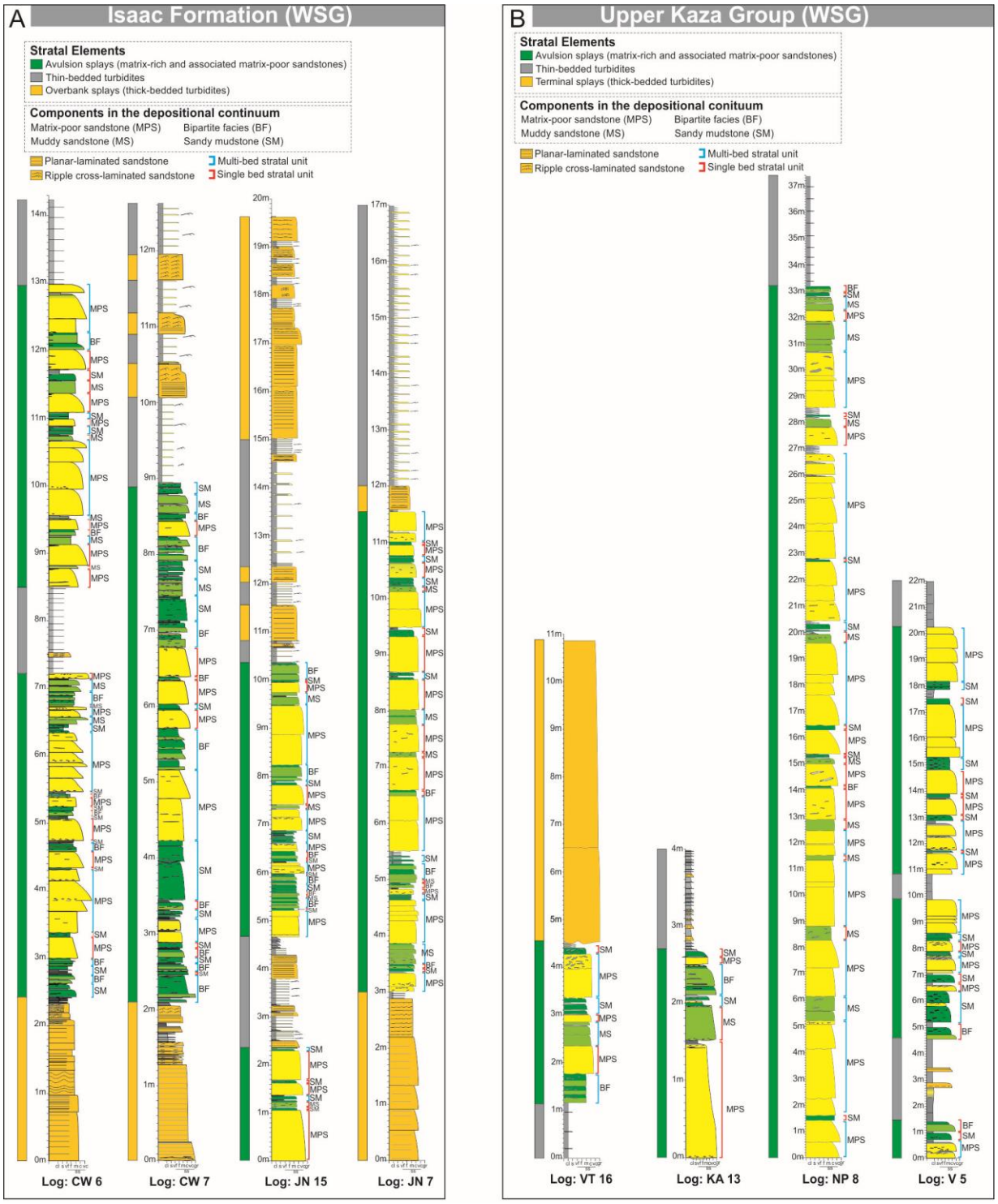

Figure 5.5: Individual stratigraphic logs used for Markov chain analysis from the Isaac Formation (A) and Upper Kaza Group (B) of the Windermere Supergroup. See Fig. 5.3 for location of individual logs. Matrix-rich and genetically related lithofacies are labelled on the right-hand side of each log. The remaining stratigraphy consists of different types of classical turbidites. Blue brackets indicate beds that are organized into multi-bed stratal units, whereas red brackets single bed stratal units. MPS – matrix-poor sandstone, MS – muddy sandstone, BF – bipartite facies and SM – sandy mudstone.

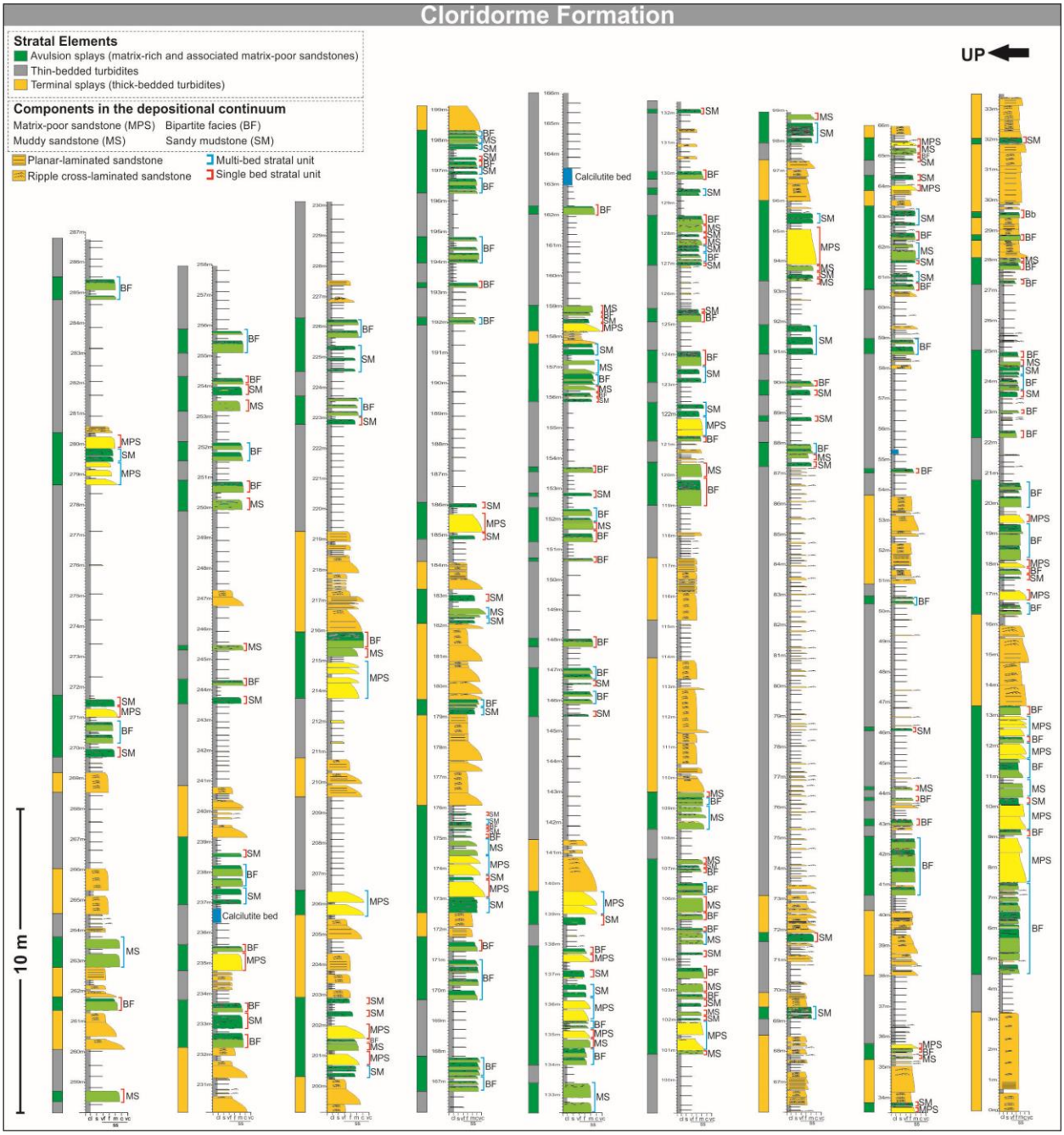

Figure 5.6: A continuous vertical stratigraphic log in the Petite Vallée study area. Matrix-rich and genetically related lithofacies are labelled on the right-hand side of each log. The remaining stratigraphy consists of different types of classical turbidites. Blue brackets indicate beds that are organized into into multi-bed stratal units, whereas red brackets single bed stratal units. MPS – matrix-poor sandstone, MS – muddy sandstone, BF – bipartite facies and SM – sandy mudstone.

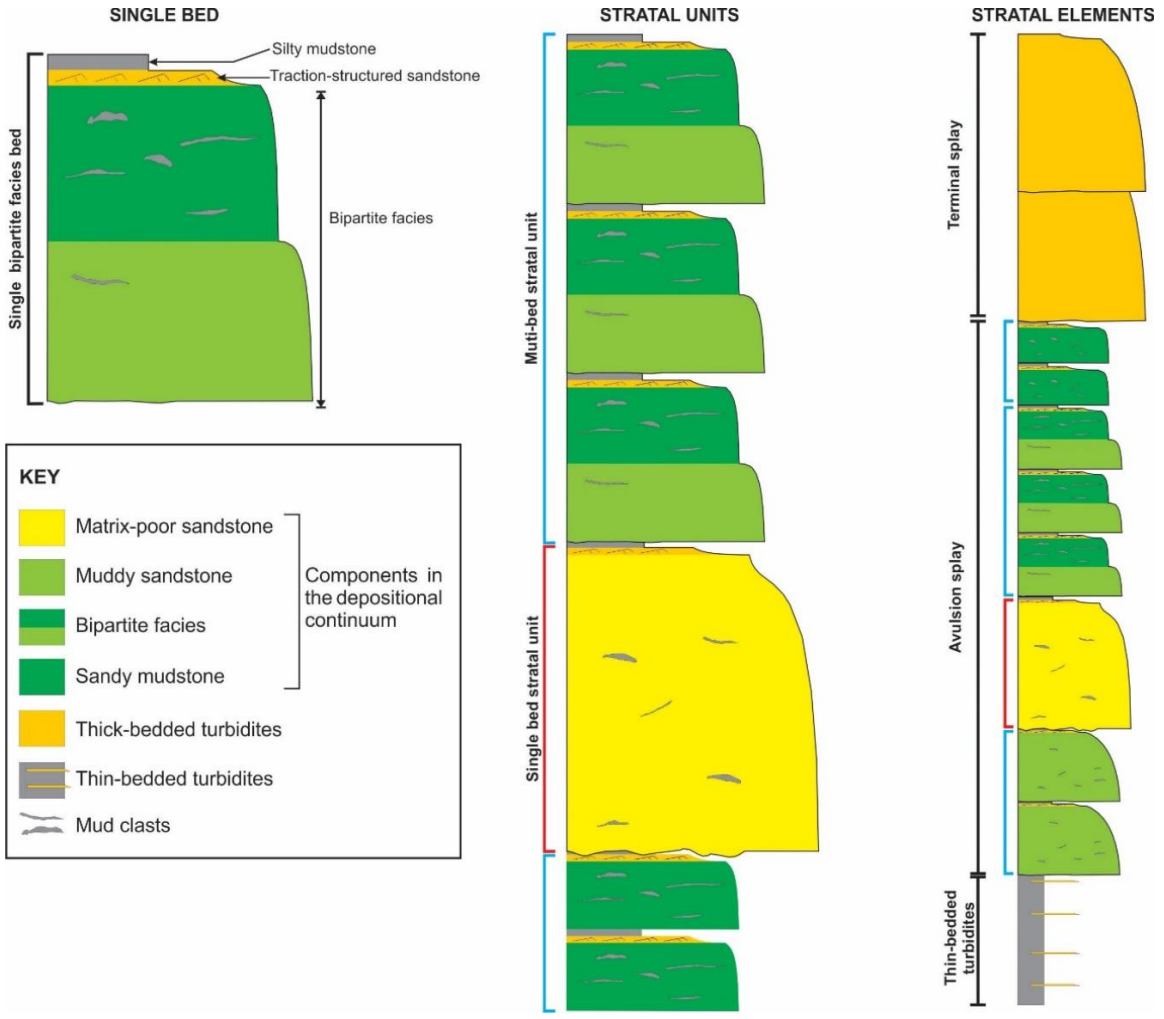

Figure 5.7: Schematic diagram showing the components of a single bed (left). A single bed, or more commonly multiple self-similar beds stack to form a stratal unit (center). Stratal unit boundaries are abrupt and marked by a change to a lithology deposited at a different position along the depositional continuum. Units comprising matrix-rich and associated matrix-poor strata then stack to form a stratal element, here termed an "avulsion splay" (sensu Terlaky and Arnott, 2014) (left).

5.5 RESULTS

5.5.1 Stacking pattern (bed scale)

Based on field observations in both study areas, beds of similar lithofacies, but of variable thickness, typically stack (70% of all measured beds in WSG and 65% in CF) to form multi-bed stratal units consisting of 2 – 9 beds (e.g., Figs. 5.5, 5.6). Less commonly (30% in WSG and 35%

in CF), the succession consists of single bed stratal units, which in some places stack, but are differentiated from turbidites or other single beds based on unique textural and dimensional attributes (e.g., Figs. 5.5, 5.6). Stratal unit boundaries are abrupt and typically marked by a change in lithofacies (Figs. 5.5, 5.6, 5.7). Beds within a multi-bed stratal unit undergo a transformation from one facies to the next in the lateral depositional continuum (see above; see also Fig. 5.8), for example MS to BF, BF to SM, at about the same lateral position (Fig. 5.8). Additionally, in the WSG, at any position along a multi-bed stratal unit, the D90 (coarse fraction) and D50 (median) of the grain size distribution, subtly and progressively decrease upward (Fig. 5.9). In the CF, on the other hand, grain size distribution shows a slight but nonetheless abrupt decrease, and only in the topmost bed in each multi-bed stratal unit (Fig. 5.10). In both study areas matrix content changes negligibly upward within a multi-bed stratal unit (e.g., Figs. 5.9 and 5.10).

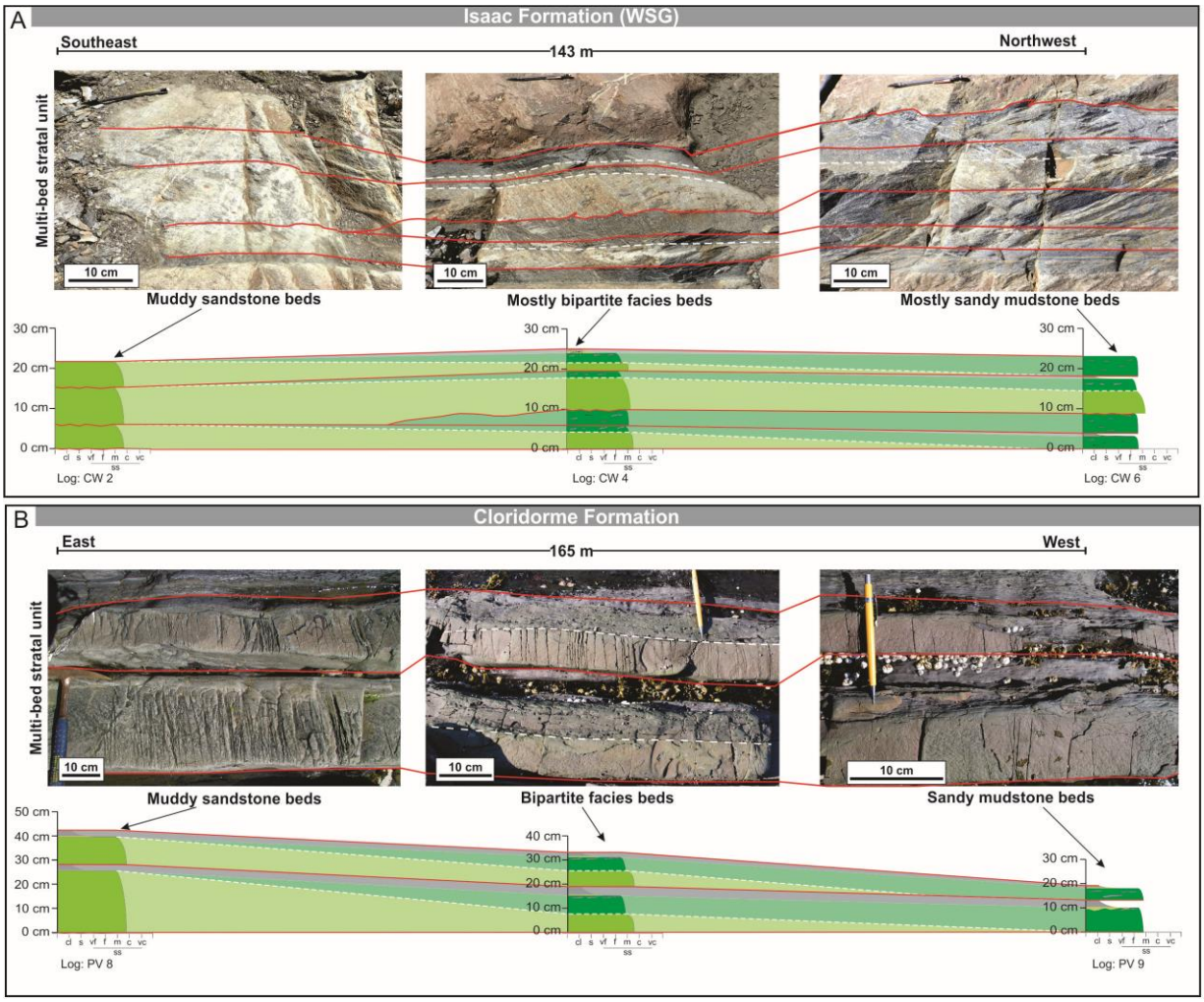

Figure 5.8: Stratigraphic correlation panel and associated outcrop photographs of a multi-bed stratal element in slope deposits of the Isaac Formation, Windermere Supergroup (A) and distal basin-floor deposits of the Petite Vallée Member, Cloridorme Formation (B) (see Figs. 3.11 and 3.13 for locations). Note how a stack of lithologically similar beds transitions from more proximal facies (left) to more distal facies (right) at about the same lateral position. Red lines indicate bed contacts and white dashed lines the interface in a bipartite facies.

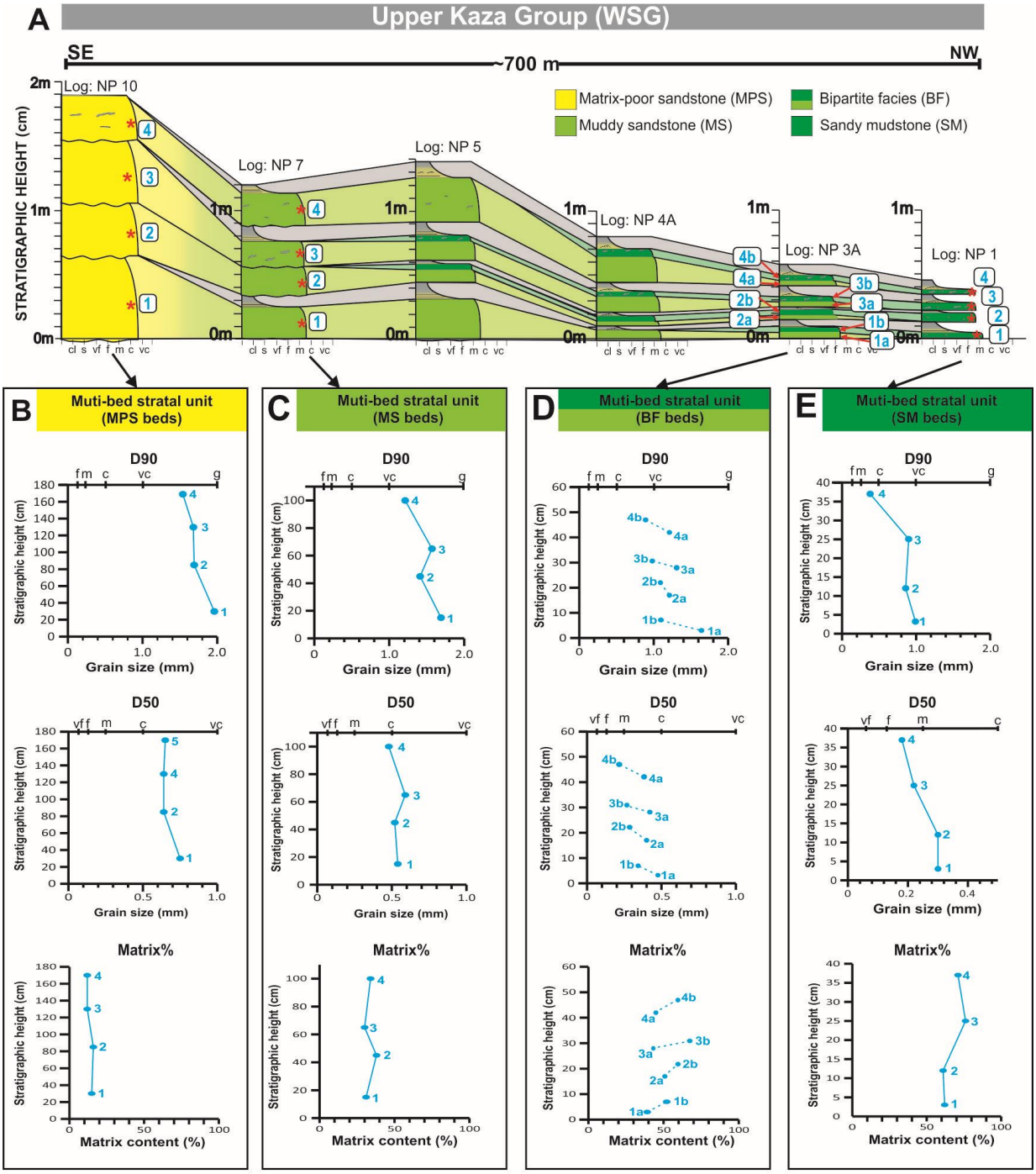

Figure 5.9: A) Stratigraphic correlation panel of a multi-bed stratal unit consisting of four individual beds in basin-floor deposits of the Upper Kaza Group, Windermere Supergroup (see Appendix A2 for location). Note that in all beds the transition from matrix-poor sandstone (MPS) to muddy sandstone (MS) to bipartite facies (BF) and sandy mudstone (SM) occurs at about the same lateral position. Samples for microscopic grain size analysis were collected where one facies transitioned to the next. Sample locations are labelled 1, 2, 3, 4; the "a" and "b" suffix indicates the lower and upper parts, respectively, in a bipartite facies. B, C, D, E) Graphs showing D90, D50 and matrix content of a multi-bed stratal unit of MPS, MS, BF and SM, respectively. Note that at any position along the correlation panel, the matrix content changes little upward, however, the D90 and D50 subtly but progressively decrease upward.

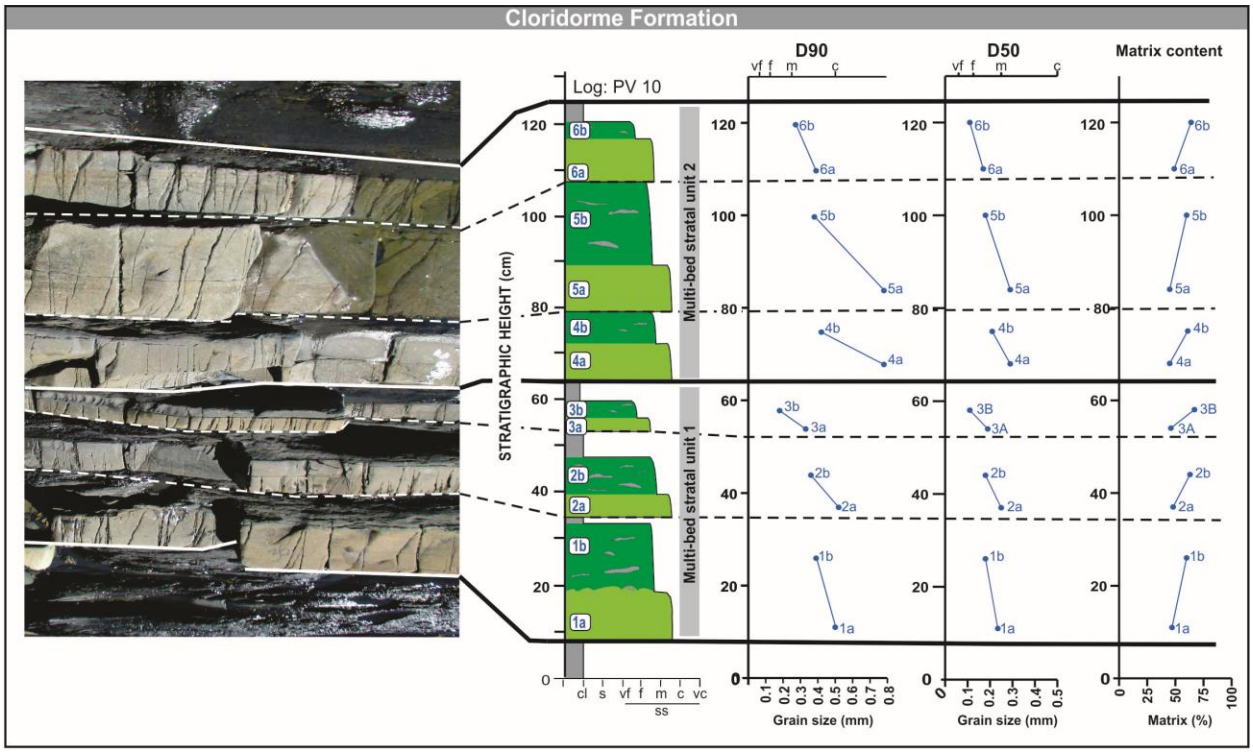

Figure 5.10: Outcrop photograph and accompanying stratigraphic log of a continuous vertical section showing two multi-bed stratal units consisting of bipartite facies (BF) in the Cloridorme Formation (see Fig. 3.13 and Appendix A9 for location). Graphs represent D90, D50 and matrix content of the individual beds; "a" and "b" indicate position in the lower and upper parts of the bed, respectively. Note that the stratal unit boundary between beds 3 and 4 is based on an abrupt grain-size increase (D90 and D50). Also, note that within each stratal unit, the D90 and D50 show an abrupt decrease in the topmost bed of both stratal units, whereas matrix content changes little.

5.5.2 Markov chain analysis (bed scale)

Descriptive Statistics — A total of 333 and 304 bed transitions were observed in CF and WSG, respectively. Results of the observed and expected transitions of beds in both study areas are summarized in the transition matrix and state diagrams (Fig. 5.11). In WSG, MPS beds comprise 36% of all beds (i.e., states) observed and are most frequently overlain by similar MPS beds (48% of observed transitions). Less commonly, MPS beds are overlain by beds of SM (28%), MS (20%) or BF (5%). MS beds make up 15% of all the observed beds, and are most commonly overlain by other MS beds (34%), and less commonly by beds of SM (28%), MPS (26%) or BF

(13%). BF beds constitute 17% of all the beds observed and are most frequently overlain by other BF beds (48%) followed by beds of MPS (25%), SM (21%) or MS (6%). Lastly, SM beds comprise 32% of all the observed beds and are usually overlain by other SM beds (44%), and less commonly by beds of MPS (34%), BF (16%) or MS (6%).

In CF, MPS beds make up 12% of all observed beds and are most commonly overlain by beds of SM (32%) and BF (32%), and less commonly by beds of MPS (29%) or MS (7%). MS beds comprise 16% of all the observed beds and are most frequently overlain by other BF beds (48%). Less frequently, MS beds are overlain by other MS beds (25%), and beds of SM (17%) or MPS (10%). BF beds constitute 41% of all observed beds and are most commonly overlain by other BF beds (50%) followed by beds of SM (26%), MS (15%) or MPS (9%). Lastly, SM beds make up 31% of all the observed beds and are most frequently overlain by other SM beds (44%), and less frequently by beds of BF (29%), MS (15%) or MPS (12%).

Significance Test — In the statistical analysis, the degrees of freedom are $(n-1)^2 = (4-1)^2 = 9$, where n is the number of discrete states (i.e., MPS, MS, BF and SM beds) and the minimum Chi-squared (X^2) value to reject the null hypothesis (at 5% significance level) is 16.92. The values in the X^2 matrix are calculated using $X^2 = (\text{observed} - \text{expected})^2 / \text{expected}$. The respective sums of the X^2 matrices are 75 for WSG and 34 for CF (Figs. 11C and G). Accordingly, the null hypothesis can be rejected for both study areas and the observed vertical stacking of beds is non-random.

More specifically, comparing the expected and observed transition matrices in both study areas show that beds of similar lithofacies type typically succeed one another, whereas all other transitions are either less than expected, random or very close to random (Figs. 5.11C, D, G, H). Importantly, in CF, for example, a statistically significant transition does not necessarily correlate

with a high or low transition percentage. For example, the transitions from MPS bed to BF bed and MPS bed to SM bed are both 32%, whereas MPS bed to another MPS bed is 29%. Despite the first two transitions being more frequent than the third, the first two are statistically very close to random or random, whereas the third is statistically more likely than random (Fig. 5.11G). This shows that the most or the least likely transitions in terms of absolute number of occurrences are not necessarily statistically significant, and in fact may only be the result of random chance.

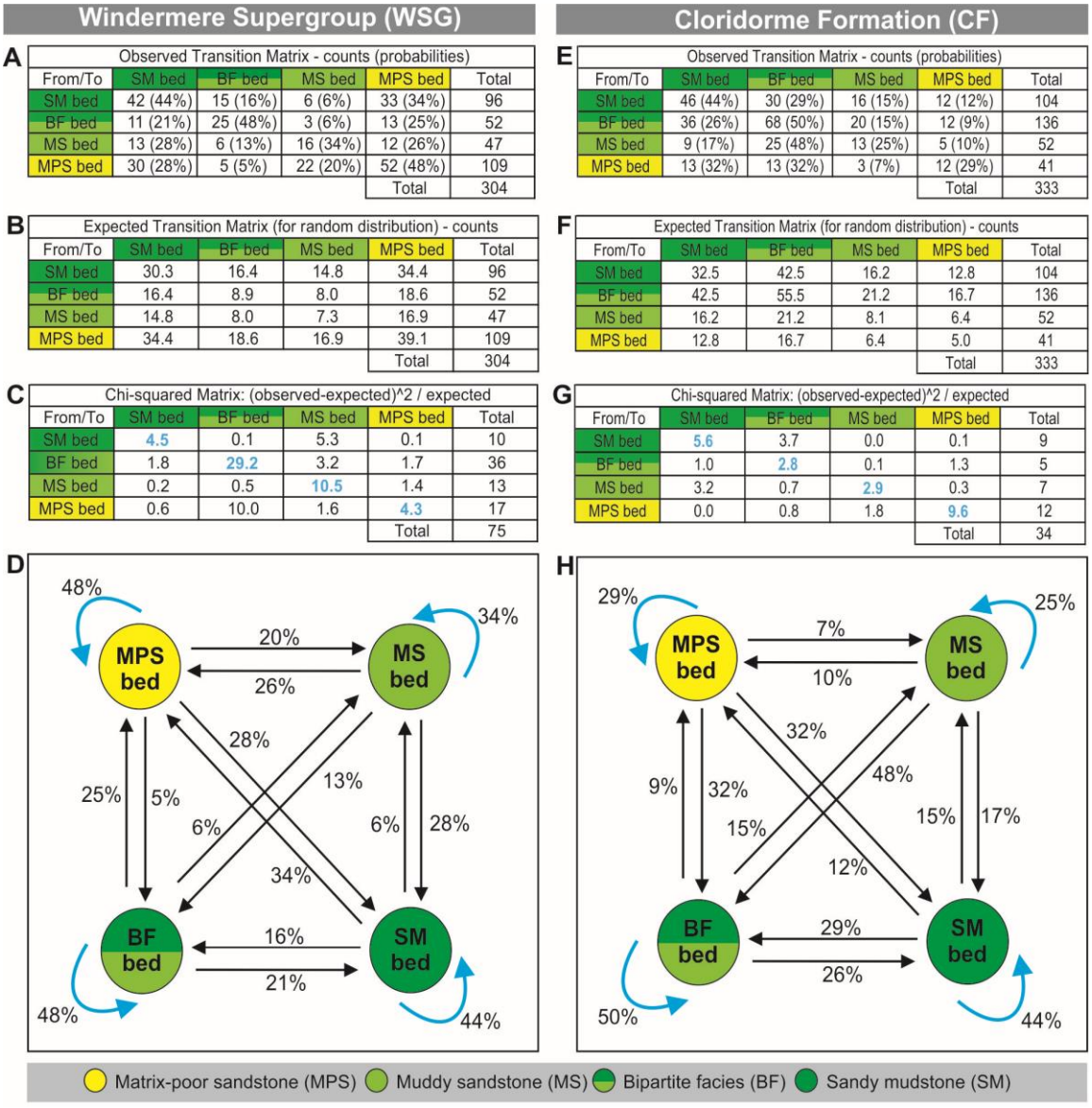

Windermere Supergroup (WSG)

A Observed Transition Matrix - counts (probabilities)

From/To	SM bed	BF bed	MS bed	MPS bed	Total
SM bed	42 (44%)	15 (16%)	6 (6%)	33 (34%)	96
BF bed	11 (21%)	25 (48%)	3 (6%)	13 (25%)	52
MS bed	13 (28%)	6 (13%)	16 (34%)	12 (26%)	47
MPS bed	30 (28%)	5 (5%)	22 (20%)	52 (48%)	109
				Total	304

B Expected Transition Matrix (for random distribution) - counts

From/To	SM bed	BF bed	MS bed	MPS bed	Total
SM bed	30.3	16.4	14.8	34.4	96
BF bed	16.4	8.9	8.0	18.6	52
MS bed	14.8	8.0	7.3	16.9	47
MPS bed	34.4	18.6	16.9	39.1	109
				Total	304

C Chi-squared Matrix: (observed-expected)^2 / expected

From/To	SM bed	BF bed	MS bed	MPS bed	Total
SM bed	4.5	0.1	5.3	0.1	10
BF bed	1.8	29.2	3.2	1.7	36
MS bed	0.2	0.5	10.5	1.4	13
MPS bed	0.6	10.0	1.6	4.3	17
				Total	75

D

Cloridorme Formation (CF)

E Observed Transition Matrix - counts (probabilities)

From/To	SM bed	BF bed	MS bed	MPS bed	Total
SM bed	46 (44%)	30 (29%)	16 (15%)	12 (12%)	104
BF bed	36 (26%)	68 (50%)	20 (15%)	12 (9%)	136
MS bed	9 (17%)	25 (48%)	13 (25%)	5 (10%)	52
MPS bed	13 (32%)	13 (32%)	3 (7%)	12 (29%)	41
				Total	333

F Expected Transition Matrix (for random distribution) - counts

From/To	SM bed	BF bed	MS bed	MPS bed	Total
SM bed	32.5	42.5	16.2	12.8	104
BF bed	42.5	55.5	21.2	16.7	136
MS bed	16.2	21.2	8.1	6.4	52
MPS bed	12.8	16.7	6.4	5.0	41
				Total	333

G Chi-squared Matrix: (observed-expected)^2 / expected

From/To	SM bed	BF bed	MS bed	MPS bed	Total
SM bed	5.6	3.7	0.0	0.1	9
BF bed	1.0	2.8	0.1	1.3	5
MS bed	3.2	0.7	2.9	0.3	7
MPS bed	0.0	0.8	1.8	9.6	12
				Total	34

H

Matrix-poor sandstone (MPS) Muddy sandstone (MS) Bipartite facies (BF) Sandy mudstone (SM)

Figure 5.11: Results of a first-order Markov chain analysis of matrix-rich and associated matrix-poor beds in the Windermere Supergroup (WSG; left column) and Cloridorme Formation (CF; right column). The input data are derived from a 137 m-long composite log in WSG with 304 transitions and a vertically continuous 287 m-long stratigraphic log in the CF with 333 transitions. MPS – matrix-poor sandstone, MS – muddy sandstone, BF – bipartite facies, SM – sandy mudstone. A and E) Observed transition matrix counts and probabilities (%). B and F) Transition matrices showing expected number of transitions in a random system. C and G) Chi-square matrices. Blue numbers indicate transitions that are observed more frequently than expected in a random distribution. D and H) State diagrams showing transition probabilities. Blue arrows indicate transitions observed significantly more frequently than expected based on a random distribution.

5.5.3 Stacking pattern (stratal unit scale)

In both study areas, stratal units of matrix-rich and associated matrix-poor lithologies, stack exclusively to form 0.4 – 33.2 m (average 2.7 m thick) avulsion splays (Figs. 5.5, 5.6). These avulsion splays are equivalent in hierarchy to 'lobe elements' of Prélat et al. (2009), and in the WSG abruptly underlie sand-rich stratal elements such as slope channels (e.g., Arnott, 2007a, b: Schwarz and Arnott, 2007; Angus et al., 2019; Ningthoujam et al., 2022) (e.g., Fig. 5.3); distributary channels and terminal splays in the channel-lobe transition zone (Navarro and Arnott, 2020) and proximal basin floor (Terlaky and Arnott, 2014; Terlaky et al., 2016; Angus et al., 2019; Ningthoujam et al., 2022) (e.g., Fig. 5.3). In distal basin-floor strata of the Petite Vallée study area, the avulsion splays typically underlie terminal splays (see Ningthoujam et al., 2022) (e.g., Fig. 5.4).

5.5.4 Markov chain analysis (stratal unit scale)

Descriptive Statistics — A total of 203 and 184 stratal unit transitions were observed in CF and WSG, respectively. Results of the observed and expected transitions of stratal units in both study areas are summarized in the transition matrix and state diagrams (Fig. 5.12). In the WSG,

MPS stratal units comprise 34% of all stratal units observed and are most frequently overlain by stratal units of SM (52% of observed transitions). Less commonly, MPS stratal units are overlain by stratal units of MS (30%), BF (14%) or MPS (3%). MS stratal units make up 17% of all observed stratal units and are most commonly overlain by stratal units of SM (50%), and less commonly by MPS (38%) or BF (13%). Furthermore, MS stratal units were not observed to overlie one another. Stratal units of BF constitute 14% of all stratal units observed and are most frequently overlain by stratal units of SM (46%) or MPS (46%), and less commonly by MS (26%). Additionally, BF stratal units were not observed to overlie one another. Lastly, SM stratal units comprise 35% of all observed stratal units and are most commonly overlain by stratal units of MPS (59%), and less commonly by BF (21%), MS (17%) or SM (3%).

In the CF, MPS stratal units make up 12% of all observed stratal units and are most commonly overlain by stratal units of SM (54%), and less commonly by BF (38%) or MS (8%). Additionally, MPS stratal units were not observed to overlie one another. Stratal units of MS comprise 21% of all observed stratal units and are most frequently overlain by BF stratal units (62%). Less frequently, MS stratal units are overlain by stratal units of SM (24%), MPS (7%) or MS (7%). BF stratal units constitute 36% of all observed stratal units and are most commonly overlain by stratal units of SM (47%) followed by MS (26%), MPS (15%) or BF (12%). Lastly, SM stratal units make up 31% of all the observed stratal units and are most frequently overlain by stratal units of BF (45%), and less frequently by MS (28%), MPS (16%) or SM (11%).

Significance Test — In the statistical analysis, the degrees of freedom are $(n-1)^2 = (4-1)^2 = 9$, where n is the number of discrete states (i.e., MPS, MS, BF and SM stratal units) and the minimum Chi-squared (X^2) value to reject the null hypothesis (at 5% significance level) is 16.92. The respective sums of the X^2 matrices are 76 for WSG and 53 for CF (Figs. 5.12C and G).

Therefore, the null hypothesis can be rejected for both study areas and the observed vertical stacking of stratal units is non-random.

Notably, comparison of the expected and observed transition matrices in both study areas show that similar stratal units are less likely to overlie themselves than expected (Figs. 5.12C, D, G, H). With the exception of MPS to MS, MPS to SM and SM to MPS in the WSG, and MPS to SM, MS to BF and BF to SM in the CF, all other stratal units' transitions are either random or very close to random (Figs. 5.12C, D, G, H).

Windermere Supergroup (WSG)

A

Observed Transition Matrix - counts (probabilities)

From/To	SM (su)	BF (su)	MS (su)	MPS (su)	Total
SM (su)	2 (3%)	13 (21%)	11 (17%)	37 (59%)	63
BF (su)	12 (46%)	0 (0%)	2 (8%)	12 (46%)	26
MS (su)	16 (50%)	4 (13%)	0 (0%)	12 (38%)	32
MPS (su)	33 (52%)	9 (14%)	19 (55%)	2 (3%)	63
				Total	184

B

Expected Transition Matrix (for random distribution) - counts

From/To	SM (su)	BF (su)	MS (su)	MPS (su)	Total
SM (su)	21.6	8.9	11.0	21.6	63
BF (su)	8.9	3.7	4.5	8.9	26
MS (su)	11.0	4.5	5.6	11.0	32
MPS (su)	21.6	8.9	11.0	21.6	63
				Total	184

C

Chi-squared Matrix: (observed-expected)^2 / expected

From/To	SM (su)	BF (su)	MS (su)	MPS (su)	Total
SM (su)	17.8	1.9	0.0	11.0	31
BF (su)	1.1	3.7	1.4	1.1	7
MS (su)	2.3	0.1	5.6	0.1	8
MPS (su)	6.1	0.0	5.9	17.8	30
				Total	76

D

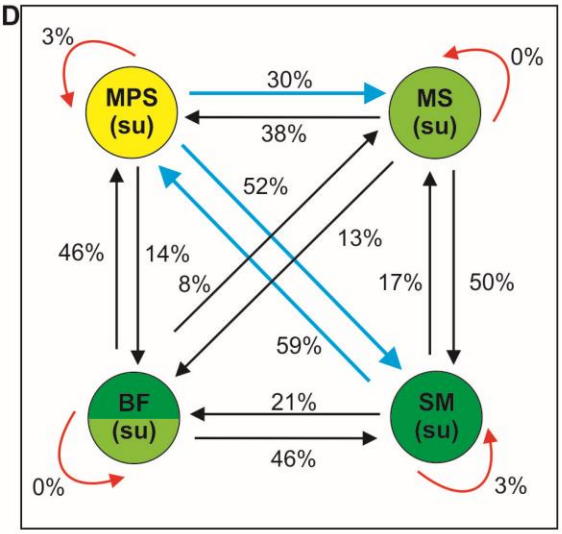

Cloridorme Formation (CF)

E

Observed Transition Matrix - counts (probabilities)

From/To	SM (su)	BF (su)	MS (su)	MPS (su)	Total
SM (su)	7 (11%)	29 (45%)	18 (28%)	10 (16%)	64
BF (su)	34 (47%)	9 (12%)	19 (26%)	11 (15%)	73
MS (su)	10 (24%)	26 (62%)	3 (7%)	3 (7%)	42
MPS (su)	13 (54%)	9 (38%)	2 (8%)	0 (0%)	24
				Total	203

F

Expected Transition Matrix (for random distribution) - counts

From/To	SM (su)	BF (su)	MS (su)	MPS (su)	Total
SM (su)	20.2	23.0	13.2	7.6	64
BF (su)	23.0	26.3	15.1	8.6	73
MS (su)	13.2	15.1	8.7	5.0	42
MPS (su)	7.6	8.6	4.9	2.8	24
				Total	203

G

Chi-squared Matrix: (observed-expected)^2 / expected

From/To	SM (su)	BF (su)	MS (su)	MPS (su)	Total
SM (su)	8.6	1.6	1.7	0.8	13
BF (su)	5.2	11.3	1.0	0.7	18
MS (su)	0.8	7.9	3.7	0.8	13
MPS (su)	3.9	0.0	1.8	2.8	9
				Total	53

H

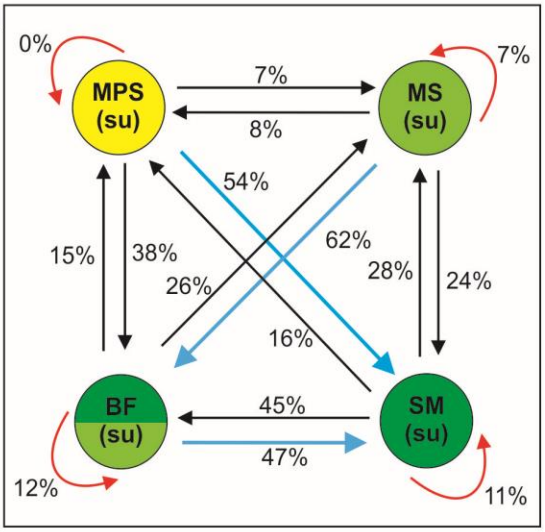

Matrix-poor sandstone (MPS) Muddy sandstone (MS) Bipartite facies (BF) Sandy mudstone (SM)

Figure 5.12: Results of a first-order Markov chain analysis of matrix-rich and associated matrix-poor stratal units (su) in the Windermere Supergroup (WSG; left column) and Cloridorme Formation (CF; right column). The input data are derived from 137 m-long composite log in WSG with 184 transitions and 287 m-long vertically continuous stratigraphic log in the CF with 203 transitions. MPS (su) – matrix-poor sandstone stratal unit, MS (su) – muddy sandstone stratal unit, BF (su) – bipartite facies stratal unit, SM (su) – sandy mudstone stratal unit. A and E) Observed transition matrix counts and probabilities (%). B and F) Transition matrices showing the expected number of transitions in a random system. C and G) Chi-square matrices. Colored numbers indicate the statistically significant transitions: blue numbers indicate transitions that are observed more frequently and red numbers less frequently than expected in a random distribution. D and H) State diagrams showing transition probabilities. Statistically significant transitions are colored: blue arrows indicate transitions that are significantly more frequent and red arrows less frequent than expected in a random distribution.

5.6 DISCUSSION

5.6.1 Vertical stacking (bed scale)

Based on field observations and verified statistically, beds of similar lithofacies, but often of different thickness, typically succeed one another vertically and form multi-bed (2 – 9 beds) stratal units; all other transitions are either less than expected, random or very close to random (Fig. 5.11). Within a discrete multi-bed stratal unit, successive beds transition from one facies to the next at about the same lateral position (Fig. 5.8). Also, grain size shows a subtle but nevertheless consistent upward decrease; matrix content changes negligibly upward (Figs. 5.9, 5.10). Collectively, these observations suggest that beds within a multi-bed stratal unit are more or less texturally self-similar and therefore deposited from flows with similar hydraulic and compositional character, albeit exhibiting a minor but nevertheless progressive decrease in flow energy. Superimposed on this temporal regularity is the deposition of the traction-structured turbidite overlain by mudstone that caps each bed. Each cap signals a dramatic change in depositional conditions, which then revert to conditions that resembled those that deposited the underlying bed, albeit often with a slightly finer-grained sediment supply. This, then, raises the obvious question as to the origin of such systematic sedimentation and whether deposition of a multi-bed stratal unit is a consequence of multiple flow events or one flow event with multiple

pulses. With respect to multiple flow events, it has been shown experimentally that oversized turbidity currents traversing a partially confined sinuous channel equilibrate to the channel's cross-sectional area by flow stripping and overspill in channel bends, which ultimately reduces size variability in the flows (Straub et al., 2008). More recently, Kelly et al., (2019) described a process termed flow tuning where saline currents passing through a partially confined straight channel adjusted their flow size either by overspilling (oversized flows) or by inflating through ambient fluid entrainment (undersized flows) to achieve an equilibrium flow condition in which overbank losses are balanced with ambient fluid entrainment. Intriguingly, the self-similarity of beds within a multi-bed stratal unit could be consistent with successive flows that had undergone flow tuning, however, variability in the thickness of individual beds within a multi-bed stratal unit (e.g., Figs. 5.5, 5.6), and the subtle but nonetheless consistent upward decrease of grain size observed in multi-bed stratal units makes this problematic (Figs. 5.9, 5.10).

A second possibility is that self-similar beds were deposited from multiple pulses of a single turbidity current. Pulsing in turbidity currents has been recognized in direct monitoring of natural flows (e.g., Shepard et al., 1975; Best et al., 2005; Menczel and Kostaschuk, 2013) and studied experimentally and simulated numerically (e.g., Dai, 2008; Ho et al., 2018a, 2018b; Kostaschuk et al., 2018), however, relatively few studies have described evidence of this in the ancient sedimentary record. In Lowe (1982) and Larue and Provine (1988), stacks of self-similar turbidites lacking evidence of intervening erosion were suggested to be formed by pulsations or surges in velocity during a single flow event. Additionally, alternating arenite and pelite turbidite facies, equivalent to stacked Bouma Tcd/e divisions, were reported from Oligocene and Carboniferous rocks in eastern France by Duringer et al. (1991) and interpreted to be deposited by a single, continuous muddy turbidity current with episodic higher-energy pulses forming the Tc

divisions. Also, in the Precambrian Kongsfjord Formation, Pickering (1979) interpreted ~ 2 – 5 m thick bedsets comprising at least 5 beds, each composed mostly of upper division turbidites, and exhibiting a progressive upward fining and thinning, to record pulses of traction-transport deposition separated by lower energy suspension deposition in a single continuously waning flow event. Most recently, Cunningham and Arnott (2021) described thin-bedded, upper division turbidites in interpreted continental slope levee deposits in the WSG to form bedsets of ~ 2 – 10 self-similar beds, which they attribute to deposition from multiple, episodic pulses of a single channelized flow event.

Although it seems clear from these outcrop examples that stacked bed self-similarity is suggestive of turbidity current pulsing, the cause for the pulsing still remains poorly understood. To-date a variety of mechanisms have been proposed to explain pulsing, including: high swell waves and high tides generating pulsating turbidity currents (Shepard et al., 1975); retrogressive slumping that evolved downslope into multi-pulsed turbidity currents (Piper et al., 1999; Canals et al., 2004; Ho et al., 2018a); multi-pulsed flows formed downflow of channel confluences by discrete flows triggered simultaneously (e.g., by an earthquake) in different upflow channels such as tributaries in a canyon system (Nakajima and Kanai, 2000; Ho et al., 2018a); velocity pulsing caused by hydrodynamic instabilities in plunging hyperpycnal flows (Kostaschuk et al., 2018); hypo- and mesopycnal flows generating multiple secondary turbidity currents through settling driven Rayleigh-Taylor convection (Hoyal et al., 1999; Parsons et al., 2001; Davarpanah Jazi and Wells, 2016, 2018). Most of these mechanisms, except for retrogressive slope failures, are expected to have short delay times (few minutes to hours) between pulses, which would preclude the emplacement of the traction-structured sandstone and mud cap over individual beds in a stratal unit. In a multi-pulsed flow initiated by retrogressive slumping, the time between successive slope

failures can be sufficient to allow for the deposition and preservation of traction-structured sandstone and mud cap, but it is highly unlikely to result in consistent self-similarity of successive pulses of sediment transport and deposition. Additionally, the subtle but nevertheless consistent upward-fining trend observed in all multi-bed stratal unit is difficult to reconcile with any of these mechanisms (Figs. 5.9, 5.10). An alternative mechanism builds on recent direct monitoring of turbidity currents in the Congo Canyon by Azpiroz-Zabala et al. (2018). Unlike typical laboratory-generated surge-type turbidity currents, where the body is faster than the head and continuously feeds the head with sediment (e.g., Middleton, 1966), Azpiroz-Zabala et al. report that Congo canyon turbidity currents consist of a dense, fast-moving and erosive head, termed a 'frontal cell', and a trailing body and tail (Fig. 5.13A). Here, the flow is sustained by the frontal cell through continuous erosion and incorporation of new sediment from the seafloor while simultaneously shedding sediment-laden fluid into the trailing part of the flow. The difference in density, and hence the velocity between the frontal cell and the rest of the flow (i.e., the body and tail), allows the frontal cell to out-run the trailing flow and stretches the flow downstream. This process also allowed turbidity currents to last up to ten days compared to a few minutes to hours in previous flow measurements in other modern systems (e.g., Xu et al., 2004; Khripounoff et al., 2012; Liu et al., 2012; Clarke, 2016). Considering that the flow monitoring by Azpiroz-Zabala et al. was limited to the submarine canyon, and that at least some turbidity currents are capable of reaching further downslope and even onto the basin floor, it is possible that as the turbidity current continues to be stretched, the dense frontal cell eventually becomes detached from the rest of the flow and forms a separate turbidity current (Fig. 5.13B). With the detachment of the head, the remaining (main) turbidity current is cut-off from its major source of sediment, which then causes it to be diluted and slow. Additionally, elevated stagnation pressure at the new leading edge of the main

flow causes it to move more slowly than the trailing part, which then feeds sediment forward and into a newly developing head (Middleton, 1966; Kneller and Buckee, 2000; Cartigny et al., 2013). With time, increased density in the head would cause it to accelerate and erode the seafloor, which then would feed new sediment into the head and also shed into the trailing body. Farther downflow, the head evolves into a new frontal cell (Fig. 5.13C) that eventually detaches from the main flow and becomes a second discrete turbidity current (Fig. 5.13D). With time and distance downslope this process is possibly repeated several times creating multiple surges from a single flow event. Accordingly, each bed in a multi-bed stratal unit would correlate with a single surge (Fig. 5.13E), and the progressive decrease in grain size reflects the gradual long-term waning of the parent turbidity current. Additionally, the random intercalation of single bed stratal units separating multi-bed stratal units may indicate flows where only the initial surge (i.e., first detached head) reached that downslope position while the rest of flow terminated some distance further upslope.

Importantly, the delay time between successive surges must have been sufficient to allow for the emplacement of traction-structured, very fine-grained sandstone (0.2 to 3 cm thick) and overlying mud cap. Similar low frequency pulses have also been suggested by Cunningham and Arnott (2021) to allow for the deposition and semi-consolidation of silty and muddy Td/e divisions overlying self-similar sand-rich Tc divisions in levee strata of the Isaac Formation. Potentially more significant is the mud cap, which typically is massive and 3 – 5 cm thick. Here the rapid accumulation of fine-grained sediment is attributed to very high near-bed sediment concentration and extensive particle-particle interaction that promoted mud flocculation and aggregation (McAnally et al., 2007; see also discussion in Cunningham and Arnott, 2021). Particle aggregation may also have been enhanced by mud particle adhesion to suspended microbial extra-cellular polymeric substances (EPS) (Bennett et al., 1992). Given the absence of bioturbation in WSG and

CF strata, it is possible that the mud-rich seabed was anomalously enriched in microbes and associated EPS, which when eroded during avulsion, resulted in rapid and extensive particle aggregation in the near-bed region. Eventually, the concentration of flocculated and aggregated particles led to gelling and *en masse* deposition of the mud layer. Notably, the contact between a mud cap and the overlying bed in a multi-bed stratal unit is typically sharp and planar. This indicates that the mud caps had sufficient strength and load-bearing capacity to resist shearing and loading during deposition of the overlying bed. If strength were to develop through self-weight consolidation (i.e., normal consolidation; Skempton, 1969), the timeframe would have greatly exceeded the predicted delay time between surges associated with a single flow event. However, based on observations of modern deep marine sediments in offshore Angola and Nigeria, the Nova Scotian Slope, and in the Pacific Ocean (Baltzer et al., 1994; Meadows and Meadows, 1994; Ehlers et al., 2005; Kuo and Bolton, 2013), a zone of exceptionally high strength, albeit with high water content, and termed the 'crust' (sensu Kuo and Bolton, 2008), occurs a few tens of centimeters to about a meter below the seafloor with strength that is an order of magnitude higher than from normal consolidation. Although development of the crust is still poorly understood, microbially mediated strength enhancement of marine sediments through production of EPS has been proposed in several studies (e.g., Dade et al., 1990; Tolhurst et al., 2002; Bhaskar and Bhosle, 2005). Additionally, Parkes et al. (2000) show that bacteria in the uppermost meter of the marine sediment pile can exceed 10^9 cells per cubic centimeter of sediment and rival that in the terrestrial realm. Using similar concentration of microbes (i.e., 10^9 cells per cubic centimeter of sediment) as measured in modern subsurface marine sediments, Dade et al. (1996) experimentally showed that a glue-like exopolymer produced by marine bacteria (*A. atlantica*) enhanced the yield stress of a kaolinite clay and seawater mixture by 60% in ~ 0.5 to 9 days. Collectively, the combination of

biophysically enhanced mud particle aggregation in the near-bed that led to gelling and *en masse* deposition of the mud layer, as well as microbe-induced post-depositional strength enhancement of the mud layer, allowed for the deposition and preservation of mud caps associated with successive surges in a single flow event.

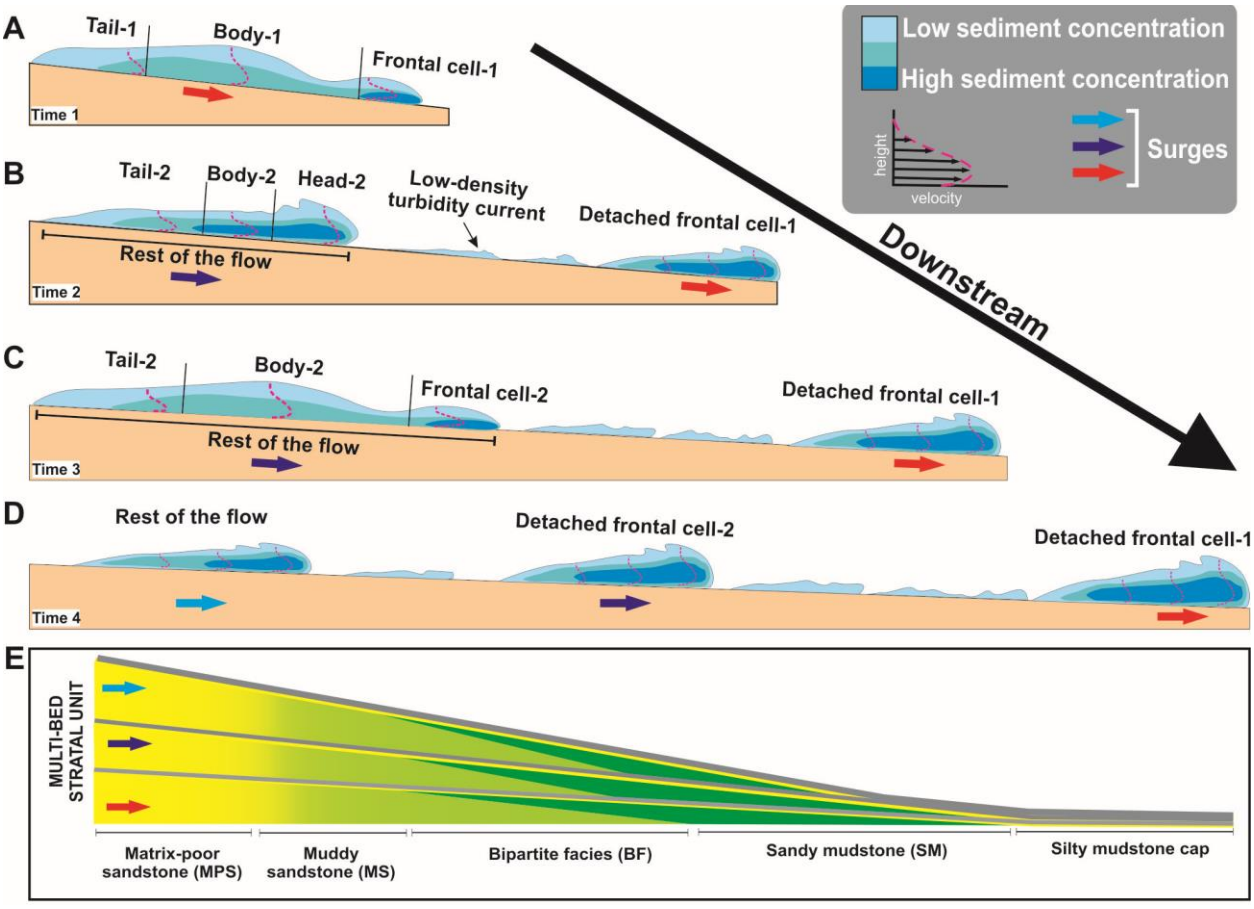

Figure 5.13: Schematic illustrating the development of multiple surges from a single turbidity current. Figures are not to scale. A) Turbidity current consisting of a dense, fast moving erosive head (frontal cell), and a trailing body and tail. B) Frontal cell detaches from the rest of the flow and becomes a separate turbidity current. C) Increased density in the new head causes it to accelerate, possibly eroding the seafloor, and forms a new frontal cell (frontal cell-2). D) Frontal cell-2 then detaches from the rest of the flow and becomes a discrete turbidity current. With time and distance downslope this process is possibly repeated several times creating multiple surges from a single flow event. E) Successive surges deposit a stack of self-similar beds that buildup a multi-bed stratal unit. Importantly, the time lag between surges is sufficient to allow for the deposition of the traction-structured sandstone and/or mudstone cap.

5.6.2 Vertical stacking (stratal unit scale)

Results of the Markov-chain analysis of matrix-rich and associated matrix-poor lithologies at the stratal unit scale show that similar lithologies that make up part of the depositional continuum in each of their respective stratal units stack less commonly than expected in a random distribution in both study areas, whereas stratal unit transitions of MPS to SM, SM to MPS and MPS to MS in the WSG and MS to BF, BF to SM and MPS to SM in the CF are observed significantly more frequently than expected in a random distribution (Fig. 5.12C, D, G, H). This indicates that the observed vertical stacking in both study areas is more heterogeneous than predicted by a random distribution of stratal units, and as this statistical analysis (see above) assumes no external forcing (e.g., variations in sediment supply, changes in relative sea level, tectonic variability), but also the commonality of these distinctive strata in the deep-water stratigraphy of both the WSG and CF, imply an internal forcing.

In WSG strata, the stack of the thickest and most proximal lithofacies in a single stratal unit (i.e., MPS stratal unit) is preferentially overlain by a stack of the thinnest and most distal lithofacies in the overlying stratal unit (i.e., SM stratal unit), or vice versa (Fig. 5.12C and D). Considering that these strata were deposited on opposite ends of the depositional continuum, the stacking pattern indicates an abrupt and long-distance lateral displacement of facies. This is the stratigraphic manifestation of compensational stacking, which here resulted from the flows being diverted around topographic highs formed by deposition of the previous stratal unit and directed into adjacent topographic lows (Terlaky and Arnott, 2016) (Fig. 5.14A). Flow diversion was followed by a temporary stabilization of flow and sedimentation conditions and deposition of the next stratal unit. MPS stratal units are also preferentially overlain by slightly more distal MS stratal units, however, the opposite transition (i.e., MS to MPS) is shown not to be statistically significant

(X^2 value of 0.1) (Fig. 5.12 C and D). The MPS overlain by MS transition indicates a minor back-step of successive stratal units that might reflect flow deceleration against the positive relief created by deposition of the underlying stratal unit (Pratson et al., 2000, Ferguson et al., 2020) (Fig. 5.14A). In the CF strata, on the other hand, preferential stacking of stratal units including MS to BF, BF to SM and MPS to SM are observed (Fig. 5.12 G and H). Notably, however, the inverse of these transitions shows no statistical significance, suggesting a strong preference for systematic back-stepping at the stratal unit scale. As noted earlier, matrix-rich and associated matrix-poor strata in the CF form mouth-bar deposits at the downflow terminus of the flow (see Ningthoujam et al., 2022); therefore, this systematic back-stepping of stratal units most likely represents accretion on the upflow side of the mouth bar (Fig. 5.14B).

Overall, results of the statistical analysis suggest a preferred growth pattern of stratal units consisting of initiation followed by gradual back-stepping and then side-stepping into an adjacent topographic low (WSG) or consistent back-stepping (CF). The stacking pattern can either occur once or repeat multiple times building up several-meters-thick stratal elements termed avulsion splays (Terlaky and Arnott, 2014). A similar growth pattern is commonly reported from submarine fans and at a variety of scales, including beds/bedsets (e.g., Deptuck et al., 2008; Jobe et al., 2017), lobe elements (e.g., Deptuck et al., 2008; Jegou et al., 2008) and lobes (e.g., Twichell et al., 1991; Vittori et al., 2000). The cause for this systematic growth pattern is still a topic of debate, and studies have either associated it with allogenic controls, like sea level and climate (Hodgson et al., 2006; Marsset et al., 2009; Romans et al., 2009; Jobe et al., 2017), or internal autogenic controls, like the interaction between flows and the evolving topography (Gervais et al., 2006; Jegou et al., 2008; Prélat et al., 2009). Although, allogenic forcing may exert some influence on the depositional pattern of the packages described here, Cantelli et al. (2011) and Fernandez et al.

(2014) showed experimentally that similar depositional patterns (i.e., forward-stepping, back-stepping and then side-stepping of the depocenter) can be generated with no change in allogenic conditions. Additionally, more recent numerical modelling (Burgess et al., 2019) and physical experiments (Ferguson et al., 2020) showed that in unconfined settings like the basin-floor, even when external factors change, in these studies being sediment supply, the effect of depositional topography (i.e., autogenic forcing) on the evolution and orientation of the flows dominated and generated depositional patterns were largely similar to those in earlier studies with constant sediment supply.

Even though results of the statistical analysis show that the stacking pattern of lithofacies stratal units making up an avulsion splay is similar to many of the beds/bedsets to lobe scale stacking patterns recognized in both modern and ancient deep-marine systems, the composite strata are unique in their high mud content, which then requires an abrupt and temporarily sustained supply of mud. As interpreted above, and previously by Terlaky and Arnott (2014), Angus et al. (2019) and Ningthoujam et al. (2022), the abrupt development of matrix-rich strata is caused by an upflow avulsion that activates the local transport system. During avulsion, the flow loses confinement and forms a wall-jet that locally scoured the muddy interchannel area, thereby charging the flow with mud (see Ningthoujam et al., 2022). The scour locally steepened the seafloor gradient forming an upflow-migrating knickpoint that increased the erosive potential of successive flows. Knickpoint retreat not only charged the flows with fine-grained sediments, but in conjunction with the depositional bulge created by the underlying stratal unit drove the systematic back-stepping of successive stratal units (e.g., Fig. 5.14B). A similar history of knickpoint formation and headward migration associated with local submarine channel avulsion has been interpreted from seismic images in the Late Pleistocene Amazon and Rhone submarine

fans by Pirmez et al. (2000). Downflow of the avulsion node these authors note a lobate, high-amplitude (i.e., sand-rich), sheetlike deposit they termed a 'high-amplitude reflection packet' (HARP), which here, like Terlaky and Arnott (2014), is termed an avulsion splay. As stratal units accumulated, local topography increased and eventually caused flows to be diverted into adjacent topographic lows, such as the thin, fine-grained fringes of the depositional continuum. With these diverted flows experiencing an abrupt gradient change, a new knickpoint is created (see also Pirmez et al., 1997), and the process repeats with the deposition of the next stratal unit of matrix-rich lithologies. This combination of knickpoint migration and local topographical steering continues to form matrix-rich deposits until the supply of mud from local seafloor erosion becomes exhausted, quite possibly due to scour down to a sufficiently compacted subsurface layer, the avulsion node heals, the muddy substrate becomes buried in sand, or the parent channel diverts to a new location.

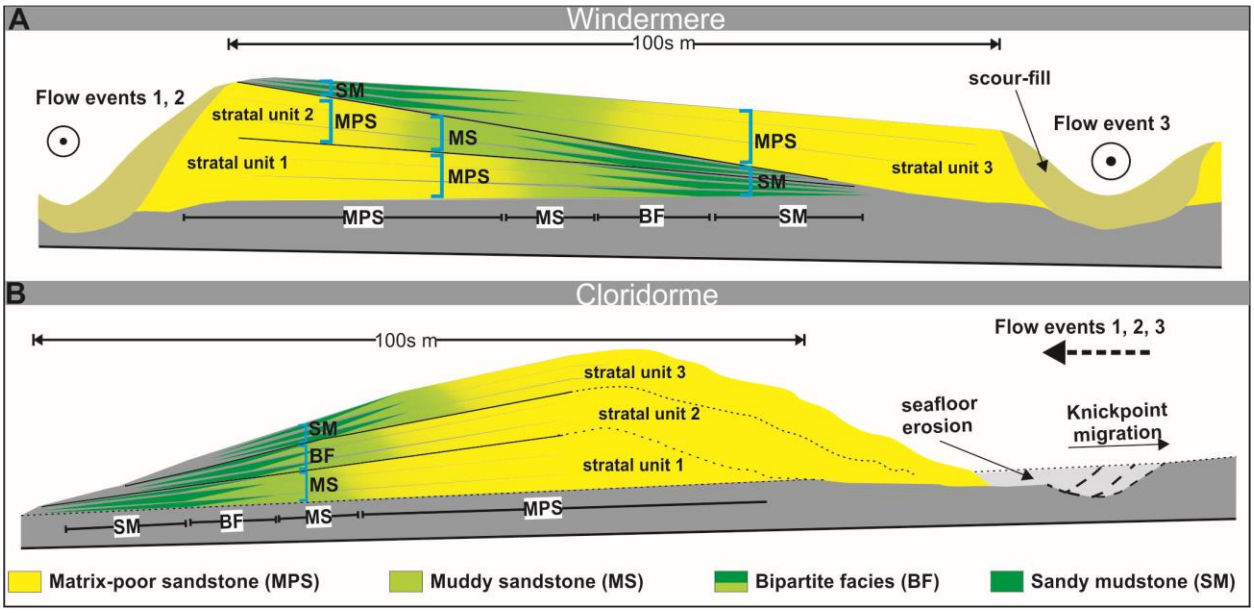

Figure 5.14: A and B) Schematics illustrating the statistically preferred stacking patterns of matrix-rich and associated matrix-poor stratal units in the (A) Windermere Supergroup (WSG) and (B) Cloridorme Formation (CF). Figures are not to scale. In (A) local flow is into or out of the page, whereas flow is from right to left in (B). MPS – matrix-poor sandstone stratal unit, MS – muddy sandstone stratal unit, BF – bipartite facies stratal unit and SM – sandy mudstone stratal unit. Stratal units 1, 2 and 3 collectively buildup an avulsion splay. Each stratal unit, consisting of one or more

beds, correlates to a single flow event. A) In the WSG, note the minor back-stepping of stratal unit 1 to 2 that is manifest by the vertical transition of MPS to MS. This is then followed by a significant side-stepping of stratal unit 3 marked by MPS overlain by SM and vice versa. B) In the CF, note the preference for stratal unit back-stepping, which at a point is expressed by the systematic stacking of MS to BF to SM.

5.7 CONCLUSIONS

Matrix-rich and associated matrix poor sandstones typically underlie sand-rich stratal elements like slope channel, distributary channel and terminal splay deposits in the WSG and terminal splays in the CF. This association is interpreted to be related to the activation of the local transport system caused by an upflow avulsion. Avulsion formed a wall jet that locally scoured the mud-rich interchannel area and charged the flow with fine-grained sediment, namely very fine sand to clay, in addition to low-density mud clasts. The local incorporation of easily suspended fine-grained sediment resulted in an abrupt increase in local effective viscosity and a dramatic change in the characteristics and reduction in the diffusion of turbulence required to maintain the particle suspension. This caused the sediment suspension to rapidly exceed transport capacity and collapse, forming a negligibly sheared suspension that deposited a systematic along-flow depositional continuum consisting of matrix-poor sandstone (MPS) to muddy sandstone (MS) to bipartite facies (BF) and then sandy mudstone (SM) over a distance of 100s meters, and collectively overlain by a thin-bedded, traction-structured sandstone and/or silty mudstone cap. Deposition of this transect occurred along the margins of the high-energy wall jet in WSG, but at the downflow terminus of the flow in the CF.

Vertically, and at the bed scale, similar lithofacies tend to preferentially stack and buildup multi-bed stratal units 2–9 beds thick. The grain-size distribution within a multi-bed stratal unit shows a subtle but nevertheless consistent upward-fining trend, whereas the matrix content changes little upward. Additionally, within a discrete multi-bed stratal unit, individual beds

undergo a transformation from one facies to the next in the lateral depositional continuum at about the same lateral position. Collectively, these observations suggest that beds within discrete multi-bed stratal unit are more or less texturally self-similar and therefore deposited from flows with similar hydraulic and compositional character, albeit exhibiting a minor but nevertheless progressive upward decrease in flow energy. This spatial and temporal regularity is argued to be generated by multiple avulsion-related surges of a single, gradually waning turbidity current. Importantly, the time between the successive surges is estimated to be of sufficient duration to allow for the emplacement of the traction-structured sandstone and overlying mud cap. Furthermore, the upward stacking at successive stratal units is dominated by side-stepping with minor back-stepping in the WSG compared with mostly back-stepping in the CF. Overall, the initiation, back-stepping and side-stepping of stratal units are interpreted to be related to a combination of knickpoint migration and local topographical steering of the flows, which continued until the supply of mud from local seafloor erosion became exhausted.

CHAPTER 6: THESIS CONCLUSIONS

Sandstones rich in detrital matrix (> 10% silt–clay) have long been recognized in the ancient sedimentary record and most commonly in deep-marine turbidite systems. In the last century, these strata were described as greywacke and was debated on topics related to identifying its appropriate classification criteria, and origin of its matrix (i.e., detrital vs. diagenetic). However, in the 21st century, the debate on deep-marine matrix-rich strata that are unlike classical turbidites or debrites has shifted towards understanding their physical origin. Termed slurry beds, linked debrite and co-genetic debrite-turbidite beds, hybrid event beds, transitional flow deposits, and matrix-rich sandstones, these strata are commonly characterized by a sandier basal part overlain by a muddier and mud clast-rich upper part with the transition from the upper to the lower part observed to be either sharp and planar or sharp and irregular or gradational marked by an intervening unit with alternating light (mud-poor) and dark (mud-rich) bands. These deposits are commonly reported to occur downflow of clean (less muddy) sand in the distal reaches of submarine lobes; however, the variable distance (100s m to 10s of kms) over which this lithological change is inferred to take place has resulted in a variety of physical models including slurry flows being an intermediate flow type between non-cohesive turbidity currents and cohesive debris flows; longitudinal partitioning of a mud-enriched sediment suspension into a forerunning turbidity current and a trailing debris flow; generation of a forerunning turbidity current from ambient fluid mixing along the upper surface of a debris flow; longitudinal flow transformation from turbulent to transitional to laminar flow regime; vertical stratification effects and turbulence suppression in a high-concentration sediment suspension; and particle settling in a negligibly sheared mixed sand–mud suspension. Part of this uncertainty can be attributed to most studies being based on observations in drill core and discontinuous outcrops where details of any vertical

and/or lateral changes in stratal characteristics are based on interpretation. Exceptional vertical and along-strike exposures of matrix-rich and associated matrix-poor deposits in the slope to proximal basin-floor strata of the passive margin Neoproterozoic Windermere Supergroup and distal basin-floor strata of the foreland basin Ordovician Cloridorme Formation, provide an unparalleled opportunity to document such characteristics, and therein a sampling of paleogeographic settings extending from continental slope to distal basin-floor.

In both study areas, matrix-poor sandstone (MPS) occurs as thick- to medium bedded, fine- to coarse-grained, massive to coarse-tail graded sandstone with < 20% matrix, whereas matrix-rich sandstone occurs as medium- to thin-bedded, fine- to coarse-grained, massive to coarse-tail graded sandstone with 20–90% matrix. Based on matrix content, matrix-rich sandstone can be subdivided into: muddy sandstone (MS) (20-50%); bipartite facies (BF) with a basal sandy (30–60%) part overlain sharply by a planar- to irregular-based muddier portion (40–80%); and sandy mudstone (SM) (50–90%). These lithofacies form a horizontal depositional continuum consisting of MPS to MS to BF and then SM over 100s m, which collectively are overlain by a thin- to very thin-bedded traction-structured sandstone and/or silty mudstone cap. Notably, strata occur exclusively as several-meters-thick stratigraphic units that abruptly underlie sandy slope channels, basin-floor distributary channels and terminal splays in the Windermere, and terminal splays in the Cloridorme. Accordingly, these distinctive strata represent deposition during the initiation, or activation of the local sedimentary system caused by an upflow avulsion that formed an unconfined plane-wall jet. Additionally, the consistent along-flow lithofacies changes are interpreted to reflect particle settling in a rapidly but systematically evolving, negligibly-sheared, sand-mud suspension developed along the margins of the avulsion-wall jet in proximal-basin-floor and slope deposits (Windermere), or at the downflow terminus of the flow in more distal basin-floor deposits

(Cloridorme). More importantly, irrespective of paleogeographic location, the length of the various lithological elements that build up the depositional continuum, after MPS transitions to MS (i.e., MS to BF to SM and ultimately to the pinch-out of SM), occur in equally proportioned lengths. This suggests that, once formed, the mud-enriched, momentum-driven flow evolved in a spatially systematic and dimensionally proportionate manner, and therefore mechanistic consistency.

Vertically, similar lithofacies typically succeed one another to form stratal units 2–9 beds thick; all other transitions are less than expected or random. Notably, within a single stratal unit, beds undergo transformation from one part of the depositional continuum to the next at about the same lateral position. Additionally, within an individual stratal unit, the grain-size distribution subtly but nevertheless consistently decreases stratigraphically upward, whereas the matrix content changes little. This spatial and temporal regularity is interpreted to be caused by multiple avulsion-related surges of a single, progressively waning turbidity current, with sufficient lag between successive surges to allow for the deposition of a traction-structured sandstone overlain by mudstone cap. Furthermore, vertical stacking of stratal units in the Windermere shows a statistical preference for minor back-stepping but a strong preference for side-stepping, whereas in the Cloridorme, stratal units show a strong preference for systematic back-stepping. Side-stepping in the Windermere is probably a consequence of compensational stacking caused by local evolution of seafloor topography, possibly biased also by the outcrop being oriented at a high-angle to the direction of the main flow. In the Cloridorme, on the other hand, the systematic back-stepping of stratal units is interpreted to represent accretion on the upflow side of a terminal mouth bar and upflow migration of an area of flow expansion — the paucity of side-stepping may only be an artifact of the outcrop being oriented parallel to the main flow direction. Collectively, the initiation, back-stepping and side-stepping of stratal units are interpreted to be driven by a combination of

knickpoint migration and local topographic steering of the flows, respectively, which then continued until the supply of mud from local seafloor erosion became exhausted, the main channel avulsed elsewhere, or a new stratal element developed.

CHAPTER 7: RECOMMENDATIONS FOR FUTURE RESEARCH

- By walking out individual beds, this study shows that the downflow lithofacies trend of matrix-poor sandstone to a two-part (bipartite) facies and then to an argillaceous facies, which in most cases is inferred to develop over several kilometers to tens of kilometers, in fact occurs over several hundreds of meters in both the Windermere and the Cloridorme. As such, future study should focus on (continuous) bed tracing in outcrops beyond the Windermere and Cloridorme to address this spatial disparity.
- The statistically significant vertical stacking patterns described for matrix-rich and associated matrix-poor strata at both individual bed and stratal unit scales in this study is based on limited data acquired from only two turbidite systems. Therefore, a wider array of data is needed to verify if the vertical stacking patterns reported in this study is typical of such strata. Accordingly, future work should consider performing similar statistical analysis (i.e., a first order Markov chain analysis) using data from several other turbidite systems.
- Aside from being used as paleocurrent indicators, sole marks have been generally ignored in the depositional models of matrix-rich strata, including this study. However, recently, Baas et al. (2021) proposed a new depositional model for hybrid event beds based on the observation of groove marks below these distinctive beds (see chapter 4), advocating that sole mark could be associated with the flow type and, by inference, the type of deposit. If

present, sole marks in Windermere cannot be observed due to the flat, glacially polished nature of the outcrop. However, well-exposed bedding planes and well-preserved sole marks are present in the Cloridorme; for example, Parkash, 1970; Parkash and Middleton, 1970. At the time of these earlier studies, the understanding of matrix-rich strata was quite limited, and as such warrants a revisit with the current state of knowledge. Therefore, future work in the Cloridorme should consider a thorough analysis of individual matrix-rich sandstone beds for lateral changes of tool marks, followed by comparison of those observations with published examples such as Peakall et al. (2020) and Baas et al. (2021).

- The depositional transect of matrix-poor sandstone to muddy sandstone to bipartite facies and then to sandy mudstone that is reported in this study is interpreted to have developed along the margins and in the downflow terminus of an avulsion-related wall jet, however, to-date, this process has not been verified experimentally. As such future experimental work should focus on understanding the mixing characteristics and sedimentation behavior along the lateral margins and downflow terminus of mud-rich plane-wall jets.

REFERENCES

Aalto, K.R., 1971, Glacial Marine Sedimentation and Stratigraphy of the Toby Conglomerate (Upper Proterozoic), Southeastern British Columbia, Northwestern Idaho and Northeastern Washington: Canadian Journal of Earth Sciences, v. 8, p. 753-787.

Ahmed, S., Bhattacharya, J.P., Garza, D.E., and Li, Y., 2014, Facies architecture and stratigraphic evolution of a river-dominated delta front, Turonian Ferron Sandstone, Utah, USA: Journal of Sedimentary Research, v. 84, p. 97-121.

Alexander, J.A.N., McLelland, S.J., Gray, T.E., Vincent, C.E., Leeder, M.R., and Ellett, S., 2008, Laboratory sustained turbidity currents form elongate ridges at channel mouths: Sedimentology, v. 55, p. 845-868.

Altosaar, A.K., 2007, Stratigraphic architecture and sedimentology of interstratified splay, levee and channel deposits: Neoproterozoic Isaac Formation (Windermere Supergroup) southern Canadian Cordillera, British Columbia, Unpublished B.Sc. thesis, University of Ottawa, 90 p.

Amy, L.A., and Talling, P.J., 2006, Anatomy of turbidites and linked debrites based on long distance (120 x 20 km) bed correlation, Marnoso Arenacea Formation, Northern Apennines, Italy: Sedimentology, v. 53, p. 161-212.

Amy, L.A., Talling, P.J., Edmonds, V.O., Sumner, E.J., and Lesueur, A., 2006, An experimental investigation of sand-mud suspension settling behaviour: Implications for bimodal mud contents of submarine flow deposits: Sedimentology, v. 53, p. 1411-1434.

Angus, K., 2016, Lateral facies trends in deep-marine slope and basin floor matrix-rich beds, Neoproterozoic Windermere Supergroup, British Columbia, Canada: Unpublished M.Sc. thesis, University of Ottawa, 152 p.

Angus, K., Arnott, R. W. C., and Terlaky, V., 2019, Lateral and vertical juxtaposition of matrix-rich and matrix-poor lithologies caused by particle settling in mixed mud–sand deep-marine sediment suspensions: Sedimentology, v. 66, p. 940-962.

Arnott, R. W. C., 2007a, Stratal architecture and origin of lateral accretion deposits (LADs) and conterminuous inner-bank levee deposits in a base-of-slope sinuous channel, lower Isaac Formation (Neoproterozoic), East-Central British Columbia, Canada: Marine and Petroleum Geology, v. 24, p. 515-528.

Arnott, R. W. C., 2007b, Stratigraphic architecture and depositional processes of a proximal crevasse splay and genetically related, sinuous channel fill, Isaac Formation, British

Columbia, Canada, *in* Nilsen, T.H., Shew, R.D., Steffens, G.S., and Studlick, J.R.J., eds., Atlas of Deep-Water Outcrops: AAPG Studies in Geology, v. 56, p. 111-114

Arnott, R.W.C., and Hand, B.M., 1989, Bedforms, primary structures and grain fabric in the presence of suspended sediment rain: Journal of Sedimentary Research, v. 59, p. 1062-1069.

Arnott, R.W.C., Tilston, M., Fraino, P., Navarro, L., Dumouchel, G., and Miklovich, N., 2021, Laterally accreting sinuous channels and their deposits: The Goldilocks of deep-water slope systems: Journal of Sedimentary Research, v. 91, p. 452-463.

Audley-Charles, M.G., 1967, Greywackes with a primary matrix from the Viqueque Formation (upper Miocene-Pliocene), Timor: Journal of Sedimentary Petrology, v. 37, p. 5–11.

Awadallah, S. A. M., 2002, Architecture and depositional history of the Lower cloridorme formation, Gaspé Peninsula, Québec, Canada: Unpublished Ph.D. thesis, Memorial University of Newfoundland, 376 p.

Awadallah, S. A., and Hiscott, R. N., 2004, High-resolution stratigraphy of the deep-water lower Cloridorme Formation (Ordovician), Gaspé Peninsula, based on K-bentonite and megaturbidite correlations: Canadian Journal of Earth Sciences, v. 41, p. 1299-1317.

Azpiroz-Zabala, M., Cartigny, M. J. B., Talling, P. J., Parsons, D. R., Sumner, E. J., Clare, M. A., Simmons, S. M., Cooper, C., and Pope, E. L., 2017, Newly recognized turbidity current structure can explain prolonged flushing of submarine canyons: Science Advances, v. 3, e1700200.

Baas, J.H., and Best, J.L., 2002, Turbulence modulation in clay-rich sediment-laden flows and some implications for sediment deposition: Journal of Sedimentary Research, v. 72, p. 336-340.

Baas, J. H., Best, J. L., Peakall, J., and Wang, M., 2009, A Phase Diagram for Turbulent, Transitional, and Laminar Clay Suspension Flows: Journal of Sedimentary Research, v. 79, p. 162-183.

Baas, J.H., Best, J.L., and Peakall, J., 2011, Depositional processes, bedform development and hybrid bed formation in rapidly decelerated cohesive (mud–sand) sediment flows: Sedimentology, v. 58, p. 1953-1987.

Baas, J.H., Best, J.L., and Peakall, J., 2016a, Predicting bedforms and primary current stratification in cohesive mixtures of mud and sand: Journal of the Geological Society, v. 173, p. 12-45.

Baas, J.H., Best, J.L., and Peakall, J., 2016b, Comparing the transitional behaviour of kaolinite and bentonite suspension flows: Earth Surface Processes and Landforms, v. 41, p. 1911-1921.

Baas, J.H., Tracey, N.D., and Peakall, J., 2021, Sole marks reveal deep-marine depositional process and environment: Implications for flow transformation and hybrid event bed models: Journal of Sedimentary Research, v. 91, p. 986-1009.

Bailey, E.B., 1930, New light on sedimentation and tectonics: Geological Magazine, v. 67, p. 77-92.

Baker, M.L., and Baas, J.H., 2020, Mixed sand–mud bedforms produced by transient turbulent flows in the fringe of submarine fans: Indicators of flow transformation: Sedimentology, v. 67, p. 2645-2671.

Balachandar, S., and Eaton, J.K., 2010. Turbulent dispersed multiphase flow: Annual review of fluid mechanics, v. 42, p. 111-133.

Baltzer, A., Cochonat, P., and Piper, D. J. W., 1994, In situ geotechnical characterization of sediments on the Nova Scotian Slope, eastern Canadian continental margin: Marine Geology, v. 120, p. 291-308.

Barnes, H.A., Hutton, J.F., and Walters, K., 1989, An introduction to rheology (Vol. 3): Elsevier, 220 p.

Barker, S.P., Haughton, P.D., McCaffrey, W.D., Archer, S.G., and Hakes, B., 2008, Development of rheological heterogeneity in clay-rich high-density turbidity currents: Aptian Britannia Sandstone Member, UK continental shelf: Journal of Sedimentary Research, v. 78, p. 45-68.

Batchelor, G.K., and Green, J., 1972, The determination of the bulk stress in a suspension of spherical particles to order c2: Journal of Fluid Mechanics, v. 56, p. 401-427.

Bates, C.C., 1953, Rational theory of delta formation: American Association Petroleum Geologists, Bulletin, v. 37, p. 2119-2162.

Beeden, D.R., 1983, Sedimentology of some turbidites and related rocks from the Cloridorme Group, Ordovician, Quebec: Unpublished MSc. thesis, McMaster University, 229 p.

Bennett, H.R., O'Brian, N.R. and Hulbert, M. H., 1992, Determinants of Clay and Shale Microfabric Signatures: Processes and Mechanisms, *in* Bennett, H.R., Bryant, W.R., and Hulbert, M. H., eds., Microstructure of Fine-Grained Sediments: From Mud to Shale: Springer- Verlag, New York, v. 4, p. 5-32.

Bennett, S. J., Hou, Y., and Atkinson, J. F., 2014, Turbulence suppression by suspended sediment within a geophysical flow: Environmental Fluid Mechanics, v. 14, p. 771-794.

Berlamont, J., Ockenden, M., Toorman, E., and Winterwerp, J., 1993, The characterisation of cohesive sediment properties. Coastal Engineering, v. 21, p. 105-128.

Best, J. L., Kostaschuk, R. A., Peakall, J., Villard, P. V., and Franklin, M., 2005, Whole flow field dynamics and velocity pulsing within natural sediment-laden underflows. Geology, v. 33, p. 765-768.

Best, J., Bennett, S., Bridge, J., and Leeder, M., 1997, Turbulence modulation and particle velocities over flat sand beds at low transport rates: Journal of Hydraulic Engineering, v. 123, p. 1118-1129.

Bhaskar, P. V., and Bhosle, N. B., 2005, Microbial extracellular polymeric substances in marine biogeochemical processes: Current Science, v. 88, p. 45-53.

Bokman, J., 1955, Sandstone classification: relation to composition and texture: Journal of Sedimentary Petrology, v. 25, p. 201–206.

Boswell, P.G.H., 1930, The action of colloids in precipitating fine-grained sediments: Geological Magazine, v. 67, p. 371–381.

Bouma, A. H., 1962, Sedimentology of some Flysch deposits: a graphic approach to facies interpretation: Published Ph.D. (Doctoral dissertation), Elsevier, 168p.

Brooks, H.L., Hodgson, D.M., Brunt, R.L., Peakall, J., Hofstra, M., and Flint, S.S., 2018, Deep-water channel-lobe transition zone dynamics: Processes and depositional architecture, an example from the Karoo Basin, South Africa: Geological Society of America Bulletin, v. 130, p. 1723–1746.

Buller, A.T., and McManus, J., 1972, Modes of turbidite deposition deduced from grain-size analyses: Geological Magazine, v. 109, p. 491–500.

Burgess, P. M., Masiero, I., Toby, S. C., and Duller, R. A., 2019, A big fan of signals? Exploring autogenic and allogenic process and product in a numerical stratigraphic forward model of submarine-fan development: Journal of Sedimentary Research, v. 89, p. 1-12.

Campbell, R. B., Mountjoy E. W., and Young F. G., 1973, Geology of McBride map-area, British Columbia: Geological Survey of Canada, v. 72, 104 p.

Canals, M., Lastras, G., Urgeles, R., Casamor, J. L., Mienert, J., Cattaneo, A., De Batist, M., Haflidason, H., Imbo, Y., Laberg, J. S., Locat, J., Long, D., Longva, O., Masson, D. G.,

Sultan, N., Trincardi, F., and Bryn, P., 2004, Slope failure dynamics and impacts from seafloor and shallow sub-seafloor geophysical data: Case studies from the COSTA project: Marine Geology, v. 213, p. 9–72.

Cantelli, A., Pirmez, C., Johnson, S., and Parker, G., 2011, Morphodynamic and stratigraphic evolution of self-channelized subaqueous fans emplaced by turbidity currents: Journal of Sedimentary Research, v. 81, p. 233-247.

Cantero, M.I., Balachandar, S., and Parker, G., 2009, Direct numerical simulation of stratification effects in a sediment-laden turbulent channel flow: Journal of Turbulence, v. 10, p. 1-28.

Cantero, M.I., Cantelli, A., Pirmez, C., Balachandar, S., Mohrig, D., Hickson, T.A., Yeh, T.H., Naruse, H., and Parker, G., 2012a, Emplacement of massive turbidites linked to extinction of turbulence in turbidity currents: Nature Geoscience, v. 5, p. 42-45.

Cantero, M.I., Shringarpure, M., and Balachandar, S., 2012b. Towards a universal criteria for turbulence suppression in dilute turbidity currents with non-cohesive sediments: Geophysical Research Letters, v. 39, L14603.

Carr, D.D., Horowitz, A., Hrabar, S.V., Ridge, K.F., Rooney, R., Straw, W.T., Webb, W., and Potter, P.E., 1966, Stratigraphic sections, bedding sequences, and random processes: Science, v. 154, p. 1162–1164.

Cartigny, M. J. B., Eggenhuisen, J. T., Hansen, E. W. M., and Postma, G., 2013, Concentration-dependent flow stratification in experimental high-density turbidity currents and their relevance to turbidite facies models: Journal of Sedimentary Research, v. 83, p. 1046-1064.

Cerato, A.B., and Lutenegger, A.J., 2002, Determination of surface area of fine-grained soils by the ethylene glycol monoethyl ether (EGME) method: Geotechnical Testing Journal, v. 25, p. 315-321.

Chien, N., and Wan, Z., 1999, Mechanics of sediment transport: American Society of Civil Engineers, 913 p.

Cochrane, D., 2018, Stratigraphic and Carbon Isotope Evolution of an Ediacaran Mixed Siliciclastic Deep-Marine Base-of-Slope System, First Isaac Carbonate, Windermere Supergroup, Canadian Cordillera, British Columbia: Unpublished MSc. thesis, University of Ottawa, 211 p.

Cochrane, D.J., Navarro, L. and Arnott, R.W.C., 2019, Sedimentological and geochemical evolution of an Ediacaran mixed carbonate-siliciclastic continental slope system,

Windermere Supergroup, southern Canadian Cordillera, British Columbia, Canada: Precambrian Research, v. 327, p. 47-67.

Colpron, M., Logan, J.M., and Mortensen, J.K., 2002, U-Pb zircon age constraint for late Neoproterozoic rifting and initiation of the lower Paleozoic passive margin of western Laurentia: Canadian Journal of Earth Sciences, v. 39, 133-143.

Crook, K.A., 1960, Classification of arenites: American Journal of Science, v. 258, p. 419-428.

Cummins, W.A., 1962, The greywacke problem: Geological Journal, v. 3, p. 51-72.

Cunningham, C.M., and Arnott, R.W.C., 2021, Systematic organization of thin-bedded turbidites in ancient deep-marine levees: possible evidence of rhythmic pulsing in turbidity currents: Journal of Sedimentary Research, v. 91, p. 1257-1274.

Cuthbertson, A., Dong, P., King, S., and Davies, P., 2008, Hindered settling velocity of cohesive/non-cohesive sediment mixtures: Coastal Engineering, v. 55, p. 1197-1208.

Dade, W. B., Davis, J. D., Nichols, P. D., Nowell, A. R. M., Thistle, D., Trexler, M. B., White, D. C., and Davis, J. D., 1990, Effects of bacterial exopolymer adhesion on the entrainment of sand: Geomicrobiology Journal, v. 8, p. 1-16.

Dade, W. B., Self, R. L., Pellerin, N. B., Moffet, A., Jumars, P. A., and Nowell, A. R. M., 1996, The effects of bacteria on the flow behavior of clay-seawater suspensions: Journal of Sedimentary Research, v. 66, p. 39-42.

Dai, H., 2008, Analysis and modeling of plunging flows. Unpublished Ph.D. thesis, University of Illinois. 121 p.

Daniller-Varghese, M.S., Kim, W., and Mohrig, D.C., 2020, The effect of flood intermittency on bifurcations in fluviodeltaic systems: Experiment and theory: Sedimentology, v. 67, p. 3055-3066.

Dapples, E.C., and Mitchum, R.C., 1955, Petrographic characteristics of sandstones of the Pennsylvanian of the Central Appalachian Coal Field: Geological Society of America Bulletin, v. 66, 1547 p.

Dapples, E.C., Krumbein, W.C., and Sloss, L.L., 1953, Petrographic and lithologic attributes of sandstones: The Journal of Geology, v. 61, p. 291–317.

Davarpanah Jazi, S., and Wells, M. G., 2016, Enhanced sedimentation beneath particle-laden flows in lakes and the ocean due to double-diffusive convection: Geophysical Research Letters, v. 43, p. 10883-10890.

Davarpanah Jazi, S., and Wells, M. G., 2020, Dynamics of settling-driven convection beneath a sediment-laden buoyant overflow: Implications for the length-scale of deposition in lakes and the coastal ocean: Sedimentology, v. 67, p. 699-720.

Davies, R., 1968, The experimental study of the differential settling of particles in suspension at high concentrations: Powder Technology, v. 2, p. 43-51.

Davis, J.C., 1986, Statistics and Data Analysis in Geology: New York, John Wiley and Sons, 646 p.

Davis, R.H., and Birdsell, K.H., 1988, Hindered settling of semidilute monodisperse and polydisperse suspensions: American Institute of Chemical Engineers Journal, v. 34, p. 123-129.

Davis, C., Haughton, P., McCaffrey, W., Scott, E., Hogg, N., and Kitching, D., 2009, Character and distribution of hybrid sediment gravity flow deposits from the outer Forties Fan, Palaeocene Central North Sea, UKCS: Marine and Petroleum Geology, v. 26, p. 1919-1939.

Davis, L., 2011, Architecture of deep-marine interchannel deposits: Isaac Formation, Windermere Supergroup (Neoproterozoic), southern Canadian Cordillera: Unpublished M.Sc. thesis, University of Ottawa, 188 p.

Deptuck, M. E., Piper, D. J. W., Savoye, B., and Gervais, A., 2008, Dimensions and architecture of late Pleistocene submarine lobes off the northern margin of East Corsica: Sedimentology, v. 55, p. 869-898.

Dorrell, R., and Hogg, A.J., 2010, Sedimentation of bidisperse suspensions: International Journal of Multiphase Flow, v. 36, p. 481-490.

Dorrell, R.M., Hogg, A.J., Sumner, E. J., and Talling, P.J., 2011, The structure of the deposit produced by sedimentation of polydisperse suspensions: Journal of Geophysical Research: Earth Surface, v. 116, no. F01024.

Dorrell, R.M., Peakall, J., Darby, S.E., Parsons, D.R., Johnson, J., Sumner, E.J., Wynn, R.B., Özsoy, E., and Tezcan, D.E.V.R.İ.M., 2019, Self-sharpening induces jet-like structure in seafloor gravity currents: Nature Communications, v. 10, p.1-10.

Dott, R.H., 1964, Wacke, graywacke and matrix; what approach to immature sandstone classification?: Journal of Sedimentary Research, v. 34, p. 625-632.

Druitt, T.H., 1995, Settling behaviour of concentrated dispersions and some volcanological Applications: Journal of Volcanology and Geothermal Research, v. 65, p. 27-39.

Dumouchel, I.G., 2015, Stratigraphic architecture and depositional history of laterally-accreted channel fills in the lower Isaac Formation, Windermere Supergroup, British Columbia, Canada, Unpublished M.Sc. thesis, 108 p.

Dunbar, C.O., and Rodgers, J., 1957, Principles of stratigraphy: John Wiley and Sons, New York, 356 p.

Duringer, P., Paicheler, J. C., and Schneider, J. L., 1991, Un courant d'eau continu peut-il générer des turbidites? Résultats d'expérimentations analogiques: Marine Geology, v. 99, p. 231-246.

Eggenhuisen, J.T., Cartigny, M.J., and de Leeuw, J., 2017, Physical theory for near-bed turbulent particle suspension capacity: Earth Surface Dynamics, v. 5, p. 269-281.

Ehlers, C. J., Chen, J., Roberts, H. H., and Lee, Y. C., 2005, The origin of near-seafloor crust zones in deepwater, *in* Proceedings of the International Symposium on Frontiers in Offshore Geotechnics: ISFOG 2005, Perth, p. 927-934.

Einstein, A., 1905, Eine neue bestimmung der moleküldimensionen: Doctoral dissertation, ETH Zurich, 25 p.

Einstein, A., 1911, Berichtigung zu meiner arbeit: Eine neue bestimmung der moleküldimensionen: Annalen der Physik, v. 339, p. 591-592.

Elghobashi, S., 1994, On predicting particle-laden turbulent flows: Applied Scientific Research, v. 52, p. 309-329.

Enos, P., 1969, Anatomy of a flysch: Journal of Sedimentary Petrology, v. 39, p. 680-723.

Evenchick, C.A., Parrish, R.R., and Gabrielse, H., 1984, Precambrian gneiss and Late Proterozoic sedimentation in north-central British Columbia: Geology, v. 12, p. 233-237.

Ferguson, R. A., Kane, I. A., Eggenhuisen, J. T., Pohl, F., Tilston, M., Spychala, Y. T., and Brunt, R. L., 2020, Entangled external and internal controls on submarine fan evolution: an experimental perspective: The Depositional Record, p. 1-20.

Fernandez, R. L., Cantelli, A., Pirmez, C., Sequeiros, O., and Parker, G., 2014, Growth patterns of subaqueous depositional channel lobe systems developed over a basement with a downdip break in slope: Laboratory experiments: Journal of Sedimentary Research, v. 84, p. 168-182.

Fidolini, F., and Ghinassi, M., 2016, Friction and inertia-dominated effluents in a lacustrine, river-dominated deltaic succession (Pliocene upper Valdarno Basin, Italy): Journal of Sedimentary Research, v. 86, p. 1083-1101.

Fildani, A., Clark, J., Covault, J.A., Power, B., Romans, B.W., and Aiello, I.W., 2018, Muddy sand and sandy mud on the distal Mississippi fan: Implications for lobe depositional processes: Geosphere, v. 14, p. 1051–1066.

Fisher, R.V., 1983, Flow transformation in sediment gravity flows: Geology, v. 11, p. 273-274.

Folk, R.L., 1954, The distinction between grain size and mineral composition in sedimentary-rock nomenclature: The Journal of Geology, v. 62, p. 344-359.

Folk, R.L., 1974, Petrology of Sedimentary Rocks: Hemphill, Publishing Company, Austin, TX, 182 p.

Fonnesu, M., Felletti, F., Haughton, P. D., Patacci, M., and McCaffrey, W. D., 2018, Hybrid event bed character and distribution linked to turbidite system sub-environments: The North Apennine Gottero Sandstone (north-west Italy): Sedimentology, v. 65, p. 151-190.

Fonnesu, M., Haughton, P., Felletti, F., and McCaffrey, W., 2015, Short length-scale variability of hybrid event beds and its applied significance: Marine and Petroleum Geology, v. 67, p. 583-603.

Fonnesu, M., Patacci, M., Haughton, P. D., Felletti, F., and McCaffrey, W. D., 2016, Hybrid event beds generated by local substrate delamination on a confined-basin floor: Journal of Sedimentary Research, v. 86, p. 929-943.

Galloway, W.E., 1974, Deposition and diagenetic alteration of sandstone in northeast Pacific arc-related basins: implications for graywacke genesis: Geological Society of America Bulletin v. 85, p. 379-390.

Gervais, A., Savoye, B., Mulder, T., and Gonthier, E., 2006, Sandy modern turbidite lobes: A new insight from high resolution seismic data: Marine and Petroleum Geology, v. 23, p. 485-502.

Gilbert, C.M., 1954, Sedimentary rocks, *in* Williams, H., Turner, F.J., and Gilbert, C.M., eds., Petrography, San Francisco, W.H. Freeman and Company, 406 p.

Girard, F., Ghienne, J.F., and Rubino, J.L., 2012, Occurrence of hyperpycnal flows and hybrid event beds related to glacial outburst events in a Late Ordovician proglacial delta (Murzuq Basin, SW Libya): Journal of Sedimentary Research, v. 82, p. 688-708.

Gore, R.A., and Crowe, C.T., 1989, Effect of particle size on modulating turbulent intensity: International Journal of Multiphase Flow, v. 15, p. 279-285.

Gutenberg, B., 1939, Tsunamis and earthquakes: Bulletin of the Seismological Society of America, v. 29, p. 517-526.

Hadlari, T., Arnott, R.W.C, Mathews, W.A., Poulton, T.P., and Madronich, L.I., 2021, Provenance of the incipient passive margin of NW Laurentia (Neoproterozoic): detrital zircon from continental slope and basin floor deposits of the Windermere Supergroup, southern Canadian Cordillera: Lithosphere, v. 2021, 10 p.

Hailwood, E., and Ding, F., 2000, Sediment transport and dispersal pathways in the Lower Cretaceous sands of the Britannia Field, derived from magnetic susceptibility: Petroleum Geoscience, v. 6, p. 369-379.

Hamilton, D.A., 2002, Mafic and felsic derived soils in the Georgia Piedmont: parent material uniformity, reconstruction, and trace metal contents: Unpublished MSc. thesis, University of Georgia, 70 p.

Hamilton, P.B., Strom, K.B., and Hoyal, D.C., 2015, Hydraulic and sediment transport properties of autogenic avulsion cycles on submarine fans with supercritical distributaries: Journal of Geophysical Research: Earth Surface, v. 120, p.1369-1389.

Hampton, M., 1975, Competence of fine-grained debris flows: Journal of Sedimentary Research, v. 45, p. 834–844.

Haughton, P. D. W., Barker, S. P., and McCaffrey, W. D., 2003, “Linked” debrites in sand-rich turbidite systems - Origin and significance: Sedimentology, v. 50, p. 459-482.

Haughton, P., Davis, C., McCaffrey, and W., Barker, S., 2009, Hybrid sediment gravity flow deposits–classification, origin and significance: Marine and Petroleum Geology, v. 26, p. 1900-1918.

Hay, R.L., 1957, Mineral alterations in rocks of Middle Eocene age, Absaroka Range, Wyoming: Journal of Sedimentary Petrology, v. 27, p. 32–40.

Heezen, B.C., and Ewing, W.M., 1952, Turbidity currents and submarine slumps, and the 1929 Grand Banks [Newfoundland] earthquake: American Journal of Science, v. 250, p. 849-873.

Hermidas, N., Eggenhuisen, J.T., Jacinto, R.S., Luthi, S.M., Toth, F., and Pohl, F., 2018, A classification of clay-rich subaqueous density flow structures: Journal of Geophysical Research: Earth Surface, v. 123, p. 945-966.

Hetsroni, G., 1989, Particles–turbulence interaction: International Journal of Multiphase Flow, v. 15, p. 735-746.

Hiscott, R.N., 1984, Ophiolitic source rocks for Taconic-age flysch: Trace-element evidence: Geological Society of America Bulletin, v. 95, p. 1261-1267.

Hiscott, R.N., and Middleton, G.V., 1979, Depositional mechanics of thick-bedded sandstones at the base of a submarine slope, Tourelle Formation (Lower Ordovician), Quebec, Canada. Society of Economic Paleontologists and Mineralogists, Special Publication, v. 27, p. 307-326.

Hiscott, R.N., Pickering, K.T., and Beeden, D. R., 1986, Progressive filling of a confined Middle Ordovician foreland basin associated with the Taconic Orogeny, Québec, Canada, *in* Allen, P.A., and Homewood, P., eds., Foreland basins: International Association of Sedimentologists, Special Publication 8, p. 309-325.

Ho, V. L., Dorrell, R. M., Keevil, G. M., Burns, A. D., and McCaffrey, W. D., 2018a, Pulse propagation in turbidity currents: Sedimentology, v. 65, p. 620-637.

Ho, V. L., Dorrell, R. M., Keevil, G. M., Burns, A. D., and McCaffrey, W. D., 2018b, Scaling analysis of multipulsed turbidity current evolution with application to turbidite interpretation: Journal of Geophysical Research: Oceans, v. 123, p. 3668-3684.

Hodgson, D. M., 2009, Distribution and origin of hybrid beds in sand-rich submarine fans of the Tanqua depocentre, Karoo Basin, South Africa: Marine and Petroleum Geology, v. 26, p. 1940-1956.

Hodgson, D. M., Flint, S. S., Hodgetts, D., Drinkwater, N. J., Johannessen, E. P., and Luthi, S. M., 2006, Stratigraphic evolution of fine-grained submarine fan systems, Tanqua depocenter, Karoo Basin, South Africa: Journal of Sedimentary Research, v. 76, p. 20-40.

Hollister, C.D., and Heezen, B.C., 1964, Modern graywacke-type sands: Science, v. 146, p. 1573-1574.

Hoyal, D. C., Bursik, M. I., and Atkinson, J. F., 1999, Settling-driven convection: A mechanism of sedimentation from stratified fluids: Journal of Geophysical Research: Oceans, v. 104, p. 7953-7966.

Hubert, J.F., 1960, Petrology of the Fountain and Lyons formations, Front Range. Colorado School of Mines Quarterly, v. 55, p. 725-737.

Huckenholz, H.G., 1963, Mineral composition and texture in graywackes from the Harz Mountains (Germany) and in arkoses from the Auvergne (France): Journal of Sedimentary Petrology, v. 33, p. 914-918.

Hughes Clarke, J. E., 2016, First wide-angle view of channelized turbidity currents links migrating cyclic steps to flow characteristics: Nature Communications, v. 7, p. 1-13.

Hussain, A., Haughton, P.D., Shannon, P.M., Morris, E.A., Pierce, C.S., and Omma, J.E., 2021. Mud-forced turbulence dampening facilitates rapid burial and enhanced preservation of terrestrial organic matter in deep-sea environments: Marine and Petroleum Geology, v. 130, 105101.

Hussain, A., Haughton, P.D., Shannon, P.M., Turner, J.N., Pierce, C.S., Obradors-Latre, A., Barker, S.P., and Martinsen, O.J., 2020, High-resolution X-ray fluorescence profiling of hybrid event beds: Implications for sediment gravity flow behaviour and deposit structure: Sedimentology, v. 67, p. 2850-2882.

Ito, M., 2008, Downfan transformation from turbidity currents to debris flows at a channel-to-lobe transitional zone: the lower Pleistocene Otadai Formation, Boso Peninsula, Japan: Journal of Sedimentary Research, v. 78, p. 668-682.

Jackson, C.A.L., Zakaria, A.A., Johnson, H.D., Tongkul, F., and Crevello, P.D., 2009. Sedimentology, stratigraphic occurrence and origin of linked debrites in the West Crocker Formation (Oligo-Miocene), Sabah, NW Borneo. Marine and Petroleum Geology, v. 26, p. 1957–1973.

Jameson, R., 1808, A system of mineralogy, volume 3: Archibald Constable and Co, Edinburgh, 368 p.

Jegou, I., Savoye, B., Pirmez, C., and Droz, L., 2008, Channel-mouth lobe complex of the recent Amazon Fan: The missing piece: Marine Geology, v. 252, p. 62-77.

Jiang, W. T., and Peacor, D. R., 1994, Prograde transitions of corrensite and chlorite in low-grade pelitic rocks from the Gaspe Peninsula, Quebec: Clays and Clay Minerals, v. 42, p. 497-517.

Jin, L., Shan, X., Shi, X., Fonnesu, M., Qiao, S., Kandasamy, S., Wang, H., Liu, S., Fang, X., and Zou, X., 2021, Hybrid event beds generated by erosional bulking of modern hyperpycnal flows on the Choshui River delta front, Taiwan Strait: Sedimentology, v. 68, p. 2500-2522.

Jobe, Z. R., Sylvester, Z., Howes, N., Pirmez, C., Parker, A., Cantelli, A., Smith, R., Wolinsky, M. A., O'Byrne, C., Slowey, N., and Prather, B., 2017, High-resolution, millennial-scale

patterns of bed compensation on a sand-rich intraslope submarine fan, western Niger Delta slope: Geological Society of America Bulletin, v. 129, p. 23-37.

Julien, P. S., and Hubert, C., 1975, Evolution of the Taconian orogen in the Quebec Appalachians: American Journal of Science, v. 275, p. 337-362.

Kane, I. A., and Pontén, A. S. M., 2012, Submarine transitional flow deposits in the Paleogene Gulf of Mexico: Geology, v. 40, p. 1119-1122.

Kane, I. A., Pontén, A. S. M., Vangdal, B., Eggenhuisen, J. T., Hodgson, D. M., and Spychala, Y. T., 2017, The stratigraphic record and processes of turbidity current transformation across deep-marine lobes: Sedimentology, v. 64, p. 1236-1273.

Keeley, J.A., Link, P.K., Fanning, C.M. and Schmitz, M.D., 2013, Pre-to synglacial rift-related volcanism in the Neoproterozoic (Cryogenian) Pocatello Formation, SE Idaho: New SHRIMP and CA-ID-TIMS constraints: Lithosphere, v. 5, p. 128-150.

Kelly, R. W., Dorrell, R. M., Burns, A. D., and McCaffrey, W. D., 2019, The Structure and Entrainment Characteristics of Partially Confined Gravity Currents: Journal of Geophysical Research: Oceans, v. 124, p. 2110-2125.

Kendall, B.S., Creaser, R.A., Ross, G.M. and Selby, D., 2004, Constraints on the timing of Marinoan "Snowball Earth" glaciation by 187Re–187Os dating of a Neoproterozoic, post-glacial black shale in Western Canada: Earth and Planetary Science Letters, v. 222, p. 729-740.

Khan, Z., 2012, Origin and architecture of deep-water levee deposits: insight from the ancient rock record and experiments: Unpublished Ph.D. thesis, University of Ottawa, 312 p.

Khan, Z.A., and Arnott, R.W.C., 2011, Stratal attributes and evolution of asymmetric inner- and outer-bend levee deposits associated with an ancient deep-water channel-levee complex within the Isaac Formation, southern Canada, Marine and Petroleum Geology, v. 28, p. 824-842.

Khripounoff, A., Crassous, P., Lo Bue, N., Dennielou, B., and Silva Jacinto, R., 2012, Different types of sediment gravity flows detected in the Var submarine canyon (northwestern Mediterranean Sea): Progress in Oceanography, v. 106, p. 138-153.

Klein, G.D.V., 1963, Analysis and review of sandstone classifications in the North American geological literature, 1940–1960: Geological Society of America Bulletin, v. 75, p. 555-576.

Kneller, B., and Buckee, C., 2000, The structure and fluid mechanics of turbidity currents: A review of some recent studies and their geological implications: Sedimentology, v. 47, p. 62-94.

Koo, W. M., Mohrig, D., Buttles, J., Sturmer, D., Pontén, A., and Hess, T., 2020, Sand–mud couplets deposited by spontaneous remobilization of subaqueous transitional flows: Sedimentology, v. 67, p. 78-95.

Kostaschuk, R., Nasr-Azadani, M. M., Meiburg, E., Wei, T., Chen, Z., Negretti, M. E., Best, J., Peakall, J., and Parsons, D. R., 2018, On the Causes of Pulsing in Continuous Turbidity Currents: Journal of Geophysical Research: Earth Surface, v. 123, p. 2827-2843.

Krynine, P.D., 1937, Petrography and genesis of the Siwalik Series: American Journal of Science, v. 5, p. 422-446.

Krynine, P.D., 1948, The megascopic study and field classification of sedimentary rocks: The Journal of Geology, v. 56, p. 130-165.

Kuenen, P.H., 1966, Matrix of turbidites: experimental approach: Sedimentology, v. 7, p. 267-297.

Lagaly, G., 1989, Principles of flow of kaolin and bentonite dispersions, Applied Clay Science, v. 4, p. 105-123.

Lang, J., Fedele, J.J., and Hoyal, D.C., 2021, Three-dimensional submerged wall jets and their transition to density flows–morphodynamics and implications for the depositional record: Sedimentology, v. 68, p. 1297-1327.

Larue, D. K., and Provine, K. G., 1988, Vacillatory turbidites, Barbados: Sedimentary geology, v. 57, p. 211-219.

Leclair, S.F., and Arnott, R.W.C., 2005, Parallel lamination formed by high-density turbidity currents: Journal of Sedimentary Research, v. 75, p.1-5.

Lehrmann, D.J., and Goldhammer, R.K., 1999, Secular variation in parasequence and facies stacking patterns of platform carbonates: a guide to application of stacking pattern analysis in strata of diverse ages and settings, in Harris, P.M., Saller, A.H., and Simo, J.A., eds., Advances in Carbonate Sequence Stratigraphy: Application to Reservoirs, Outcrops and Models: SEPM, Special Publication 63, p. 187–225.

Liu, J. T., Wang, Y. H., Yang, R. J., Hsu, R. T., Kao, S. J., Lin, H. L., and Kuo, F. H., 2012, Cyclone-induced hyperpycnal turbidity currents in a submarine canyon: Journal of Geophysical Research: Oceans, v. 117, C04033.

Liu, Z., Colin, C., Li, X., Zhao, Y., Tuo, S., Chen, Z., Siringan, F.P., Liu, J.T., Huang, C.Y., You, C.F., and Huang, K.F., 2010, Clay mineral distribution in surface sediments of the northeastern South China Sea and surrounding fluvial drainage basins: source and transport: Marine Geology, v. 277, p. 48-60.

Liu, Z., Zhao, Y., Colin, C., Siringan, F.P., and Wu, Q., 2009, Chemical weathering in Luzon, Philippines from clay mineralogy and major-element geochemistry of river sediments: Applied Geochemistry, v. 24, p. 2195-2205.

Lockett, M.J., and Al-Habbooby, H.M., 1974, Relative particle velocities in two-species settling. Powder technology, v. 10, p. 67-71.

Lovell, J.P.B., 1972, Diagenetic origin of graywacke matrix minerals: a discussion: Sedimentology, v. 19, p. 141-143.

Lowe, D.R., 1982, Sediment gravity flows; II, depositional models with special reference to the deposits of high-density turbidity currents: Journal of Sedimentary Research, v. 52, p. 279-297.

Lowe, D.R., 1982, Sediment gravity flows; II, Depositional models with special reference to the deposits of high-density turbidity currents: Journal of sedimentary research, v. 52, p. 279-297.

Lowe, D.R., and Guy, M., 2000, Slurry-flow deposits in the Britannia Formation (Lower Cretaceous), North Sea: a new perspective on the turbidity current and debris flow problem: Sedimentology, v. 47, p. 31-70.

Lowe, D.R., Guy, M., and Palfrey, A., 2003, Facies of slurry-flow deposits, Britannia Formation (Lower Cretaceous), North Sea: implications for flow evolution and deposit geometry: Sedimentology, v. 50, p. 45-80.

Lund, K., Aleinikoff, J.N., Evans, K.V. and Fanning, C.M., 2003, SHRIMP U-Pb geochronology of Neoproterozoic Windermere Supergroup, central Idaho: Implications for rifting of western Laurentia and synchroneity of Sturtian glacial deposits: Geological Society of America Bulletin, v. 115, p. 349-372.

Ma, C., 1996, Continuity of sandstone beds in the Ordovician Cloridorme Formation Gaspé Peninsula, Quebec: Unpublished MSc. thesis, Memorial University of Newfoundland, 105 p.

Macdonald, F.A., Schmitz, M.D., Strauss, J.V., Halverson, G.P., Gibson, T.M., Eyster, A., Cox, G., Mamrol, P. and Crowley, J.L., 2018, Cryogenian of Yukon: Precambrian Research, v. 319, p.114-143.

Marsset, T., Droz, L., Dennielou, B., and Pichon, E., 2009, Cycles in the Architecture of the Quaternary Zaire Turbidite System: A Possible Link with Climate. External Controls of Deep-Water Depositional Systems: SEPM, Special Publication 92, p. 89-106.

McAnally, W. H., Friedrichs, C., Hamilton, D., Hayter, E., Shrestha, P., Rodriguez, H., Sheremet, A., and Teeter, A., 2007, Management of Fluid Mud in Estuaries, Bays, and Lakes. I: Present State of Understanding on Character and Behavior: Journal of Hydraulic Engineering, v. 133, p. 9-22.

McMechan, M. E., 2015, The Neoproterozoic succession of the central Rocky Mountains, Canada: Bulletin of Canadian Petroleum Geology, v. 63, p. 243-273.

Meadows, A., and Meadows, P. S., 1994, Bioturbation in deep sea Pacific sediments: Journal of the Geological Society, v. 151, p. 361-375.

Meiburg, E., and Kneller, B., 2010, Turbidity currents and their deposits: Annual Review of Fluid Mechanics, v. 42, p.135-156.

Menczel, A., and Kostaschuk, R., 2013, Interfacial Waves as Coherent Flow Structures associated with Continuous Turbidity Currents: Lillooet Lake, Canada, *in* Venditti, J.G., Best, J.L., Church, M., and Hardy, R.J., eds., Coherent Flow Structures at Earth's Surface: John Wiley and Sons, p. 371-383.

Mesri, G., and Olson, R.E., 1971, Mechanisms controlling the permeability of clays: Clays and Clay minerals, v. 19, p. 151-158.

Metzner, A.B., 1985, Rheology of suspensions in polymeric liquids: Journal of Rheology, v. 29, p. 739-775.

Middleton, G. V., 1966, Experiments on Density and Turbidity Currents: I. Motion of the Head: Canadian Journal of Earth Sciences, v. 3, p. 523-546.

Middleton, G.V., and Hampton, M.A., 1973, Sediment gravity flows: mechanics of flow and deposition, in Middleton, G.V., and Bouma, A.H., eds., Turbidity and Deep-Water Sedimentation, SEPM Pacific Section, Short Course Lecture Notes, p. 1-38.

Mooney, M., 1951, The viscosity of a concentrated suspension of spherical particles: Journal of Colloid Science, v. 6, p. 162-170.

Mountjoy, E.W., and Aitken, J.D., 1963, Early Cambrian and later Precambrian paleocurrents, Banff and Jasper national parks, Bulletin of Canadian Petroleum Geology, v. 11, p. 161-168.

Mueller, P., Patacci, M., and Di Giulio, A., 2017, Hybrid event beds in the proximal to distal extensive lobe domain of the coarse-grained and sand-rich Bordighera turbidite system (NW Italy): Marine and Petroleum Geology, v. 86, p. 908-931.

Mulder, T., and Alexander, J. 2001, The physical character of subaqueous sedimentary density flow and their deposits: Sedimentology, v. 48, p. 269-299.

Muste, M., and Yu, K., 2005, Two-phase versus mixed-flow perspective on suspended sediment transport in turbulent channel flows: Water Resources Research, v. 41, W10402.

Nakajima, T., and Kanai, Y., 2000, Sedimentary features of seismoturbidites triggered by the 1983 and older historical earthquakes in the eastern margin of the Japan Sea: Sedimentary Geology, v. 135, p. 1-19.

Navarro, L., 2016, Stratigraphic architecture depositional processes and reservoir implications of the basin floor to slope transition, Neoproterozoic Windermere turbidite system, Canada: Unpublished Ph.D. thesis, University of Ottawa, 450 p.

Navarro, L., and Arnott, R.W.B.C., 2020, Stratigraphic record in the transition from basin floor to continental slope sedimentation in the ancient passive-margin Windermere turbidite system: Sedimentology, v. 67, p.1710-1749.

Nielsen, O.B., Rasmussen, E.S., and Thyberg, B.I., 2015, Distribution of clay minerals in the northern North Sea Basin during the Paleogene and Neogene: a result of source-area geology and sorting processes: Journal of Sedimentary Research, v. 85(6), p. 562-581.

Ningthoujam, J., Wearmouth, C., and Arnott, R.W.C., 2022, Stratal characteristic and depositional origin of two-part (mud-poor overlain by mud-rich) and associated deep-water strata—components in a lateral depositional continuum related to particle settling in negligibly sheared mud-rich suspensions: Journal of Sedimentary Research, v. 92, p. 503-529.

Normark, W.R., and Piper, D.J., 1991, Initiation processes and flow evolution of turbidity currents: implications for the depositional record, in Osborne, R.H., eds., From Shoreline to Abyss: Contributions in Marine Geology in Honor of Francis Parker Shepard, SEPM Special Publication, v. 46, p. 207-230.

O' Byrne, C.J., Barton, M.D., Steffens, G.S., Pirmez, C., and Buergisser, H., 2007, Architecture of a laterally migrating channel complex: channel 4, Isaac Formation, Windermere Supergroup, Castle Creek north, British Columbia, Canada, *in* Nilsen, T.H., Shew, R.D., Steffens, G.S., and Studlick, J.R.J., eds., Atlas of Deep-Water Outcrops: American Association of Petroleum Geologists, Studies in Geology 56, p. 115-118.

Ogg, C.M., and Smith, B.R., 1993, Mineral Transformations in Carolina Blue Ridge-Piedmont Soils Weathered from Ultramafic Rocks: Soil Science Society of America, Journal, v. 57, p. 461-472.

van Olphen, H., 1963, An Introduction to Clay Colloid Chemistry: New York, Interscience Publishers, 301 p.

Packham, G.H., 1954, Sedimentary structures as an important factor in the classification of sandstones: American Journal of Science, v. 252, p. 466-476.

Parkash, B., 1970, Downcurrent changes in sedimentary structures in Ordovician turbidite greywackes: Journal of Sedimentary Research, v. 40, p. 572-590.

Parkash, B., and Middleton, G. V., 1970, Downcurrent Textural Changes in Ordovician Turbidite Greywackes: Sedimentology, v. 14, p. 259-293.

Parkes, R. J., Cragg, B. A., and Wellsbury, P., 2000, Recent studies on bacterial populations and processes in subseafloor sediments: A review: Hydrogeology Journal, v. 8, p. 11-28.

Parrish, R.R., and Scammell, R.J., 1988, The age of the Mount Copeland syenite gneiss and its metamorphic zircons, Monashee Complex, southeastern British Columbia: Radiogenic age and isotopic studies: Report 2, Geological Survey of Canada Paper, v. 88, p. 21-28.

Parsons, J. D., Bush, J. W. M., and Syvitski, J. P. M., 2001, Hyperpycnal plume formation from riverine outflows with small sediment concentrations: Sedimentology, v. 48, p. 465-478.

Patacci, M., Haughton, P.D., and McCaffrey, W.D., 2014, Rheological complexity in sediment gravity flows forced to decelerate against a confining slope, Braux, SE France: Journal of Sedimentary Research, v. 84, p. 270-277.

Patacci, M., Marini, M., Felletti, F., Di Giulio, A., Setti, M., and McCaffrey, W., 2020, Origin of mud in turbidites and hybrid event beds: Insight from ponded mudstone caps of the Castagnola turbidite system (north-west Italy): Sedimentology, v. 67, p. 2625-2644.

Peakall, J., Best, J., Baas, J.H., Hodgson, D.M., Clare, M.A., Talling, P.J., Dorrell, R.M., and Lee, D.R., 2020, An integrated process-based model of flutes and tool marks in deep-water

environments: Implications for palaeohydraulics, the Bouma sequence and hybrid event beds: Sedimentology, v. 67, p. 1601-1666.

Perillo, M.M., Minton, B., Buttles, J., and Mohrig, D., 2015, Acoustic imaging of experimental subaqueous sediment-laden flows and their deposits, Journal of Sedimentary Research, v. 85, p. 1-5.

Pettijohn, F.J., 1949, Sedimentary rocks (first edition): Harper and Brothers, New York, 526 p.

Pickering, K. T., 1979, Possible retrogressive flow slide deposits from the Kongsfjord Formation: a Precambrian submarine fan, Finnmark, N. Norway: Sedimentology, v. 26, p. 295-306.

Pickering, K. T., and Hiscott, R. N., 1985, Contained (reflected) turbidity currents from the Middle Ordovician Cloridorme Formation, Quebec, Canada: an alternative to the antidune hypothesis: Sedimentology, v. 32, p. 373-394.

Pickering, K.T., 1987, Deep-marine foreland basin and forearc sedimentation: a comparative study from the Lower Palaeozoic Northern Appalachians, Quebec and Newfoundland, *in* Leggett, J.K., and Zuffa, G.G., eds., Marine Clastic Sedimentology, Springer, Dordrecht, p. 190-211.

Pierce, C. S., Haughton, P. D., Shannon, P. M., Pulham, A. J., Barker, S. P., and Martinsen, O. J., 2018, Variable character and diverse origin of hybrid event beds in a sandy submarine fan system, Pennsylvanian Ross Sandstone Formation, western Ireland: Sedimentology, v. 65, p. 952-992.

Piper, D. J. W., Cochonat, P., and Morrison, M. L., 1999, The sequence of events around the epicentre of the 1929 Grand Banks earthquake: Initiation of debris flows and turbidity current inferred from sidescan sonar: Sedimentology, v. 46, p. 79-97.

Piper, D.J., and Normark, W.R., 2009, Processes that initiate turbidity currents and their influence on turbidites: a marine geology perspective: Journal of Sedimentary Research, v. 79, p. 347-362.

Pirmez, C., Beaubouef, R. T., Friedmann, S. J., Mohrig, D. C., 2000, Equilibrium profile and base level in submarine channels: examples from Late Pleistocene systems and implications for the architecture of deep-water reservoirs, *in* Weimer, P., Slatt, R.M., Coleman, J., Rosen, N.C., Nelson, H., Bouma, A.H., Styzen, M.J., and Lawrence, D.T., eds., Deep-Water Reservoirs of the World: Gulf Coast Society of the Society of Economic Paleontologists and Mineralogists Foundation, 20th Annual Research Conference, p. 782-805.

Pirmez, C., Hiscou, R. N., and Kronen, J. K., 1997, Sandy turbidite successions at the base of channel-levee systems of the Amazon Fan revealed by FMS logs and cores: unraveling the facies architecture of large submarine fans, *in* Flood, R.D., Piper, D.J.W., Klaus, A., and Peterson, L.C., eds., Proceedings ODP, Scientific Results, v. 155, p. 7-22.

Pohl, F., Eggenhuisen, J.T., Tilston, M., and Cartigny, M.J. B., 2019, New flow relaxation mechanism explains scour fields at the end of submarine channels: Nature Communications, v. 10, p. 1-8.

Popović, N., 2016, Sedimentology and Stratigraphy of a Matrix-Poor to Matrix-Rich Depositional Continuum in Proximal Basin Floor Strata, Upper Kaza Group, Windermere Supergroup, B.C., Canada: Unpublished M.Sc. thesis, University of Ottawa, 138 p.

Potter, P.E., and Glass, H.D., 1958, Petrology and sedimentation of the Pennsylvanian sediments in southern Illinois: a vertical profile: Illinois State Geological Survey, Report of Investigations, v. 204, 60 p.

Powell, R.D., 1990, Glacimarine processes at grounding-line fans and their growth to ice-contact deltas, *in* Dowdeswell, J.A., and Scourse, J.D., eds., Glacimarine Environments: Process and Sediments: Geological Society of London, Special Publication, 53, p.53-73.

Pratson, L. E., Imran, J., Parker, G., Syvitski, J. P., and Hutton, E., 2000, Debris Flows versus Turbidity Currents: A Modeling Comparison of their Dynamics and Deposits, *in* Bouma, A.H., and Stone C.G., eds., Fine-grained Turbidite Systems, AAPG Memoir 72, p. 57-72.

Prélat, A., Hodgson, D. M., and Flint, S. S., 2009, Evolution, architecture and hierarchy of distributary deep-water deposits: a high-resolution outcrop investigation from the Permian Karoo Basin, South Africa: Sedimentology, v. 56, p. 2132–2154.

Pyles, D.R., and Jennette, D.C., 2009, Geometry and architectural associations of co-genetic debrite–turbidite beds in basin-margin strata, Carboniferous Ross Sandstone (Ireland): Applications to reservoirs located on the margins of structurally confined submarine fans: Marine and Petroleum Geology, v. 26, p. 1974-1996.

Rahmani, R.A., 1968, Greywackes with a primary matrix from the Viqueque Formation (upper Miocene-Pliocene), Timor: comment on a paper by M.G. Audley-Charles: Journal of Sedimentary Petrology, v. 38, p. 271-273.

Rashidi, M., Hetsroni, G., and Banerjee, S., 1990, Particle-turbulence interaction in a boundary layer: International Journal of Multiphase Flow, v. 16, p. 935-949.

Rassat, S.D., Gauglitz, P.A., Mahoney, L.A., Pires, R.P., Rector, D.R., Fort, J.A., Boeringa, G.K., Tran, D.N., Elmore, M.R., Buchmiller, W.C., and Kimura, M.L., 2014, Gas release due to Rayleigh-Taylor instability within sediment layers in Hanford Double-Shell experiments, modelling, and extrapolation to full scale: Pacific Northwest National Laboratory, United States Department of Energy, PNNL-23060 Rev.1, 242 p.

Reimer, T.O., 1972, Diagenetic reactions in early precambrian graywackes of the Barberton Mountain land (South Africa): Sedimentary Geology, v. 7, p. 263-282.

Revil, A., and Cathles III, L.M., 1999, Permeability of shaly sands: Water Resources Research, v. 35, p. 651-662.Ross, G.M., and Murphy, D.C., 1988, Transgressive stratigraphy, anoxia, and regional correlations Within the late Precambrian Windermere grit of the southern Canadian Cordillera: Geology, v. 16, p. 139-143.

Richardson, J.F., and Zaki, W.N., 1954, The sedimentation of a suspension of uniform spheres under conditions of viscous flow: Chemical Engineering Science, v. 3, p. 65-73.

Riva, J., 1968, Graptolite faunas from the Middle Ordovician of the Gaspé north shore. Naturaliste Canadien, v. 93, p. 1379-1400.

Romans, B. W., Normark, W. R., McGann, M. M., Covault, J. A., and Graham, S. A., 2009, Coarse-grained sediment delivery and distribution in the Holocene Santa Monica Basin, California: Implications for evaluating source-to-sink flux at millennial time scales: Geological Society of America Bulletin, v. 121, p. 1394-1408.

Ross, G. M., Bloch, J. D., and Krouse, H. R., 1995, Neoproterozoic strata of the southern Canadian Cordillera and the isotopic evolution of seawater sulfate: Precambrian Research, v. 73, p. 71-99.

Ross, G.M. and Arnott, R. W. C., 2007, Regional Geology of the Windermere Supergroup, Southern Canadian Cordillera and Stratigraphic Setting of the Castle Creek Study Area in Nilsen, T.H., Shew, R.D., Steffens, G.S., and Studlick, J.R.J., eds., Atlas of Deep-Water Outcrops: American Association of Petroleum Geologists, Studies in Geology 56, 15 p.

Ross, G.M., 1991, Tectonic setting of the Windermere Supergroup revisited: Geology, v. 19, p. 1125-1128.

Ross, G.M., and Murphy, D.C., 1988, Transgressive stratigraphy, anoxia, and regional correlations within the late Precambrian Windermere grit of the southern Canadian Cordillera: Geology, v. 16, p. 136-143.

Ross, G.M., and Parrish, R.R., 1991, Detrital zircon geochronology of metasedimentary rocks in the southern Omineca Belt, Canadian Cordillera: Canadian Journal of Earth Sciences, v. 28, p. 1254-1270.

Rubey, W.W., 1933, Settling velocities of gravel, sand and silt particles: American Journal of Science, v. 25, p. 325-338.

Russell, H.A.J., and Arnott, R.W.C., 2003, Hydraulic-jump and hyperconcentrated-flow deposits of a glacigenic subaqueous fan: Oak Ridges Moraine, southern Ontario, Canada: Journal of Sedimentary Research, v. 73, p. 887-905.

Rust, B.R., 1965, The sedimentology and diagenesis of Silurian turbidites in south-east Wigtownshire, Scotland: Scottish Journal of Geology, v. 1, p. 231–246.

Schwarz, E., and Arnott, R. W. C., 2007, Anatomy and evolution of a slope channel-complex set (Neoproterozoic Isaac Formation, Windermere Supergroup, southern Canadian Cordillera): implications for reservoir characterization: Journal of Sedimentary Research, v. 77, p. 89-109.

Schwarzacher, W., 1975, Chapter 5: Markov chains, in Sedimentation Models and Quantitative Stratigraphy: Amsterdam, Elsevier Scientific Publishing, Developments in Sedimentology 19, p. 91-121.

Shanmugam, G., 2006, Deep-water processes and facies models: Implications for sandstone petroleum reservoirs. Elsevier, 475 p.

Shanmugam, G., 2019, Slides, slumps, debris flows, turbidity currents, hyperpycnal flows, and bottom currents: Henry Bokuniewicz Patricia Yager Encyclopedia of Ocean Sciences, v. 4, p. 228-257.

Shannon, P.M., 1978, The petrology of some lower Palaeozoic greywackes from South-east Ireland; a clue to the origin of the matrix: Journal of Sedimentary Petrology, v. 48, p. 1185–1192.

Shepard, F. P., Marshall, N. F., and McLoughlin, P. A., 1975, Pulsating turbidity currents with relationship to high swell and high tides: Nature, v. 258, p. 704-706.

Sherman, I., 1953, Flocculent structure of sediment suspended in Lake Mead: Transactions American Geophysical Union, v. 34, p. 394–406.

Shrock, R.R., 1948, A classification of sedimentary rocks: The Journal of Geology, v. 56, p. 118–129.

Skempton, A. W., 1969, The consolidation of clays by gravitational compaction. Quarterly: Journal of the Geological Society of London, v. 125, p. 373-408.

Smits, A., 2000, A physical introduction to fluid mechanics: John Wiley and Sons Incorporated, 338 p.

Smith, M.D., Arnott, R.W.C., Ross, G.M. and Stockmal, G., 2014, The Old Fort Point Formation: Redefinition and formal subdivision of a distinctive stratigraphic marker in the Neoproterozoic Windermere Supergroup, southern Canadian Cordillera: Bulletin of Canadian Petroleum Geology, v. 62, p. 1-13.

Southern, S.J., Patacci, M., Felletti, F., and McCaffrey, W.D., 2015. Influence of flow containment and substrate entrainment upon sandy hybrid event beds containing a co-genetic mud-clast-rich division: Sedimentary Geology, v. 321, p. 105-122.

Southern, S.J., Kane, I.A., Warchoł, M.J., Porten, K.W., and McCaffrey, W.D., 2017, Hybrid event beds dominated by transitional-flow facies: character, distribution and significance in the Maastrichtian Springar Formation, north-west Vøring Basin, Norwegian Sea: Sedimentology, v. 64, p. 747-776.

Spychala, Y. T., Hodgson, D. M., Prélat, A., Kane, I. A., Flint, S. S., and Mountney, N. P., 2017a, Frontal and lateral submarine lobe fringes: comparing sedimentary facies, architecture and flow processes: Journal of Sedimentary Research, v. 87, p. 75-96.

Spychala, Y.T., Hodgson, D.M., and Lee, D.R., 2017b, Autogenic controls on hybrid bed distribution in submarine lobe complexes. Marine and Petroleum Geology, v. 88, p. 1078-1093.

Stewart, J.H., 1972, Initial deposits in the Cordilleran Geosyncline: evidence of a Late Precambrian (<850 m.y.) continental separation: Geological Society of America Bulletin, v. 83, p. 1345-1360.

St-Julien, P., and Hubert, C., 1975, Evolution of the Taconian orogen in the Quebec Appalachians: American Journal of Science, v. 275, p. 337-362.

Straub, K. M., Mohrig, D., McElroy, B., Buttles, J., and Pirmez, C., 2008, Interactions between turbidity currents and topography in aggrading sinuous submarine channels: A laboratory study: Geological Society of America Bulletin, v. 120, p. 368-385.

Sumner, E.J., Talling, P.J., and Amy, L.A., 2009, Deposits of flows transitional between turbidity current and debris flow: Geology, v. 37, p. 991-994.

Sylvester, Z., and Lowe, D.R., 2004, Textural trends in turbidites and slurry beds from the Oligocene flysch of the East Carpathians, Romania: Sedimentology, v. 51, p. 945–972.

Talling, P. J., 2013, Hybrid submarine flows comprising turbidity current and cohesive debris flow: Deposits, theoretical and experimental analyses, and generalized models: Geosphere, v. 9, p. 460-488.

Talling, P. J., Amy, L. A., Wynn, R. B., Peakall, J., and Robinson, M, 2004, Beds comprising debrite sandwiched within co-genetic turbidite: Origin and widespread occurrence in distal depositional environments: Sedimentology, v. 51, p. 163-194.

Talling, P.J., Wynn, R.B., Masson, D.G., Frenz, M., Cronin, B.T., Schiebel, R., Akhmetzhanov, A.M., Dallmeier-Tiessen, S., Benetti, S., Weaver, P.P.E., and Georgiopoulou, A., 2007, Onset of submarine debris flow deposition far from original giant landslide: Nature, v. 450, p. 541-544.

Talling, P.J., Wynn, R.B., Schmmidt, D.N., Rixon, R., Sumner, E., and Amy, L., 2010, How did thin submarine debris flows carry boulder-sized intraclasts for remarkable distances across low gradients to the far reaches of the Mississippi Fan?: Journal of Sedimentary Research, v. 80, p. 829-851.

Talling, P.J., Malgesini, G., Sumner, E.J., Amy, L.A., Felletti, F., Blackbourn, G., Nutt, C., Wilcox, C., Harding, I.C., and Akbari, S., 2012a, Planform geometry, stacking pattern, and extrabasinal origin of low strength and intermediate strength cohesive debris flow deposits in the Marnoso-arenacea Formation, Italy: Geosphere, v. 8, p. 1207–1230.

Talling, P.J., Masson, D.G., Sumner, E.J., and Malgesini, G., 2012b, Subaqueous sediment density flows: Depositional processes and deposit types: Sedimentology v. 59, p. 1937-2003.

Talling, P.J., Malgesini, G., and Felletti, F., 2013, Can liquefied debris flows deposit clean sand over large areas of sea floor? Field evidence from the Marnoso-arenacea Formation, Italian Apennines: Sedimentology, v. 60, p. 720-762.

Talling, P.J., Clare, M.L., Urlaub, M., Pope, E., Hunt, J.E., and Watt, S.F., 2014, Large submarine landslides on continental slopes: geohazards, methane release, and climate change: Oceanography, v. 27, p. 32-45.

Tallman, S.L., 1949, Sandstone types: their abundance and cementing agents: The Journal of Geology, v. 57, p. 582–591.

Tan, K.H., 1982, Principles of Soil Chemistry: New York, Marcel Dekker, 267 p.

Terlaky, V., and Arnott, R. W. C., 2014, Matrix-rich and associated matrix-poor sandstones: Avulsion splays in slope and basin-floor strata: Sedimentology, v. 61, p. 1175-1197.

Terlaky, V., and Arnott, R. W. C., 2016, The control of terminal-splay sedimentation on depositional patterns and stratigraphic evolution in avulsion-dominated, unconfined, deep-marine basin-floor systems: Journal of Sedimentary Research, v. 86, p. 786-799.

Terlaky, V., Rocheleau, J., and Arnott, R. W. C., 2016, Stratal composition and stratigraphic organization of stratal elements in an ancient deep-marine basin-floor succession, Neoproterozoic Windermere Supergroup, British Columbia, Canada: Sedimentology, v. 63, p. 136-175.

Thomas, C.U., and Muthukumar, M., 1991a, Convergence of multiple scattering series for two-body hydrodynamic effects on shear viscosity of suspensions of spheres: The Journal of Chemical Physics, v. 94, p. 4557-4567.

Thomas, C.U., and Muthukumar, M., 1991b, Three-body hydrodynamic effects on viscosity of suspensions of spheres. The Journal of Chemical Physics, v. 94, p. 5180-5189.

Tilston, M., Arnott, R.W., Rennie, C.D., and Long, B., 2015, The influence of grain size on the velocity and sediment concentration profiles and depositional record of turbidity currents. Geology, v. 43, p. 839-842.

Tolhurst, T. J., Gust, G., and Paterson, D. M., 2002, The influence of an extracellular polymeric substance (EPS) on cohesive sediment stability: Proceedings in Marine Science, v. 5, p. 409-425.

Tripsanas, E.K., Bryant, W.R., and Phaneuf, B.A., 2004, Slope-instability processes caused by salt movements in a complex deep-water environment, Bryant Canyon area, northwest Gulf of Mexico: American Association of Petroleum Geologists Bulletin, v. 88, p. 801-823.

Tucker, M.E., 2001, Sedimentary Petrology: An Introduction to the Origin of Sedimentary Rocks: John Wiley and Sons, 272 p.

Twichell, D. C., Kenyon, N. H., Parson, L. M., and McGregor, B. A., 1991, Depositional Patterns of the Mississippi Fan Surface: Evidence from GLORIA II and High-Resolution Seismic Profiles, *in* Weimer, P., and Link, M.H., eds., Seismic facies and sedimentary processes of submarine fans and turbidite systems: Springer, New York, p. 349-363.

Van Andel, T.H., 1958, Origin and classification of Cretaceous, Paleocene, and Eocene sandstones of western Venezuela: American Association of Petroleum Geologists Bulletin, v. 42, p. 734-763.

Vittori, J., Morash, A., Savoye, B., Marsset, T., Lopez, M., Droz, L., and Cremer, M., 2000, The Quaternary Congo deep-sea fan: preliminary results on reservoir complexity in turbiditic systems using 2D high resolution seismic and multibeam data, *in* Deep-Water Reservoirs of the World: Gulf Coast Section SEPM 20th Annual Research Conference, p. 1045-1058.

Wang, Z., and Plate, E.C.J., 1996, A preliminary study on the turbulence structure of flows of non-Newtonian fluid: Journal of Hydraulic Research, v. 34, p. 345-361.

Wang, Z.Y., Larsen, P., Nestmann, F., and Dittrich, A., 1998, Resistance and drag reduction of flows of clay suspensions: Journal of Hydraulic Engineering, v. 124, p. 41-49.

Wang, Z.Y., Larsen, P., Nestmann, F., and Dittrich, A., 1998. Resistance and drag reduction of flows of clay suspensions. Journal of Hydraulic Engineering, v. 124, p. 41-49.

Warren, M.J., 1997, Crustal Extension and Subsequent Crustal Thickening Along the Cordilleran Rifted Margin of Ancestral North America, Western Purcell Mountains, Southeastern British Columbia: Unpublished Ph.D. thesis, Queen's University, 361 p.

Wearmouth, C., 2018, Stratal, Temporal and Physical Origin of Matrix-Poor to Matrix-Rich Sandstones, Neoproterzoic Windermere Supergroup, British Columbia, Canada: Unpublished MSc. thesis, University of Ottawa, 152 p.

Weirich, F.H., 1988, Field evidence for hydraulic jumps in subaqueous sediment gravity flows: Nature, v. 332, p. 626-629

Wellner, R., Beaubouef, R., Van Wagoner, J., Roberts, H., and Sun, T., 2005, Jet-plume depositional bodies—the primary building blocks of Wax Lake Delta, Gulf Coast: Association of Geological Societies Transactions, v. 55, p. 867-909.

Wilson, M.D., and Pittman, E.D., 1977, Authigenic clays in sandstones; recognition and influence on reservoir properties and paleoenvironmental analysis: Journal of Sedimentary Petrology, v. 47, p. 3–31.

Winsemann, J., Hornung, J.J., Meinsen, J., Asprion, U., Polom, U., Brandes, C., Bubmann, M., and Weber, C., 2009, Anatomy of a subaqueous ice-contact fan and delta complex, Middle Pleistocene, North-west Germany: Sedimentology, v. 56, p. 1041-1076.

Winterwerp, J.C., and van Kesteren, W.G., 2004. Introduction to the physics of cohesive sediment dynamics in the marine environment. Elsevier, 576 p.

Wood, A., and Smith, A.J., 1958, The sedimentation and sedimentary history of the Aberystwyth Grits (Upper Llandoverian): Quarterly Journal of the Geological Society, v. 114, p. 163–195.

Woodland, A.W., 1938, Petrological studies in the Harlech Grit Series of Merionethshire. II: the petrography and petrology of some of the Grits: Geological Magazine, v. 75, p. 440–454.

Wright, L.D., 1977, Sediment transport and deposition at river mouths: a synthesis: Geological Society of America, Bulletin, v. 88, p. 857-868.

Xu, J. P., Noble, M. A., and Rosenfeld, L. K., 2004, In-situ measurements of velocity structure within turbidity currents: Geophysical Research Letters, v. 31, L09311.

APPENDICES

APPENDIX A1–A10: INTERPRETED DRONE PHOTOMOSAICS AND ASSOCIATED STRATIGRAPHIC CORRELATION PANELS OF THE WINDERMERE SUPERGROUP AND THE CLORIDORME FORMATION.

APPENDIX B: TERNARY DIAGRAM SHOWING FRAMEWORK GRAIN COMPOSTION OF THE LITHOFACIES.

APPENDIX C: GRAIN-SIZE DISTRIBUTION (MODE AND D90) AND MATRIX CONTENT OF THE LITHOFACIES.

APPENDIX D: ROSE DIAGRAMS SHOWING PAELOCURRENT DIRECTIONS IN THE CLORIDORME FORMATION

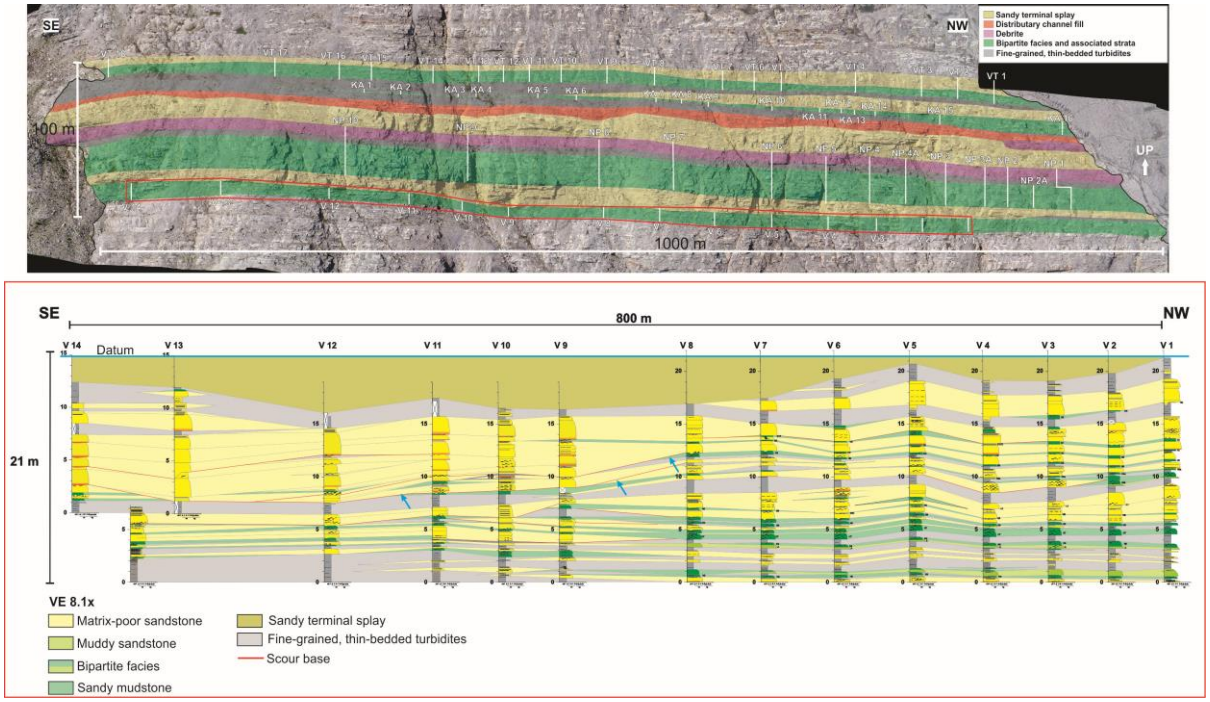

Appendix A1: Interpreted photomosaic (top figure) of the study area in the Upper Kaza Group, Windermere Supergroup. Red polygon in the top figure shows the location of the stratigraphic correlation panel (bottom figure). Correlation panel (VE 8.1X) shows a succession of matrix-rich and associated matrix-poor strata erosively overlain by a sandy terminal splay. Red lines highlight major scour surfaces. Note that in the upper half of the correlation panel, intercalated matrix-rich and matrix-poor strata (right side of the panel) are truncated (blue arrows) by several-meter-deep scours filled with matrix-poor strata.

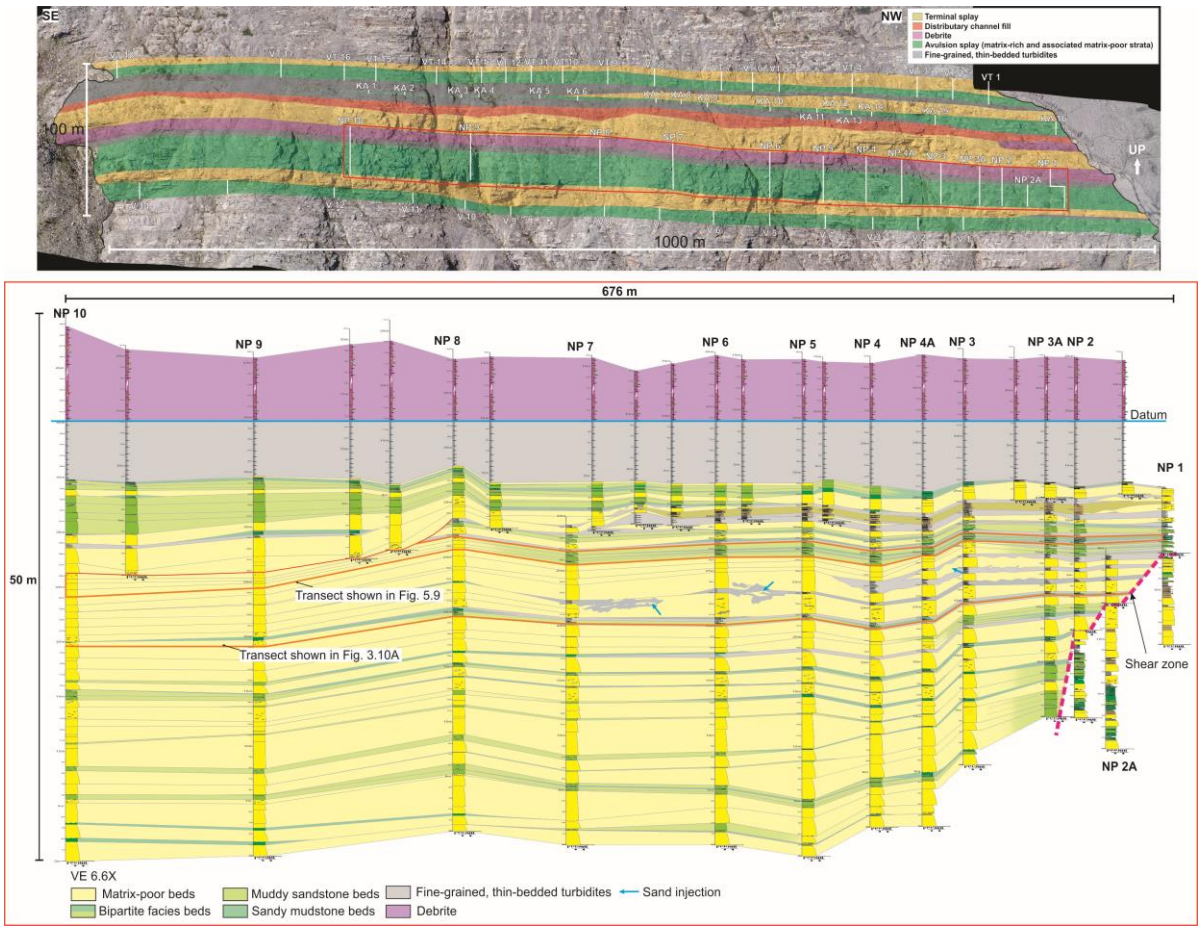

Appendix A2: Interpreted photomosaic (top figure) of the study area in the Upper Kaza Group, Windermere Supergroup. Red polygon in the top figure shows the location of the stratigraphic correlation panel (bottom figure). Correlation panel (VE 6.6X) comprises matrix-rich and associated matrix-poor strata overlain by thin-bedded turbidites and capped by a debrite. Matrix-rich strata show a proximal to distal trend from left to right across the correlation panel. Note that between Logs NP3 and NP7 strata have been locally disrupted by sand injection (blue arrows).

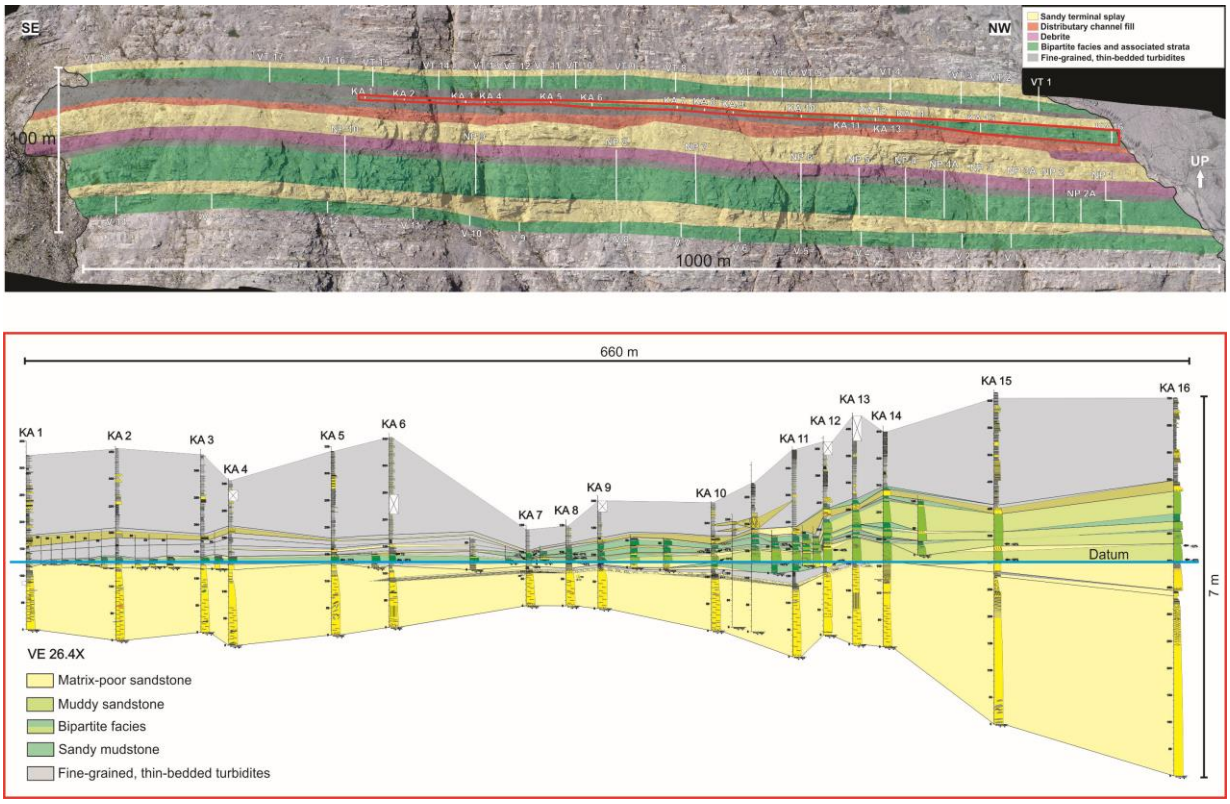

Appendix A3: Interpreted photomosaic (top figure) of the study area in the Upper Kaza Group, Windermere Supergroup. Red polygon in the top figure shows the location of the stratigraphic correlation panel (bottom figure). Correlation panel (VE 26.4X) of matrix-rich and associated matrix-poor strata overlain by a succession of thin-bedded turbidites. Note that the matrix-rich strata show a proximal to distal trend from right to left across the correlation panel.

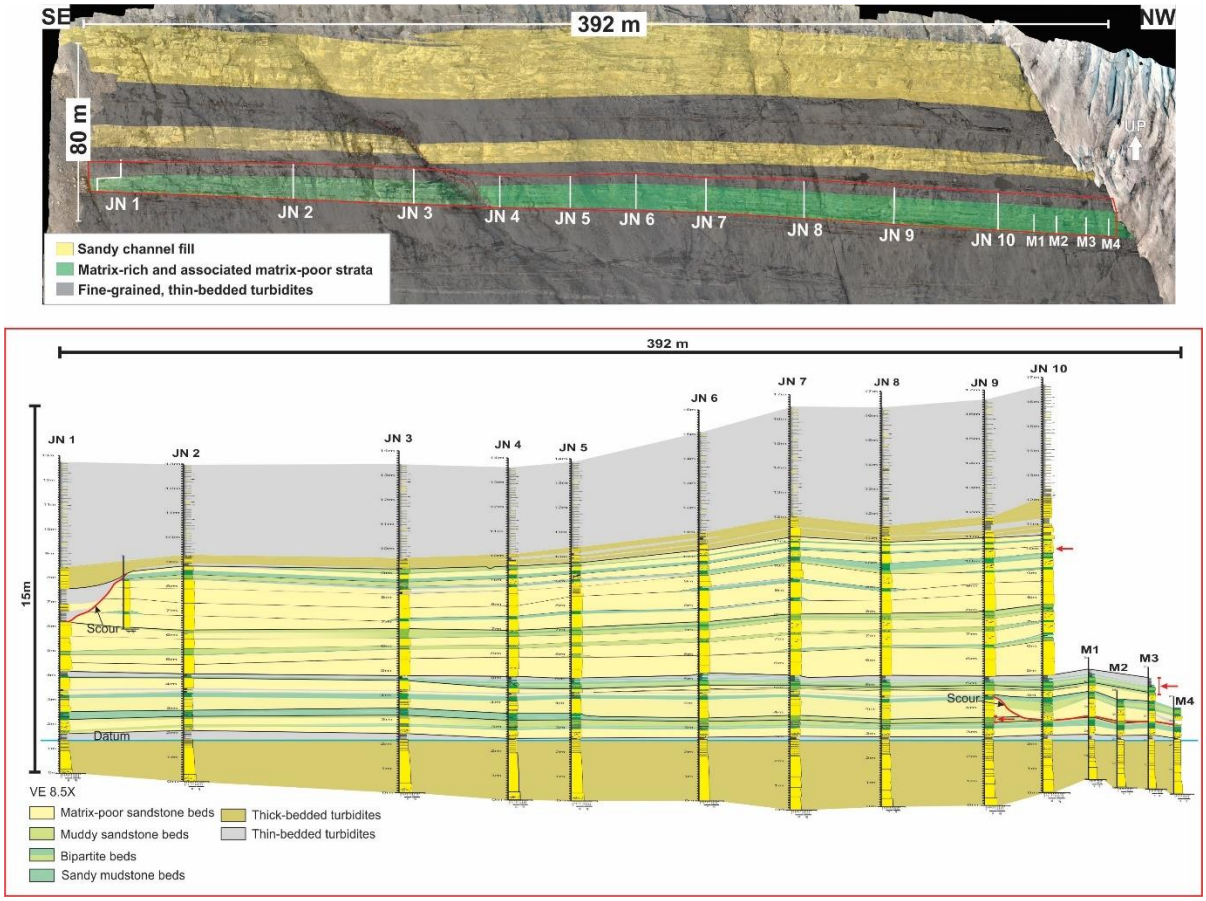

Appendix A4: Interpreted photomosaic (top figure) of a study area in the Isaac Formation, Windermere Supergroup. Red polygon in the top figure shows the location of the stratigraphic correlation panel (bottom figure). Correlation panel (VE 8.5X) showing matrix-rich and associated matrix-poor strata sandwiched between thick- and thin-bedded, traction-structured turbidites. Red lines highlight major scour surfaces. Matrix-rich strata show a general proximal to distal trend from left to right, but also from right to left (red arrows). Red lines highlight major scour surfaces. Note, the top scour postdates the deposition of the stratigraphic unit; however, the lower scour is more problematic and requires further investigation.

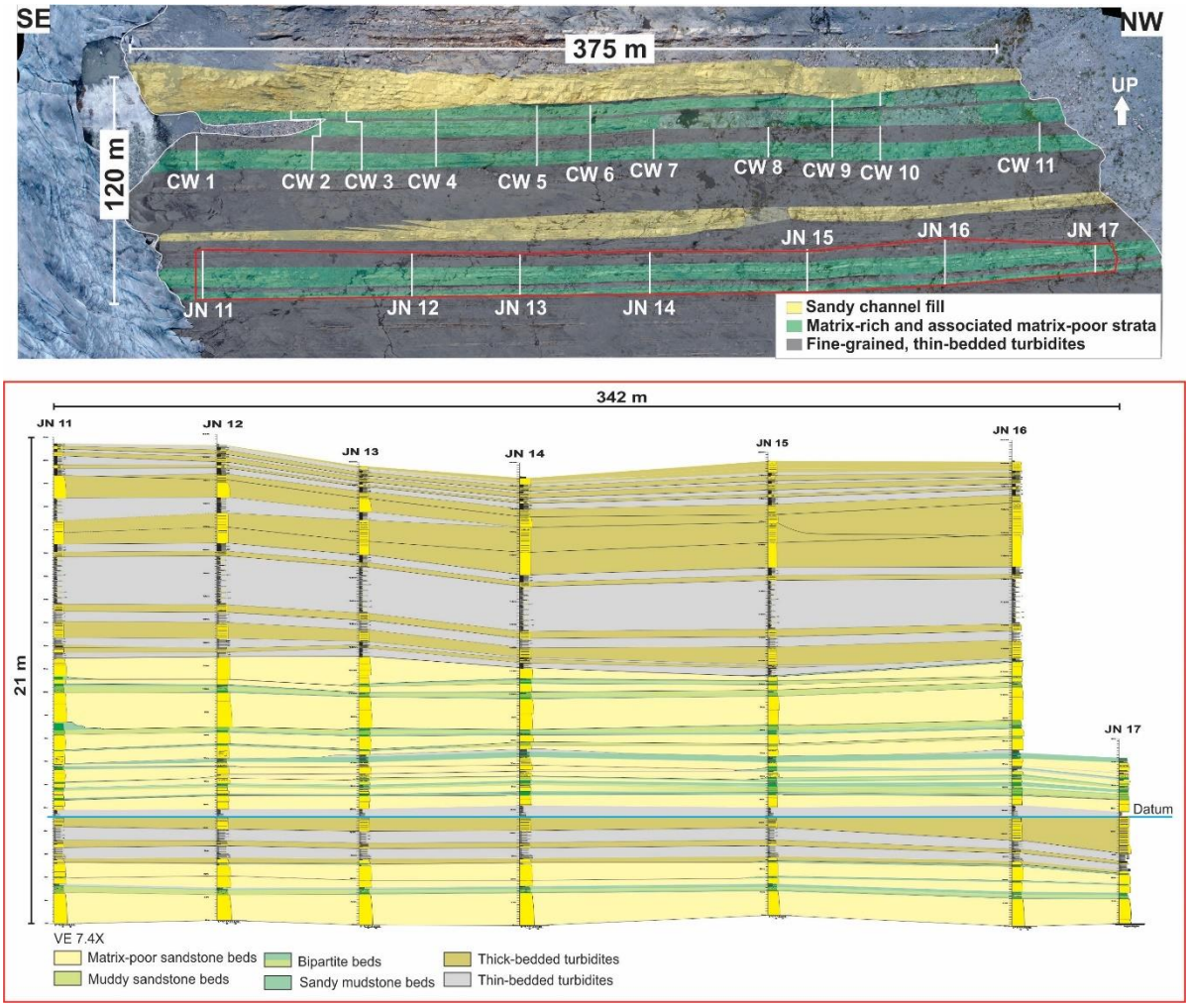

Appendix A5: Interpreted photomosaic (top figure) of a study area in the Isaac Formation, Windermere Supergroup. Red polygon in the top figure shows the location of the stratigraphic correlation panel (bottom figure). Correlation panel (VE 7.4X) showing units of matrix-rich and associated matrix-poor strata interspersed between thin- and thick-bedded traction-structured turbidites. Matrix-rich strata show a general proximal to distal trend from left to right.

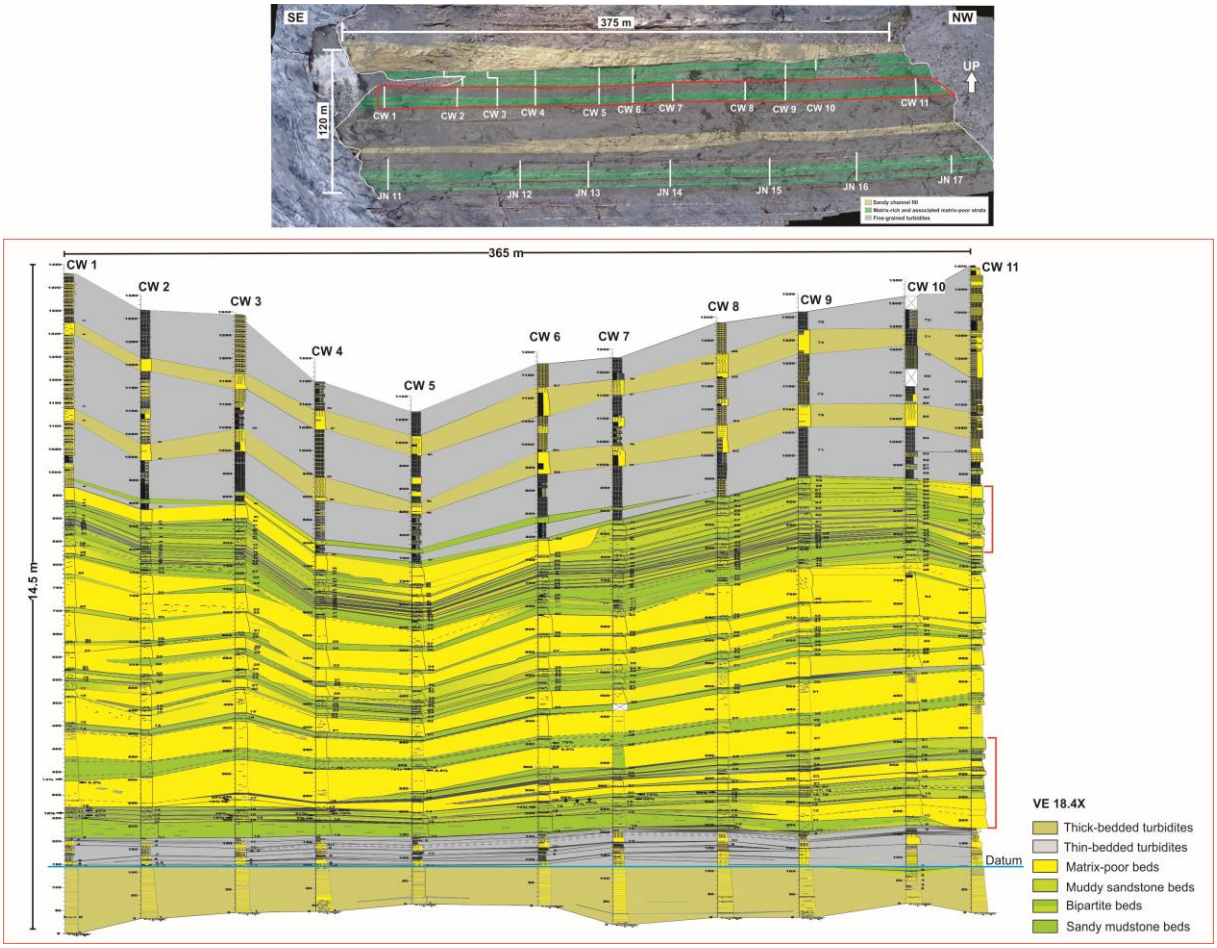

Appendix A6: Interpreted photomosaic (top figure) of a study area in the Isaac Formation, Windermere Supergroup. Red polygon in the top figure shows the location of the stratigraphic correlation panel (bottom figure). Correlation panel (VE 18.4X) shows several-m-thick succession of matrix-rich and associated matrix-poor strata sandwiched between thin- and thick-bedded, traction-structured turbidites. Matrix-rich strata show a general proximal to distal trend from left to right but also from right to left (red brackets).

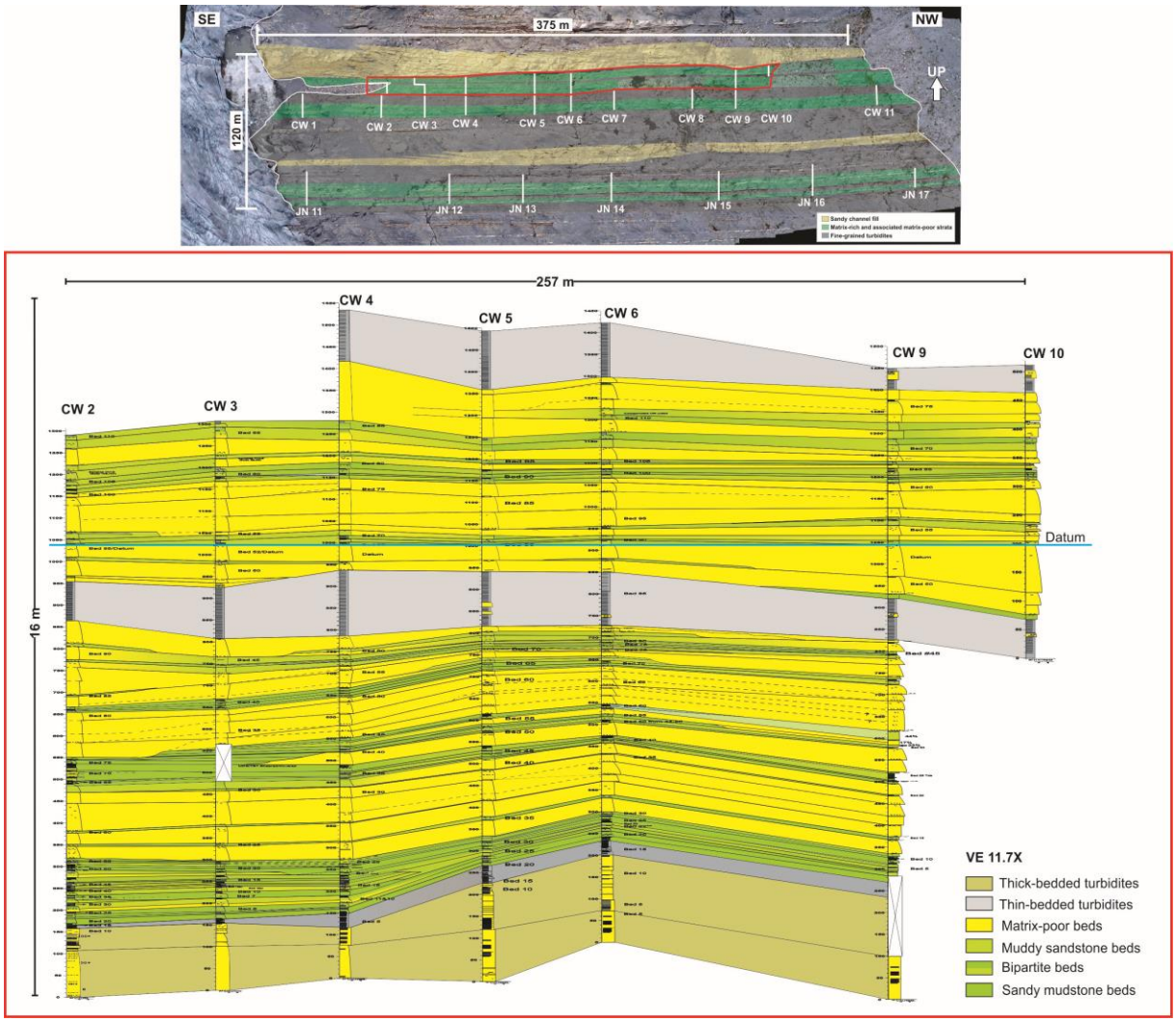

Appendix A7: Interpreted photomosaic (top figure) of a study area in the Isaac Formation, Windermere Supergroup. Red polygon in the top figure shows the location of the stratigraphic correlation panel (bottom figure). Correlation panel (VE 11.7X) comprises units of matrix-rich and associated matrix-poor strata bounded by thin- and thick-bedded traction-structured turbidites. Matrix-rich strata show a general proximal to distal trend from left to right.

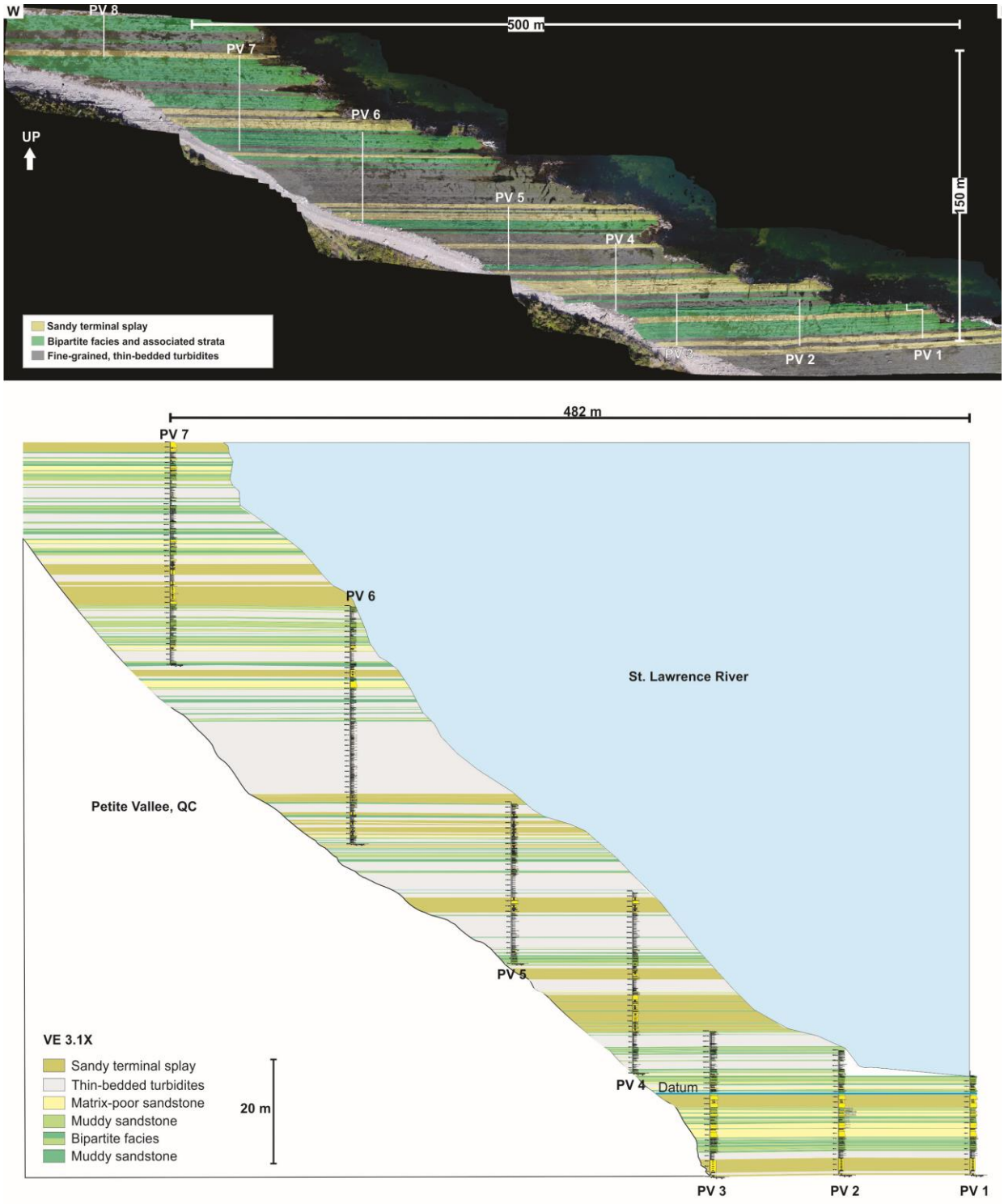

Appendix A8: Interpreted photomosaic and accompanying stratigraphic correlation panel (VE 3.1X) of an ~ 150 m-thick unit in the Petite Vallée Member, Cloridorme Formation. Note that matrix-rich and associated matrix poor strata are intercalated between sandy terminal splay deposits and units of thin-bedded turbidites. The correlation panel is oriented parallel to the main paleoflow direction (to the west).

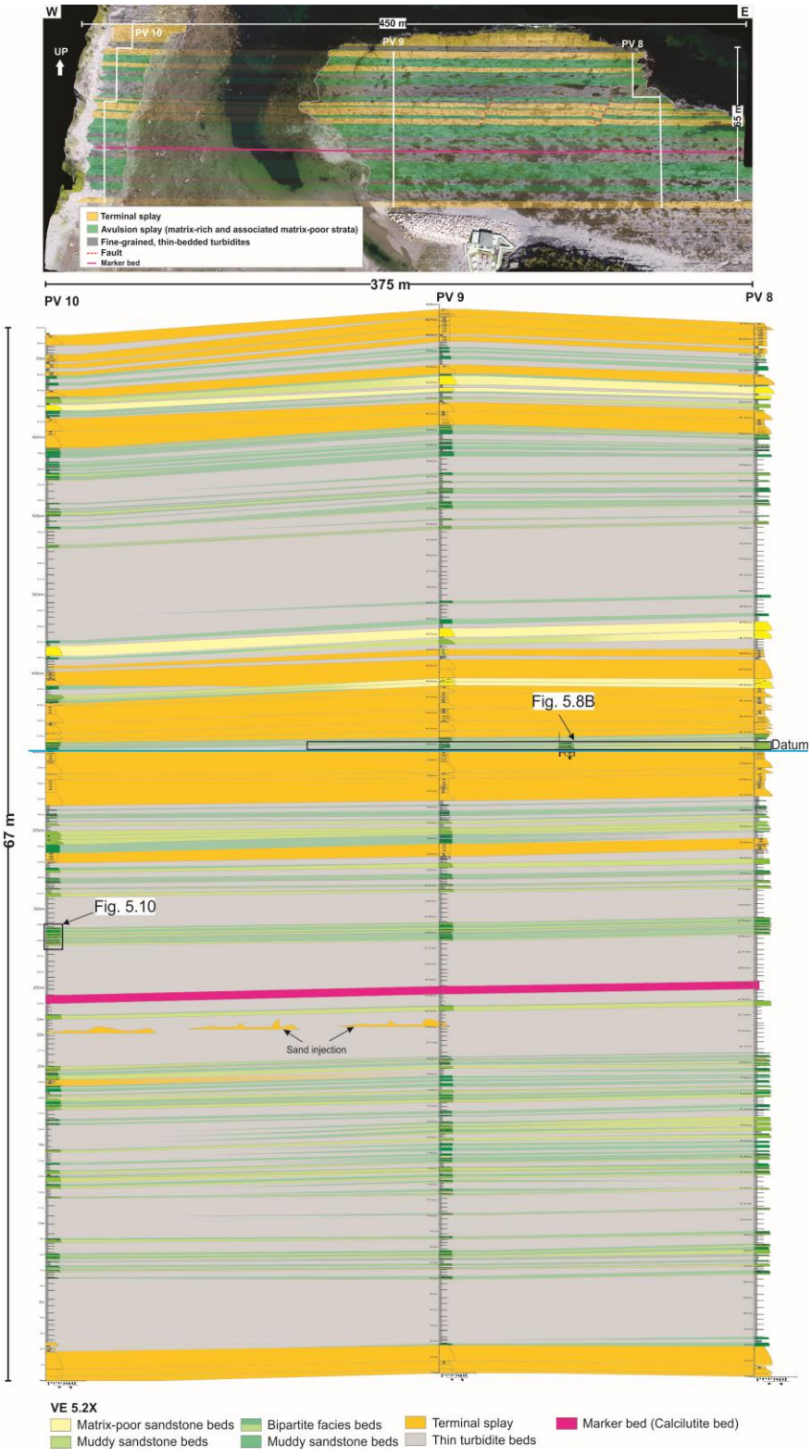

Appendix A9: Interpreted photomosaic and accompanying stratigraphic correlation panel (VE 5.2X) in the Petite Vallée Member, Cloridorme Formation. Note that matrix-rich and associated matrix-poor strata are intercalated with sandy terminal splay deposits and units made up of thin-bedded turbidites and show a proximal to distal trend toward the right (west), which is parallel to the main paleoflow direction (to the west).

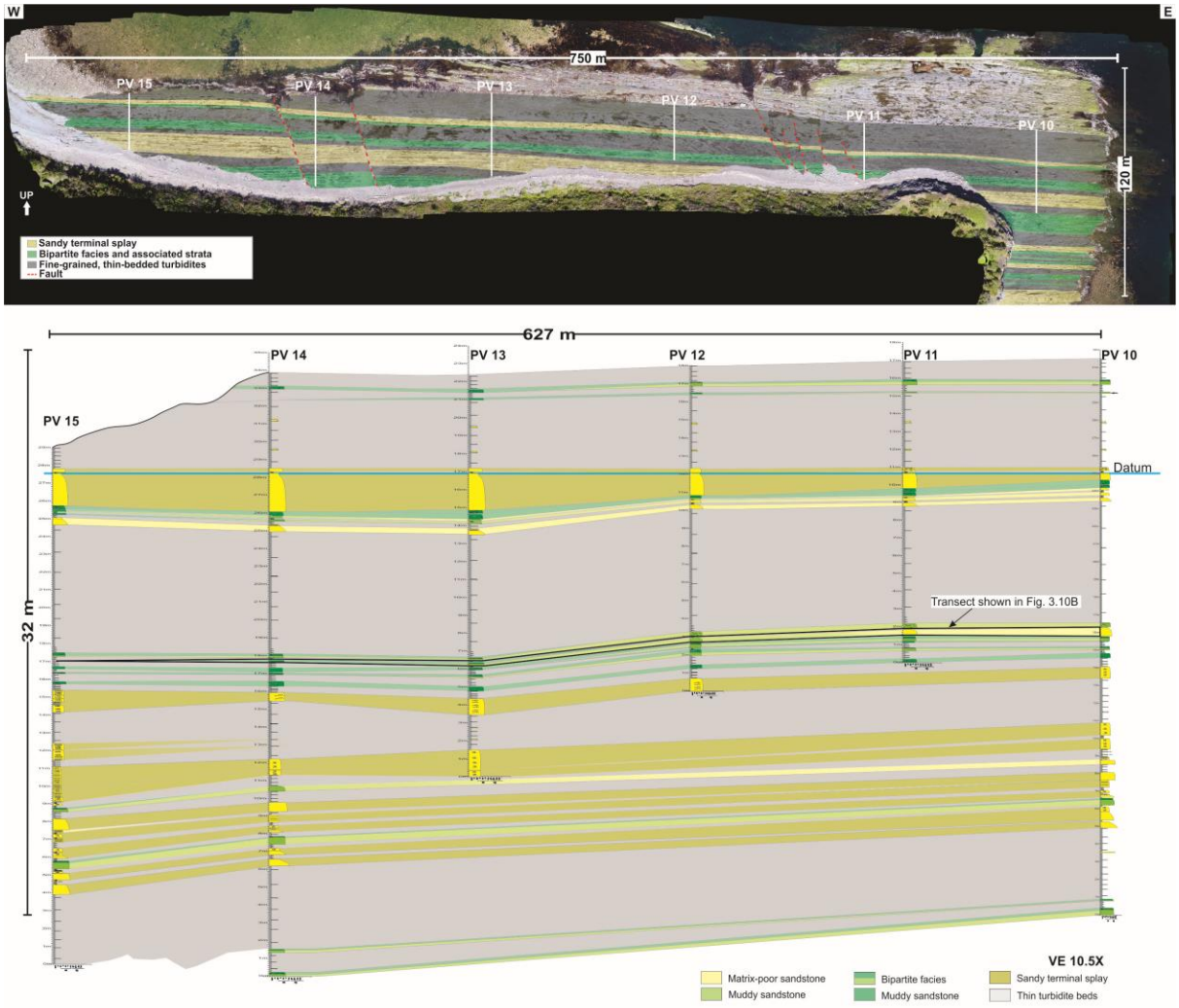

Appendix A10: Interpreted photomosaic and accompanying stratigraphic correlation panel (VE 10.5X) of matrix-rich and associated matrix poor strata intercalated between sandy terminal splay deposits and units of thin-bedded turbidites. Proximal to distal trend in the matrix-rich and matrix-poor units is toward the right (west), which parallels the main paleoflow direction.

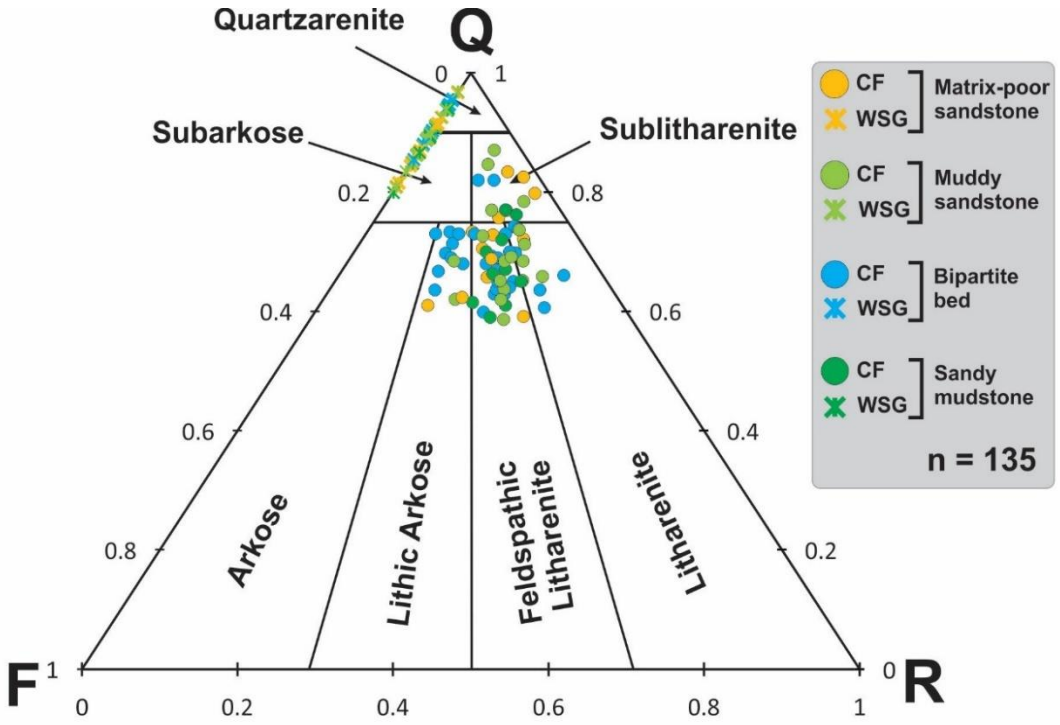

Appendix B: Framework grain composition of the four main lithofacies plotted on a quartz (Q), feldspar (F), rock fragment (R) diagram (Folk 1980). 'n' refers to the number of samples; crosses indicate samples from the Windermere Supergroup (WSG) and circles the Cloridorme Formation (CF). Note the quartz-rich composition of the passive margin WSG compared to the more mineralogically immature composition of foreland-basin strata in the Cloridorme Formation.

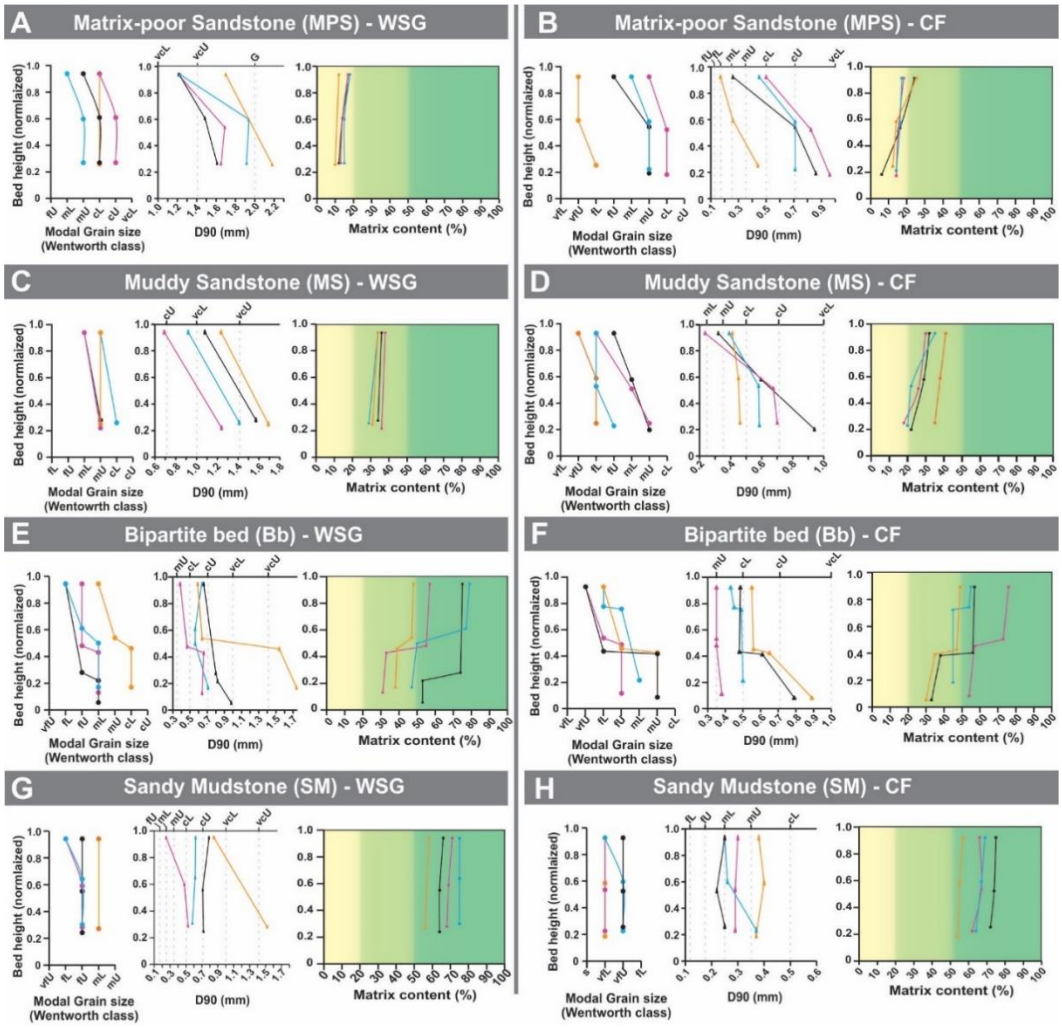

Appendix C: Grain-size distribution (mode and D90) and matrix content of four representative beds sampled in each of the four main lithofacies in the Windermere Supergroup (WSG; left column) and Cloridorme Formation (CF; right column). Positions where data were measured are normalized by total bed thickness. Matrix versus framework grain percentages were calculated by counting ≥ 300 points in each thin section; grain size was determined by measuring the longest dimension of each framework grain. For each lithofacies the colors (black, blue, orange and pink) correspond to data from each of the four different beds. Note that the modal grain-size in all lithofacies either decreases slightly upward or shows no change. A and B) In matrix-poor sandstone (MPS), D90 (coarse fraction) decreases upward, whereas the matrix content changes negligibly. C and D) In muddy sandstone (MS), D90 decreases upward, excepting a single bed (orange) in the CF that shows little change. Matrix content shows negligible upward change in the WSG but increases slightly in the CF. E and F) Bipartite beds (Bb): note the abrupt grain size decrease and concomitant increase in the matrix content across the Bb interface. In the lower part of Bb, D90 exhibits either no upward change or subtle to prominent upward fining, whereas in the upper part, D90 shows only slight upward fining or no change. G and H) In sandy mudstone (SM), D90 either decreases upward or changes little. Matrix content changes negligibly in all SM beds.

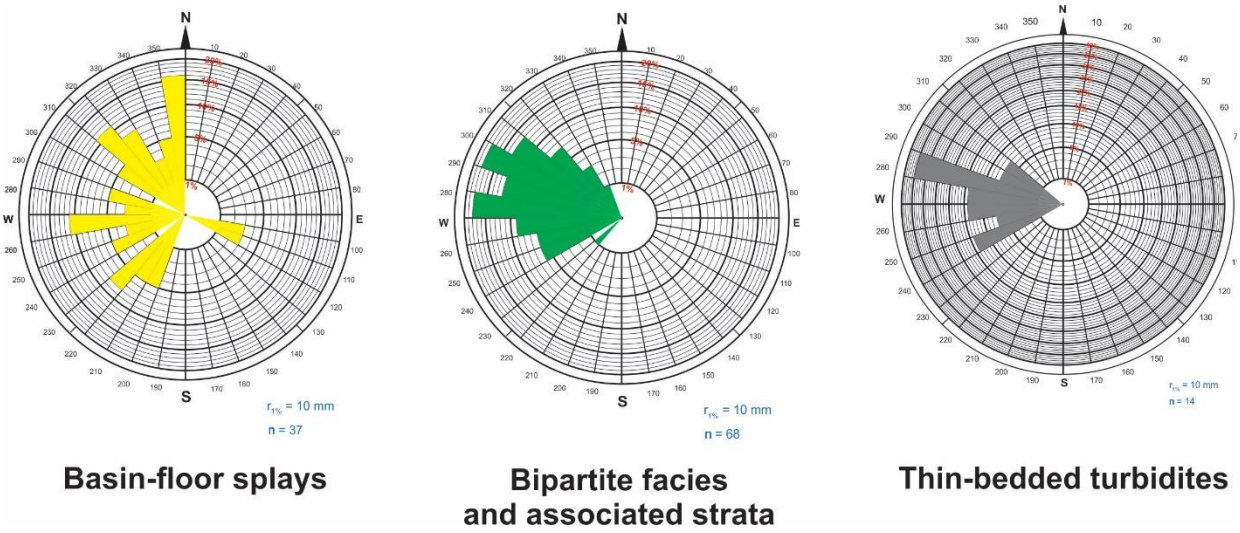

Appendix D: Rose diagrams showing paelocurrent directions in the Cloridorme Formation.